# Investigation on structure and properties of bioactive glass materials for therapeutic applications

# Thesis Submitted to DELHI TECHNOLOGICAL UNIVERSITY

For the Award of the Degree of DOCTOR OF PHILOSOPHY

Submitted By
DIVYA GOEL
2K20/PHDAC/02

Under the Guidance of Dr. Deenan Santhiya



Department of Applied Chemistry
Delhi Technological University
Shahbad Daulatpur, Main Bawana Road,
Delhi- 110042, INDIA
October 2025

# Copyright © Delhi Technological University-2024 ALL RIGHTS RESERVED

#### **DELHI TECHNOLOGICAL UNIVERSITY**

(Formerly Delhi College of Engineering)

#### **Department of Applied Chemistry**

Shahbad Daulatpur, Bawana Road, Delhi- 110042, India



#### **DECLARATION**

This is to declare that the research work embodied in this thesis entitled "Investigation on structure and properties of Bioactive Glass materials for Therapeutic Applications" submitted to the Delhi Technological University is an original work and carried out by me for the degree of Doctor of Philosophy under the supervision of Dr. Deenan Santhiya, Associate Professor, Department of Applied Chemistry. This thesis is a contribution to my original research work. The extent of information derived from the existing literature has been indicated in the body of the thesis at appropriate places giving the source of information. Every effort has been made to make sure that the scientific contributions of others are appropriately cited. To the best of my knowledge, this research work has not been submitted in part or full for award of any degree or diploma in Delhi Technological University or in any other university/institution.

Date: Divya Goel

Research Scholar Reg. No. 2K20/PHDAC/02

#### **DELHI TECHNOLOGICAL UNIVERSITY**

(Formerly Delhi College of Engineering)

Shahbad Daulatpur, Bawana Road Delhi- 110042, India



#### CERTIFICATE

This is to certify that the thesis entitled "Investigation on structure and properties of Bioactive Glass materials for Therapeutic Applications" submitted to the Delhi Technological University, Delhi-110042, in fulfilment of the requirement for the award of the degree of Doctor of Philosophy has been carried out by the candidate, Ms. Divya Goel, (Reg. No. 2K20/PHDAC/02) under the supervision of Dr. Deenan Santhiya, Associate Professor, Department of Applied Chemistry. It is further certified that the work embodied in this thesis has neither partially nor fully been submitted to any other university or institution for the award of any degree or diploma.

Dr. Deenan Santhiya

Supervisor

Department of Applied Chemistry

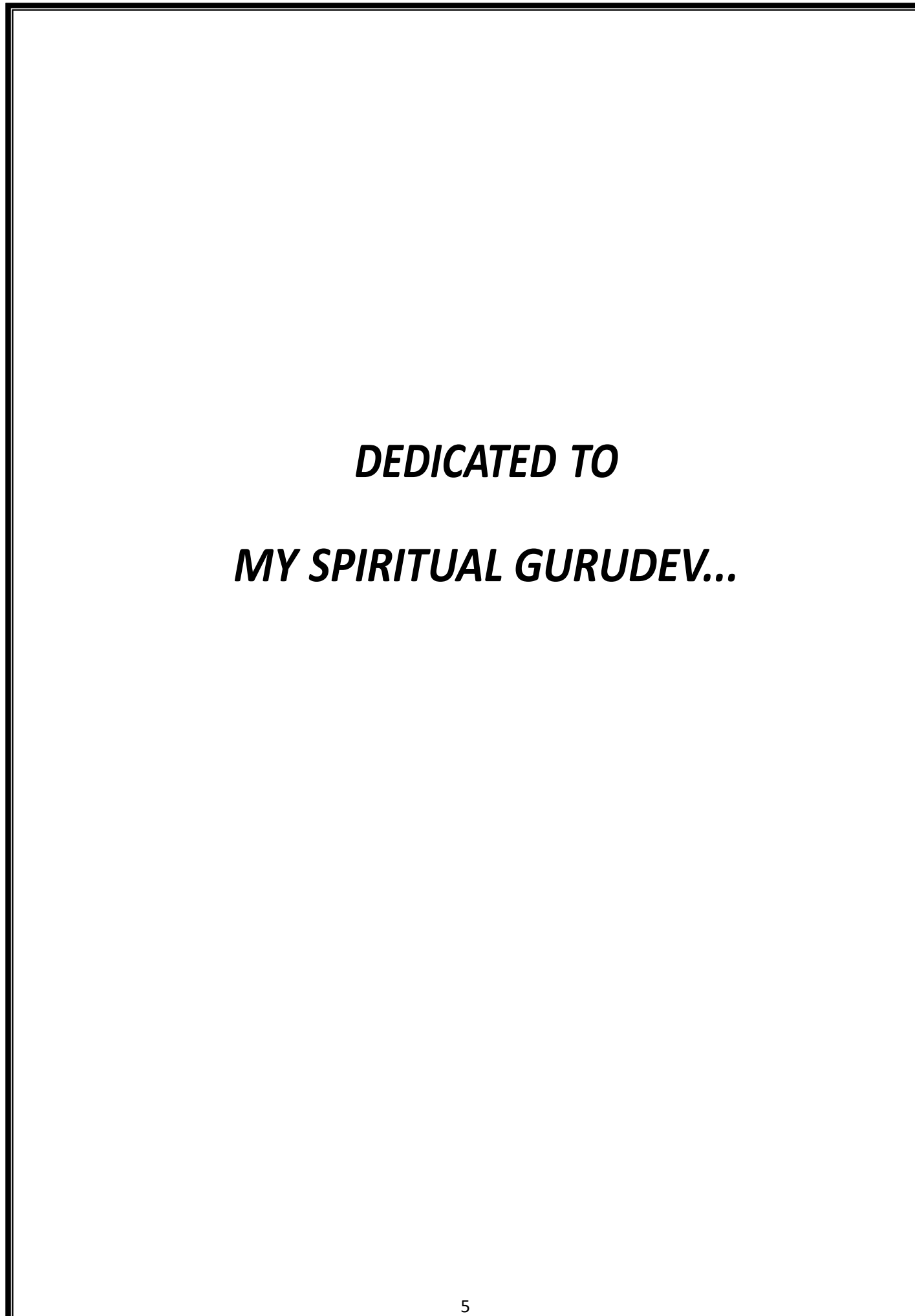
Delhi Technological University, Delhi

**Prof. Anil Kumar** 

Head of the Department

Department of Applied Chemistry

Delhi Technological University, Delhi



#### Acknowledgment

"I am blessed with everything I need. I am working hard towards everything I want, and most ofall, I appreciate & Thank God for what I have."

I would like to thank the Almighty God for the successful completion of my research work.

Coming to the end of my Ph.D., I pour out my thoughts and hope that reflect the deep gratitude I hold for people that have made it possible for me to surmount this hurdle and achieve my dream.

The life of a Ph.D student is anchored by their supervisor and I am extremely fortunate to have **Dr.Deenan**Santhiya as my mentor, an individual with years of experience and possibly the most encouraging person I have come across in my educational years. She is not only the person behindinnumerable success stories of her doctoral students but also the one who established a pioneeringresearch ethics amongst young researchers. A life filled with such scholarly achievements is only possible when the person is immensely talented and truly committed to their cause. I have witnessed her humility in response to gratitude, strength in face of adversity, decisiveness in matters of dilemma and undistinguished love for science at every step. Her scientific aptitude and clarity of even complex concepts helped me in testing times of research while her ability to motivate students to discover their hidden talents has introduced me to my own strengths. Her extensive generosity taught me the value of being generous, and her promptness taught me the value of time management. Her concept of "work hard, play hard" has been inspiring throughout the duration of my association with her. I am incrediblyfortunate to have been trained and introduced to the world of research under her guidance.

I am extremely grateful to Professor Anil. Kumar (Head, Department of Applied Chemistry) for providing the necessary research facilities and an excellent working environment in the department. His work exhibits the ideal fusion of punctuality, enthusiasm, commitment, organization, and excellent administrative abilities. We are fortunate to have a visionary like him in our department.

I would also like to thank our former Head, Professor S.G Warkar, who helped me in the initial days of my research and stood by my side in all difficult times.

I would also like to thank Professor D. Kumar, Professor R. C. Sharma, Professor R. K. Gupta, Professor Archana Rani, Professor Ram Singh, Professor Roli Purwar, Dr. Richa Srivastava, Dr. Manish Jain, Dr. Raminder Kaur, Dr. Saurabh Mehta, and Dr. Poonam, faculty members, Department of Applied Chemistry, DTU for their time-to-time valuable support.

No word and no language is ever adequate to express my heartfelt admiration for my respected parents, Mrs. Asha Goel (Mother), Mr. Ravinder Goel (Father), My younger brother (Vaibhav Goel) and My younger sister (Dr. Shweta Goel), who have been pillars of inspiration for my academic expedition and I am thankful for their blessings and unconditional love, without which I would have failed to complete this work.

For efficaciously accomplishing a project, a healthy environment is a must.

- I am grateful to all my labmates and deepest thanks to Dr. Namit Dey and Dr. Himansh Goel for their help and support whenever needed and for being such a good friend.
- ➤ I thank all the non-teaching and official staff of the Department of Applied Chemistry for their obligatory help whenever needed.
- ➤ I am grateful to Prof. Prateek Sharma (Vice Chancellor) and Prof. Jai Prakash Saini (former Vice Chancellor) of Delhi Technological University for giving me this opportunity to conduct my research work.
- ➤ I must also thank CIF-Delhi Technological University, USIC-University of Delhi, AIRF-Jawaharlal Nehru University, CIF-IIT Delhi, SAIF-AIIMS Delhi and CNMS-Jain University Bangalore for providing various instrumentation facilities.

>	Finally, I must thank all those, whom I have failed to mention specifically and personally, but they have helped
	me in various ways during this work.
	Thank you so much!!!!!
	(Divya Goel)

#### **ABSTRACT**

The primary purpose of biomaterials is to substitute tissues that are infected, injured, or damaged. The initial biomaterials used were bioinert, aiming to minimize the formation of scar tissue at the interface between the implant and the tissue. Dr. Larry Hench discovered Bioglass in 1969, which possesses the ability to bond with bone without being surrounded by fibrous tissues. It has been observed that Bioglass exhibits a significantly greater bonding capacity than other biomaterials. Its capability to generate hydroxyapatite with body fluid renders it unparalleled when compared to hydroxyapatite crystals. Besides providing a platform for cell development, the presence of silicon ions serves as a catalyst to accelerate cellular proliferation. Recent findings indicate that Bioglass is not only suitable for hard tissue regeneration but can also be applied beyond bone regeneration, such as in soft tissue engineering. Since the late 1960s, various techniques, including the meltquench method, the sol-gel method, flame spray synthesis, microwave synthesis, and others, have been developed for Bioglass formation. Additionally, a novel, cost-effective, environmentally friendly synthetic approach known as the bioinspired route was introduced by Santhiya et al. in 2013. This method draws inspiration from naturally synthesized nanostructured materials like silica in diatoms, following the guidance of biomacromolecule templates. Over the past two decades, bio-inspired synthesis of nanostructured ceramic oxides below 100°C has been well-established using organic templates. Santhiya et al. investigated the impact of various templates on the textural and morphological properties of Bioglass particles. In this current study, magnetic nanoparticles were templated on BG NPs, thus developing magnetism in BG. Further we developed PTAs showing luminescence and magnetic properties in BG which are mesoporous in nature. In this thesis, considering the huge importance of bioactive glass hybrid materials for both soft and hard tissue

engineering applications, various in-situ mineralized bioactive glass hybrid materials are synthesized and characterized in detail. This thesis has been summarized in 4 chapters.

**Chapter 1** gives a broad overview of biomaterial generations, bioactive glass as a third-generation biomaterial in soft and hard tissue engineering, and applications of bioglass beyond bone regeneration. Furthermore, a comprehensive review of research on the synthesis of bioactive glass and the mechanism of bioactivity in simulated body fluid is presented. Synthetic techniques for doped magnetic and non-magnetic bioactive glasses are briefly described, along with their importance in biological applications.

Chapter 2 Multiple biological advances have made use of bioactive glass (BG) nanoparticles (NPs) in regenerative medicine, bone and tooth repair, drug and gene transfer, cancer treatment, and cosmetics. Normal biocompatible coatings alongside hydrocarbons, polymers, and silica significantly affect fundamental attributes of NPs. In this study, we synthesized a novel mesoporous BG NPs with magnetite core shell (AMAG\_BG) using L-arginine as a template processing magnetic hyperthermia (MH). BG network coverage on magnetite (AMAG) NPs were orchestrated first time by bio-inspired synthesis in watery dissolvable. AMAG and AMAG\_BG NPs were characterized by utilizing FE-SEM, HR-TEM, and BET analysis. The elemental composition of L-arginine templated magnetite (AMAG) and AMAG\_BG NPs was also determined by XPS and EDX analysis. Characteristics of AMAG\_BG were contrasted with bare AMAG NPs in morphology, particle size, porosity, and composition. The fabricated BG NPs' in-vitro bioactivity and heat studies were successfully monitored after interaction with simulated bodily fluid (SBF). Magnetic studies and in-vitro heat studies together demonstrated the behavior of BG NPs towards MH treatment of cancerous cells. Cytotoxicity tests on AMAG\_BG NPs using U2OS and human blood cells with appropriate control experiments revealed

biocompatibility. The study represents magnetic and thermal property-dependent sustainable synthetic process of AMAG\_BG NPs for cancer treatment.

Chapter 3 The nanosized 45S5 bioactive glass (BG) containing iron (Fe) and bismuth (Bi) as magnetic photothermal agent (PTA) (B F FABG) was first time synthesized by Bio-inspired route using folic acid (FA) template. Similarly, for a comparative analysis, BG doped with Fe/Bi separately (F\_FABG and B FABG) were also synthesized. XPS and FTIR analysis of B F FABG revealed the presence of folic acid (FA) and dopants Fe and Bi in the BG network. Based on the XRD pattern, B F FABG was semi-crystalline in nature, with an average crystallite size of 0.2 ± 0.04 nm. Fe ions and FA molecules have a lower affinity for the BG network than the heaviest and most polarizable Bi ions, according to TGA analysis. An increase of Q4 species in B F FABG network was revealed by 29Si NMR investigation, due to the presence of Fe and Bi ions. For B\_F\_FABG, there was also a rise in Q3 and Q2 species due to the dual dopants. B\_F\_FABG is nano-crystalline, with an average diameter of 12.8 ± 0.3 nm, according to HR-TEM and SAED pattern. The BG samples, both doped and undoped, were found to be mesoporous, with pore diameters ranging from 2 nm to 50 nm. Due to the presence of Bi ions, B F FABG showed remarkable photoluminescence along with bone bonding ability during excitation in the range of ~1092 nm. The magnetic characteristics were also induced in B F FABG due to Fe doping. The novel B F FABG NPs reported least toxicity through in-vitro haemolysis assay and is an ultimate multifunctional material to treat bone abnormalities.

Chapter 4 The current study focused to synthesize magnesium (Mg2+) and bismuth (Bi3+) co-doped bioactive glass (BG) nanoparticles (NPs) at ambient conditions. Curcumin (CC) a therapeutic agent was used as a template to synthesize BG NPs along with 1 mol% MgO and increasing amount of Bi2O3 (From 0.5 mol% to 1.5 mol%). XPS confirmed the presence of doped elements in BG samples.

XRD reported an increase in mean crystallite size that was from 0.1 ± 0.02 nm to 0.3 ± 0.02 nm with the increase in Bi3+ ions concentration, which has metallic nature. The FTIR study confirmed silicate network development in CCBG with CC template and largely highlights the Si–O–Bi stretching vibrations. TGA revealed that co-doping of Mg2+ and Bi3+ to the BG samples increased their thermal stability in comparison to the control. Co-doping in BG NPs indicated more open SiO2 network as depicted by NMR. FE-SEM and HR-TEM along with SAED pattern confirmed that co-doped BG NPs were nanosized with increased crystallinity with increasing Bi3+ concentration. The optical transmittance behaviour showed a strong emission peak at 480 nm with decreased intensity with increasing Bi3+ ion concentration. Co-doped BG NPs were found to be mesoporous, with pore diameters ranging from 2 nm to 50 nm according to BET analysis. In-vitro bioactivity revealed excellent bone bonding ability of BG. The novel co-doped BG reported least toxicity and excellent biocompatibility through in-vitro haemolysis assay and MTT assay.

#### **LIST OF PUBLICATIONS**

- Divya Goel, Deenan Santhiya, Subodh Kumar, Ajit Kumar Mahapatro. "Synthesis of Mesoporous Core Shell Magnetite Bioactive Glass Nanoparticles for Magnetic Hyperthermia Treatment of Cancer." "ChemistrySelect" 9 (2024): e202302119. (SCIE indexed) (Impact Factor: 2.307)
- Divya Goel, Deenan Santhiya. "Mesoporous bioactive glass nanoparticles with dopants bismuth and iron as magnetic photothermal agents for biomedical applications." "Bio Nano Science" (2024). (ESCI indexed) (ImpactFactor: 3.0)
- 3. Divya Goel, and Deenan Santhiya. "Effect of Magnesium and Bismuth Co-doping on Structural Optical and Bioactive properties of Bioactive Glass Nanoparticles for Biomedical Applications." (SCIE indexed) (ImpactFactor: 2.7)

#### **Book Chapters:**

- Divya Goel, Deenan Santhiya, Biosafety aspects of nanobiotechnology for use in livestock industries, in Nanobiotechnology for the livestock industry, Elsevier (2023) pp.395-423.
   (Invited Book Chapter)
- Divya Goel, Deenan Santhiya, Controlling the Size, Shape, and Composition of Nanogel, in Nanogels: Fundamentals to Pharmaceutical and Biomedical Applications, Elsevier (2025). (Manuscript under review)

### **Contents**

Title	Page
List of Figures	20-22
List of Tables	23
List of Abbreviations	24
Chapter 1: Introduction	
1.1 Introduction	26
1.2 Bioactive Glass	29
1.3 Bioactivity Mechanism for Bioactive Glass	30
1.4 Doping of Magnetic Nanoparticles in Bioactive Glasses	31
1.5 Synthetic methods to prepare magnetic nanoparticles	34
1.5.1 Organic Phase Synthesis	35
1.5.2 Hydrothermal Synthetic Method	35
1.5.3 Chemical Co-Precipitation	36
1.5.4 Mechanical Grinding Method	36
1.5.5 Wet Method Synthesis	37
1.5.6 Film Deposition Technology	37
1.6 Sustainable Synthesis of Magnetic Nanoparticles	37
1.7 Bio-inspired synthesis of doped bioactive glass nanoparticles	38
1.8 Doped Bioactive glass Nanoparticles as effective photothermal agents (PTAs)	39
1.9 Biomedical Applications	41
1.9.1 Ability of Magnetic field to Repair Bone Cells or Bone Tissue	41
1.9.2 Magnetic nanoparticles in imaging	43
1.9.3 Magnetic nanoparticles in cancer treatment	44
1.9.4 Drug Targeted Therapy of Magnetic Nanoparticles	46
1.9.5 Magnetic nanoparticles in Isolation and purification of bio-analytes	47
1.9.6 Magnetic nanoparticles for Chemotherapeutic treatment	48
1.9.7 Magnetic nanoparticles for treating genetic and acquired human diseases	50

2.0 Research Gap	51
2.1 Objectives	52
References	53
Chapter 2:	
Synthesis of mesoporous core shell magnetite Bioactive Glass nanoparticles for magnetic hyperthermia treatment of cancer	
2.1 Introduction	62
2.2 Experimental Section	65-66
2.2.1 Materials	65
2.2.1 Synthesis of L-arginine templated magnetite (AMAG) nanoparticles	66
2.2.3 Synthesis of L-arginine templated core shell magnetite- bioactive glass (AMAG_BG) nanoparticles	66
2.3 Characterization of AMAG and AMAG_BG nanoparticles (NPs)	67-72
2.3.1 X-ray photoelectron spectroscopy (XPS)	67
2.3.2 X-ray Diffraction (XRD) Analysis	67
2.3.3 Fourier Transform Infrared Spectroscopy (FTIR)	68
2.3.4 Thermogravimetric (TGA) Analysis	68
2.3.5 CHNSO analysis	68
2.3.6 Morphological Studies	68
2.3.6.1 Field Emission Scanning Electron Microscopy (FE-SEM) and Energy Dispersive X-Ray Analysis (EDX)	68
2.3.6.2 Transmission electron microscopy (TEM)	69
2.3.7 Nitrogen Sorption Analysis	69
2.3.8 Magnetic Measurement	69
2.3.9 Bioactivity Test	69
2.3.10 In- vitro Heat Studies	70 70
2.3.11 In- vitro Hemolysis Assay	71
2.3.12 MTT Assay	72
2.4 Results and Discussion	73-78
2.4.1 X-ray photoelectron spectroscopy (XPS)	73

	74
2.4.2 X-ray Diffraction (XRD) Analysis 2.4.3 Fourier Transform Infrared Spectroscopy (FTIR)	76
	77
2.4.4 Thermogravimetric (TGA) Analysis	78
2.4.5 CHNSO analysis	79-80
2.4.6 Morphological Studies	79
2.4.6.1 Field Emission Scanning Electron Microscopy (FE-SEM) and Energy Dispersive X-Ray Analysis (EDX)	80
2.4.6.2 Transmission electron microscopy (TEM) 2.4.7 Nitrogen Sorption Analysis	
	81
2.4.8 Magnetic Measurement	82
2.4.9 <i>In- vitro</i> Heat Studies	84
2.4.10 Bioactivity Test	87
2.4.11 <i>In- vitro</i> Hemolysis Assay	91
2.4.12 MTT Assay	92
2.5 Interaction Mechanism	93
2.6 Conclusion	95
References	96
Chapter 3:	
Mesoporous bioactive glass nanoparticles with dopants bismuth and iron as magnetic photothermal agents for biomedical applications	
3.1 Introduction	102
3.2 Experimental Section	105
3.2.1 Materials	105
3.2.1 Bio-inspired Synthesis of FABG NPs doped with metals 3.3 Characterization of FABG, F FABG, B FABG and B F FABG nanoparticles (NPs)	105 106-109
3.3.1 X-ray photoelectron spectroscopy (XPS)	106
3.3.2 X-ray Diffraction (XRD) Analysis	106
3.3.3 Fourier Transform Infrared Spectroscopy (FTIR)	106
3.3.4 Thermogravimetric (TGA) Analysis	107
3.3.5 29Si solid state nuclear magnetic resonance (NMR):	107
3.3.6 Morphological Studies	107

3.3.6.1 Field Emission Scanning Electron Microscopy (FE-SEM) and Energy	107
Dispersive X-Ray Analysis (EDX)	107
3.3.6.2 Transmission electron microscopy (TEM)	107
3.3.7 Nitrogen Sorption Analysis	108
3.3.8 Magnetic Measurement	108
3.3.9 Bioactivity Test	108
3.3.10 Photoluminescence study (PL)	109
3.3.11 <i>In- vitro</i> Hemolysis Assay	
3.4 Results and Discussion	110-128
3.4.1 X-razy photoelectron spectroscopy (XPS)	110
3.4.2 X-ray Diffraction (XRD) Analysis	113
3.4.3 Fourier Transform Infrared Spectroscopy (FTIR)	114
3.4.4 Thermogravimetric (TGA) Analysis	115
3.4.5 29Si solid state nuclear magnetic resonance (NMR):	117
3.4.6 Morphological Studies	118
3.4.6.1 Field Emission Scanning Electron Microscopy (FE-SEM) and Energy Dispersive X-Ray Analysis (EDX)	118
3.4.6.2 Transmission electron microscopy (TEM)	116
3.4.7 Nitrogen Sorption Analysis	119
3.4.8 Magnetic Measurement	122
3.4.9 Bioactivity Test	123
3.4.10 Photoluminescence study (PL)	128
3.4.11 <i>In- vitro</i> Hemolysis Assay	120
3.5 B_F_FABG as an efficient magnetic photothermal agent (PTA)	131
3.6 Conclusion	132
References	133
Chapter 4:	
Effect of magnesium and bismuth co-doping on structural optical and bioactive properties of bioactive glass nanoparticles for biomedical applications	
4.1 Introduction	138
4.2 Experimental Section	141

4.2.1 Materials	141
4.2.1 Materials 4.2.2 Bio-inspired Synthesis of co-doped (Bi3+ and Mg2+) CCBG nanoparticles (NPs)	141
4.3 Characterization of CCBG, M_CCBG and co-doped CCBG	142-146
4.3.1 X-ray photoelectron spectroscopy (XPS)	142
4.3.2 X-ray Diffraction (XRD) Analysis	143
4.3.3 Fourier Transform Infrared Spectroscopy (FTIR)	143
4.3.4 Thermogravimetric (TGA) Analysis	143
4.3.5 Morphological Studies 4.3.5.1 Field Emission Scanning Electron Microscopy (FE-SEM) and Energy	143
Dispersive X-Ray Analysis (EDX) 4.3.5.2 Transmission electron microscopy (TEM)	144
4.3.6 Nitrogen Sorption Analysis	144
4.3.7 <sup>29</sup> Si solid state nuclear magnetic resonance (NMR)	144
4.3.8 Photoluminescence study (PL)	144
4.3.9 Bioactivity Test	145
	145
4.3.10 <i>In- vitro</i> Hemolysis Assay	146
4.3.11 MTT Assay	
4.4 Results and Discussion	147-169
4.4.1 X-ray photoelectron spectroscopy (XPS)	147
4.4.2 X-ray Diffraction (XRD) Analysis	150
4.4.3 Fourier Transform Infrared Spectroscopy (FTIR)	152
4.4.4 Thermogravimetric (TGA) Analysis	153
4.4.5 Morphological Studies 4.4.5.1 Field Emission Scanning Electron Microscopy (FE-SEM) and Energy	154
Dispersive X-Ray Analysis (EDX)	154
4.4.5.2 Transmission electron microscopy (TEM)	
4.4.6 Nitrogen Sorption Analysis	157
4.4.7 29Si solid state nuclear magnetic resonance (NMR)	
4.4.8 Photoluminescence study (PL)	163
4.4.9 Bioactivity Test	103

4.4.10 <i>In- vitro</i> Hemolysis Assay	166
4.4.11 MTT Assay	169
4.5 Discussion	171
4.6 Conclusion	172
References	173
Future Prospects	178

## List of Figures

Fig. No	Figure Caption	Page No.		
Chapter 1: Introduction				
Fig.1.1	Musculoskeletal disorders that typically develop and affect bone densities	26		
Fig.1.2	Crucial attributes of three age biomaterials	28		
Fig.1.3	Methods to prepare Magnetic Nanoparticles	35		
Fig.1.4	Synthetic techniques and Biomedical applications of the Magnetic Nanoparticles	41		
Chanter '	2: Synthesis of mesoporous core shell magnetite Bioa	activa Class nanonarticles for		
Спарист	magnetic hyperthermia treatment of o	•		
Fig. 2.1	XPS spectra, XRD pattern and FTIR spectra of AMAG and AMAG BG NPs	75		
Fig. 2.2	TGA, SEM and HR-TEM of AMAG and AMAG_BG NPs	78		
Fig. 2.3	Nitrogen adsorption-desorption isotherm and pore size distribution of AMAG and AMAG_BG NPs	82		
Fig. 2.4	Magnetization curve and Time-dependent temperature curves of AMAG and AMAG_BG under AC magnetic field of 110 Oe	83		
Fig. 2.5	FTIR, XRD and SEM micrographs of AMAG and AMAG_BG after 4 days, 7 days, 15 days and 30 days of bioactivity in SBF solution	89		
Fig. 2.6	Magnetization curve and Time-dependent temperature curves under AC magnetic field of 110 Oe with two different concentrations of 1 mg/mL and 5 mg/mL of AMAG and AMAG_BG after 4 d, 7 d, 15 d and 30 d of bioactivity in SBF solution respectively.	90		
Fig. 2.7	In-vitro hemolysis assay of AMAG and AMAG_BG NPs and MTT asaay of AMAG_BG NPs.	92		
Fig. 2.8	Representative structure of AMAG_BG NPs showing multi-centred interaction of L-arginine with magnetite and BG network.	94		
Chapter	r 3: Mesoporous bioactive glass nanoparticles with d	_		
	magnetic photothermal agents for biomedica			
Fig. 3.1	XPS, XRD of FABG, F_FABG, B_FABG and B_F_FABG NPs and FTIR spectrum of FABG, F_FABG, B_FABG, B_F_FABG and FA NPs.	112		
	T_TADO, D_TADO, D_T_TADO aliu TA NES.			

Fig. 3.2	TGA of FABG, F_FABG, B_FABG, B_F_FABG	116
	and FA NPs, NMR, FE-SEM and HR-TEM of	
	FABG, F_FABG, B_FABG and B_F_FABG	
	NPs.	
Fig. 3.3	Nitrogen adsorption-desorption isotherm and	121
	pore size distribution of FABG, F_FABG,	
	B_FABG and B_F_FABG NPs and	
	Magnetization curve of F_FABG and	
	B_F_FABG NPs.	
Fig. 3.4	XRD and FTIR spectra of FABG, F_FABG,	125
	B_FABG and B_F_FABG after 4 d, 7 d, 15 d and	
	30 d of bioactivity in SBF solution.	
Fig. 3.5	FE-SEM micrographs of FABG, F FABG,	126
	B FABG and B F FABG and Magnetization	
	Curve of F FABG and B F FABG after 4 d, 7 d,	
	15 d and 30 d of bioactivity in SBF solution.	
Fig. 3.6	Emission spectra and Excitation spectra of	128
6 -10	B_FABG and B_F_FABG	
Fig. 3.7	<i>In-vitro</i> hemolysis assay of FABG, F FABG,	130
	B FABG and B F FABG NPs.	
	Chapter 4:	
Effect of ma	gnesium and bismuth co-doping on structural opti	cal and bioactive properties of
	bioactive glass nanoparticles for biomedical	applications
Fig. 4.1	XPS survey spectra of CCBG, M CCBG,	149
	M_B1_CCBG, M_B2_CCBG and M_B3_CCBG	
	NPs.	
Fig. 4.2	XRD and FTIR of CCBG, M CCBG,	152
	M B1 CCBG, M B2 CCBG NPs and TGA of	
	CC, CCBG, M CCBG, M B1 CCBG,	
	M B2 CCBG NPs.	
Fig. 4.3	FE-SEM, HR-TEM micrographs in bright field	156
	and SAED pattern of CCBG, M CCBG,	
	M B1 CCBG, M B2 CCBG and M B3 CCBG	
	NPs.	
Fig. 4.4	Nitrogen Sorption Analysis of CCBG, M CCBG,	159
-8	M B1 CCBG, M B2 CCBG and M B3 CCBG	
	NPs.	
Fig. 4.5	NMR spectra of CCBG, M CCBG,	162
-8	M B1 CCBG, M B2 CCBG and M B3 CCBG	- 3-2
	NPs, and Photoluminescence spectra of	
	•	
i contract of the contract of	T M D L CCDG, M DZ CCDG and M D3 CCDG	
	M_B1_CCBG, M_B2_CCBG and M_B3_CCBG NPs.	
Fig. 4.6	NPs.	165
Fig. 4.6	NPs.  XRD patterns of CCBG, M_CCBG,	165
Fig. 4.6	NPs.  XRD patterns of CCBG, M_CCBG, M_B1_CCBG, M_B2_CCBG and M_B3_CCBG	165
Fig. 4.6	NPs.  XRD patterns of CCBG, M_CCBG,	165

Fig. 4.7	FE-SEM micrographs of CCBG, M_CCBG,	166
	M_B1_CCBG, M_B2_CCBG and M_B3_CCBG	
	after 1 d, 4 d, 7 d, and 15 d of bioactivity in SBF	
	solution.	
Fig. 4.8	<i>In-vitro</i> hemolysis assay of CCBG, M_CCBG,	168
	M_B1_CCBG, M_B2_CCBG and M_B3_CCBG	
	NPs.	
Fig. 4.9	MTT assay of CCBG, M_CCBG, M_B1_CCBG,	170
	M_B2_CCBG and M_B3_CCBG NPs at 24 h	
	interaction.	

## **List of Tables**

Table. No	Table Caption	Page No.
Table 2.1	Binding energy (eV) of AMAG and AMAG_BG by XPS	74
	analysis.	
Table 2.2	Elemental composition of AMAG and AMAG_BG by CHNSO	79
	(for C, N and O) analysis	
Table 2.3	Elemental composition of AMAG and AMAG_BG by EDX	70
	analysis.	
Table 2.4	Surface area, pore volume and pore size data of AMAG and	82
	AMAG_BG.	
Table 2.5	Saturation and Remanent Magnetization of AMAG and	84
	AMAG_BG NPs	
Table 2.6	SAR values of AMAG and AMAG_BG for 1 mg/mL and 5	87
	mg/mL concentrations	
Table 2.7	SAR values of AMAG and AMAG_BG at 1 mg/mL and 5	90
	mg/mL concentrations after bioactivity of 4 d, 7 d, 15 d and 30	
	d in SBF solution.	
Table 3.1	Binding energy (eV) of FABG, F_FABG, B_FABG and	111
	B_F_FABG by XPS analysis.	
Table 3.2	Q <sup>n</sup> content and chemical shift data (δ) of FABG and	118
T. 1. 2.2	B_F_FABG.	100
Table 3.3	Surface area, pore volume and pore size data of FABG,	120
T. 1.1. 2.4	F_FABG, B_FABG and B_F_FABG.	122
Table 3.4	Saturation and Remanent Magnetization of F_FABG and	122
	B_F_FABG NPs	
Table 4.1	Disting assert (AV) affected M CCDC M D1 CCDC	1.40
Table 4.1	Binding energy (eV) of CCBG, M_CCBG, M_B1_CCBG, M_B2_CCBG and M_B3_CCBG by XPS analysis.	148
Table 4.2	,	158
1able 4.2	Surface area, pore volume and pore size data of CCBG, M CCBG, M B1 CCBG, M B2 CCBG and M B3 CCBG.	138
Table 4.3	$M$ _CCBG, $M$ _B1_CCBG, $M$ _B2_CCBG and $M$ _B3_CCBG.	161
1able 4.5	CCBG, M CCBG, M B1 CCBG, M B2 CCBG and	101
	M B3 CCBG.	
	M_DJ_CCDU.	

# List of Abbreviations and Symbols

BG	Bioactive Glass
NPs	Nanoparticles
CE	Conformite Europeenne
HA	Hydroxyapatite
MBGCs	magnetic bioactive glass-ceramics
Fe	Iron
EAF	external attractive field
MNPs	magnetic nanoparticles
TON	turnover number
TOF	turnover recurrence
Fe <sub>3</sub> O <sub>4</sub>	Iron oxide
BGCs	glass-ceramics
MBGs	Mesoporous bioactive glasses
PTT	Photothermal effect
NIR	near infrared
Bi	Bismuth
PEG	Poly- ethylene glycol
MRI	magnetic resonance imaging
AMF	Alternating Magnetic Field
SAR	Specific absorption rate
SPIONs	Superparamagnetic iron oxide nanoparticles
DOX	Doxorubicin
PLGA	Poly (lactic-co-glycolic acid)
5-FU	5-fluorouracil
PANI	Polyaniline

# CHAPTER 1

# Introduction

# **CHAPTER 1**

### **INTRODUCTION**

#### 1.1 Introduction:

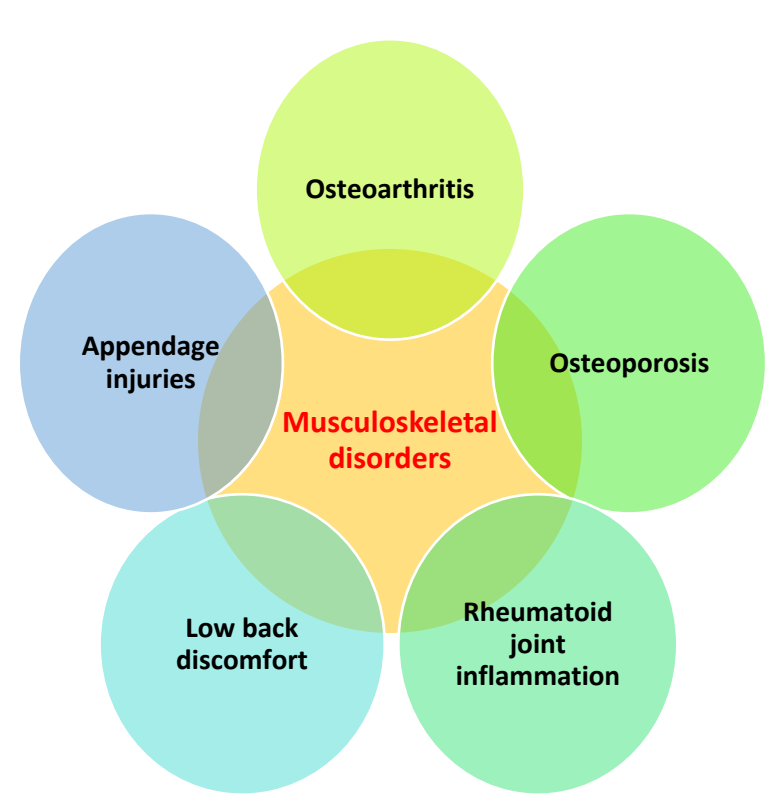


Fig.1.1 Musculoskeletal disorders that typically develop and affect bone densities

Although composed of living bone cells suspended in a biomineral media, bone is not uniformly robust. Taking everything into account, the hardening of this medium of nearly entangled cells becomes bone. Collagen filaments and tiny crystals of an inorganic bone mineral make up most of the bone itself. In addition to being the primary structural support, bone serves as a mechanical aid, the attachment points for muscles, tendons, and ligaments, and a shield for the most important tissues. Furthermore, bone marrow structure provides essential mineral elements and site for haematopoiesis. Osteoarthritis, osteoporosis, rheumatoid joint inflammation, low back discomfort, and appendage

injuries are examples of musculoskeletal disorders that typically develop and affect bone densities [1].

The normal process of bone recovery is particularly more effective against minor cracks or small bone deformities. In any case, the challenge emerges with an increment in the severity of fractures or complications brought about in different bony illnesses, prompting reduced vascularity or enormous bony tissue loss. This poses a significant challenge to our health system. Even after the colossal progression in the field of biomedical designing, surgery stays the lone choice for the therapy of bone illnesses and wounds [2], which further leads to the danger of unfavorable response to sedation and prosthetic joint, bleeding, blood clots, delayed skin healing, instability or firmness in the joints, damage to the nerves and veins, dislocation or extricating of the artificial joint and many more.

The connection among bone and cancer has gone through significant changes lately and oncology needs to deal with an expansion of bone metastases occurrence with an extreme difference in epidemiological information and a strong clinical effect. Consequently, at present bone metastases are answerable for the high dismalness in malignant cancer patients [3]. This bioactive glass (BG) is thought to be the first man-made material to attach to living tissue and has been successfully moved to industry and clinics with Food and Drug Administration (FDA) endorsements and CE marking certificate for dental and orthopedic products. Nanosized bioactive glass has likewise been created and joined with other natural materials to improve nanocomposites for muscular health. For example, 45S5 BG nanoparticles (NPs) with size circulation of 20 nm to 50 nm can be prepared by flame spray method [4] and added to polymeric frameworks to shape nanocomposites. [5]

Diverse kind of biomaterials as a bone replacement material are notable from late hundreds of years and were arranged under three distinct ages. Generally, the motivation behind original biomaterials was to replace unhealthy, diseased, or aging tissues. Along with it, the actual property of the chosen material needs to coordinate with the supplanted tissue with least toxic reaction for example it must be bioinert, corrosion-resistant, nontoxic. It should not trigger any response in the host, neither

dismissed nor perceived. The quality of 'Bio-inert' tissue reaction results in the development of non-adherent fibrous capsules at the material-host interface. The second-age biomaterials are bioactive for example they can bond with the living tissues so they can connect with the organic climate to upgrade the natural reaction and are bioresorbable. For example, they can degrade while new tissue forms and recovers. BG as a bone regeneration material goes under the second-age biomaterials. For example, on interaction with the injury site of bone, BG NPs prompts the disintegration of particles which brings out a healthy bone. The third-age biomaterials are bioresorbable, biodegradable, and furthermore have the capacity for cell and gene activation [6]. Because of three-dimensional permeable structures, they can activate genes that prompts the recovery of living tissue. For these biomaterials, the bioactivity and biodegradability ideas are consolidated, so the blend of bioactivity and biodegradability is the most crucial attributes of the third-age biomaterials. The work of BG as third-age biomaterials can be stretched out to various applications.

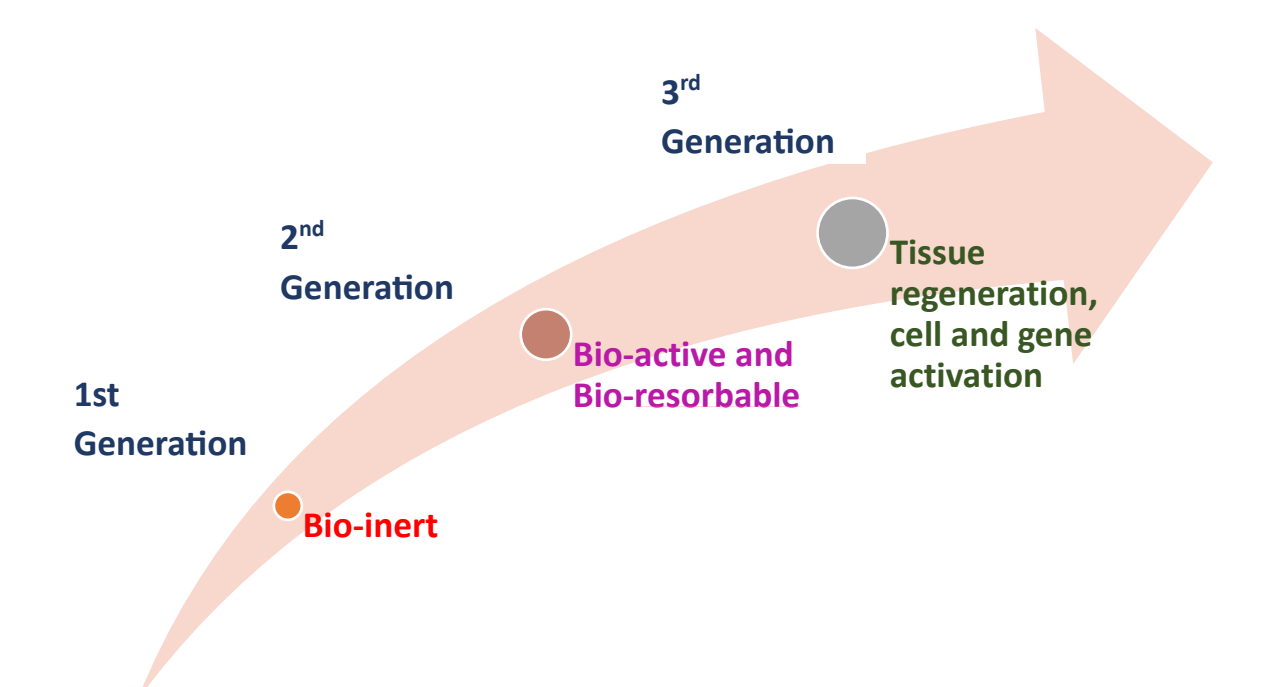


Fig.1.2 Crucial attributes of three age biomaterials

#### 1.2 Bioactive Glass:

The origins of BG can be traced back to late spring 1967, when Larry Hench, a leading figure in contemporary biomaterials science, happened to meet a US Army colonel while travelling to the US Army Materials Research Conference [7]. Hench initiated the groundbreaking work that resulted in the discovery of 45S5 Bioglass®, the first BG, and all following research in that field [8].

The main example of a substance that may adhere to living tissues without becoming "disengaged" in a collagenous capsule were BG, which also paved the way for a novel concept involving three materials in medicine. Remarkably, substances that could not only last inside the human body without becoming toxic or deteriorating but also actively participate in tissue healing processes were used [9]. Particles of calcium and phosphate found in BG are available to the same degree as hydroxyapatite (HA) found in bone. These glasses are biocompatible and stick to the tissue. They are currently used as covering material, scaffolds, and bone grafts in the context of muscle health and have a broad range of clinical uses [10]. Silica is used as a key component of the glass structure in the construction of BG. SiO4 tetrahedron, which is joined at the oxygen centres, provides the basis for the amorphous structure found in silicate glasses. The open structure of silica in silicate glasses is a result of nonconnecting oxygen particles attached to the silicon.

Network modifier expansion, such as that of Na<sup>+</sup> and Ca<sup>2+</sup>, also contributes to the opening of silica network structures. These particles open the glass structure by replacing the structure's crossing over oxygens with non-connecting oxygens. A few characteristics of the comparison glass are determined by the amount of modifier ion-oxygen bonds and non-connecting oxygen links [11]. Every silica tetrahedron has more than 2.6 non-bridging oxygen particles because of BG, which is necessary for bioactivity [12]. BG composition differs slightly from that of traditional soda-lime-silica glasses, which contain more than 65% silica by weight. The components SiO<sub>2</sub>, Na<sub>2</sub>O, CaO, and P<sub>2</sub>O<sub>5</sub> are necessary for a glass to gain bioactivity [13].

SiO<sub>2</sub> levels should range between 45 and 60 weight percent, while high levels of Na<sub>2</sub>O, CaO, and CaO/P<sub>2</sub>O<sub>5</sub> ratios are desirable. Increased SiO<sub>2</sub> content slows down the rate at which the glass particles break down on the surface, which reduces bioactivity. Moreover, exceptionally low silica content results in completely soluble monomeric SiO<sub>4</sub> units. When in contact with physiological fluid, silica content also plays a major role in the formation of hydroxyapatite carbonate (HCA), which initiates the synthetic bond to hard or fragile tissues. When a body liquid is absorbed, a high CaO/P<sub>2</sub>O<sub>5</sub> ratio will often encourage the arrival of particles from the material's surface, forming a surface layer of HCA in a very short interval of time.

Since phosphate particles are also available in physiological fluid, bioactivity can be free of P<sub>2</sub>O<sub>5</sub> [14].

# 1.3 Bioactivity mechanism for Bioactive Glass:

The system proposed by Hench for clarifying the nucleation and precipitation of crystalline HA (or when all is said in done, apatite-like stages) on the glass surface is a 5- stage process dependent on the disintegration of ionic species from the glass network [15,16]:

1) Cation exchange: the principal stage includes the trading of monovalent and bivalent cations, specifically Na<sup>+</sup> furthermore, Ca<sup>2+</sup> inside the glass, and H<sup>+</sup> particles from the solution. This will prompt the development of silanol bonds (Si-OH) on the outside of the glass as per the reaction:

$$Si-O-Na^{2+} + H^+ + OH^- \rightarrow Si-OH^+ + Na^+ (aq) + OH^-$$

As a result, the arrangement pH will increase and a silica-rich layer will form. If present in the glass composition, additionally phosphate particles can be released. Since monovalent particles are less firmly attached to the glass network, they will be lost quicker than bivalent ones;

2) With the progressing of the exchanging reaction and the ascending of the pH towards alkalinity, Si-O-Si bonds are captured by hydroxyl particles. At the point when all the four Si-O bonds of a solitary Si atom are broken, soluble silica, Si(OH)<sub>4</sub>, is lost in the arrangement. This builds the quantity of silanols at the glass-liquid interface;

- 3) Since hydroxyl gatherings can respond and condensate between one another, the third step includes the buildup and the polymerization of silanol groups. Doing as such, a silica-rich amorphous layer is shaped (silica gel). It can assimilate particles from the arrangement and serve as a decent atmosphere for the precipitation of HA;
- 4) Diffusion of calcium (Ca<sup>2+</sup>) and phosphate (PO<sub>4</sub><sup>3-</sup>) particles through the silica gel and from the arrangement, consequently forms a amorphous CaO<sup>-</sup> and P<sub>2</sub>O<sub>5</sub><sup>-</sup> rich film on the silica gel layer. A short time later, the undefined calcium-phosphate film begins to solidify;
- 5) Crystallization of the calcium-and phosphate-rich layer and arrangement of HA. Due to the presence of extra ionic species, like carbonates which relocate from the solution to the glass surface and F<sup>-</sup> particles delivered by the glass (if it contains fluorides [17]), the HA shaped on the embed surface may not be stoichiometric yet is really a blended apatite including hydroxycarbonate apatite and fluorapatite.

#### 1.4 Doping of Magnetic Nanoparticles in Bioactive glasses:

Applications of magnetic hyperthermia in cancer treatment have been investigated in detail for ferromagnetic, ferrimagnetic, and superparamagnetic materials [1]. Applying an alternating external magnetic field to a magnetic material result in magnetic losses that are dissipated as heat, raising the local temperature and creating magnetic hyperthermia. The placement of these materials adjacent to tumours may cause the cancer cells to weaken or die, while maintaining the viability of the healthy cells [1]. It is conceivable since cancer cells can only withstand temperature stress up to 43 °C, whereas healthy cells may withstand stress up to 46 °C. Thus, cancer cells are specifically destroyed while healthy cells are little impacted by increased temperature that is carefully regulated [2], [3].

The most readily available materials for applications involving hyperthermia are superparamagnetic iron oxide nanoparticles (SPIONs) [4, 5, 6, 7]. However, other ceramics with appropriate magnetic properties can also be used for this purpose, such as magnetic bioactive glass-ceramics (MBGCs), which have been suggested as a means of treating bone cancer through hyperthermia. These intriguing glass-ceramics, known as MBGCs, are made from the partial crystallisation of BG and have the potential to treat bone cancer by inducing hyperthermia and promoting repair of the tumor-caused bone defect. Their bioactivity, or their capacity to develop an apatite-like layer on their surface in a host tissue, is what gives them the capacity for regeneration [8].

As in the case of MBGCs, the bioactivity behaviour can be affected by several glass structure-related factors, including the inclusion of therapeutic ions in the glass network or the crystallisation of the glass matrix [9]. Thus, the primary concerns with MBGCs are optimisation of both bioactivity and magnetization. Biomaterials known as MBGCs are used to treat bone cancer by magnetic hyperthermia, which not only heals the injured bone but also treats the bone tumour. However, because the heat treatment procedure that is used to generate magnetic phases is also associated with bioactivity loss, thus maintaining high bioactivity and high saturation magnetization remains difficult. A special blend of organic and inorganic components makes up bone. [4] The natural component is dominated by stringy collagen, while most of the inorganic ingredient is translucent HA. Bone may self-heal and mend. However, the bony abnormalities caused by external damage, bone infections, cancers, or aberrant bone development cannot be met by the bone's ability to heal itself. [5] Using clinical supplies such as artificial, allogeneic, and autologous bone tissues are essential. [6,7] Both techniques depend on recovering adjacent bone tissue. [8] Conditions that are recognised as vital in this cycle include pressure stimulation, synthetic stimulation, [9] organic component stimulation, magnetic field, electric field, and so on. [10,11] It has been demonstrated that the magnetic field affects cell metabolic activity, which improves the repairing of bone tissue.

Due to its para-attraction, iron (Fe) is the substance that has garnered the most interest in recent

studies. [12] Unpaired electrons in the farthest layer twist, causing the particle to keep a certain magnetic moment. When activated by an external attractive field, this nuclear magnetic moment exhibits a weak attractive power that adapts to that field as it is constructed along the same field. This is known as paramagnetic character. [13] Nuclear magnetic moments made of unpaired electrons are present in ferromagnetic materials. These moments are equally well-organized and exhibit strong outward attraction in the absence of any attractive field. The bone has a small amount of paramagnetic iron which is superbly conductive. Thus, it is used in bone implant materials.

It is due to their extraordinary appealing qualities and excellent biocompatibility, magnetic nanoparticles (MNPs) are exploited as biomaterials. [14] Recent applications include drug transfer, attractive hyperthermia, natural division, and atomic attractive imaging. Under the influence of the attractive field, the attracted particles are gradually saved on the outer layer of the cell film. [15] The enticing particles are engulfed by the cells as they endocytose them. Once within a cell, it is simpler to alter its physiological capabilities. Each magnetic molecule will turn into an attractive source if the magnetic field is utilized, allowing the magnetic framework material to be used in the therapy of bone tissue damage. [16,17] The magnetically attracting particles rapidly charge up when they come into contact with an external attractive field (EAF). [18] The EAF and the attracted particles work together to increase the effectiveness of their treatment for bone tissue modelling. [19] Different MNPs like iron, nickel, cobalt, chromium, manganese, gadolinium etc. have been employed in the clinical industry, either stacked with or without medications. MNPs have proved to be effective, particularly in the repair of bone tissue. The employment of appealing NPs in the field of bone tissue regeneration is examined in this article together with conventional synthetic techniques, equipment, and applications. [20] Because of recent developments in biomedical applications, synthesis and processing of biomaterials should follow safer and sustainable techniques for clinical diagnosis and therapies. Sustainable technology is currently most significant in biological applications. [21] Since they have distinct synthetic, organic, and physical properties, NPs provide a number of advantages. [22] The structures (lipids, metals, peptides, and polymers) and forms (circles, pyramids, poles, and blooms) of NPs are influenced by mixing methods and functionalization processes.

Biomedical NPs evaluating novel pharmaceuticals were the main focus for the development of a practical nano system that simultaneously provides imaging and are useful to medical experts as well.

[23,24]

#### 1.5 Synthetic Methods to prepare Magnetic Nanoparticles:

Fe<sub>3</sub>O<sub>4</sub>, Fe, Co, Ni, MgFe<sub>2</sub>O<sub>4</sub>, and Co Fe<sub>2</sub>O<sub>4</sub> are just a few of the interesting nanostructures that utilise various fundamental arrangements. The most creative and usual invention of alluring nanomaterials is Fe<sub>3</sub>O<sub>4</sub>. With endless potential applications, effective strategies have tremendously advanced. The two most common attractive Fe<sub>3</sub>O<sub>4</sub> arrangement procedures are the dry strategy and the wet technique. [25] The wet method, which includes the accompanying method, aqueous strategy, hydrothermal synthetic method, synthetic co-precipitation method, mechanical grinding method, wet-synthesis method, and film deposition technology, is the one most commonly employed. [26,27] Depending on the ready circumstances, planning techniques, and driving forces used, the turnover number (TON) and turnover recurrence (TOF) in the amalgamation of MNPs could be variable. [28] With the aid of various impetuses, the Suzuki reaction and Heck response of halogenated benzene can be successfully carried out in the synthesis of MNPs for bone fixing. [29] The average TOF and TON can be greater than 50,000 h<sup>-1</sup> and 30.000 mol, respectively. [30]



Fig.1.3 Methods to prepare Magnetic Nanoparticles

#### 1.5.1 Organic phase synthesis

MNPs may also be created in response to natural arrangement patterns. MNPs can be made via wet chemical methods that involve watery environments, such as microwave amalgamation, aqueous reactions, and synthetic co-precipitation techniques. [31] Using a natural stage blend, MNPs have been planned while accounting for Fe, Co, and Ni oxides, centre/shell structures, and free weight structures. Provisional Magnetic Nanomaterials in Bone Tissue Repair is a temporary record. The last set article shape, and organisation of MNPs are not affected by at least one response boundary, such as reactant focus, dissolvable extremity, and reaction temperature/time. [32] Here, the primary concern is the combination of monodisperse MNPs.

# 1.5.2 Hydrothermal Synthetic Method

The aqueous approach is a better method for creating attractive nanocomposites. A reactor, which has several benefits like easy operation and excellent response efficiency, is also used to manage the reaction. [33] The metastable state and nano morphology obtained by aqueous/hydrothermal processes are challenging to obtain using alternative approaches. Most of the times, Fe<sub>3</sub>O<sub>4</sub> is

introduced to a high-pressure reactor along with FeCl<sub>2</sub>, FeCl<sub>3</sub>, and NaOH utilizing an aqueous approach. [34] The response criteria for the solvothermal approach and aqueous strategy are comparable despite variances in the methods for using the ethylene glycol medium. The approach is suitable for larger temperature range since the dissolvable employed has a higher edge of boiling over water. [35] Using decreasing solvents, materials could be shielded from oxidation during high-temperature planning. Experts have effectively pre-arranged basic metals, compounds, and attractive metal oxides using aqueous/hydrothermal processes. [35]

# 1.5.3 Chemical co-precipitation

The most readily approach for Fe<sub>3</sub>O<sub>4</sub> is synthetic co-precipitation. To create an expedient or hydrated precursor, basic medium substance is added to the mixture of dissolvable iron salt and ferrous salt. [36] After washing, drying, and consumption methods, attractive NPs would be added. This technique is easy to apply and can produce a large quantity of NPs. The only aspect of grain growth that can be regulated is its dynamic component. Hence this strategy's weakness is the inability to influence molecular size and transportation. [37]

#### 1.5.4 Mechanical Grinding Method

Through solid plastic mis-shaping, mechanical crushing reduces big particles (Fe<sub>3</sub>O<sub>4</sub> with an average molecular size of 10 mm) to nanometre size. [38] The principal process for repurposing coarse-grained material in the planetary ball plant is impact, either between the steel balls itself or between the steel balls and the interior mass of the crushing tank. Dry crushing interactions can be used to create NPs, but the end result is micron-sized molecule totals with nanograin structure because to repeat crushing virus welding. [39] To obtain deeply disseminated NPs, a moist crushing contact with a strong crushing and pounding force is required. Ceramic powder is more suitable for ball processing since it is weaker than metal. [40] Excellent molecule size reproducibility is provided by the actual ball processing technique. Due to prohibitively expensive technology, lengthy production cycle, and limited expertise, modern creativity is difficult to fulfil. [41]

#### 1.5.5 Wet Method Synthesis

The best wet technique is a wet chemical approach to produce nano metal oxide. To structure a "sol" of NPs, this technique depends on hydroxylation and the accumulation of subatomic precursors. In supercritical environments, scientists organised Fe<sub>3</sub>O<sub>4</sub> NPs using the wet chemical technique. [42] The particles had a monodisperse dispersion with size typically close to 8 nm, according to the data. Because of the particles' small molecular size and robust dispersion, the authors hypothesised that they might be employed in biological magnetotherapy. It was found that by combining Co(NO<sub>3</sub>)<sub>2</sub>6H<sub>2</sub>O, chromium nitrate, Cr (NO<sub>3</sub>)<sub>3</sub>9H<sub>2</sub>O, and iron nitrate, monodisperse circular Co-Cr-Ferrite nanomaterials could be produced easily. Co-Cr-Ferrite NPs were constructed in monodisperse layers that were stable and showed incredibly alluring properties. [43]

# 1.5.6 Film Deposition Technology

Recently, film layer deposition has emerged as a crucial thin film deposition invention. It is frequently employed in thin film evidence on the outer layer of different semiconductors, metal oxides, and polymers. [44] This process has lot of benefits, including high consistency and accurate item thickness control. For multi-part structures, it is a useful technique for integrating controlled composite materials. Researchers used SiO<sub>2</sub>-coated -Fe<sub>2</sub>O<sub>3</sub> nanofibers along with film deposition techniques. It served as an electromagnetic wave absorber. According to the results, the generated attractive carbon nanowires have a uniform shape, less attractive reflection loss, and a larger recurring ingestion area than basic carbon nanowires. This shows that electromagnetic waves have a larger retention limit. [45]

# 1.6 Sustainable Synthesis of Magnetic Nanoparticles:

As it facilitates the creation of less polluting chemical processes and synthetic pathways to get desired

products using sustainable resources, catalysis is a crucial instrument in green chemistry. Catalysts must be able to recover, for them to be used on an industrial scale; this is a sine qua non need. Although heteroelement-containing molecules and metal complexes of rhodium, palladium, and iron have shown superiority in terms of activity and selectivity, the bulk of industrial catalysts continue to be heterogeneous due to the latter's ease of recovery. [46] Metal-containing NPs are desirable catalyst choices in this situation because they offer increased opportunities for recycling along with high activity, selectivity, and tunability. Size, crystallinity, the type of exposed facets, monodispersity, and composition of NPs are among those which influence catalytic process the most. [47]

#### 1.7 Bio-Inspired Synthesis of doped Bioactive Glass Nanoparticles:

A golden mean between synthetic and bio-based solutions has been found, considering the drawbacks of the bio-based approaches. Using a technique known as "bioinspiration," one can create synthetic molecules with the desired motifs by first comprehending the chemical principles that underlie the biological pathways. These artificial molecules enable control over important characteristics of nanomaterials, including particle size, crystallinity, and porosity, at the laboratory scale, while preserving the gentle, environmentally friendly character of biological production [26]. These bioinspired procedures typically work in water and at room temperature, taking a few minutes to complete. These characteristics lead to mild, one-step process that uses non-hazardous chemicals and significantly reduces time and energy consumption while allowing the synthesis of high-value compounds for specified applications.

The design of surfactants as templates for ordered mesoporous materials is the one used for bioinspired synthesis techniques [27]. Since its first report in 1992 [28], the surfactant-templated synthesis route has revolutionised the field of inorganic porous nanomaterials research. Nevertheless, because surfactants are frequently single-use substances, the strategy continues to have problems with poor resource (raw material) efficiency 27, 29. Renewable surfactants can take the place of

conventional synthetic surfactants by adding bioinspired motifs to their chemical structures [30]. This lessens the problem of materials' intensity during their manufacture.

# 1.8 Doped Bioactive glass Nanoparticles as effective photothermal agents (PTAs):

Due to their extraordinary qualities, which are essential for creating multifunctional systems, such as good biocompatibility, controllable degradation rate, osteo-inductivity, antibacterial capability, and pro-angiogenic effect, BG and glass-ceramics (BGCs) have been used since 1969 for a variety of applications in tissue engineering, implantology, and pharmaceutics.6–8 Since 21<sup>st</sup> century, several compounds have been seriously examined for the treatment of cancer.9, 10 They are altered to serve this goal by adding uncommon and biologically active components, which expands the scope of their functionality.11, 12 The various cancer treatment modalities that employ BG and BGCs are mentioned, including phototherapy, medication delivery, radiation, and hyperthermia.

Mesoporous bioactive glasses (MBGs) are a more targeted treatment for malignant tumours because they include built-in features such as the capacity to control gene expression and regenerate damaged tissue or bone, along with the ability to load and release medications under control. In order to selectively improve treatment of medications depending on the pH difference between normal and malignant tissues, new drug delivery methods based on pH-triggered drug release by MBGs are being developed. These intelligent devices exhibit specific tumour damage in vivo and increase the toxicity of cancer cells in vitro.

Since laser penetration may be controlled, a locally heated malignant area exposed to laser radiation may occur in photothermal effect (PTT). Here, hot cancer cells are eliminated without endangering surrounding tissues or organs. As PT conversion agents, a variety of NPs have been used to absorb near infrared (NIR) light and convert it to heat. Thermal apoptosis of malignant cells can also be produced by the PT effect brought on by light input. Research revealed that the glass structure's doping of metal ions may have PTT therapeutic potential. The first PTT effect in BG doped with

copper, iron, manganese, and cobalt ions was reported by a researcher. Moreover, carbon dots (148) and bismuth (Bi) (147) caused a PTT effect in BG. One novel concept involved utilising BG to rebuild bone while combining PTT, medication administration, radiotherapy, and spectacles to create multifunctional cancer treatment devices. To achieve the best possible therapeutic impact for bone tumours, multifunctional glasses with anticancer and bone-regenerative capabilities that can remove bone tumours and frequently stimulate the production of new bones are being developed. Bi-doped BG were created by another researcher to induce PTT and bioactivity response for bone tumour therapy and tissue restoration. Bi-doped BG enhances remineralization of bone tissue and provides photo-induced hyperthermia. Depending on the irradiation time and Bi concentration, the high PTT transformation of Bi raised the temperature locally from 42 °C to 86 °C.

The nonradiative and radiative techniques were controlled to regulate the PTT effects. Additionally, Bi-doped BGs had a strong inhibitory effect on the survival of malignant cells and were noncytotoxic before and after laser irradiation. It was demonstrated that exposure to NIR killed over 80% of human osteosarcoma line U2OS tumour cells. These dual-functional materials present novel opportunities for the treatment of bone tumours due to their exceptional bioactivity and tumour therapy. Another element that can be added to MBGs to provide PTT effect while preserving bioactivity is copper. Owing to their superior biocompatibility, antimicrobial qualities, bone-regenerating capacity, and cancer theragnostic, copper-doped BG offer promising prospects for biomedical uses. In PTT, it is essential to administer a very homogeneous laser to the treated region to prevent tissue damage from localised hot spots.

#### 1.9 Biomedical Applications

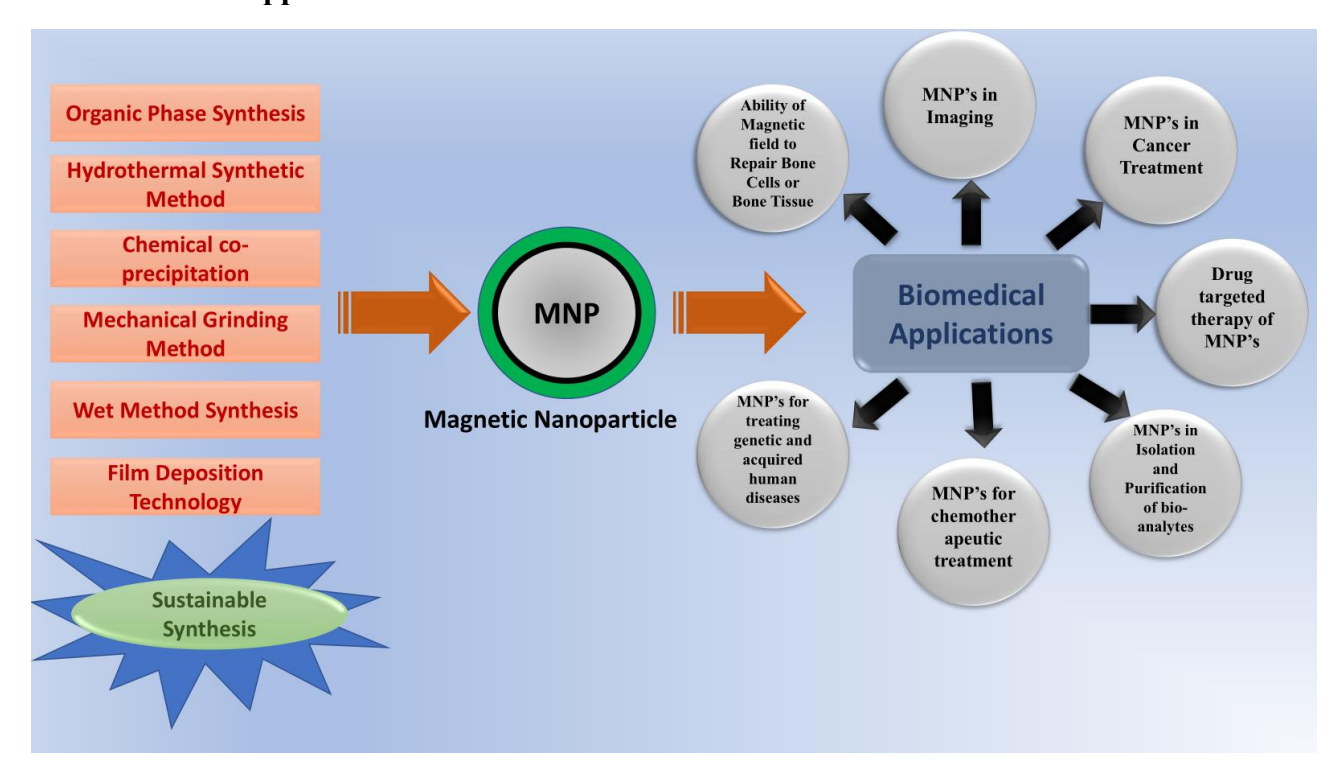


Fig.1.4 Synthetic techniques and Biomedical Applications of the Magnetic Nanoparticles

#### 1.9.1 Ability of Magnetic field to Repair Bone Cells or Bone Tissue

It is possible to manage and direct a cell's capacity when it is subjected to an external attractive field because attractive NPs can stick to the surface of the cell. The study investigated the effects of attractive 200 NPs on undifferentiated mesenchymal cells in bone marrow. [48] When an external attractive field is triggered, attractive NPs have the potential to greatly accelerate the proliferation of undifferentiated bone marrow mesenchymal cells. The experiments concentrated on the impact of attractive NPs and an applied attractive field on human mesenchymal basic microorganisms. [49] After 21 days of *in-vitro* development with accepting medium and the action of attractive NPs with attractive field, human mesenchymal immature microorganisms can separate into osteoblasts, adipocytes, and chondrocytes. [50] Defective skull bones of naked mice were filled with polished in vitro cells. However, the control group did not show any new bone shape 14 days after the cells were inserted, according to histological analyses (no embedded cells). [51] It demonstrated how combining

the effects of an attractive field and a NP attractor might hasten bone healing. It has been demonstrated that due to larger part of their own intrinsic attractive power and the external attractive field, attractive NPs can accelerate bone tissue healing. The external attractive field's impact on bone healing was the subject of studies. [52] They placed calcium phosphate-attractive NP composites under the rodent's back. When subjected to an external attractive field, this composite material can considerably speed up cell division and proliferation as well as the development of new bone tissue 30 days later. This exemplifies the ability of the field of attraction to aid in bone mending. [53] It is essential to maintain the flow of NPs among MNPs to ensure the full impact. Although this degree of misunderstanding is most obvious at the nanometre scale, it grows when molecule size lowers on the material's surface. [54,55] NPs exhibit highly pronounced impacts of material holding power, van der Waals scattering power, and Coulomb power. Reassembling particles is simple. From the standpoint of surface energy, the bulk of MNPs have high surface energies and are hydrophobic. [56,57] The tendency of these NPs to combine into large agglomerates ultimately causes molecules to grow larger in order to decrease the total surface energy. [58] As demonstrated by the agglomeration system of MNPs, the scattering problem of nanometres is largely intended to address the issue of hard agglomeration (particles agglomerated in an eye-to-eye association between NPs). Freeze drying, non-agglomeration under ultrasonic activity, naturally dissolvable washing, and surfactant against agglomeration are currently the most widely used non-agglomeration techniques. [59] The one that best inhibits agglomeration among them is the surfactant, also referred to as a surface modification. The ability of MNPs to heal bones in interesting fields will depend on how well they can re-join, deteriorate, or change in structure. [60] Particles with underlying alterations mainly show that after the action, the responsiveness of the attractive field boost, the migration of bone cells, and the bone healing work gets diminished. This is in contrast to MNPs in good condition. [61] Magnetic nanomaterials are superparamagnetic and offer desirable responsiveness in addition to the exceptional properties of nanoscale materials. [62] They can hold onto electromagnetic waves to generate heat in a variable

attractive environment and can align and orient themselves in a constant attractive field. Attractive iron oxide NPs are widely used in these processes to promote drug stacking, bone organisation with undifferentiated cells, bone arrangement with structures, and bone creation. It has been proved through various studies that attractive NPs have high application potential that can significantly heal the bone. [63]

#### 1.9.2 Magnetic nanoparticles in Imaging

The advancements in nanotechnology, cell and atomic research, and imaging modalities have led to new imaging discoveries. MRI is used in biomedical imaging to visualise a sign that manifests as a tissue response to an external attractive field that is controlled by the proton thickness of a proton and the attractive unwinding time. [64] More than 30% of MRI investigations conducted till now have focused on contrast experts. The practical applications for cancer imaging of sizes 2 -3 mm are enabled by the high spatial MRI aim and MNP accuracy to the objective. [65] Pre-arranged composites may be excellent T2 contrast specialists that improve imaging of HepG2 human hepatocellular carcinoma present in mice, according to experimental evidence from animals. [66] Despite attempts in vivo, macrophages and tumour cells absorbed poly (ethylene glycol) (PEG)coated, customised MNPs with a 15 nm centre size with little to no negative effects in in vitro experiments. [55] After injection, the tumour ingested organised nanoparticles in substantial volumes, providing unusual possibility for continual monitoring of the growth's evolution while magnetic resonance imaging (MRI) continued to contrast different specialists. Surface ligands significantly enhanced the MNPs' MRI application look. [67] MNPs have recently been combined with other NPs for multimodal imaging techniques to enhance the imaging signal for the early detection and treatment of cerebrum disorders. MNPs can be used for bimodal imaging because of their uniqueness. [10] In order to analyse diseases or internal wounds in veins, bones, delicate tissues, and other parts of the body, MNPs have been studied in registered tomography (CT) as multimodal contrast specialists. Other NPs, such as gold NPs, have been mixed with these particles.[69] Due to their high X-beam reduction and high thickness, mixture NPs can be used as CT contrast agents to help distinguish between organic and nonbiological materials and tests. MNPs with beneficial groups enable them to target certain organs or potentially even tissues, reducing their detrimental effects. [68] In ghosts for X-beam CT and T2-weighted MRI, novel multimodal contrast agents constructed of gold-covered SPIONs have been investigated. When illuminated with X-beams, the gold coating may raise the difference of these NPs. The appealing material is a well-known cause of negative differentiation in MRI. [69] Separately, gold nanospheres with amino functionalities (Au-SHPEG-NH<sub>2</sub>) and hydrophilic and carboxyl-functionalized Fe<sub>3</sub>O<sub>4</sub> NPs were mixed. By mixing hydrophilic Fe<sub>3</sub>O<sub>4</sub> NPs with gold NPs via an amide reaction, Au-Fe<sub>3</sub>O<sub>4</sub> nanohybrid composites were created. [70] MNPs have also been employed in ex vivo tissue models and as a bosom mirrored ghost for ultrasonic CT (UCT) imaging. It demonstrated an improvement in the ratio of difference to commotion and can be applied as a first step in a medical diagnosis. [71] It was also suggested that these MNPs may be used for multimodal magnetic resonance/computed tomography imaging, making it possible to detect the presence and spatial distribution of molecules in both raster-filter projection and ultrasound computed tomography imaging. These nanocomposites have incredible promise for synchronous multimodal imaging-directed malignant growth biomedical applications because of their profoundly adaptive multifunctionality. [72] These bimodal experts upgraded the double/multipurpose differentiation, which may also have the potential to occur on the watch. However, it was anticipated that additional research will highlight the clinical utility of metallic NPs. [73]

### 1.9.3 Magnetic nanoparticles in Cancer Treatment

Biocompatible MNPs have undergone substantial study as heat sensors for hyperthermia in the therapy of malignant development due to their high adequacy and a number of incidental consequences. [74] It eventually developed into a cutting-edge and creative heat therapy where MNPs are the masters of heat delivery. Effective therapeutic procedures include chemotherapy, surgery, immunotherapy, and radiation therapy in addition to the disease-treating methods presently in use.

[75] When cancer cells are exposed to a non-intrusive applied exchange alternating magnetic field (AMF), MNPs produce heat that causes attractive hyperthermia, which leads to cell death. MNPs are a treatment option for hyperthermia in general. [76] Furthermore, IONPs coated in dextran or liposomes are another class of MNPs that has attracted significant clinical attention. Due to their greater strength in aqueous arrangements, mixture nanomagnetic structures displayed higher specific absorption rates (SAR) values than exposed NPs. [77] Both in vitro and in vivo, they provide heat to cancer cells while having no negative or unfavourable impact on the cells around them. According to a recent study, the underlying reasons for the temperature increase are still not entirely understood. [78] In cultures with low MNP content and another AMF of low force, it is difficult to forecast the observable temperature rise in attractive hyperthermia. Therefore, it was investigated if cell death may be caused in this circumstance by intracellular ROS formation. It is nevertheless anticipated that strong and superior hotness nano mediators with incredible SAR values will be produced for quantified clinical applications. They are essential to overcome the different challenges previously faced because of the considerable amount of nanomaterial required for effective therapy. [24] The advantages of SAR are influenced by the attractive field's abundance and recurrence (f), as well as the morphology and synthesis of the MNPs (H). Therefore, the favourably implanted NPs should display high SAR and low f/H in the low material to achieve an influence of hyperthermia to malignancies. [79] To boost the SAR upsides when measuring SPIONs, either f or H (or both) can be extended. Still, clinical heating of prostate malignant growth is a difficult task. Clinical investigations using transmitted MNPs for thermotherapy have been successfully targeted for patients with prostate and glioblastoma problems since 2007. [81] Ten individuals had IONP liquid transperineally administered into their prostates over the course of six weeks. Six heated treatments lasting 60 minutes each. The cancer zone and peritumoral zone have mild temperatures of 40.7 °C and 40.2 °C, respectively, whereas the prostate has the greatest temperature at 55 °C. Because of experiencing no substantial post therapy-related diseases, it proved the feasibility of the theory. [80] They examined the possibility and universal acceptability of interstitial warming using IONPs in patients with locally recurring prostate malignant development and the very long-lasting maintenance of NPs in the prostate in a further modified clinical test. [81] The hyperthermia therapy can treat the most aggressive part of the tumour in people with normal glioblastoma, delaying or eliminating the need for radiotherapy or other medical intervention. The patients in this preliminary trial had a fever of 44.6 °C after receiving 4/10 medicines. All patients appeared to tolerate IONPs well, with little to no side effects. [82] Patients with metastatic bone growths have developed hyperthermia as a result of carefully manipulating "exposed" magnetite NPs and calcium phosphate concrete, a biocompatible bone substitute, before implanting it. [83] Future preclinical research should focus on developing MNPs with improved targeting and heating capabilities for tumours. Additionally, other hyperthermia enhancers should be investigated in conjunction with attractive hyperthermia in order to attain clinical viability. [84]

# 1.9.4 Drug Targeted Therapy of Magnetic Nanoparticles

Attractive drug delivery systems with a therapeutic component embedded in composites of MNPs and polymers or bonded to shallow MNPs. The direct distribution of medications to an infection site without causing systemic side effects is known as targeted drug delivery. This can happen under a range of circumstances, including electric flow, attractive fields, temperature, light, and ultrasound. [85] The surface charge, charge thickness, substance compliance, shape, inner morphology, size, debasement, and aversion to upgrades of MNPs are among their intriguing and promising therapeutic qualities for the treatment of disorders. In a rodent intravenous growth model, IONPs coated in aminosilane were administered as a vaccine. The growth was then heated to a temperature of around 43 °C to initiate the AMF growth inversion. [86] After the mice had been dead for 30 minutes, researchers discovered that, in an AMF, directly injecting an IONP solution into mouse head and neck cancer cells had no effect on normal cells. The biocompatible polymer PEG, which allowed this compound to pass through the reticuloendothelial framework, also enabled longer-lasting drug control. A new nanocarrier containing magnetite NPs and DOX was made using a single emulsion process, enclosed

in a biocompatible poly (lactic-glycolic corrosive) (PLGA) shell. [87] They were employed for controlled drug administration via intra-tumorally planned distribution. For MRI examinations, representational and therapeutic superparamagnetic magnetite NPs with an oleic corrosive coating are created in uniform-size PLGA nanospheres utilising an improved two-fold emulsion technique. The inclusion of MNPs altered the acquisition properties of the marginally water-soluble anti-cancer drug camptothecin. [88] The regulated drug release can concentrate on inhibiting malignant growth in actual animal bodies because the medication is coupled with MNPs in a composite. The use of MNPs as a transporter design is so effective and has intriguing biomedical and biotechnology implications. In order to develop multidisciplinary investigations in drug-conveyance frameworks and disease therapy with superior execution and few side effects, poly(lactide-co-glycoside) (PLGA) nanocomposite particles containing 5-FU and gold-improved magnetite NPs with a raspberry-like morphology were developed. [89] The most recent test showed improved double magneto- and photothermal reactions as a result of the coexistence of gold and Fe<sub>3</sub>O<sub>4</sub> NPs. The drug delivery profile of the 5-fluorouracil (5-FU)-stacked nanocomposite particles was proven using a regulated delivery temperature of 37 °C in a phosphate-cradled saline setup. [90] Additionally, novel silica-covered iron oxide/polyaniline nanocomposites (Si-MNPs/PANI) with double stimuli-responsiveness have been created for biological applications. The findings demonstrated that Si-MNPs/PANI nanocomposites exhibited both aesthetically pleasing and electrically sensitive properties. Furthermore, these composites' in vitro cytocompatibility and hemocompatibility support their usage in particular dosages for controlled drug administration. [91] Despite its versatility and low cost advantages, electrical upgrades cannot be used in biomedical applications due to the risk of damaging healthy tissue due to its deeper penetrating action (lessening the improvement). [92]

# 1.9.5 Magnetic nanoparticles in Isolation and purification of bio-analytes

The world of biomedicine is transformed by attractive detachment thanks to sophisticated, focused, and controlled target capture. Chemicals, nucleic acids, antibodies, and proteins are examples of bio-

analytes that can be separated and filtered utilising intricate, time-consuming chromatographic and electrophoretic procedures that integrate a range of advances. [93] The transfer of intriguing biomolecules that have been immobilised on a robust framework is one of these techniques. These methods can be replaced in terms of work, time, and yield by using MNPs produced with proclivity ligands to separate biomolecules from the mixture. [94] A faultless and skilled partition stage with excellent magnetophoretic adaptation is attractively responsive. The materials' enticing helplessness and size have an impact on how rapidly they respond to the intriguing field that is distantly applied. [95] Using a few levels of schematic depiction, the bio-separation of bio-analytes bound to MNPs is introduced. Because of their strength, great biocompatibility, appealing qualities, and high limits, MNPs are being used widely in bio-separation. [96] Without causing any damage to the sample, MNPs differentiate natural analytes from synthetic samples and lessen the hazy adsorption of undesired bio-analytes. Because of their low cost, high expulsion limit, reusability, high surface-tovolume proportion, and reactivity towards eluent chemicals, MNPs are perfectly suited for detachment applications. [97] Additionally, it is more effective than centrifugation and filtration. In order to protect their surface from high temperatures and solid pH and to efficiently immobilise and separate proteins, nucleic acids, antibodies, chemicals, and other biomolecules, MNPs have replaced other substances due to their limited solubility. [98] Detachment methods have transformed into repeatable, quantitative, and arbitrary analytical instruments for biomedical applications in light of MNPs. Attractive division transforms into a quick, suitable, careful, and sensitive strategy for the improvement, cleansing, and identification of cells and macromolecules when paired with other identification approaches like microscopy. [99] It can also be produced as a fundamental part of microfluidic gadgets. MNPs can also be utilised to remove pathogens, tumours, and antigens locally or more broadly in vivo for diagnostic purposes. [101]

#### 1.9.6 Magnetic nanoparticles for Chemotherapeutic treatment

Chemotherapeutic therapy does not have the ability to target individual cells; instead, it has cytostatic

and cytotoxic effects. It is widely used to treat malignant developments and kill cancer cells. After disguising, MNPs can be trained to concentrate on a specific area. [100] These NPs include therapeutic mixtures that are delivered to the cytoplasm of the cell to carry out the intended activity. Chemotherapeutic drug experts utilise MNPs that are infused into the blood and controlled by an alluring field remotely applied to the objective specific growth area to manufacture a helpful chemical. [101] Chemotherapeutics begin with the introduction of drugs intended to harm the diseasecausing cells' architecture. Biodistribution is improved by the impact of an appealing field on MNPs for safe transit of the drug to the interior milieu. [102] MNPs make it possible to utilise pharmaceuticals at dosages that minimise their potential negative effects. For drug-conveyance frameworks, these restorative combinations have a number of advantages over standard mixtures, including an improvement in intracellular invasion, a longer drug dissemination duration, and an increase in hydrophobic solubility. [90] Reduced hazy take-up, improved focus, controlled drug release, easier administration, and rational organisational frameworks are all benefits of controlled medicine delivery systems (aspiratory, oral, transdermal, and parenteral). The DOX medicine was effectively delivered using the intended nanocarrier, which was based on IONPs. By creating heat in an AMF, it could indirectly destroy disease-causing cells. [103] The model drug for the treatment of bosom illness was delivered using DOX-stacked alluring alginate chitosan microspheres (MCF-7). To induce the release of the medication DOX, they employed SPIONs, or alluring experts in hyperthermia. Studying MCF-7 cells in vitro and comparing them to either chemotherapy or attractive heat revealed significant cell passage. [104] The MNPs provided the heat within the shell and enhanced its permeability to enable medication administration. Bosom malignant growth cell (4T1) in vitro cultures induce apoptosis similarly to chemotherapy. MNPs and a lipophilic drug, carmustine, were stacked in the lipid centre of the oleosome to treat disease. These appealing oleosomes release the medication in a burst, which starts the anticancer effect. Combining an inventive SPION hydrogel with DOX demonstrated a successful remedy design and controlled medication release. [105] This

ground-breaking hydrogel therapy technique demonstrated excellent promise for slowing the growth of certain malignancies. Fe<sub>3</sub>O<sub>4</sub>-centered NPs in an AMF can produce enough heat by the release of DOX from an alginate shell to perform dynamic hyperthermia in conjunction with chemotherapy. These NPs include folic acid, which made it easier for the finished nanocomposite to penetrate and remain in the developing cells for longer period of time. [106] Specifically in light of the existence of a folate factor, *in vivo* trial and error proved the common sense of shared therapy for cellular breakdown in the lungs of mouse. [107]

# 1.9.7 Magnetic nanoparticles for treating genetic and acquired human diseases

The most efficient method for treating both inherited and acquired human illnesses is the conveyance stage with MNPs mixed with characteristics. It has viral, polymeric, non-viral, and MNPs that improve cell uptake to cure inherited diseases. The addition of an exterior quality with a functional quality to encode the helpful protein to treat the infection-causing transformation is the fundamental idea guiding the proposed remedial framework. [108] In order to supply quality, it is essential for these actions to advance DNA security, safeguard an objective quality from nuclease contamination, and raise change viability or care. One of the major quality delivery factors is the ability to target specific tissues or cells. MNPs and gene therapies have been proved to be effective in shielding nucleic acids from enzymatic degradation and endosomal liberation following cell internalisation. [109] Human bronchial epithelial cells that have undergone full transfection in vitro serve as the foundation for MNP-based quality transfection. By attaching DNA covalently to stripped MNPs, a novel DNA nano-vector was created, which by default created an incredibly sturdy quality conveyance structure. It was the reason why mesenchymal basic microorganisms had better cell uptake and higher transfection productivity. [110] To combat the undervaluation of typical quality treatment techniques, MNPs were created with restorative quality transporters. MNPs may successfully deliver exogenous quality to large vertebrate cells, while intracellular monitoring can reveal very consistent quality articulations. Thus, a promising method for the transfection of diverse

tissue explants and cell lines for quality therapy is exquisitely focussed upon via MNPs. For the successful recycling and recovery of a catalyst, intriguing (Fe<sub>3</sub>O<sub>4</sub>) NPs with alkyltrimethoxysilane functionalization and legal alkyl lengths formed uncommon candidates for efficient transporters for immobilising lipase. Trypsin molecule was noncovalently bonded to magnetite NPs in order to immobilise it and preserve the catalytic action for future re-use. [111] Using biotin to create MNPs for protein immobilisation dramatically reduced the likelihood of denaturation or protein debasement. Due to their vast surface area and tiny size, MNPs have been developed as flexible and multifunctional devices that offer ideal backings for the immobilisation of catalyst. By combining them with the appropriate surface functionalization, a variety of MNPs have been effectively used to immobilise chemicals and proteins that had previously demonstrated promising qualities in a number of real-world bio-applications. [112]

# 2.0 Research Gap

- The possible research gaps that I have came across till date for bioactive glass are as follows:
- 1. Major studies focus on the bioactive glass as a bone regenerative material and in bone tissue engineering applications.
- 2. Studies related to therapeutic applications related to regenerative medicine, periodontology using Bioactive glass are very less.
- 3. To the best of our knowledge, therapeutic molecule laden bioactive glass for bone regeneration at a bone diseased site through topical delivery is an unexplored area which can be exploited for future benefits.

# 2.1 Objectives

- To synthesize and characterize soft templated bioactive glass nanoparticles by bio-inspired method.
  - 1. To develop magnetite templated bioactive glass nano assembly for magnetic hyperthermia treatment of cancer.
  - 2. To fabricate folic acid templated bioactive glass nanoparticles for biomedical applications.
  - 3. To synthesize curcumin templated bioactive glass nanoparticles for photothermal treatment of cancer.
- To investigate the structure and properties of anti-cancerous drugs for bone cancer treatment.
- To evaluate magnetic and photothermal properties of bioactive glass nanoparticles.
- To evaluate the cytocompatibility and *in-vitro* interaction of bioactive glass-based material with the bone cells for therapeutic applications.

#### References

- [1] W. Liu, C. Chen, F. Wang, S. Guo, Y. Hao, S. Li, Development trend and current situation of acupuncture-moxibustion indications, World Journal of Acupuncture Moxibustion. 30 (2020) 245. https://doi.org/10.1016/j.wjam.2020.07.014.
- [2] C. Zhao, Z. Xing, C. Zhang, Y. Fan, H. Liu, Nanopharmaceutical-based regenerative medicine: a promising therapeutic strategy for spinal cord injury, J. Mater. Chem. B. 9 (2021) 2367. https://doi.org/10.1039/D0TB02740E.
- [3] A.J. Jones, B.J. Tucker, L.J. Novinger, C.E. Galer, R.F. Nelson, Metastatic Disease of the Temporal Bone: A Contemporary Review, Laryngoscope 131 (2021) 1101. https://doi.org/10.1002/lary.29096.
- [4] T. Wu, S. Yu, D. Chen, Y. Wang, Bionic Design, Materials and Performance of Bone Tissue Scaffolds, Materials (Basel). 10 (2017) 1187. https://doi.org/10.3390/ma10101187.
- [5] J. Jancar, J.F. Douglas, F.W. Starr, S.K. Kumar, P. Cassagnau, A.J. Lesser, S.S. Sternstein, M.J. Buehler, Current issues in research on structure–property relationships in polymer nanocomposites, Polymer. 51 (2010) 3321. https://doi.org/10.1016/j.polymer.2010.04.074.
- [6] W. Wang, K.W.K. Yeung, Bone grafts and biomaterials substitutes for bone defect repair: A review, Bioact Mater. 2 (2017) 224. https://doi.org/10.1016/j.bioactmat.2017.05.007.
- [7] F. Shang, Y. Yu, S. Liu, L. Ming, Y. Zhang, Z. Zhou, J. Zhao, Y. Jin, Advancing application of mesenchymal stem cell-based bone tissue regeneration, Bioact Mater. 6 (2021) 666. https://doi.org/10.1016/j.bioactmat.2020.08.014.
- [8] B.A. Lipsky, J.A. Weigelt, V. Gupta, A. Killian, M.M. Peng, Skin, soft tissue, bone, and joint infections in hospitalized patients: epidemiology and microbiological, clinical, and economic outcomes, Infect Control Hosp Epidemiol. 28 (2007) 1290. https://doi.org/10.1086/520743.
- [9] X. Huang, R. Das, A. Patel, T.D. Nguyen, Physical Stimulations for Bone and Cartilage Regeneration, Regen Eng Transl Med. 4 (2018) 216. https://doi.org/10.1007/s40883-018-0064-0.
- [10] E.S. Gil, S.M. Hudson, Stimuli-reponsive polymers and their bioconjugates, Progress in Polymer Science. 29 (2004) 1173. https://doi.org/10.1016/j.progpolymsci.2004.08.003.
- [11] P. Judeinstein, C. Sanchez, Hybrid organic—inorganic materials: a land of multidisciplinarity, J. Mater. Chem. 6 (1996) 511. https://doi.org/10.1039/JM9960600511.
- [12] S. Pina, J.M. Oliveira, R.L. Reis, Natural-based nanocomposites for bone tissue engineering and regenerative medicine: a review, Adv Mater. 27 (2015) 1143. https://doi.org/10.1002/adma.201403354.
- [13] S. Lee, S.U.S. Choi, S. Li, J.A. Eastman, Measuring Thermal Conductivity of Fluids Containing Oxide Nanoparticles, J. Heat Transfer 121 (1999) 280. https://doi.org/10.1115/1.2825978.
- [14] M. Tlda, R. Rg, M. Ls, M. Brc, S. Vm, R. Kf, T. Gp, A brief review concerning the latest advances in the influence of nanoparticle reinforcement into polymeric-matrix biomaterials, Journal of Biomaterials Science. Polymer Edition. 31 (2020). https://doi.org/10.1080/09205063.2020.1781527.
- [15] B. V. Derjaguin, I.I. Abrikosova, E.M. Lifshitz, Direct measurement of molecular attraction between solids separated by a narrow gap, Q. Rev. Chem. Soc. 10 (1956) 295. https://doi.org/10.1039/qr9561000295.
- [16] H.-R. Paur, F.R. Cassee, J. Teeguarden, H. Fissan, S. Diabate, M. Aufderheide, W.G. Kreyling, O. Hänninen, G. Kasper, M. Riediker, B. Rothen-Rutishauser, O. Schmid, In-vitro cell exposure studies for the assessment of nanoparticle toxicity in the lung—A dialog between

- aerosol science and biology, Journal of Aerosol Science. 42 (2011) 668. https://doi.org/10.1016/j.jaerosci.2011.06.005.
- [17] S. Mukherjee, L. Liang, O. Veiseh, Recent Advancements of Magnetic Nanomaterials in Cancer Therapy, Pharmaceutics 12 (2020) 147. https://doi.org/10.3390/pharmaceutics12020147.
- [18] I. Langmuir, The Role of Attractive and Repulsive Forces in the Formation of Tactoids, Thixotropic Gels, Protein Crystals and Coacervates, Journal of Chemical Physics. 6 (1938) 873. https://doi.org/10.1063/1.1750183.
- [19] C.H. Kong, C. Steffi, Z. Shi, W. Wang, Development of mesoporous bioactive glass nanoparticles and its use in bone tissue engineering, J. Biomed. Mater. Res. Part B Appl. Biomater. 106 (2018) 2878. https://doi.org/10.1002/jbm.b.34143.
- [20] N. Shadjou, M. Hasanzadeh, Silica-based mesoporous nanobiomaterials as promoter of bone regeneration process, J. Biomed. Mater. Res. Part A 103 (2015) 3703. https://doi.org/10.1002/jbm.a.35504.
- [21] S. Logothetidis, Nanomedicine: The Medicine of Tomorrow, in: 2012: pp. 1–26. https://doi.org/10.1007/978-3-642-24181-9\_1.
- [22] I. Khan, K. Saeed, I. Khan, Nanoparticles: Properties, applications and toxicities, Arabian Journal of Chemistry. 12 (2019) 908. https://doi.org/10.1016/j.arabjc.2017.05.011.
- [23] S. Bamrungsap, Z. Zhao, T. Chen, L. Wang, C. Li, T. Fu, W. Tan, Nanotechnology in therapeutics: a focus on nanoparticles as a drug delivery system, Nanomedicine. 7 (2012) 1253. https://doi.org/10.2217/nnm.12.87.
- [24] J. Yao, M. Yang, Y. Duan, Chemistry, Biology, and Medicine of Fluorescent Nanomaterials and Related Systems: New Insights into Biosensing, Bioimaging, Genomics, Diagnostics, and Therapy, Chem. Rev. 114 (2014) 6130. https://doi.org/10.1021/cr200359p.
- [25] B. Shahbahrami, S.M. Rabiee, R. Shidpoor, An Overview of Cobalt Ferrite Core-Shell Nanoparticles for Magnetic Hyperthermia Applications, Advanced Ceramics Progress. 6 (2020) 1. https://doi.org/10.30501/acp.2020.105923.
- [26] S. Bettini, V. Bonfrate, L. Valli, G. Giancane, Paramagnetic Functionalization of Biocompatible Scaffolds for Biomedical Applications: A Perspective, Bioengineering (Basel). 7 (2020) 153. https://doi.org/10.3390/bioengineering7040153.
- [27] A. Baral, L. Satish, G. Zhang, S. Ju, M.K. Ghosh, A Review of Recent Progress on Nano MnO2: Synthesis, Surface Modification and Applications, J. Inorg. Organomet. Polym. Mater. 31 (2021) 899. https://doi.org/10.1007/s10904-020-01823-z.
- [28] B. Ren, Y. Huang, C. Han, M.N. Nadagouda, D.D. Dionysiou, Ferrites as Photocatalysts for Water Splitting and Degradation of Contaminants, in: Ferrites and Ferrates: Chemistry and Applications in Sustainable Energy and Environmental Remediation, American Chemical Society, 2016: pp. 79–112. https://doi.org/10.1021/bk-2016-1238.ch003.
- [29] B. Pacakova, S. Kubickova, A. Reznickova, D. Niznansky, J. Vejpravova, Spinel Ferrite Nanoparticles: Correlation of Structure and Magnetism, in: Magn. Spinels - Synth. Prop. Appl., InTech, (2017). https://doi.org/10.5772/66074.
- [30] M. Sandroni, R. Gueret, K.D. Wegner, P. Reiss, J. Fortage, D. Aldakov, M.-N. Collomb, Cadmium-free CuInS2/ZnS quantum dots as efficient and robust photosensitizers in combination with a molecular catalyst for visible light-driven H2 production in water, Energy Environ. Sci. 11 (2018) 1752. https://doi.org/10.1039/C8EE00120K.
- [31] L. García-Hevia, Í. Casafont, J. Oliveira, N. Terán, M.L. Fanarraga, J. Gallo, M. Bañobre-López, Magnetic lipid nanovehicles synergize the controlled thermal release of chemotherapeutics with magnetic ablation while enabling non-invasive monitoring by MRI for

- melanoma theranostics, Bioactive Materials. 8 (2022) 153. https://doi.org/10.1016/j.bioactmat.2021.06.009.
- [32] P. Ceci, E. Chiancone, O. Kasyutich, G. Bellapadrona, L. Castelli, M. Fittipaldi, D. Gatteschi, C. Innocenti, C. Sangregorio, Synthesis of iron oxide nanoparticles in Listeria innocua Dps (DNA-binding protein from starved cells): a study with the wild-type protein and a catalytic centre mutant, Chemistry. 16 (2010) 709. https://doi.org/10.1002/chem.200901138.
- [33] M. Mahmoudpour, M. Torbati, M.-M. Mousavi, M. de la Guardia, J. Ezzati Nazhad Dolatabadi, Nanomaterial-based molecularly imprinted polymers for pesticides detection: Recent trends and future prospects, TrAC Trends in Analytical Chemistry. 129 (2020) 115943. https://doi.org/10.1016/j.trac.2020.115943.
- [34] W. Wu, Z. Wu, T. Yu, C. Jiang, W.-S. Kim, Recent progress on magnetic iron oxide nanoparticles: synthesis, surface functional strategies and biomedical applications, Sci. Technol. Adv. Mater. 16 (2015) 023501. https://doi.org/10.1088/1468-6996/16/2/023501.
- [35] J. Guo, W. Yang, C. Wang, Magnetic Colloidal Supraparticles: Design, Fabrication and Biomedical Applications, Advanced Materials. 25 (2013) 5196. https://doi.org/10.1002/adma.201301896.
- [36] W. Wu, C.Z. Jiang, V.A.L. Roy, Designed synthesis and surface engineering strategies of magnetic iron oxide nanoparticles for biomedical applications, Nanoscale. 8 (2016) 19421. https://doi.org/10.1039/C6NR07542H.
- [37] W. Ge, W. Wang, N. Yang, J. Li, M. Kwauk, F. Chen, J. Chen, X. Fang, L. Guo, X. He, X. Liu, Y. Liu, B. Lu, J. Wang, J. Wang, L. Wang, X. Wang, Q. Xiong, M. Xu, L. Deng, Y. Han, C. Hou, L. Hua, W. Huang, B. Li, C. Li, F. Li, Y. Ren, J. Xu, N. Zhang, Y. Zhang, G. Zhou, G. Zhou, Meso-scale oriented simulation towards virtual process engineering (VPE)—The EMMS Paradigm, Chemical Engineering Science. 66 (2011) 4426. https://doi.org/10.1016/j.ces.2011.05.029.
- [38] I. Zarudi, L.C. Zhang, Mechanical property improvement of quenchable steel by grinding, Journal of Materials Science. 37 (2002) 3935. https://doi.org/10.1023/A:1019671926384.
- [39] J. Tang, J. Qiao, Z. Liu, X. Zhou, G. Yu, J. Zhao, Mechanism characteristic analysis and soft measuring method review for ball mill load based on mechanical vibration and acoustic signals in the grinding process, Minerals Engineering. 128 (2018) 294. https://doi.org/10.1016/j.mineng.2018.09.006.
- [40] P. Colomban, B. Kırmızı, G. Simsek Franci, Cobalt and Associated Impurities in Blue (and Green) Glass, Glaze and Enamel: Relationships between Raw Materials, Processing, Composition, Phases and International Trade, Minerals. 11 (2021) 633. https://doi.org/10.3390/min11060633.
- [41] G. Hao, H. Li, C. Mao, Y. Hu, L. Xiao, G. Zhang, J. Liu, W. Jiang, F. Zhao, H. Gao, Preparation of Nano-Cu-Fe Composite Metal Oxides via a Mechanical Grinding Method and Its Catalytic Performance for the Thermal Decomposition of Ammonium Perchlorate, Combustion Science and Technology. 193 (2021) 987. https://doi.org/10.1080/00102202.2019.1679125.
- [42] J.D. Holmes, D.M. Lyons, K.J. Ziegler, Supercritical Fluid Synthesis of Metal and Semiconductor Nanomaterials, Chemistry A European Journal. 9 (2003) 2144. https://doi.org/10.1002/chem.200204521.
- [43] A. Ali, H. Zafar, M. Zia, I. ul Haq, A.R. Phull, J.S. Ali, A. Hussain, Synthesis, characterization, applications, and challenges of iron oxide nanoparticles, Nanotechnol. Sci. Appl. Volume 9 (2016) 49. https://doi.org/10.2147/NSA.S99986.
- [44] A. Gulzar, P. Yang, F. He, J. Xu, D. Yang, L. Xu, M.O. Jan, Bioapplications of graphene constructed functional nanomaterials, Chemico-Biological Interactions. 262 (2017) 69. https://doi.org/10.1016/j.cbi.2016.11.019.

- [45] Z. Zhang, S. Satpathy, Electromagnetic wave propagation in periodic structures: Bloch wave solution of Maxwell's equations, Phys Rev Lett. 65 (1990) 2650. https://doi.org/10.1103/PhysRevLett.65.2650.
- [46] D. Pleissner, K. Kümmerer, Green Chemistry and Its Contribution to Industrial Biotechnology, Adv Biochem Eng Biotechnol. 173 (2020) 281. https://doi.org/10.1007/10 2018 73.
- [47] F.P. da Silva, J.L. Fiorio, L.M. Rossi, Tuning the Catalytic Activity and Selectivity of Pd Nanoparticles Using Ligand-Modified Supports and Surfaces, ACS Omega 2 (2017) 6014. https://doi.org/10.1021/acsomega.7b00836.
- [48] N. K, PatelReema, N. M, ZhengJiwen, N. J, KumarGirish, G. L, Effects of Subcytotoxic Exposure of Silver Nanoparticles on Osteogenic Differentiation of Human Bone Marrow Stem Cells, Applied In Vitro Toxicology. (2019). https://doi.org/10.1089/aivt.2019.0001.
- [49] V. Zablotskii, O. Lunov, S. Kubinova, T. Polyakova, E. Sykova, A. Dejneka, Effects of high-gradient magnetic fields on living cell machinery, J. Phys. D: Appl. Phys. 49 (2016) 493003. https://doi.org/10.1088/0022-3727/49/493003.
- [50] F. Donnaloja, E. Jacchetti, M. Soncini, M.T. Raimondi, Natural and Synthetic Polymers for Bone Scaffolds Optimization, Polymers (Basel). 12 (2020) 905. https://doi.org/10.3390/polym12040905.
- [51] S.R. Rittling, H.N. Matsumoto, M.D. McKee, A. Nanci, X.R. An, K.E. Novick, A.J. Kowalski, M. Noda, D.T. Denhardt, Mice lacking osteopontin show normal development and bone structure but display altered osteoclast formation in vitro, J Bone Miner Res. 13 (1998) 1101. https://doi.org/10.1359/jbmr.1998.13.7.1101.
- [52] M. Vallet-Regí, E. Ruiz-Hernández, Bioceramics: from bone regeneration to cancer nanomedicine, Adv Mater. 23 (2011) 5177. https://doi.org/10.1002/adma.201101586.
- [53] X. Zhai, C. Ruan, J. Shen, C. Zheng, X. Zhao, H. Pan, W.W. Lu, Clay-based nanocomposite hydrogel with attractive mechanical properties and sustained bioactive ion release for bone defect repair, J. Mater. Chem. B. 9 (2021) 2394. https://doi.org/10.1039/D1TB00184A.
- [54] A.A. Golneshan, M. Lahonian, The effect of magnetic nanoparticle dispersion on temperature distribution in a spherical tissue in magnetic fluid hyperthermia using the lattice Boltzmann method, Int J Hyperthermia. 27 (2011) 266. https://doi.org/10.3109/02656736.2010.519370.
- [55] S. Khizar, N.M. Ahmad, N. Zine, N. Jaffrezic-Renault, A. Errachid-el-salhi, A. Elaissari, Magnetic Nanoparticles: From Synthesis to Theranostic Applications, ACS Appl. Nano Mater. 4 (2021) 4284. https://doi.org/10.1021/acsanm.1c00852.
- [56] R.K. Adair, Constraints on biological effects of weak extremely-low-frequency electromagnetic fields, Phys Rev A. 43 (1991) 1039. https://doi.org/10.1103/physreva.43.1039.
- [57] A. Tsuda, N.K. Venkata, The role of natural processes and surface energy of inhaled engineered nanoparticles on aggregation and corona formation, NanoImpact. 2 (2016) 38. https://doi.org/10.1016/j.impact.2016.06.002.
- [58] S. Wintzheimer, T. Granath, M. Oppmann, T. Kister, T. Thai, T. Kraus, N. Vogel, K. Mandel, Supraparticles: Functionality from Uniform Structural Motifs, ACS Nano. 12 (2018) 5093. https://doi.org/10.1021/acsnano.8b00873.
- [59] V. Uskoković, D.P. Uskoković, Nanosized hydroxyapatite and other calcium phosphates: chemistry of formation and application as drug and gene delivery agents, J Biomed Mater Res B Appl Biomater. 96 (2011) 152. https://doi.org/10.1002/jbm.b.31746.
- [60] W.J. Chong, S. Shen, Y. Li, A. Trinchi, D. Pejak, I. (Louis) Kyratzis, A. Sola, C. Wen, Additive manufacturing of antibacterial PLA-ZnO nanocomposites: Benefits, limitations and open challenges, Journal of Materials Science & Technology. 111 (2022) 120. https://doi.org/10.1016/j.jmst.2021.09.039.

- [61] B.L. Riggs, A.M. Parfitt, Drugs used to treat osteoporosis: the critical need for a uniform nomenclature based on their action on bone remodeling, J Bone Miner Res. 20 (2005) 177. https://doi.org/10.1359/JBMR.041114.
- [62] S. Patra, E. Roy, P. Karfa, S. Kumar, R. Madhuri, P.K. Sharma, Dual-Responsive Polymer Coated Superparamagnetic Nanoparticle for Targeted Drug Delivery and Hyperthermia Treatment, ACS Appl. Mater. Interfaces. 7 (2015) 9235. https://doi.org/10.1021/acsami.5b01786.
- [63] A. Gloria, T. Russo, U. D'Amora, S. Zeppetelli, T. D'Alessandro, M. Sandri, M. Bañobre-López, Y. Piñeiro-Redondo, M. Uhlarz, A. Tampieri, J. Rivas, T. Herrmannsdörfer, V.A. Dediu, L. Ambrosio, R. De Santis, Magnetic poly(ε-caprolactone)/iron-doped hydroxyapatite nanocomposite substrates for advanced bone tissue engineering, J R Soc Interface. 10 (2013) 20120833. https://doi.org/10.1098/rsif.2012.0833.
- [64] S. Vallinayagam, K. Rajendran, Synthesis and Application of Nanomaterials for Biomedical Anticancer Therapy, in: K. Pal (Ed.), Bio-Manufactured Nanomaterials: Perspectives and Promotion, Springer International Publishing, Cham, 2021: pp. 339–373. https://doi.org/10.1007/978-3-030-67223-2 16.
- [65] C. Rümenapp, B. Gleich, A. Haase, Magnetic nanoparticles in magnetic resonance imaging and diagnostics, Pharm Res. 29 (2012) 1165. https://doi.org/10.1007/s11095-012-0711-y.
- [66] R. Ansar, S. Saqib, A. Mukhtar, M.B.K. Niazi, M. Shahid, Z. Jahan, S.J. Kakar, B. Uzair, M. Mubashir, S. Ullah, K.S. Khoo, H.R. Lim, P.L. Show, Challenges and recent trends with the development of hydrogel fiber for biomedical applications, Chemosphere. 287 (2022) 131956. https://doi.org/10.1016/j.chemosphere.2021.131956.
- [67] F. Zeinali Sehrig, S. Majidi, S. Asvadi, A. Hsanzadeh, S.H. Rasta, M. Emamverdy, J. Akbarzadeh, S. Jahangiri, S. Farahkhiz, A. Akbarzadeh, An update on clinical applications of magnetic nanoparticles for increasing the resolution of magnetic resonance imaging, Artif Cells Nanomed Biotechnol. 44 (2016) 1583. https://doi.org/10.3109/21691401.2015.1101001.
- [68] S. Akhter, Z. Ahmad, A. Singh, I. Ahmad, M. Rahman, M. Anwar, G.K. Jain, F.J. Ahmad, R.K. Khar, Cancer targeted metallic nanoparticle: targeting overview, recent advancement and toxicity concern, Curr Pharm Des. 17 (2011) 1834. https://doi.org/10.2174/138161211796391001.
- [69] F. Assa, H. Jafarizadeh-Malmiri, H. Ajamein, H. Vaghari, N. Anarjan, O. Ahmadi, A. Berenjian, Chitosan magnetic nanoparticles for drug delivery systems, Crit Rev Biotechnol. 37 (2017) 492. https://doi.org/10.1080/07388551.2016.1185389.
- [70] M. Arefi, D. Saberi, M. Karimi, A. Heydari, Superparamagnetic Fe(OH)3@Fe3O4 Nanoparticles: An Efficient and Recoverable Catalyst for Tandem Oxidative Amidation of Alcohols with Amine Hydrochloride Salts, ACS Comb. Sci. 17 (2015) 341. https://doi.org/10.1021/co5001844.
- [71] W. Sun, S. Huang, S. Zhang, Q. Luo, Preparation, Characterization and Application of Multi-Mode Imaging Functional Graphene Au-Fe3O4 Magnetic Nanocomposites, Materials. 12 (2019) 1978. https://doi.org/10.3390/ma12121978.
- [72] K. Khan, A.K. Tareen, M. Iqbal, L. Wang, C. Ma, Z. Shi, Z. Ye, W. Ahmad, R.U. Rehman Sagar, S.S. Shams, P.J. Sophia, Z. Ullah, Z. Xie, Z. Guo, H. Zhang, Navigating recent advances in monoelemental materials (Xenes)-fundamental to biomedical applications, Progress in Solid State Chemistry. 63 (2021) 100326. https://doi.org/10.1016/j.progsolidstchem.2021.100326.
- [73] V. Mirabello, D.G. Calatayud, R.L. Arrowsmith, H. Ge, S.I. Pascu, Metallic nanoparticles as synthetic building blocks for cancer diagnostics: from materials design to molecular imaging applications, J. Mater. Chem. B. 3 (2015) 5657. https://doi.org/10.1039/C5TB00841G.
- [74] R. Gupta, D. Sharma, Therapeutic response differences between 2D and 3D tumor models of magnetic hyperthermia, Nanoscale Adv. 3 (2021) 3663. https://doi.org/10.1039/D1NA00224D.

- [75] M. Izci, C. Maksoudian, B.B. Manshian, S.J. Soenen, The Use of Alternative Strategies for Enhanced Nanoparticle Delivery to Solid Tumors, Chem. Rev. 121 (2021) 1746. https://doi.org/10.1021/acs.chemrev.0c00779.
- [76] Y. Chen, H. Chen, J. Shi, Inorganic Nanoparticle-Based Drug Codelivery Nanosystems To Overcome the Multidrug Resistance of Cancer Cells, Mol. Pharmaceutics. 11 (2014) 2495. https://doi.org/10.1021/mp400596v.
- [77] Addressing the dynamical magnetic response of magnetic nanoparticles after interacting with biological entities, Doctorate Nanobio. (2020). http://doctorate-nanobio-uam.es/addressing-the-dynamical-magnetic-response-of-magnetic-nanoparticles-after-interacting-with-biological-entities/ (accessed January 12, 2023).
- [78] G. Orlando, A.C. Farney, S.S. Iskandar, S.-H. Mirmalek-Sani, D.C. Sullivan, E. Moran, T. AbouShwareb, P. De Coppi, K.J. Wood, R.J. Stratta, A. Atala, J.J. Yoo, S. Soker, Production and implantation of renal extracellular matrix scaffolds from porcine kidneys as a platform for renal bioengineering investigations, Ann Surg. 256 (2012) 363. https://doi.org/10.1097/SLA.0b013e31825a02ab.
- [79] A. Del Pozo-Rodríguez, M.Á. Solinís, A. Rodríguez-Gascón, Applications of lipid nanoparticles in gene therapy, Eur J Pharm Biopharm. 109 (2016) 184. https://doi.org/10.1016/j.ejpb.2016.10.016.
- [80] S.M. M, S. Veeranarayanan, T. Maekawa, S.K. D, External stimulus responsive inorganic nanomaterials for cancer theranostics, Adv Drug Deliv Rev. 138 (2019) 18. https://doi.org/10.1016/j.addr.2018.10.007.
- [81] L.P. Jahromi, M.-A. Shahbazi, A. Maleki, A. Azadi, H.A. Santos, Chemically Engineered Immune Cell-Derived Microrobots and Biomimetic Nanoparticles: Emerging Biodiagnostic and Therapeutic Tools, Advanced Science. 8 (2021) 2002499. https://doi.org/10.1002/advs.202002499.
- [82] M. Jeon, M. V. Halbert, Z.R. Stephen, M. Zhang, Iron Oxide Nanoparticles as T 1 Contrast Agents for Magnetic Resonance Imaging: Fundamentals, Challenges, Applications, and Prospectives, Adv. Mater. 33 (2021). https://doi.org/10.1002/adma.201906539.
- [83] E.K. Schneider-Futschik, F. Reyes-Ortega, Advantages and Disadvantages of Using Magnetic Nanoparticles for the Treatment of Complicated Ocular Disorders, Pharmaceutics. 13 (2021) 1157. https://doi.org/10.3390/pharmaceutics13081157.
- [84] S. Khan, S.M.D. Rizvi, V. Ahmad, M.H. Baig, M.A. Kamal, S. Ahmad, M. Rai, A.N.M. Zafar Iqbal, G. Mushtaq, M.S. Khan, Magnetic Nanoparticles: Properties, Synthesis and Biomedical Applications, Curr Drug Metab. 16 (2015) 685. https://doi.org/10.2174/1389200216666150812123219.
- [85] H. Kaur, A. Bhosale, S. Shrivastav, Biosensors: Classification, Fundamental Characterization and New Trends: A Review, International Journal of Health Sciences and Research. 8 (2018) 315.
- [86] J.M. Korde, B. Kandasubramanian, Fundamentals and Effects of Biomimicking Stimuli-Responsive Polymers for Engineering Functions, Ind. Eng. Chem. Res. 58 (2019) 9709. https://doi.org/10.1021/acs.iecr.9b00683.
- [87] A.U. Khan, M. Khan, M.H. Cho, M.M. Khan, Selected nanotechnologies and nanostructures for drug delivery, nanomedicine and cure, Bioprocess Biosyst. Eng. 43 (2020) 1339. https://doi.org/10.1007/s00449-020-02330-8.
- [88] A.H. Shikani, K.G. Kourelis, Patents and Recent Innovations in Topical Membrane Therapy of Refractory Rhinosinusitis, Recent Pat Inflamm Allergy Drug Discov. 9 (2015) 86. https://doi.org/10.2174/1872213x09666150531174219.
- [89] K. El-Boubbou, Magnetic iron oxide nanoparticles as drug carriers: preparation, conjugation and delivery, Nanomedicine (Lond). 13 (2018) 929. https://doi.org/10.2217/nnm-2017-0320.

- [90] S. Hooshmand, S.M.G. Hayat, A. Ghorbani, M. Khatami, K. Pakravanan, M. Darroudi, Preparation and Applications of Superparamagnetic Iron Oxide Nanoparticles in Novel Drug Delivery Systems: An Overview, Curr Med Chem. 28 (2021) 777. https://doi.org/10.2174/0929867327666200123152006.
- [91] W. Liu, H. Du, M. Zhang, K. Liu, H. Liu, H. Xie, X. Zhang, C. Si, Bacterial Cellulose-Based Composite Scaffolds for Biomedical Applications: A Review, ACS Sustain. Chem. Eng. 8 (2020) 7536. https://doi.org/10.1021/acssuschemeng.0c00125.
- [92] V.F. Cardoso, A. Francesko, C. Ribeiro, M. Bañobre-López, P. Martins, S. Lanceros-Mendez, Advances in Magnetic Nanoparticles for Biomedical Applications, Adv Healthc Mater. 7 (2018). https://doi.org/10.1002/adhm.201700845.
- [93] Q.A. Pankhurst, J. Connolly, S.K. Jones, J. Dobson, Applications of magnetic nanoparticles in biomedicine, J. Phys. D: Appl. Phys. 36 (2003) R167. https://doi.org/10.1088/0022-3727/36/13/201.
- [94] Y. Li, D. Stern, L.L. Lock, J. Mills, S.-H. Ou, M. Morrow, X. Xu, S. Ghose, Z.J. Li, H. Cui, Emerging biomaterials for downstream manufacturing of therapeutic proteins, Acta Biomaterialia. 95 (2019) 73. https://doi.org/10.1016/j.actbio.2019.03.015.
- [95] A.C. Paiva-Santos, A.M. Herdade, C. Guerra, D. Peixoto, M. Pereira-Silva, M. Zeinali, F. Mascarenhas-Melo, A. Paranhos, F. Veiga, Plant-mediated green synthesis of metal-based nanoparticles for dermopharmaceutical and cosmetic applications, International Journal of Pharmaceutics. 597 (2021) 120311. https://doi.org/10.1016/j.ijpharm.2021.120311.
- [96] M. Salvador, J.C. Martínez-García, M.P. Fernández-García, M.C. Blanco-López, M. Rivas, Biological and Medical Applications of Magnetic Nanoparticles, in: Magn. Meas. Tech. Mater. Charact., Springer International Publishing, Cham, 2021: pp. 771–804. https://doi.org/10.1007/978-3-030-70443-8 26.
- [97] P. Nicolás, M.L. Ferreira, V. Lassalle, A review of magnetic separation of whey proteins and potential application to whey proteins recovery, isolation and utilization, Journal of Food Engineering. 246 (2019) 7. https://doi.org/10.1016/j.jfoodeng.2018.10.021.
- [98] S. Khizar, A.A. Al-Dossary, N. Zine, N. Jaffrezic-Renault, A. Errachid, A. Elaissari, Contribution of magnetic particles in molecular diagnosis of human viruses, Talanta. 241 (2022) 123243. https://doi.org/10.1016/j.talanta.2022.123243.
- [99] K.D. Tawiah, D. Porciani, D.H. Burke, Toward the Selection of Cell Targeting Aptamers with Extended Biological Functionalities to Facilitate Endosomal Escape of Cargoes, Biomedicines. 5 (2017) 51. https://doi.org/10.3390/biomedicines5030051.
- [100] S. Gil, C.R. Correia, J.F. Mano, Magnetically labeled cells with surface-modified fe3 of spherical and rod-shaped magnetic nanoparticles for tissue engineering applications, Adv Healthc Mater. 4 (2015) 883. https://doi.org/10.1002/adhm.201400611.
- [101] K.R. Shoueir, N. El-Desouky, M.M. Rashad, M.K. Ahmed, I. Janowska, M. El-Kemary, Chitosan based-nanoparticles and nanocapsules: Overview, physicochemical features, applications of a nanofibrous scaffold, and bioprinting, International Journal of Biological Macromolecules. 167 (2021) 1176. https://doi.org/10.1016/j.ijbiomac.2020.11.072.
- [102] H. Gavilán, S.K. Avugadda, T. Fernández-Cabada, N. Soni, M. Cassani, B.T. Mai, R. Chantrell, T. Pellegrino, Magnetic nanoparticles and clusters for magnetic hyperthermia: optimizing their heat performance and developing combinatorial therapies to tackle cancer, Chem. Soc. Rev. 50 (2021) 11614. https://doi.org/10.1039/D1CS00427A.
- [103] N.D. Thorat, S.A.M. Tofail, B. von Rechenberg, H. Townley, G. Brennan, C. Silien, H.M. Yadav, T. Steffen, J. Bauer, Physically stimulated nanotheranostics for next generation cancer therapy: Focus on magnetic and light stimulations, Applied Physics Reviews. 6 (2019) 041306. https://doi.org/10.1063/1.5049467.

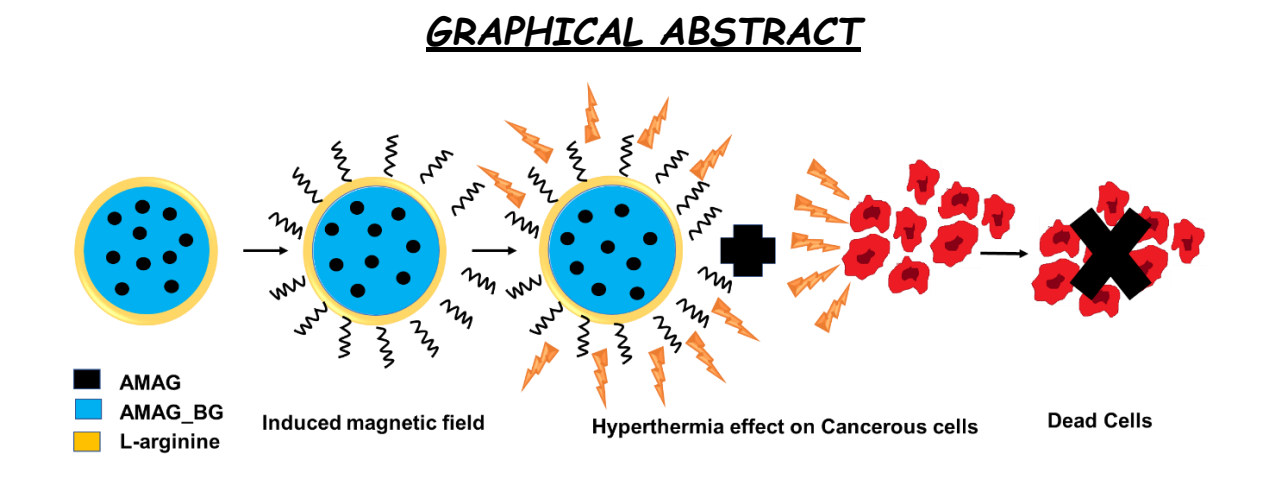
- [104] X. Zhang, C. Wang, X. Wang, T. Zhong, Y. Zhao, W.-Q. Zhang, W. Ren, D. Huang, S. Zhang, Y. Guo, X. Yao, Y.-Q. Tang, Q. Zhang, The antitumor activity of tumor-homing peptide-modified thermosensitive liposomes containing doxorubicin on MCF-7/ADR: in vitro and in vivo, Int. J. Nanomedicine (2015) 2229. https://doi.org/10.2147/IJN.S79840.
- [105] G. Tripodo, A. Trapani, M.L. Torre, G. Giammona, G. Trapani, D. Mandracchia, Hyaluronic acid and its derivatives in drug delivery and imaging: Recent advances and challenges, Eur J Pharm Biopharm. 97 (2015) 400. https://doi.org/10.1016/j.ejpb.2015.03.032.
- [106] V.S. Sivasankarapillai, S.S. Das, F. Sabir, M.A. Sundaramahalingam, J.C. Colmenares, S. Prasannakumar, M. Rajan, A. Rahdar, G.Z. Kyzas, Progress in natural polymer engineered biomaterials for transdermal drug delivery systems, Materials Today Chemistry. 19 (2021) 100382. https://doi.org/10.1016/j.mtchem.2020.100382.
- [107] D.D. Lasic, Recent developments in medical applications of liposomes: sterically stabilized liposomes in cancer therapy and gene delivery in vivo, Journal of Controlled Release. 48 (1997) 203. https://doi.org/10.1016/S0168-3659(97)00045-X.
- [108] A. Tyagi, A. Kumar, S.V. Aparna, R.H. Mallappa, S. Grover, V.K. Batish, Synthetic Biology: Applications in the Food Sector, Crit Rev Food Sci Nutr. 56 (2016) 1777. https://doi.org/10.1080/10408398.2013.782534.
- [109] I. Ali, M.N. Lone, M. Suhail, S.D. Mukhtar, L. Asnin, Advances in Nanocarriers for Anticancer Drugs Delivery, Curr Med Chem. 23 (2016) 2159. https://doi.org/10.2174/0929867323666160405111152.
- [110] Z.X. Chong, S.K. Yeap, W.Y. Ho, Transfection types, methods and strategies: a technical review, PeerJ. 9 (2021) e11165. https://doi.org/10.7717/peerj.11165.
- [111] K.B. Lintern, Immobilisation of Lactate Oxidase and Deoxyribonuclease I for use within a Bio-Artificial Liver Assist Device for the Treatment of Acute Liver Failure, Doctoral, UCL (University College London), (2013). https://discovery.ucl.ac.uk/id/eprint/1411473/ (accessed January 17, 2023).
- [112] M. Ul-Islam, K.F. Alabbosh, S. Manan, S. Khan, F. Ahmad, M.W. Ullah, Chitosan-based nanostructured biomaterials: Synthesis, properties, and biomedical applications, Adv. Ind. Eng. Polym. Res. 7 (2024) 79. https://doi.org/10.1016/j.aiepr.2023.07.002.

## CHAPTER 2

Synthesis of Mesoporous Core Shell Magnetite Bioactive Glass Nanoparticles for Magnetic Hyperthermia Treatment of Cancer

## **CHAPTER 2**

## Synthesis of Mesoporous Core Shell Magnetite Bioactive Glass Nanoparticles for Magnetic Hyperthermia Treatment of Cancer



#### 2.1 Introduction

Cancer is a comprehensive term which is used to address an enormous gathering of illnesses influencing human frame. Cancer is one of the destructive and deadly disorder causing an enormous killing of people around the globe, independent of developed nations [1,2]. There is no single treatment to fix this disorder. Rather, a blend of different methods is to be included for improved results. The most accomplished strategies for cancer treatment incorporate radiotherapy (to operate disease cells with light), chemotherapy (to operate disease cells with synthetic substances/drugs), medical procedure (by slicing), immunotherapy (by supporting resistant framework to battle against malignant growth), gene therapy (by utilizing genes), hormonotherapy (by dialing back or halting development of disease) and magnetic hyperthermia (MH) (to expose malignant growth of cells with temperature) [3,4].

MH is the encouraging method that has exhibited incredible ability to destroy malignant growth of cells through heat treatment. MH is typically utilized in mix with other therapeutic treatments like

radiation therapy and anti-angiogenic therapy of malignant growth cells [5]. It can be explained as the heat increase is due to the raise in hyperthermia cycle. This will further amplify the responsiveness of cells towards radiation therapy as well as anti-angiogenic therapy [6]. Generally, the word hyperthermia implies increasing the temperature of a particμμαr body part more than the typical internal heat level and maintaining it for a particular time span. It includes exposing of cancerous cells to excess heat (temperature close to 43 °C) without damaging the healthy cells present in that part of the human body [7]. The cell apoptosis process occurs when the temperature ranges between 42 °C to 46 °C and when the temperature rises to 48 °C, cell putrefaction begins. Both these systems lead to the killing of cells [8].

The hyperthermic potential of multiple magnetic nanoparticles (NPs) has been studied, including nanomaterials with SPIONs, NPs containing metals such as Mn, Zn, Co, Fe, Ni, Gd and related oxides [9]. Some of the best-known hyperthermic substances containing iron-oxide include magnetite (Fe3O4) NPs and maghemite (Fe2O3) NPs. Fe3O4 NPs are stabilized by ligands like hydrogel, cationic liposomes, dextran and polyvinyl alcohol while Fe2O3 NPs are stabilized by dextran. Another classification is of ferrites. It includes mixed ferrites of zinc, nickel, and copper (Ni0.65Zn0.35Cu0.1Fe1.9O4), cobalt-nickel ferrites (Cox Ni(1-x) Fe2O4), nickel ferrites (NiFe2O4), lithium ferrites (Li0.5Fe2.5O4), and manganese-nickel ferrites (MnFe2O4). Additional ferromagnetic NPs include Mn-Gd-Zn doped iron oxide composites (Mnx Znx Gdx Fe(2-x) O4), Fedoped Au and Zn-Mn-doped iron oxides (Znx Mn(1-x) Fe3O4) [10]. Out of all these materials, bioglass materials have been the most efficient in hard tissue regeneration. They are used as drug carriers in the treatment of cancer [11]. They are known for their bioactive reaction with physiological liquids within the affected bone leading to the formation of healthy bone cells. Also, they are good candidates for soft tissue engineering applications [12,13]. Thus, destroying the cancerous hard and soft tissues during treatment. Likewise, they also aid in recuperation of the affected bone parts. Despite their appealing properties, bioglass fell short on other necessary attributes. To join bioactivity, solvency, mesoporosity and magnetic properties in the same material is a strenuous task. So, as per the knowledge, an attempt has been made to synthesize first of its kind mesoporous nanosized bioactive glass (BG) network with magnetite core shell by bio-inspired synthesis.

Recently, magnetite (AMAG) NPs have been extensively studied because of their remarkable properties, like superparamagnetism, more remarkable surface region, and simple detachment system. To integrate magnetic NPs with reasonable surface science, many physical, synthetic, and organic approaches have been adopted. Therefore, we synthesized AMAG NPs by co-precipitation method to produce controlled size of mesoporous AMAG NPs [14]. L-arginine is categorized as a fundamental amino acid in this research study. Carnitine is a supplement that is produced by L-arginine and is an essential component of many human body cells [15]. Critically, L-arginine is liable for changing unsaturated fatty acids into energy. Thus, lowering down the cholesterol levels.

The novelty of the present study is to develop magnetism in 45S5 BG NPs. Magnetite was used as a template to synthesize magnetism induced BG (AMAG\_BG) through bio-inspired route for the first time. MH effect was observed in the novel AMAG\_BG which generated heat, and applicably killed the malignant cells without destroying or harming the healthy cells. In addition, BG is also known for soft and hard tissue regeneration. To the best of our knowledge, magnetism developed in core shell magnetite in 45S5 BG is not reported till today. AMAG and AMAG\_BG are tested mesoporous in nature. The mesoporous AMAG NPs and AMAG\_BG NPs helped in faster dissolution. Apart from healing to the soft and hard tissues mesoporous AMAG\_BG is expected to promote combinational therapy such as drug delivery.

The magnetically active novel mesoporous BG NPs are synthesized first time through bio-inspired route to not only treat cancer but also for the hard and soft tissue regeneration. In this, BG in surrounding conditions, is delivered without creating much difference in mechanical strength and bioactivity utilizing a natural biodegradable surface coordinating specialist. Natural templates are

picked as they hold their innovation and initiate the synthesis of inorganic particles from the arrangement work in desired surrounding conditions. Picked bio-inspired methodology is aqueous based and involves straightforward, less expensive, eco-friendly strides alongside the oversight for calcination [16]. AMAG and AMAG\_BG NPs are thoroughly characterized using techniques like XPS, XRD, FTIR, TGA, SEM-EDX, TEM and BET. The magnetic measurements were done for AMAG and AMAG\_BG NPs. They were tested for magnetic nature of particles and capability to produce heat in external magnetic field. Thus, making it competent for participating in MH treatment of cancer. The nature of magnetic BG NPs to produce heat in external alternating current magnetic field is experimented by in-vitro magnetherm studies [17]. By interacting the NPs with a simulated body fluid (SBF) solution, the bioactivity of AMAG and AMAG\_BG NPs were investigated. The cytotoxicity assays were conducted to check the biocompatibility of AMAG BG NPs.

#### 2.2 Experimental Section

#### 2.2.1 Materials:

L-arginine (CAS No- 74-79-3) and all of the precursors employed for BG synthesis, including tetraethyl orthosilicate (TEOS) (CAS No- 78-10-4), triethyl phosphate (TEP) (CAS No- 78-40-0), sodium acetate (NaAc) (CAS No- 127-09-3), and calcium acetate (CaAc) (CAS No- 114460-21-8), were purchased from Sigma-Aldrich. Also, the Hank's Balanced Salt solution (HBSS) termed as simulated body fluid (SBF) was obtained from Sigma-Aldrich. Other chemicals used are of the highest purity analytical reagent (AR) grade. Milli-Q water is used for all the experiments done. All the experiments were conducted at room temperature until mentioned specially.

## 2.2.2 Synthesis of L-arginine templated magnetite (AMAG) nanoparticles:

Template solution prepared such that L-arginine (1 mg/ml) was dissolved in 100 ml distilled water was kept on stirring for 30 minutes. To that constant stirring solution, ferrous sulphate (FeSO<sub>4</sub>.7H<sub>2</sub>O) and ferric chloride (FeCl<sub>3</sub>.6H<sub>2</sub>O) was added in 1:2 ratio. After 30 minutes, added 2 M sodium hydroxide till pH 9 to pH 11 was obtained. Black precipitate obtained, was washed with 70 % ethanol, dried in an air oven for 2 days and then stored in desiccator.

# 2.2.3 Synthesis of L-arginine templated core shell magnetite- bioactive glass (AMAG BG) nanoparticles:

The procedure for synthesis of AMAG\_BG NPs was exactly followed with minimal changes [18]. AMAG is synthesized using L-arginine as a template. L-arginine (1 mg/mL) was dissolved in 100 mL distilled water and kept on stirring for 30 min. To that constant stirring solution, ferrous sulphate (FeSO4.7H2O) and ferric chloride (FeCl3.6H2O) was added in 1:2 ratio. After 30 min, added 2 M sodium hydroxide till pH 9 to pH 11 was obtained. Black precipitate obtained, was washed with 70 % ethanol, dried in an air oven for 2 d and then stored in desiccator. For AMAG\_BG, the template AMAG (1 mg/mL) was dispersed in 100 mL trizma buffer whose pH 8 (10 mM) was maintained. The solution was kept on constant stirring at 500 rpm for 20 min at room temperature on the digital magnetic stirrer. After that the BG precursors were added sequentially after a gap of 30 min such that TEOS (9.29 g) is added first. Then, TEP (1 g) is added, followed by NaAc (6.36 g) and CaAc (4.21 g). The solution was continuously stirred for half an hour and then kept for incubation on silicone oil bath for 24 h. The obtained solution was then processed in centrifuge machine at 13000 rpm at room temperature. The resulting precipitate was cleaned, dried in an air oven at 40 °C for 48 h, and then stored in a desiccator.

The material has not undergone calcination process because this is the novelty of the bio-inspired synthesis that it omits the calcination step. The procedure has been well established in our lab for the

BG synthesis [18–20]. XRD spectra further confirms the existence of magnetite in AMAG and magnetite and BG in AMAG\_BG. The peaks in FTIR at 1077 cm-1 (Si-O stretching, Si–O–Si asymmetric stretching, Si–O–C stretching, C–O stretching), and 977 cm-1 (Si-O-Si, Si-O-C and Si-O-H), suggests the formation of BG. In TEM, the increase in particle size of AMAG\_BG (27.5  $\pm$  1.1 nm) compared to AMAG (14.6  $\pm$  0.3 nm) confirm the formation of BG network on AMAG NPs as evidenced by FTIR and XRD analysis. Synthesis of BG at ambient conditions without any compromise in mechanical strength and bioactivity via bio-inspired route using an organic biodegradable surface directing agent is taking place which has been shown in well reputed publications [21]. Chosen bio-inspired methodology is aqueous based and comprises of few simple cheaper, eco-friendly steps along with the omission for calcination.

#### 2.3 Characterization of AMAG and AMAG BG NPs:

2.3.1 X-ray photoelectron spectroscopy (XPS): In an Ultra-high vacuum (UHV) chamber with a homemade hemispherical electron energy analyser (ESA-31) and a non-monochromatized Al K X-ray source, XPS measurements were carried out. The photon beam's direction and the analyzer's axis were at a  $70^{\circ}$  angle. In a direction normal to the surface, photoelectrons were gathered. The XPS spectra were collected using the fixed retarding ratio (FRR) mode, with the survey spectra having a retarding ratio of k = 4 and the energy regions of interest having a retarding ratio of k = 8. C++ was used to write the measurement control and data collecting programme. In order to mount the samples on the sample holder, conductive double-sided adhesive tape (3M-9713-Cu) was used.

2.3.2 X-ray Diffraction (XRD) Analysis: The magnetic samples were subjected to XRD examination using a Panalytical X'Pert Pro Diffractometer that operated at 45 kV and 40 mA current with Cu-  $K\alpha$  radiations as the source of X-rays. It recorded the spectrum in the  $2\theta$  range of  $5^{\circ}$  to  $90^{\circ}$  with the slow scan speed and the very slow scan rate of 0.2 %min.

**2.3.3 Fourier Transform Infrared Spectroscopy (FTIR):** Using the spectrophotometer's ATR-FTIR mode, all samples, including AMAG and AMAG\_BG NPs, were recorded. The Perkin Elmer (Model Spectrum 2) spectrometer, which operates in the 400 cm<sup>-1</sup> to 4000 cm<sup>-1</sup> range and has a resolution of 1 cm<sup>-1</sup>, was used to evaluate the FTIR spectra of the synthesized material.

2.3.4 Thermogravimetric (TGA) Analysis: The TGA analysis of the samples was performed on the instrument Perkin Elmer thermogravimetric analyzer (Model TGA 4000). By heating the magnetic samples to temperatures between 0 °C to 800 °C under a nitrogen environment at a heating rate of 10 °C/min and nitrogen gas flow of 50 ml/min, the thermal stability of the sample was examined.

## 2.3.5 CHNSO analysis:

Using the CHNSO analyzer, Vario Micro Cube, Elementar Analysensysteme, Germany, the amount of AMAG and AMAG\_BG NPs was validated. The experiment followed the established protocol. First, a small sample size was precisely weighted into a tin capsule. Additionally, the material was burnt at 1000 °C with an excess of oxygen to produce CO<sub>2</sub>, H<sub>2</sub>O, and NXOY constituents. Inside the reduction tube, the produced NXOY was further reduced to N<sub>2</sub>. To determine the amount of C, H, and N in the sample, the final gases, including CO<sub>2</sub>, H<sub>2</sub>O, and N<sub>2</sub>, were then run through a gas chromatography (GC) column.

#### 2.3.6 Morphological Studies

## 2.3.6.1. Field Emission Scanning Electron Microscopy (FE-SEM) and Energy Dispersive X-Ray Analysis (EDX):

Using a scanning electron microscope (ZESIS EVO MA15), the morphology was examined for the AMAG and AMAG\_BG NPs. The AMAG and AMAG\_BG NPs were gold coated and observed under SEM at 10,000 magnifications and accelerating voltage of 5.0 kV. The magnetic nanoparticles were subjected to Energy Dispersive X-Ray Analysis (EDX), which was performed using a ZEISS

EVO MA15 at a voltage of 20 kV to check for the presence of Fe, O, Si, P, Na, and Ca ions in diverse samples.

#### 2.3.6.2. Transmission electron microscopy (TEM):

The size of AMAG and AMAG\_BG NPs is measured using a high-resolution Transmission Electron Microscope (HR-TEM) model (TALOS S) from Thermo Scientific in the United States, which operates at an accelerating voltage of 200 kV. For the TEM analysis, the ImageJ program that comes with 64-bit Java 1.8.0 172 was used.

## 2.3.7 Nitrogen Sorption Analysis:

The material was degassed under vacuum for 2 h at 200 °C before analysis. The nitrogen adsorption-desorption analysis is carried out using Microtrac BEL (Model BELSORP-max), Japan, at -196 °C, and nitrogen is used as the adsorptive gas (N<sub>2</sub>, cross-sectional area 0.162 nm<sup>2</sup>). This analysis measures the porosity of AMAG and AMAG\_BG NPs. The surface area of the nitrogen adsorption data was calculated using the Brunauer-Emmett-Teller (BET) equation. To analyse the pore-size distribution in the desorption portion of the isotherm, the Barret-Joyner-Halenda (BJH) method was used.

#### 2.3.8 Magnetic Measurement:

The magnetic hysteresis or M-H magnetization curve was plotted for AMAG and AMAG\_BG NPs through Vibrating Sample Magnetometer (VSM) instrument (Microsense, Model ADE – EV9) at room temperature. The magnetic field was recorded up to 2.2 Tesla. The Field resolution was 0.001 Oe and sensitivity was 0.00005 emu such that magneto resistance was maintained between 1  $\Omega$  and 10,000  $\Omega$ .

#### 2.3.9 Bioactivity Test:

The method outlined by [22] involved the formation of hydroxyapatite layer on bioactive glass surface. The method involves the evaluation of *in-vitro* bioactivity of AMAG and AMAG BG NPs.

The samples were immersed in simulated body fluid (SBF) at a concentration of 1 mg/ml and incubated for 4 days, 7 days, 15 days and 30 days under sterile conditions at 37 °C. The SBF solution is changed after every 4 days so that concentration of ions doesn't decrease in solution and also hydroxyapatite layer is formed easily. The sample is then centrifuged, dried in an oven at 48 °C, and kept in a desiccator for additional characterizations including XRD, FTIR, SEM, magnetic measurements and magnetherm studies when the appropriate time period has completed.

#### 2.3.10 In-vitro Heat Studies:

In this work we use magnetic hyperthermia (Magnetherm, NanoTherics Ltd., United Kingdom) that measures the ability of materials to generate heat energy with application of alternate magnetic field (AMF) at certain frequency [23,24]. Typically, in this experiment, magnetic NPs at various concentrations of 1.0 mg/mL and 5 mg/ml were taken in a "cylindrical" tube placed in a thermally insulating polystyrene (Thermocol) sample holder to isolate the heat generated inside the tube to the environment and cooling water was circulated to avoid heating due to application of current in the magnetic coil. Application of AC-voltage (Vac) of 32.1 V with frequency of 464 kHz could produce AC-current (Iac) of 7.9 amp for a 17 turns coil and sums up to generate a magnetic field strength (Bo) of 11 mT. The overall variation of temperature was recorded with AMF. The variation in temperature of the material slurry was measured using a T-type thermo-couple with time, maintaining the AMF as constant throughout the experiment. The size and form of the magnetic NPs have a significant impact on their magnetic characteristics. Theoretically, the prepared NPs of small particle sizes, could produce high magnetization and could generate induction heating power. Through a specified absorption rate (SAR), the amount of heat produced by the particles could be determined.

When exposed to an AMF at a specific frequency and B<sub>0</sub>, a material's SAR measures how much energy is absorbed per unit mass [25,26]. It is calculated using the watts per kilogram (W/g) and "rate of temperature rise":

SAR (W/g) = 
$$\frac{C \text{ md}}{m} \frac{dT}{dt}$$

where C is the specific heat capacity of water (C = 4.189 J/g °C), md is the dispersion medium of particles which is water, m is the mass of the sample, and dT/dt is the initial slope within first 80 seconds of the temperature versus time plot.

## 2.3.11 In-vitro Hemolysis Assay:

Minor modifications are made to the experimental method for the *in-vitro* hemolysis assay while performing it on human blood [27]. Briefly, PBS buffer was prepared in autoclaved distilled water. Human blood (0.5 ml) was taken in 7 micro-centrifuge tubes, centrifuged for 5 minutes at 4 °C, RCF= 500\*g and plasma as supernatant was discarded in surfactant. In meanwhile, sonicated 1 mg of AMAG and AMAG BG NPs in 1 ml autoclaved distilled water such that the required stock solution of 1 mg/ml is obtained. Prepared different concentrations (1 μg/ml, 5 μg/ml, 10 μg/ml, 25 μg/ml, 50 µg/ml) from 1 mg/ml stock solution. After discarding plasma, two times washing of blood is given with 500 µl of PBS at first and 1000 µl of PBS at second by mixing the content in micro-centrifuge tubes properly. Centrifuged the mixture properly and removed the supernatant carefully without disturbing the red blood cells. Washing is done until clear supernatant is obtained. As soon as clear supernatant is obtained, it is discarded and now added prepared five concentrations (1 µg/ml, 5 µg/ml, 10 μg/ml, 25 μg/ml, 50 μg/ml) in five micro-centrifuge tubes containing red human blood. Added 1 ml PBS in one micro-centrifuge tube containing red human blood which is termed as negative control and added 950 µl of PBS and 50 µl of Triton X-100 (till transparent solution is observed) in seventh micro-centrifuge tube containing blood which is termed as positive control. Absorbance at 570 nm and absorption spectrum from 300 nm to 800 nm were measured for different incubation periods of 0 h, 1 h, 2 h, 24 h. Also, fluorescent microscope imaging is recorded for 2 h. The percentage hemolysis rate was determined by the following equation:

% Hemolysis = 
$$[(A_t - A_c)/(A_{100\%} - A_c)] \times 100$$

Where,  $A_t$  is the absorbance of the supernatant of samples incubated with the particles,  $A_c$  is the absorbance of the supernatant from negative control (PBS), and  $A_{100\%}$  is the absorbance of the supernatant from positive control Triton X 100. Triplicates of experiments were performed and error analysis was done. In our studies, hemolysis less than 5 % was considered to be nontoxic. This figure has also been recorded in other sources [28] and is in accordance with ASTM 75633 [29].

## 2.3.12 MTT Assay:

In MTT assay, the cytotoxicity and biocompatibility of the BG samples was evaluated. The colorimetric MTT method was used to assess the vitality of U2OS cells (osteoblasts in osteosarcoma), in the presence of BG NPs. By evaluating the conversion of MTT into formazan crystals, which represents cellular metabolic activity, the MTT assay assesses the viability of cells. To conduct the experiment, distinct BG specimens with varying concentrations (1  $\mu$ g/mL, 5  $\mu$ g/mL, 10  $\mu$ g/mL, 25  $\mu$ g/mL, and 50  $\mu$ g/mL) were UV-sterilized for half an hour and thereafter cultured with cells (10,000 cells per well) on a 96-well plate at 37 °C for a full day. The MTT assay was then carried out by filling each well with 100  $\mu$ L of 1 mg/mL of MTT reagent. After covering the plate with foil and leaving some space for air, it was incubated under cell culture conditions for 2 h at 37 °C. Following the incubation period, the medium and MTT were aspirated, and the plate was removed. After dissolving the formazan crystals with 100  $\mu$ L of dimethyl sulfoxide, the plate was incubated for an additional 20 min under cell culture conditions. A TECAN multimode plate reader was used to read the plate at 570 nm and 630 nm wavelengths after it had been incubated. The positive control was made up of cells grown in DMEM media. Every experiment was carried out three times, and the results were reported as means  $\pm$  standard deviation.

#### 2.4 Results and Discussions

## 2.4.1 X-ray photoelectron spectroscopy (XPS):

The XPS analysis was performed to investigate the NPs' elemental composition and oxidation state of elements. The typical XPS spectra of AMAG and AMAG\_BG was displayed in Figure 1 (a-b) and their binding energies are recorded in Table 1. The magnetite phase in AMAG was given credit for the iron band that appeared at 710.1 eV [30]. At 710.1 eV and 723.8 eV. The iron peak was deconvoluted into two spectral bands. The iron in the magnetite phase is said to have the strongest peak at 710.1 eV. The appearance of a small but noticeable peak between 714 eV and 720 eV, which is a fingerprint for oxidized phases like  $\gamma$ -Fe2O3. The O1s region's XPS spectrum was displayed in supplement file Figure S1a. The lattice oxygen (O2-) in the magnetite phase is responsible for the peak with the highest energy at 530.0 eV [31].

The survey scan XPS of AMAG\_BG sample is shown in Figure 1b together with the curve-fitting spectra for Fe, O, C, Ca, and Si in supplement file Figure S1 (d-h). The L-arginine in magnetite may have been absorbed by the glass surface, producing the (C 1s) peak. The Si 2p high-resolution XPS spectra is shown in Figure 1b, with the largest peak occurring at 103.5 eV [32]. This peak is caused by tetrahedral Si coupled with four oxygen atoms (SiO4 4-), which is confirming the existence of BG network along with core shell magnetite. The O 1s XPS spectra may be seen around 532.3 eV as mentioned in Table 1. Although it is challenging to obtain O 1s data because of overlapping oxide peaks and the possibility that the material surface has been hydroxylated or carbonated, the peak at about 532.3 eV is frequently attributed to the oxygen in a silica environment that is typical of silica glasses [33]. The iron band at 710.1 eV in the BG sample indicates that magnetite is successfully templated on BG particles. The observation reveals the successful existence of magnetite phase in BG network.

**Table 2.1:** Binding energy (eV) of AMAG and AMAG\_BG by XPS analysis.

	Various Elements	Binding energy (eV)		
		AMAG	AMAG_BG	
	O (1s)	530, 531.2, 534	529.7, 532.3	
	C (1s)	284.3, 287.6	284.5, 286.3	
XPS	Fe (2p)	710.1, 718, 723.6, 732.3	710.1, 718.5, 725, 734	
	Ca (2p)	-	346.9, 350.5	
	Si (2p)	-	103.5	

## 2.4.2 X-ray Diffraction (XRD) Analysis:

The synthesized AMAG and AMAG\_BG NPs were characterized by XRD. The 2 $\theta$  values of characteristic diffraction peaks reported in Figure 1a. are listed as follows: 30.28 $^{o}$  (220), 35.62 $^{o}$  (222), 43.21 $^{o}$  (400), 57.21 $^{o}$  (511), and 62.80 $^{o}$  (440); the inverse cubic spinel structure is suitably indexed by these values for AMAG. (JCPDS card 00-001-1111, Fe3O4). This proves that AMAG can be obtained by co-precipitation method [34]. The Debye-Scherrer formula, which is (D =  $k\lambda$  /  $\beta$ cos $\theta$ ) where K is the constant,  $\lambda$  is the X-ray wavelength,  $\beta$  is the peak width of the half-maximum of the diffraction peak, and  $\theta$  is the X-ray diffraction angle, can be used to quantitatively compute the mean crystallite size of 12  $\pm$  0.2 nm shown by the XRD patterns.

The AMAG\_BG NPs (Figure 1c) is semi-crystalline, as shown by the sharp, intense diffraction maxima at 2θ values of 31.53° (102), 37.12° (222), 43.03° (400), 54.95° (104), 59.59° (300), and 62.31° (114) and the broad hump in the 2θ range of 15°-30° in the AMAG\_BG (Figure 1c) sample is observed. The Ca0.89Na0.11O3P0.11Si0.89 phase corresponds to the diffraction maxima reported for BG elsewhere in JCPDS file No. 00-033-1229 [35]. Few of 2θ values at 30.28° (220), 57.21° (511), and 62.80° (440) are originated from Fe3O4 and 31.53° (102), 54.95° (104), 59.59° (300), and 62.31° (114) peaks corresponds to AMAG\_BG alone and two peaks 37.12° (222), 43.03° (400) are overlapping diffraction maxima. The average crystallite size "D" by Debye-Scherrer formula of AMAG\_BG NPs was calculated using the X-ray measurements and this comes out to be around 0.5

 $\pm$  0.04 nm. XRD spectra further confirms the existence of magnetite in AMAG and magnetite and BG in AMAG BG.

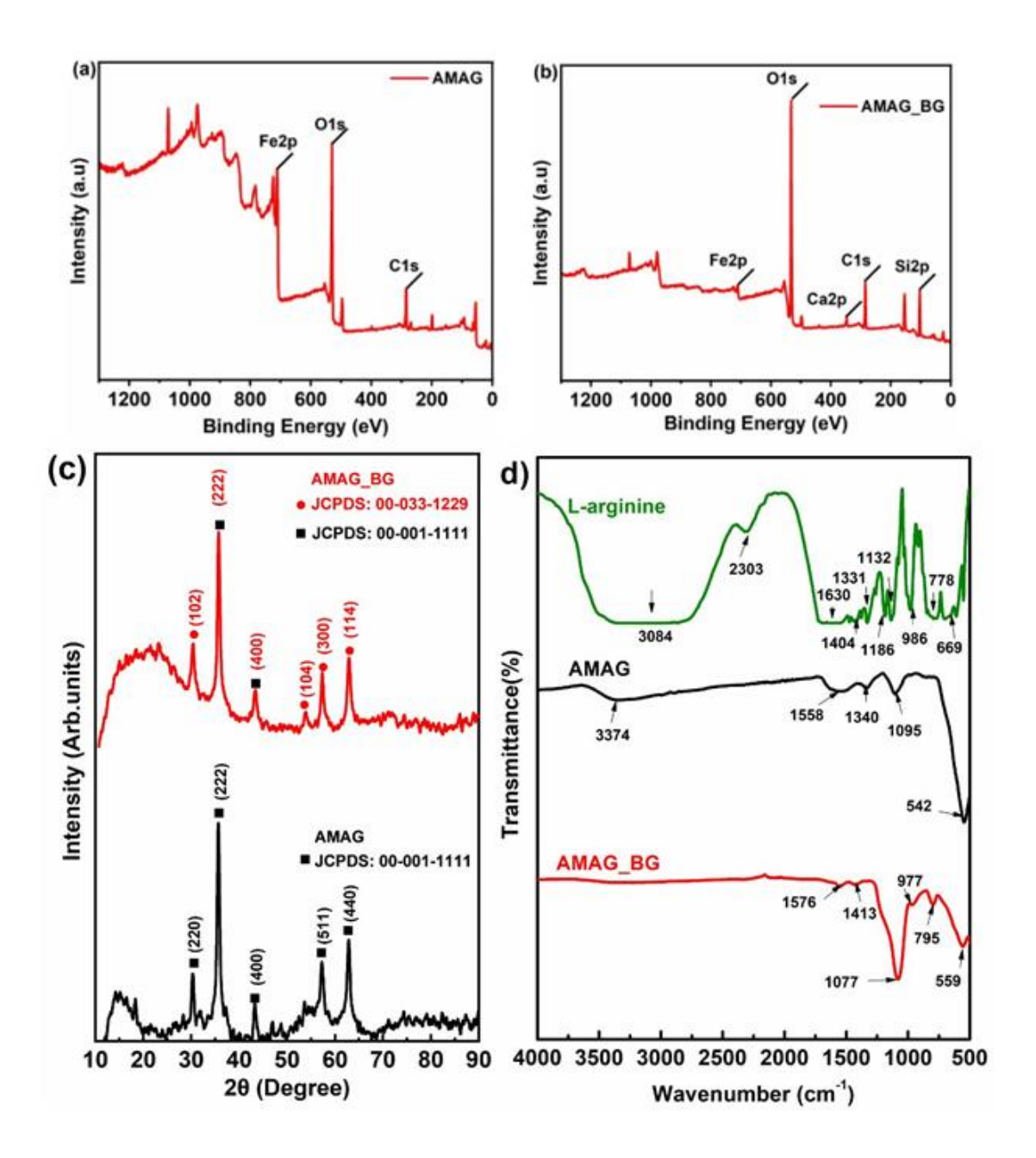


**Figure 2.1:** (a-b) XPS spectra of AMAG and AMAG\_BG, (c) XRD pattern of AMAG and AMAG\_BG and (d) FTIR spectrum of AMAG and AMAG\_BG respectively.

## 2.4.3 FTIR Analysis:

Figure 1d displays FTIR diagrams of pure L-arginine. The peak at 3084 cm-1 in L-arginine firstly represents primary and secondary amines. The vibration of C-H stretching and the higher frequency vibration of N-H stretching is due to the peak at 2303 cm-1. At 1630 cm-1 and 1404 cm-1, L-arginine amino acid exhibits the C=O and C-O stretching vibrations respectively. The observations and reported FTIR data are well-concordant [36].

Figure 1d depicts the FTIR spectrum made from pure AMAG NPs. It is interesting to note that the interaction of L-arginine with iron oxide species caused the primary and secondary amine peaks absorbed from L-arginine, centered at 3084 cm-1, to shift to a higher wavenumber of 3374 cm-1. While, C-O stretching shifted from 1404 cm-1 to 1558 cm-1. The sharp peak at 542 cm-1 is caused by the stretching vibration mode connected to the metal-oxygen Fe-O bonds in the crystalline lattice of Fe3O4 [37]. For ferrites, they are distinctively evident in all spinel forms.

During the synthesis of AMAG\_BG NPs, FTIR spectra for each BG precursor added to an AMAG suspension, were recorded at pH 7.4. A peak at 1576 cm-1 corresponds to AMAG\_BG. The L-arginine content of AMAG (1558 cm-1) originated the COO- peak. The significant rise in wavenumber in the absorbed peak of COO- at 1578 cm-1 in AMAG\_BG from 1558 cm-1 in AMAG indicate its chemical interaction. So, this observation indicates the significant interaction of AMAG template with BG network. Other peaks at 1077 cm-1 (Si-O stretching, Si-O-Si asymmetric stretching, Si-O-C stretching, C-O stretching), and 977 cm-1 (Si-O-Si, Si-O-C and Si-O-H), suggests the formation of BG. A silicate network's distinctive ring structure can be seen at 795 cm-1 [38]. A shift in peak from 542 cm-1 of AMAG to 559 cm-1 is seen indicating chemical interaction of BG precursors with AMAG.

## 2.4.4 Thermogravimetric (TGA) Analysis:

For pure L-arginine sample, the breakdown begins around 217.4 °C. The only melting point is the definite indicator of a crystal's perfect crystallinity [39]. The thermogram displays barely any residue at 700 °C as shown in Figure 2a.

TGA thermograms of AMAG and AMAG\_BG are shown in Figure 2b. AMAG saw an early weight loss of 3.13 % at (180.8 °C to 390 °C) and a further steady weight loss of 0.8 % at (390 °C to 769 °C). The evaporation of surface water and sorbed water, respectively, are the reason for this change. Additionally, a 6.9 % weight loss from (53 °C to 769 °C) is seen which is attributed to the decomposition of organic content (L-arginine) of AMAG NPs [40].

In the case of AMAG\_BG (Figure 2b), a preliminary weight loss of 4.2 % was noted in the (269.9 °C to 427.4 °C) range. Then, a weight reduction of 2.2 % between 427.4 °C to 721 °C was noted. Additionally in the range (721 °C to 844.9 °C), weight loss of 1.6 % was also seen. In contrast to AMAG, AMAG\_BG required the highest temperature (400 °C) to eliminate the water content. The finding suggests that there is water content inside both the BG network as well as the AMAG template. A gradual drop in weight loss for NPs from 269 °C to 427.4 °C indicates the decomposition of organic matter probably due to L-arginine molecules which are retained in AMAG\_BG. These observations and FTIR findings are well concordant (Figure 1b) which reveal the interaction between L-arginine and inorganic components. Interestingly, slight decrease (1.6 %) in weight continues from 721 °C to around 844.9 °C and thereafter slight increase up to 896 °C, corresponding to stabilization of inorganic network.

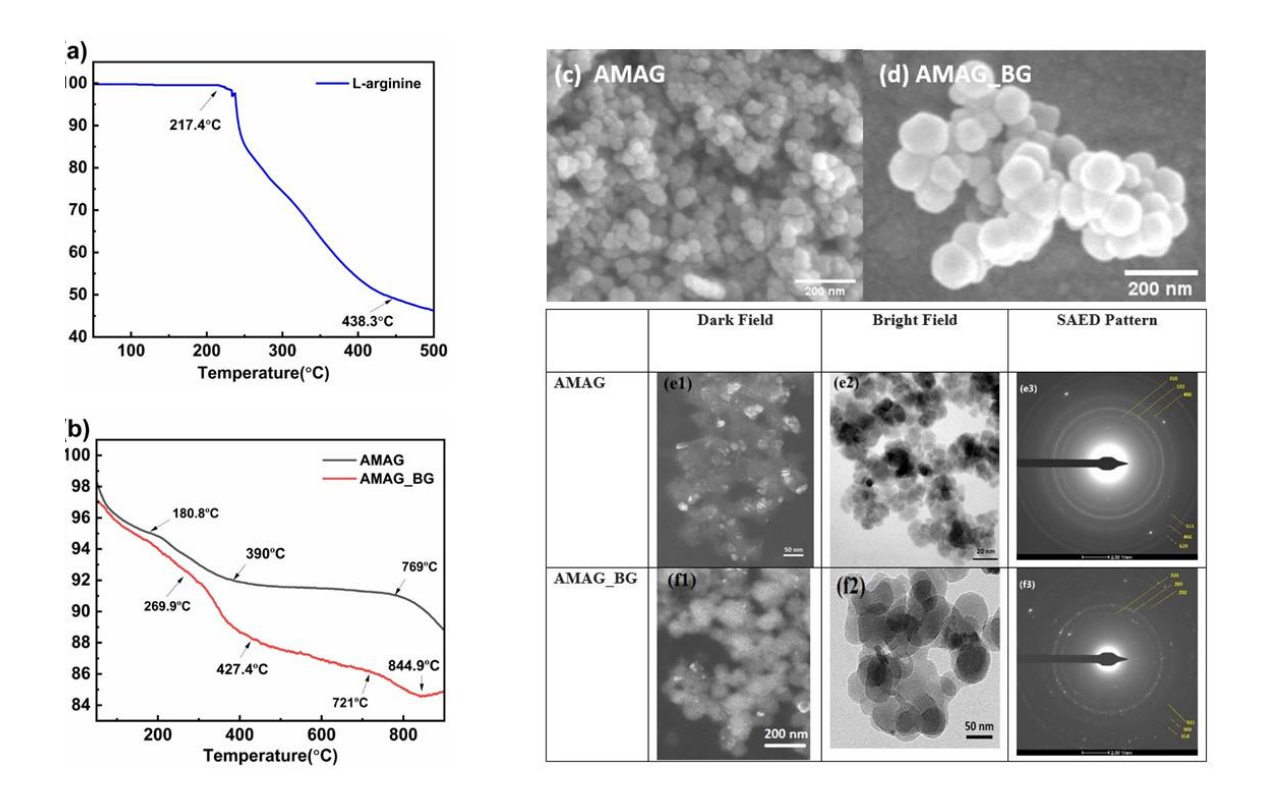


**Figure 2.2(a):** Thermogravimetric analysis of L-arginine, (b) Thermogravimetric analysis of AMAG and AMAG\_BG NPs, (c-d) SEM micrographs of AMAG and AMAG\_BG, (e-f) HR-TEM micrographs and SAED patterns of AMAG (e1, e2 and e3) and AMAG\_BG (f1, f2 and f3) under dark field and bright field

## 2.4.5 CHNSO Analysis:

The compositions of AMAG and AMAG\_BG NPs were analyzed using CHNSO (for C, N and H) and results are portrayed in Table 2.  $14.6 \pm 0.2$  w/w %,  $0.26 \pm 0.1$  w/w %,  $0.67 \pm 0.1$  w/w % and  $15.54 \pm 0.2$  w/w % were of organic contents (C, N and H respectively) reported from AMAG while  $20.47 \pm 0.2$  w/w %,  $0.07 \pm 0.1$  w/w %,  $0.998 \pm 0.1$  w/w % and  $21.53 \pm 0.2$  w/w % were of organic contents (C, N and H respectively) reported from AMAG\_BG NPs. These findings corroborate the L-arginine molecule's presence in the magnetite and BG network.

**Table 2.2:** Elemental composition of AMAG and AMAG\_BG by CHNSO (for C, N and O) analysis.

	Various Elements	Experimental Values (w/w %)	
		AMAG	AMAG_BG
	Carbon (C)	$14.6 \pm 0.2$	$20.47 \pm 0.2$
CHNSO	Nitrogen (N)	$0.26 \pm 0.1$	$0.07 \pm 0.1$
	Hydrogen (H)	$0.67 \pm 0.1$	$0.998 \pm 0.1$
	Total Organic Content	$15.54 \pm 0.2$	$21.53 \pm 0.2$

## 2.4.6 Morphological Studies:

## 2.4.6.1 Field Emission Scanning Electron Microscopy (FE-SEM) and Energy Dispersive X-Ray Analysis (EDX):

The Figure 2(c-d) shows the micrographs of AMAG and AMAG\_BG NPs. AMAG appears to have homogenous, uniform-sized particles in the FE-SEM image. The morphology of AMAG and AMAG\_BG with exceptionally smooth surfaces can be seen in the micrographs, which further suggests that the particles were properly formed. It is important to note that the corresponding surfaces of the AMAG and AMAG\_BG NPs were found to be exceedingly devoid of any intriguing morphological traits when they were examined using FE-SEM. The composition of the AMAG and AMAG\_BG by Energy Dispersive X-Ray Analysis (EDX) is displayed in Table 3. Fe (35.6 %) and O (48.7 %) in AMAG and O (31.5 %) and Si (7.3 %), P (1.3 %), Ca (0.7 %), Na (4.2 %) and Fe (33.2 %) in AMAG\_BG, respectively, are equivalent to this. The elemental compositions confirm the success of the synthesis, which has been documented in numerous investigations like XPS (Figure 1 (a-b)). According to the EDX spectrum, the iron oxide structures solely include Fe and O. The statistics attest to the samples' great purity. Interestingly, Si, P, Na and Ca elements were found on these globular structures in the AMAG\_BG EDX spectra (Table 3). These observations supported the FTIR spectra's conclusions that bioactive glass particles had mineralized along with L-arginine templated magnetite.

**Table 2.3:** Elemental composition of AMAG and AMAG\_BG by EDX analysis.

	Various Elements	Experimental Values (w/w %)		Observed Values (w/w %)	
		AMAG	AMAG_BG	AMAG	AMAG_BG
	Total Organic Content	15.54	21.53	$15.6 \pm 0.2$	$21.2 \pm 0.2$
	Iron (Fe)	35.6	33.2	$35.5 \pm 0.1$	$33.3 \pm 0.1$
EDX	Oxygen (O)	48.7	31.5	$48.61 \pm 0.2$	$31.7 \pm 0.1$
Analysis	Silicon (Si)	-	7.3	-	$7.46 \pm 0.2$
	Phosphorus (P)	-	1.3	-	$1.21 \pm 0.1$
	Calcium (Ca)	-	0.7	-	$0.8 \pm 0.2$
	Sodium (Na)	-	4.2	-	$4.31 \pm 0.2$

#### 2.4.6.2 Transmission electron microscopy (TEM):

The HR-TEM results (Figure 2(e-f)) show morphological characteristics of AMAG and AMAG\_BG NPs. The NPs with a limited size distribution make up the majority of the AMAG NPs. The average particle size of AMAG is  $14.6 \pm 0.3$  nm while that of AMAG\_BG was  $27.5 \pm 1.1$  nm by Image J analysis (Figure S2 (a-b)). The increase in particle size of AMAG\_BG (27.5  $\pm 1.1$  nm) compared to AMAG (14.6  $\pm 0.3$  nm) confirm the formation of BG network on AMAG NPs as evidenced by FTIR and XRD analysis (Figure 1(c-d)). The shape of the AMAG NPs is almost uniform. The Figure 2(e-f) also demonstrates some agglomeration between the particles, which might result from the magnetic interaction of the NPs. In comparison to AMAG, there is less agglomeration among the particles in AMAG\_BG due to the formation of BG network on magnetite core and are in good agreement with FE-SEM results (Figure 2(c-d)). HR-TEM dark field and bright field images of AMAG and AMAG\_BG are displayed which clearly shows porous structure of AMAG and AMAG\_BG NPs which supports the BET results. According to the classification of core/shell NPs [41], the multiple

small core materials coated by single shell material is also very well depicted by HR-TEM dark field images of AMAG\_BG NPs. It is clearly depicted with the two contrasting colours which is observable in HR-TEM images of AMAG\_BG NPs. SAED pattern depicts those two (hkl) values (220) and (511) of AMAG are also present in AMAG\_BG which proves that magnetite is present in BG and is well corroborated with XRD result.

## 2.4.7 Nitrogen Sorption Analysis:

Fig. 3(a-b) shows the AMAG and AMAG\_BG NPs' nitrogen adsorption-desorption isotherms and their pore size distribution. Data are presented in Table III for surface area, pore volume, and pore size. Based on BET analysis, AMAG\_NPs were reported with surface area (93.02 m<sup>2</sup>g<sup>-1</sup>), pore volume (0.1627 cm<sup>3</sup>g<sup>-1</sup>) and pore diameter (6.99) nm which is not in much difference with AMAG\_BG NPs with surface area (80.39 m<sup>2</sup>g<sup>-1</sup>), pore volume (0.1443 cm<sup>3</sup>g<sup>-1</sup>) and pore diameter (7.18 nm).

The type IV adsorption isotherm and hysteresis loop H3 is observed in the nitrogen adsorption-desorption isotherms for AMAG and AMAG\_BG NPs which confirms that the material is mesoporous (as its diameter ranges from 2 to 50 nm) in nature, with slit-like pores [42]. The analysis of the pore size (Table III) distribution reported by the Barrett-Joyner Halenda (BJH) method provided additional evidence in favor of the identification of AMAG's and AMAG\_BG's consistently sized mesopores. It will be important to keep in mind that the bio-inspired process does not involve calcination because mostly drying occurs at ambient temperature for the particles by retaining the template molecules (L-arginine). In context of this, the formation of AMAG and AMAG-BG network might naturally possess mesoporous properties due to the interaction with L-arginine as indicated in FTIR (Fig. 1b) and CHNSO analysis (Table II). Additionally, the surface area for AMAG determined by BET was found to be 93.02 m<sup>2</sup>g<sup>-1</sup>, which is higher than AMAG\_BG (80.397 m<sup>2</sup>g<sup>-1</sup>), indicating a small particle size for AMAG compared to AMAG\_BG as revealed by TEM analysis (Fig. 2(e-f)) [43].

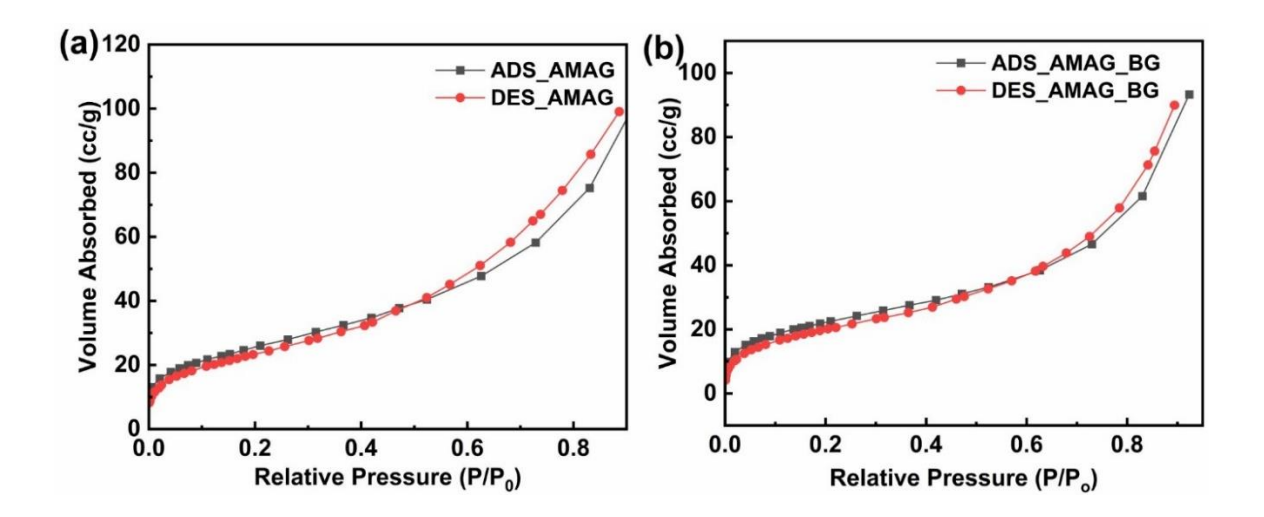


Fig. 2.3(a-b): Nitrogen adsorption-desorption isotherm and pore size distribution

Table 2.4: Surface area, pore volume and pore size data of AMAG and AMAG BG.

	AMAG	AMAG_BG
Total Surface Area (a <sub>s,BET</sub> [m <sup>2</sup> g <sup>-1</sup> ])	93.022	80.397
Total pore volume( $p/p_0$ =0.944) [cm <sup>3</sup> g <sup>-1</sup> ]	0.1627	0.1443
Mean pore diameter [nm]	6.9958	7.1801

#### 2.4.8 Magnetic Measurement:

The VSM measurement for the AMAG and AMAG\_BG NPs shows a superparamagnetic behavior in the form of a hysteresis curve of magnetization with the magnetic field, as represented in the Figure 4a. The saturation magnetization (Ms) and remanent magnetization (Mr) values of AMAG and AMAG\_BG NPs are determined by the hysteresis curve, as given in the Table 5. When working with superparamagnetic materials, such as NPs of magnetite, the coercivity value ought to be nearly zero which is clearly depicted in the inset of the graph (Figure 4a). The lack of coercivity in superparamagnetism allows for easy magnetization and demagnetization of the NPs without the need for a residual magnetic field. Superparamagnetism can be explained by proving that the coercivity is small or nearly equal to zero [44]. So, by using magnetite as templating agent for BG NPs,

superparamagnetism is also developed in AMAG\_BG NPs whose coercivity is again nearly equal to zero. The saturation magnetization (Ms) values for AMAG and AMAG\_BG were determined to be 1 emu/g and 0.25 emu/g, respectively, using the magnetization plots. The remanent magnetization (Mr) values for AMAG and AMAG\_BG are determined to be 0.24 emu/g and 0.06 emu/g, respectively, from the hysteresis curve. The saturation magnetization (Ms) values of AMAG NPs were less as compared to the reported value [43]. This is due to the retention of L-arginine in AMAG NPs and in good agreement with FTIR (Figure 1d) results and CHNSO analysis (Table 2) which reports peaks corresponding to L-arginine. The addition of AMAG template increases the size of AMAG\_BG from 14.6 ± 0.3 nm to 27.5 ± 1.1 nm significantly (Figure 2(e-f)) and drops saturation magnetization value from 1 emu/g of AMAG to 0.25 emu/g of AMAG\_BG. These findings confirm the incorporation of magnetic properties in BG NPs. Since AMAG\_BG has low remanence, it is a soft magnetic material compared to AMAG. They have lower coercivity with potential change in polarity, and suffer comparatively little electrical losses. Whereas AMAG has high remanence and is a hard magnetic material. The saturation magnetization of AMAG is higher that poses it as a highly magnetic material in nature. Thus, successfully creating magnetism in AMAG\_BG.

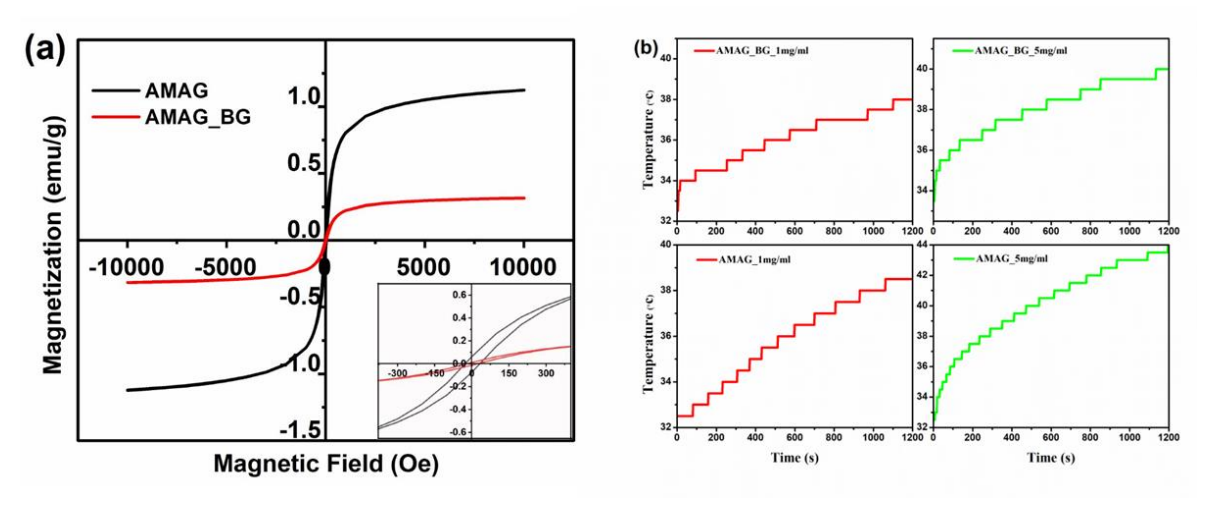


**Figure 2.4(a):** Magnetization curve of AMAG and AMAG\_BG (Inset shows zoomed image of magnetization curve of AMAG and AMAG\_BG from -350 Oe to 350 Oe). (b) Time-dependent temperature curves of AMAG and AMAG\_BG under AC magnetic field of 110 Oe with two different concentrations of 1 mg/ml and 5 mg/ml respectively.

Table 2.5: Saturation and Remanent Magnetization of AMAG and AMAG BG NPs

	Saturation Magnetization (M <sub>s</sub> )	Remanent Magnetization (M <sub>r</sub> )
	(emu/gram)	(emu/gram)
AMAG	1.0	0.24
AMAG_BG	0.25	0.06

## 2.4.9 *In-vitro* Heating Studies:

Magnetic hyperthermia is used to examine the heating capabilities of AMAG and AMAG BG NP's at the concentration of both the magnetic NP slurry of 1 mg/mL and 5 mg/mL as shown in Figure 4b [45,46]. Before switching on the system to run the magnetic NPs AMAG and AMAG BG, it was ensured that everything was connected properly especially water supply to magnetherm setup. After which it was looked to the reference matrix sheet for the combination of coil-capacitor box, power supply and function generator settings to get the required AMF strength (Bo). To test the samples AMAG and AMAG BG NPs at 464 kHz with 11 mT field strength (Bo), the function generator must first be turned on and 464 kHz inputted to ensure that the DC power supply's current and voltage are set to their maximum and minimum values, respectively. Living organisms and biological material are generally deemed to be safe at magnetic field strengths of about 110 Oersted (Oe) which has been used in in-vitro heat studies [47]. Compared to industrial and natural magnetic field intensities, including the Earth's magnetic field, this level of magnetic field used is much weaker. Higher natural magnetic fields are what biological systems are used to. Since BG is frequently used in biomedicine, it is intended to be biocompatible and is unlikely to be compromised in any way by exposure to a 110 Oe magnetic field while samples are being prepared. Biological samples and researchers are protected by safety regulations and guidelines, and a 110 Oe field usually conforms with these regulations [48].

As soon as the sample was in contact with the thermocouple probe, it was monitored for changes in temperature in real time. The polystyrene sample holder that was used to contain the test sample was prevented from non-specific heating. The sample slurry's initial temperature was set at room temperature (27 °C). Now that the DC power supply is turned on and the voltage knob has been gradually raised to 32.1 V, we will see a rise in the oscilloscope signal's peak-to-peak voltage and be able to record the sample's temperature change in real time. The temperature variation with time in AMAG and AMAG BG NP's is due to the magnetite NPs exhibiting superparamagnetism at room temperature. Superparamagnet NPs have a large magnetic moment. There are three mechanisms responsible for heat dissipation (a) Hysteresis power loss, due to irreversibility of magnetization process (b) Neel relaxation, when the magnetic moment of the particles was rotating (c) Brownian rotation, frictional loss due to rotation [49]. The particles' magnetic moments constantly align with the direction of the field when they are subjected to an AMF, releasing energy in the form of heat [50]. The number of magnetic domains in magnetite NPs diminishes with magnetite particle size; this threshold size is around 128 nm, after which only one magnetic domain is left [51]. Superparamagnetism is seen in magnetite NPs below this size, and in the presence of an AMF, heat is mostly produced via Néel and Brownian relaxation. When exposed to an AMF, a particle experiences rapid changes in its magnetic moment known as Néel relaxation. This resistance from the particle's crystalline structure causes the particle to generate heat. Conversely, Brownian relaxation produces frictional heat as a result of particles physically rotating within a supporting medium in an effort to realign with the shifting magnetic field [52,53]. Similarly, superparamagnetism is seen in AMAG and AMAG BG in presence of an AMF. Thus, producing heat capable of MH effect in cancerous cells.

The heat generation with time for AMAG and AMAG\_BG NPs was shown in Figure 4b and the corresponding frequency dependence SAR field is estimated from the data measured at AMF strength B0 = 11 mT and frequency 464 kHz, tabulated in Table 6.

It was seen that from both the concentration 1 mg/mL and 5 mg/mL of AMAG and AMAG\_BG, the temperature rise was more and in lesser time for 5 mg/mL concentration that is around 44 °C in 1200 s. The SAR value is inversely proportional to the mass of the samples (Supplementary file section 2.10). As we increase the concentration of both the magnetic NP slurry AMAG and AMAG BG from 1 mg/mL to 5 mg/mL the corresponding SAR value decreases. So, 1 mg/mL concentration shows higher SAR value for individual magnetic anisotropy. Both AMAG (14.849) and AMAG BG (8.106) NPs show high SAR values. AMAG BG NPs shows higher SAR value due to the BG network coverage on the magnetite core that are in good agreement with XRD (Figure 1c) and FTIR (Figure 1d) findings. AMAG BG is synthesized at ambient conditions in aqueous solvent omitting the requirement of calcination. The SAR values from 2.439 W/g to 14.849 W/g discovered in this study are suitable for the MH therapy of cancer. The SAR values in melt-derived magnetic bioactive glassceramics (MBGC) range from 19 W/g to 61 W/g when magnetite crystals doped in glass ceramics shows ferrimagnetic properties, while SAR value ranges between 4 W/g and 26 W/g when synthesized from zinc ferrites crystals [54,55]. For biphasic MBGC SAR values are seen from 3.5 W/g and 10 W/g. Additionally, the SAR values range from 0.039 W/g to 8.4 W/g for those MBGC that are totally synthesised by the sol-gel process, which is significantly lower [56,57]. Similar to the nanocomposite that is demonstrated in this study, researcher [58] developed a heterostructure system Fe2O3@SiO2-CaO that consists of maghemite NPs templated BG. The reported SAR values for the heterostructures ranged from 4.45 W/g to 5.8 W/g.

Hence, we can say that in current study, the synthesized material is nanosized mesoporous in nature that can cause hyperthermia and become potential treatment for cancer. The obtained sizes of AMAG and AMAG\_BG NPs are small and therefore obtained SAR values are sufficient to kill cancerous cells (close to 42 °C). Also, at higher temperatures the tissue might be burnt. Therefore, findings suggest that BG is known for soft and hard tissue regeneration which will further aid in wound healing after cancer treatment.

Table 2.6: SAR values of AMAG and AMAG BG for 1 mg/mL and 5 mg/mL concentrations

Sample	Concentration	Slope (°C/s)	SAR (W/g)
	(mg/mL)		
AMAG	1	0.00392	14.849
AMAG	5	0.0077	5.833
AMAG_BG	1	0.00214	8.106
AMAG_BG	5	0.00322	2.439

## 2.4.10 *In-vitro* Bioactivity:

BG biomaterials are distinguished from silica particles by their ability to regenerate bone. Bioactivity is evaluated through the deposition of hydroxyapatite (HAP) like bone bonding formation. It is characterized in terms of in-vitro biological reaction at bioactive glass and biological fluid (SBF) contact. Bioactivity of AMAG and AMAG BG NPs was observed in SBF by XRD, FTIR, FE-SEM, magnetization curve and in-vitro heat studies analysis as represented in Figure (5-6). Figure 5(a-b) shows the FTIR spectra of AMAG and AMAG BG after 4 d, 7 d, 15 d, and 30 d of interaction with SBF respectively. It was seen that during the interaction with SBF, the L-arginine and AMAG characteristic peaks in the AMAG BG samples (Figure 5(a-b)) either lost their strength or vanished, while HAP peaks simultaneously developed [59] (Figure 5b), distinctive FTIR peaks for hydroxyl groups (1631 cm-1), carbonate (789 cm-1), and phosphate (1117 cm-1 and 971 cm-1). This is because, after 30 d of contact with SBF, HAP began to accumulate on the surface of AMAG BG NPs. Similarly, XRD study (Figure 5d) of AMAG BG for 30 d in SBF revealed a few additional diffraction maxima in addition to the broad hump seen in (2θ range of 15° to 30°). After 4 d of interaction between AMAG BG and SBF, numerous additional diffraction maxima emerge, and their intensities considerably rise. When in contact with SBF, these novel XRD diffractions showed interfacial activity on the surface of AMAG BG. According to the JCPDS file number 01-086-0740, the observed reflections in the matching XRD pattern pertain to (Ca5(PO4)3(OH)). This demonstrates that the microcrystals of bone-like HAP developed on the surface of the AMAG\_BG after interaction with SBF. After 15 d of interaction with SBF and due to the HAP deposition, FE-SEM micrographs of AMAG (Figure 5(e-h)) showed a substantially different rough surface morphology compared to the comparable bare surface morphology of AMAG\_BG (Figure 5(i-l)). It is interesting that AMAG corroborated the findings of the XRD measurements and demonstrated a thin layer or no layer of HAP deposition when compared to AMAG\_BG (Figure 5(c-d)). Mesoporosity in general was the main cause of the AMAG\_BG sample's fast HAP deposition. Even after 15 d of contact with SBF, the AMAG showed weak or no HAP deposition, as indicated in the Figure 5(e-h) [60].

The VSM measurement for bioactivity of AMAG and AMAG\_BG NPs for 4 d, 7 d, 15 d and 30 d indicates a hysteresis curve of magnetization with the magnetic field, as shown in Figure 6(a-b). It clearly showed that there is not much difference in saturation magnetization of AMAG NPs after bioactivity of 4 d, 7 d, 15 d and 30 d. But in case of AMAG\_BG, saturation magnetization (Ms) is clearly increasing from 7 d to 15 d to 30 d which shows that ability of magnetization is maximum when deposition of HAP is maximum.

MH is also used to test the AMAG and AMAG\_BG NPs' ability to heat up after interacting with SBF for 4 d, 7 d, 15 d, and 30 d respectively. The heat generation with time for bioactivity of AMAG and AMAG\_BG NPs was shown in Figure 6(c-d). At AMF strength B0=11 mT for the AMAG and AMAG\_BG NPs, the SAR value is measured and the calculated SAR values of AMAG and AMAG\_BG NPs were shown in Table 7. It was seen that in AMAG concentration of 1 mg/mL for 4 d, 7 d, 15 d, and 30 d respectively, the change in SAR value was not so evident in individual concentrations. But as we compare the SAR value of AMAG 1 mg/mL concentration to AMAG 5 mg/mL concentration, its value changes rapidly. Here, the 1 mg/mL concentration have higher SAR value hence showing a better hyperthermia effect.

Now, in case of AMAG\_BG, for both the concentrations 1 mg/mL and 5 mg/mL, the change in SAR value is very evident. As the bioactivity increases from 4 d to 30 d, the temperature increases in lesser time interval. And for 15 d bioactivity of both the concentration sample slurry 1 mg/mL and 5 mg/mL, AMAG\_BG NPs shows better hyperthermia effect. Considering together hyperthermia effect and bioactivity (Figure (5-6)), AMAG\_BG shows good in-vitro hyperthermia effect. Hence, AMAG\_BG would be a novel material for cancer treatment as well as tissue regeneration.

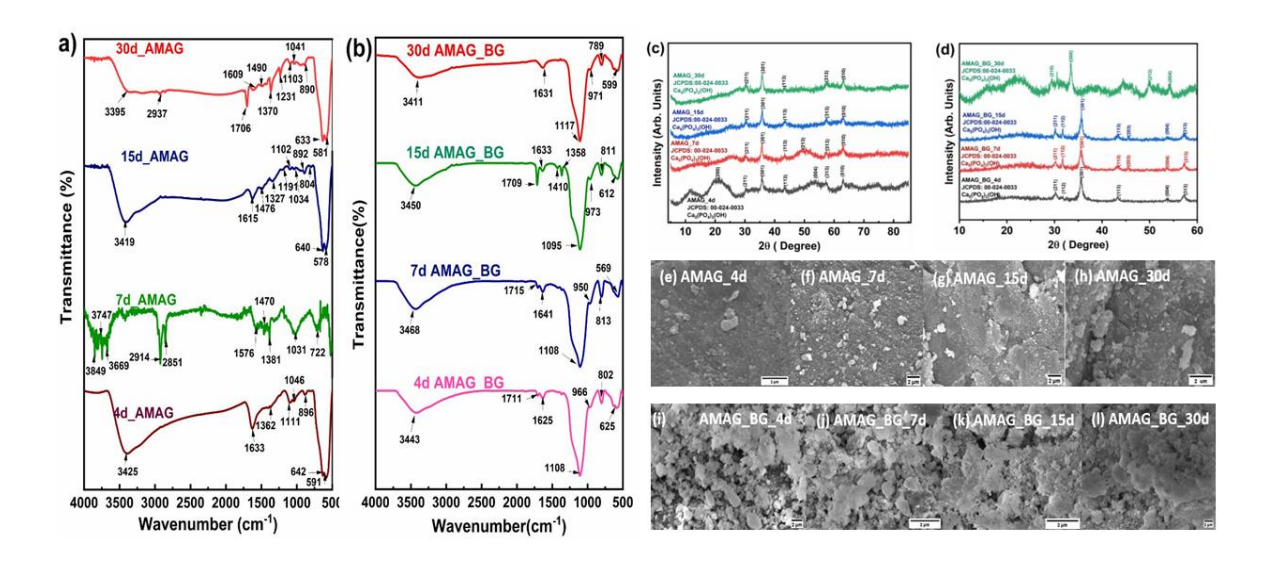


**Figure 2.5:** (a – b) FTIR spectra, (c-d) XRD patterns and (e-l) SEM micrographs of AMAG and AMAG\_BG after 4 d, 7 d, 15 d and 30 d of bioactivity in SBF solution.

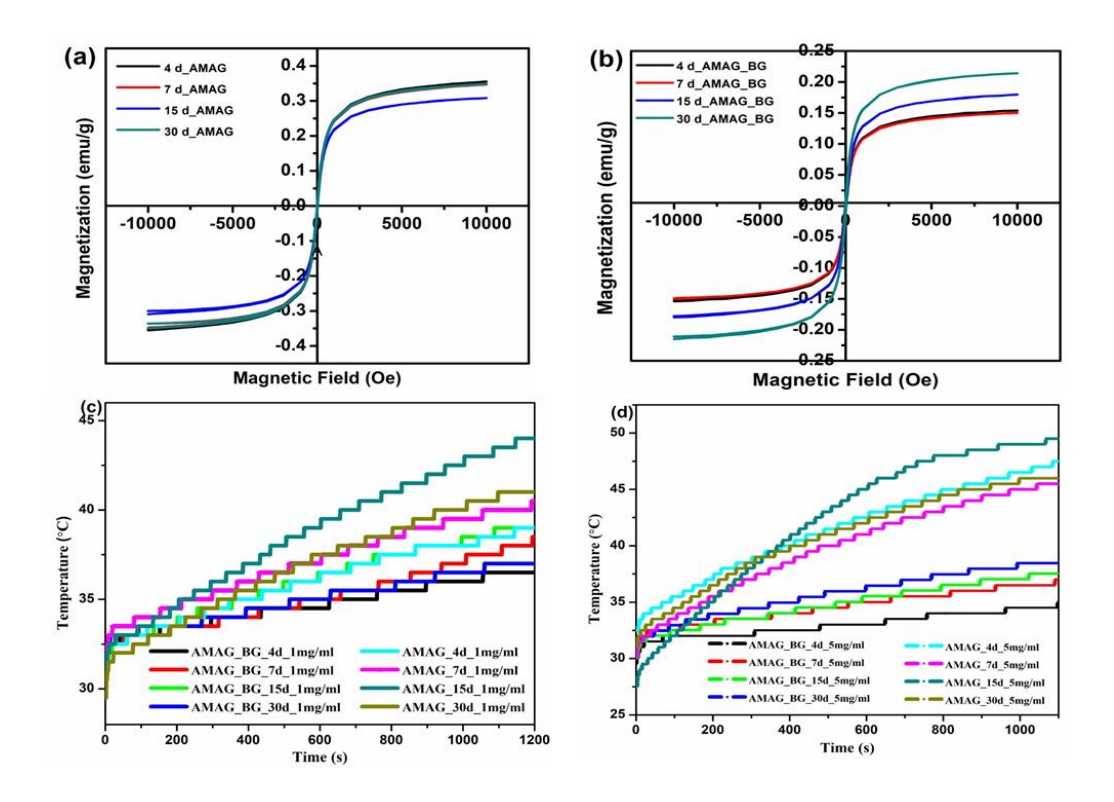


**Figure 2.6: (a-b)** Magnetization curve and (c-d) Time-dependent temperature curves under AC magnetic field of 110 Oe with two different concentrations of 1 mg/mL and 5 mg/mL of AMAG and AMAG\_BG after 4 d, 7 d, 15 d and 30 d of bioactivity in SBF solution respectively.

**Table 2.7:** SAR values of AMAG and AMAG\_BG at 1 mg/mL and 5 mg/mL concentrations after bioactivity of 4 d, 7 d, 15 d and 30 d in SBF solution.

Sample	Concentration	Slope (°C/s)	SAR (W/g)
(Bioactivity)	(mg/mL)		
AMAG (4 d)	1	0.00613	23.221
AMAG (4 d)	5	0.01012	7.667
AMAG (7 d)	1	0.00589	22.312
AMAG (7 d)	5	0.01254	9.500
AMAG (15 d)	1	0.00947	35.873
AMAG (15 d)	5	0.02396	18.152
AMAG (30 d)	1	0.00785	29.736
AMAG (30 d)	5	0.01399	10.599
AMAG_BG (4 d)	1	0.00319	12.084
AMAG_BG (4 d)	5	0.00297	2.250
AMAG_BG (7 d)	1	0.00414	15.682
AMAG_BG (7 d)	5	0.00396	3.000
AMAG_BG (15 d)	1	0.00553	20.948
AMAG_BG (15 d)	5	0.00547	4.144
AMAG_BG (30 d)	1	0.00361	13.675
AMAG_BG (30 d)	5	0.00447	3.386

## 2.4.11 *In-vitro* Hemolysis Assay:

Hemolysis is a process that causes red blood cells (RBCs) to release the iron-containing protein haemoglobin into the plasma [61]. NPs may interact with erythrocytes differently than traditional medicines do because of their small size and distinct physicochemical features. They may also cause problems for the in-vitro assays that are used to standardize procedures. Separating true hemolytic responses from misleading positive or negative results caused by particle interference is essential for accurate interpretation of these tests [62]. The cytotoxicity of the produced NPs was evaluated using the hemolysis assay. The AMAG hemocompatibility was evaluated by in-vitro hemolysis assay using human blood (declaration for human blood has been attached in supplementary file S4). Images of different variants like Triton X 100 (positive control), PBS (negative control), AMAG and AMAG BG NPs  $(1, 5, 10, 25, 50 \,\mu\text{g/mL})$  were centrifuged at  $(500 \times \text{g})$  for 5 min till a complete clear solution was obtained as depicted in Figure 7(a-b). Hemoglobin absorbance at 570 nm was measured spectrophotometrically to determine how NPs affected the lysis of human red blood cells. As represented in (Figure S3 (a-h), each of the produced NPs demonstrated a very modest hemolytic activity. AMAG and AMAG BG NPs are hemocompatible and may not be harmful at the prescribed doses, according to this representation. Hemolysis typically follows a dose-dependent pattern, wherein the rate of hemolysis increases at higher test material concentrations. However, this is not the case with AMAG and AMAG BG NPs. Therefore, it can be assumed that it may occur at the lower pH ranges examined. Hence, it can be concluded that AMAG and AMAG BG NPs exhibits minimal hemolysis at physiological pH of 7.4 as shown in Figure 7(c-d). As observed from UV based data and optical micrographs, we further tried to explain the compatibility of the material with RBCs through optical microscopy (Figure 7(e-h)). Through observation of slides, we could see intact RBCs present at random position of the slide in case of control and samples. However, in case of Triton X 100 no intact RBCs could be observed rather overall distribution of debris was observed which could possibly be a result of breakdown of RBCs.

The obtained results (Figure 7) demonstrate that hemolysis activity was present in all NPs and was concentration dependent. Maximum hemolysis was seen when the NP concentration was 50 µg/mL, and was found to be 20 % in AMAG and 8 % in AMAG\_BG. As previously reported, <5% of hemolysis was seen at lower concentrations, which can be safely employed [63,64]. The percentage of hemolysis activity revealed that lower doses of nanoparticles were safe and biocompatible. The best sample was then used to test the hemolytic activity with concentration variations over time (Figure 7). Under all different concentrations, the synthesized samples showed low hemolytic activity. Therefore, optimised samples are suitable for application as anticancer agents.

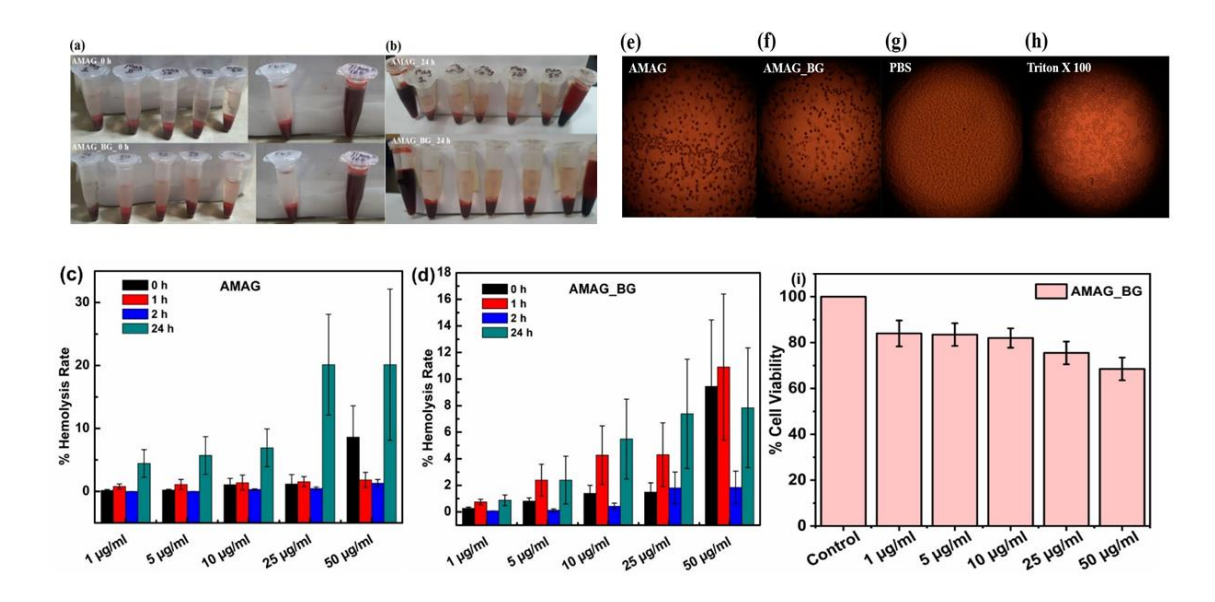


**Figure 2.7: (a-b)** Determination of hemolytic activity through images of each variant (centrifugation  $500 \times g$ , 5 min to a completely clear solution). (c-d) Relative comparison of hemolytic activity after 0 h, 1 h, 2 h and 24 h of AMAG and AMAG\_BG NPs (1, 5, 10, 25, 50 µg/mL) with 100% of Triton X 100 as a positive control and PBS as the negative control. (e-h) Determination of hemolytic activity through microscope images of AMAG, AMAG\_BG, Negative Control (PBS) and Positive Control (Triton X 100) after 2 h interaction. (i) MTT assay of AMAG\_BG NPs. All experiments were carried out in three replications.

#### **2.4.12 MTT Assay:**

The study was mainly concerned with the application of BG in the treatment of bone-related disorders. We used cytocompatibility testing with the 3-(4,5-Dimethylthiazol-2-Yl)-2,5-Diphenyltetrazolium Bromide (MTT) assay to evaluate the compatibility of BG with human bone cells, particularly the

U2OS osteosarcoma cell line. The existence of live cells was assessed using the MTT assay following a 24 h exposure of the cells to varying concentrations of AMAG\_BG NPs, as shown in Figure 7i below. The cells cultivated in media without any treatment were represented by the "Control" group. The results showed that the AMAG\_BG NPs showed biocompatibility with over 80% cell viability from 1  $\mu$ g/mL to 10  $\mu$ g/mL of tested doses. It showed around 70% cell viability for 25  $\mu$ g/mL and 50  $\mu$ g/mL of dose. Notably, we saw a small decrease in cellular viability at higher concentrations.

#### 2.5. Interaction Mechanism

The structure-directing molecule for the magnetite and BG sample in this investigation is L-arginine, an important amino acid, at a constant pH condition (pH 7.4). At physiological pH, L-arginine has a net positive charge (Figure 8). The L-arginine molecules can interact through carboxylic acid groups, primary and secondary amino groups (Figure 8). The observed interaction between iron oxide species and L-arginine was evidenced by FTIR analysis (Figure 1b). In AMAG BG sample, the chemical interaction of L-arginine coating on magnetite and BG network was indicated through COO- group of L-arginine (Figure 8). Such interactions of L-arginine molecules in AMAG BG nanoparticles are evident by TGA and CHNSO analysis (Figure 2(a-b) and Table 1). In this study, the L-arginine templated magnetite core shell reacted with the BG network under ambient conditions to produce AMAG BG. The interaction of L-arginine with BG precursors leads to the formation of BG network around L-arginine coated magnetite core shell. As a result, nanosized, mesoporous AMAG BG (Average pore diameter: 7.1801 nm) could be synthesized with surface area (80.39 m2g-1) at ambient conditions. Mesoporous AMAG BG interacted with SBF forming HAP on its surface thus demonstrating good in-vitro bioactivity. The observation promises for AMAG BG's capacity to bind to bones. The core shell AMAG when encounters BG network, it tends to develop magnetic properties in AMAG BG such that its saturation magnetization is 0.25 emu/g and remanent magnetization is 0.06 emu/g. AMAG BG NPs tends to develop heat (≈ 43 °C) successfully with SAR value 8.106 W/g for 1 mg/mL concentration thus becoming successful for hyperthermia treatment of cancer. To our knowledge, for the first time BG NPs have been synthesized using L-arginine templated magnetite core shell through bio-inspired route. Importantly, using the above-mentioned methods, it becomes challenging to synthesize such property-dependent BG samples for biological applications. Hence, there is no doubt that AMAG\_BG is a magnetic property dependent BG material for cancer treatment.

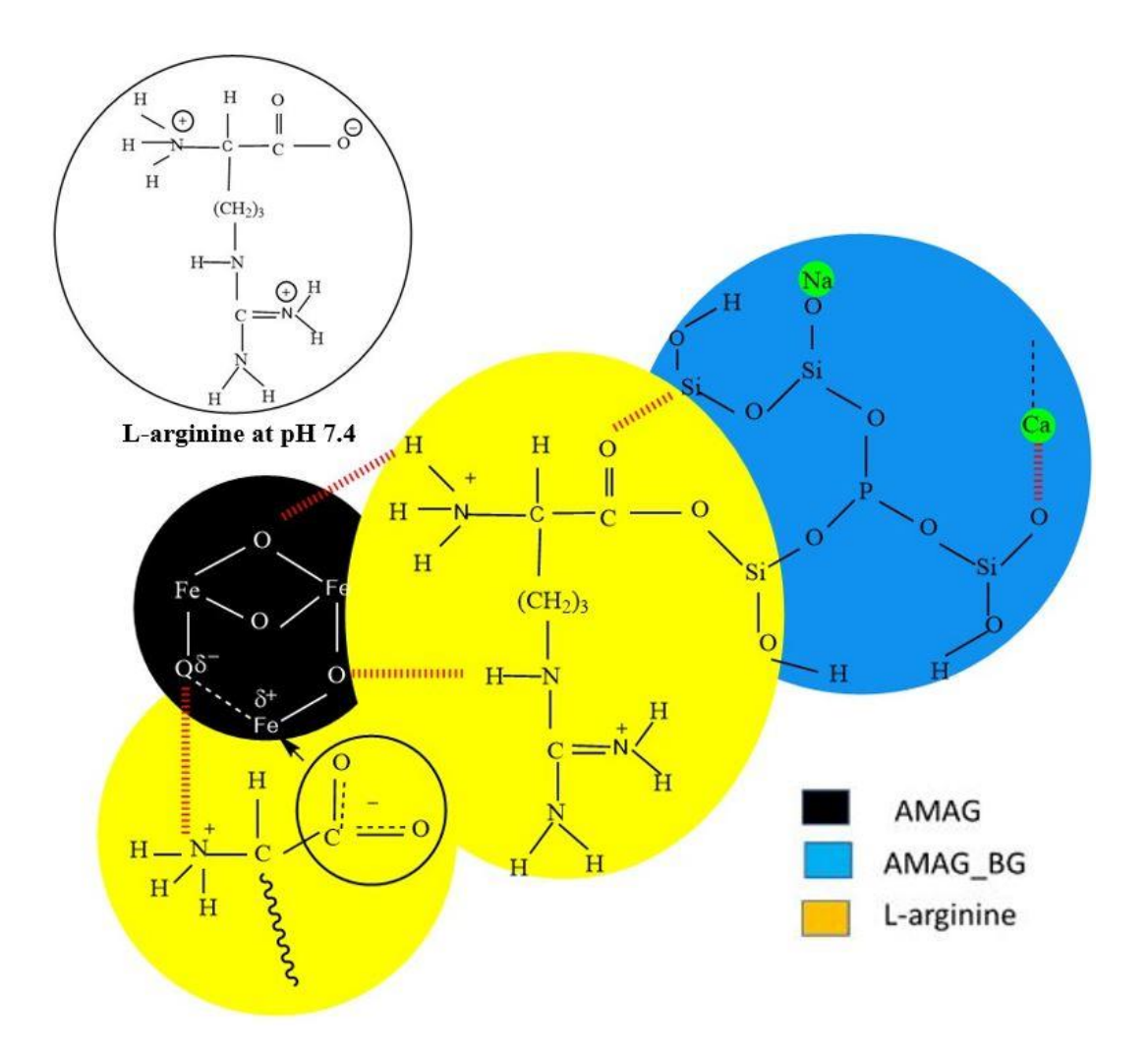


**Fig. 2.8:** Representative structure of AMAG\_BG NPs showing multi-centred interaction of Larginine with magnetite and BG network.

#### 2.6 Conclusion:

In answer to magneto heat transfer of the nano-carrier to diseased sites, magnetic NPs have been developed through a simple bio-inspired process. It is significant to note that AMAG not only functions as a templating agent for the synthesis of AMAG\_BG NPs but also acts as a precursor for network formers and network modifiers in it. FTIR, CHNSO analysis revealed the existence of BG network and L-arginine in AMAG\_BG NPs. The XPS and EDX gave the elemental composition of magnetic NPs. The XRD confirmed the existence of nanosized crystallites in the magnetic samples and FE-SEM, TEM portrayed the formation of nanosized particles. BET analysis proves that magnetic NPs are mesoporous in nature. The in-vitro heat studies, bioactivity studies and hemolysis assay along with magnetic studies depicts that AMAG NPs are successful in developing magnetism in BG network. Thus, making it suitable for hyperthermia treatment of cancer, combinational therapy and promises for regeneration of hard and soft tissues. So, obtained magnetic material is a good candidate to show significant impact on clinical use and therapeutics with distinct surface characteristics and biocompatibility for cancer treatment.

#### References

- [1] B. Galjart, D.J. Höppener, J.G.J.V. Aerts, C.H. Bangma, C. Verhoef, D.J. Grünhagen, Follow-up strategy and survival for five common cancers: A meta-analysis, Eur J Cancer. 174 (2022) 185. https://doi.org/10.1016/j.ejca.2022.07.025.
- [2] S. Nisar, T. Masoodi, K.S. Prabhu, S. Kuttikrishnan, L. Zarif, S. Khatoon, S. Ali, S. Uddin, A.A.-S. Akil, M. Singh, M.A. Macha, A.A. Bhat, Natural products as chemo-radiation therapy sensitizers in cancers, Biomedicine & Pharmacotherapy. 154 (2022) 113610. https://doi.org/10.1016/j.biopha.2022.113610.
- [3] X. Meng, Y. Lei, X. Zhang, K. Sun, L. Zhang, Z. Wang, Cancer immunotherapy: Classification, therapeutic mechanisms, and nanomaterial-based synergistic therapy, Applied Materials Today. 24 (2021) 101149. https://doi.org/10.1016/j.apmt.2021.101149.
- [4] D. Wu, M. Chen, J. Liang, S. Li, W. Zhang, Y. Lei, J. Ding, Y. Wang, Z. Chen, N. Li, S. Luo, J. Li, M. Hong, Z. Yan, Consensus on informed consent for participants in cancer clinical studies (2021 edition), Asia-Pacific Journal of Oncology Nursing. 9 (2022) 100130. https://doi.org/10.1016/j.apjon.2022.100130.
- [5] M. Dunne, M. Regenold, C. Allen, Hyperthermia can alter tumor physiology and improve chemo- and radio-therapy efficacy, Advanced Drug Delivery Reviews. 163–164 (2020) 98. https://doi.org/10.1016/j.addr.2020.07.007.
- [6] E. Seyyednia, F. Oroojalian, B. Baradaran, J.S. Mojarrad, A. Mokhtarzadeh, H. Valizadeh, Nanoparticles modified with vasculature-homing peptides for targeted cancer therapy and angiogenesis imaging, J Control Release. 338 (2021) 367. https://doi.org/10.1016/j.jconrel.2021.08.044.
- [7] R. Baghban, M. Afarid, J. Soleymani, M. Rahimi, Were magnetic materials useful in cancer therapy?, Biomedicine & Pharmacotherapy. 144 (2021) 112321. https://doi.org/10.1016/j.biopha.2021.112321.
- [8] S. Singh, N. Sharma, A. Bansal, N. Kanojia, S. Sethi, J. Madan, R.K. Sodhi, Apoptosis modulating nanochemotherapeutics in the treatment of cancer: Recent progress and advances, Clinical Perspectives and Targeted Therapies in Apoptosis. (2021) 153.
- [9] C.S.S.R. Kumar, F. Mohammad, Magnetic nanomaterials for hyperthermia-based therapy and controlled drug delivery, Advanced Drug Delivery Reviews. 63 (2011) 789. https://doi.org/10.1016/j.addr.2011.03.008.
- [10] T. Dippong, E.A. Levei, O. Cadar, Recent Advances in Synthesis and Applications of MFe<sub>2</sub>O<sub>4</sub> (M = Co, Cu, Mn, Ni, Zn) Nanoparticles, Nanomaterials. 11 (2021) 1560. https://doi.org/10.3390/nano11061560.
- [11] J.R. Jones, Reprint of: Review of bioactive glass: From Hench to hybrids, Acta Biomater. 23 Suppl (2015) S53. https://doi.org/10.1016/j.actbio.2015.07.019.
- [12] S. Majumdar, S. Gupta, S. Krishnamurthy, Multifarious applications of bioactive glasses in soft tissue engineering, Biomaterials Science. 9 (2021) 8111.
- [13] V. Miguez-Pacheco, L.L. Hench, A.R. Boccaccini, Bioactive glasses beyond bone and teeth: Emerging applications in contact with soft tissues, Acta Biomaterialia. 13 (2015) 1. https://doi.org/10.1016/j.actbio.2014.11.004.
- [14] A.G. Roca, L. Gutiérrez, H. Gavilán, M.E. Fortes Brollo, S. Veintemillas-Verdaguer, M. del P. Morales, Design strategies for shape-controlled magnetic iron oxide nanoparticles, Advanced Drug Delivery Reviews. 138 (2019) 68. https://doi.org/10.1016/j.addr.2018.12.008.
- [15] G. Wu, F.W. Bazer, T.A. Davis, S.W. Kim, P. Li, J. Marc Rhoads, M. Carey Satterfield, S.B. Smith, T.E. Spencer, Y. Yin, Arginine metabolism and nutrition in growth, health and disease, Amino Acids. 37 (2009) 153. https://doi.org/10.1007/s00726-008-0210-y.

- [16] M. Vallet-Regí, Nanostructured mesoporous silica matrices in nanomedicine, J Intern Med. 267 (2010) 22. https://doi.org/10.1111/j.1365-2796.2009.02190.x.
- [17] Z. Li, M. Kawashita, N. Araki, M. Mitsumori, M. Hiraoka, M. Doi, Magnetite nanoparticles with high heating efficiencies for application in the hyperthermia of cancer, Materials Science and Engineering: C. 30 (2010) 990. https://doi.org/10.1016/j.msec.2010.04.016.
- [18] D. Santhiya, H. kumari Alajangi, F. Anjum, S. Murugavel, M. Ganguli, Bio-inspired synthesis of microporous bioactive glass-ceramic using CT-DNA as a template, J. Mater. Chem. B. 1 (2013) 6329. https://doi.org/10.1039/C3TB21212B.
- [19] N. Gupta, D. Santhiya, A. Aditya, Tailored smart bioactive glass nanoassembly for the dual antibiotic in vitro sustained release against osteomyelitis, J. Mater. Chem. B. 4 (2016). https://doi.org/10.1039/C6TB01528J.
- [20] N. Dey, D. Santhiya, A. Das, Bio-Inspired Synthesis of Hollow Mesoporous Bioactive Glass Nanoparticles Using Calcium Carbonate as Solid Template, ChemistrySelect. 7 (2022). https://doi.org/10.1002/slct.202200392.
- [21] N. Gupta, D. Santhiya, A. Aditya, K. Badra, Dendrimer templated bioactive glass-ceramic nanovehicle for gene delivery applications †, (2020).
- [22] T. Kokubo, H. Takadama, How useful is SBF in predicting in vivo bone bioactivity?, Biomaterials. 27 (2006) 2907. https://doi.org/10.1016/j.biomaterials.2006.01.017.
- [23] A.B. Salunkhe, V.M. Khot, S.H. Pawar, Magnetic hyperthermia with magnetic nanoparticles: a status review, Curr Top Med Chem. 14 (2014) 572. https://doi.org/10.2174/1568026614666140118203550.
- [24] S.D. Shingte, A.H. Phakatkar, E. McKiernan, K. Nigoghossian, S. Ferguson, R. Shahbazian-Yassar, D.F. Brougham, Correlating Magnetic Hyperthermia and Magnetic Resonance Imaging Contrast Performance of Cubic Iron Oxide Nanoparticles with Crystal Structural Integrity, Chem. Mater. (2022). https://doi.org/10.1021/acs.chemmater.2c00708.
- [25] W. Mekseriwattana, P. Guardia, B. Torres Herrero, J.M. de la Fuente, C. Kuhakarn, A. Roig, K. Prapainop Katewongsa, Riboflavin–citrate conjugate multicore SPIONs with enhanced magnetic responses and cellular uptake in breast cancer cells, Nanoscale Advances. 4 (2022) 1988. https://doi.org/10.1039/D2NA00015F.
- [26] A.R. Sebastian, H.J. Kim, S.H. Kim, Analysis and control of heating of magnetic nanoparticles by adding a static magnetic field to an alternating magnetic field, Journal of Applied Physics. 126 (2019) 134902. https://doi.org/10.1063/1.5097415.
- [27] S. Dumoga, Y. Rai, A.N. Bhatt, A.K. Tiwari, S. Singh, A.K. Mishra, D. Kakkar, Block Copolymer Based Nanoparticles for Theranostic Intervention of Cervical Cancer: Synthesis, Pharmacokinetics, and in Vitro/in Vivo Evaluation in HeLa Xenograft Models, ACS Appl. Mater. Interfaces. 9 (2017) 22195. https://doi.org/10.1021/acsami.7b04982.
- [28] P. Zhang, H. Zhang, W. He, D. Zhao, A. Song, Y. Luan, Disulfide-Linked Amphiphilic Polymer-Docetaxel Conjugates Assembled Redox-Sensitive Micelles for Efficient Antitumor Drug Delivery, Biomacromolecules. 17 (2016) 1621. https://doi.org/10.1021/acs.biomac.5b01758.
- [29] F. Molly, W. Sean, S. Mark, M. Colleen, A. Scott, R. Don, Standard practice for assessment of hemolytic properties of materials, American Society for Testing of Materials. ASTM F756-00. (2000).
- [30] K.-C. Kim, E.-K. Kim, J.-O. Lee, Y.-S. Kim, Characterization of magnetic nanoparticles synthesized by sonomechanical method, in: 2006 IEEE Nanotechnology Materials and Devices Conference, 2006: pp. 600–601. https://doi.org/10.1109/NMDC.2006.4388922.
- [31] D. Maity, S.N. Kale, R. Kaul-Ghanekar, J.-M. Xue, J. Ding, Studies of magnetite nanoparticles synthesized by thermal decomposition of iron (III) acetylacetonate in tri(ethylene glycol), Journal of Magnetism and Magnetic Materials. 321 (2009) 3093. https://doi.org/10.1016/j.jmmm.2009.05.020.

- [32] S. Mashjoor, M. Yousefzadi, H. Zolgharnein, E. Kamrani, M. Alishahi, Mater. Sci. Eng. C 102 (2019) 324.
- [33] G. Li, Z. Pei, K. Zhang, N. Zhang, S. Zhao, N. Jiang, Y. Qi, R. He, R. Zhu, Y. He, G. Liang, Study on the interface between bioactive glass and magnetite, Composite Interfaces. 27 (2020) 687. https://doi.org/10.1080/09276440.2019.1688046.
- [34] T.Q. Bui, S.N.-C. Ton, A.T. Duong, H.T. Tran, Size-dependent magnetic responsiveness of magnetite nanoparticles synthesised by co-precipitation and solvothermal methods, Journal of Science: Advanced Materials and Devices. 3 (2018) 107. https://doi.org/10.1016/j.jsamd.2017.11.002.
- [35] H. Goel, D. Santhiya, Effect of pH on bio-inspired synthesis of L-Lysine templated bioactive glass hybrid xerogels for tailored textural and rheological properties, Materials Chemistry and Physics. 281 (2022) 125828. https://doi.org/10.1016/j.matchemphys.2022.125828.
- [36] A. Ebrahiminezhad, Y. Ghasemi, S. Rasoul-Amini, J. Barar, S. Davaran, Impact of Amino-Acid Coating on the Synthesis and Characteristics of Iron-Oxide Nanoparticles (IONs), Bulletin of the Korean Chemical Society. 33 (2012) 3957. https://doi.org/10.5012/bkcs.2012.33.12.3957.
- [37] A.F.R. Rodriguez, C.C. dos Santos, K. Lüdtke-Buzug, A.C. Bakenecker, Y.O. Chaves, L.A.M. Mariúba, J.V. Brandt, B.E. Amantea, R.C. de Santana, R.F.C. Marques, M. Jafelicci, M.A. Morales, Evaluation of antiplasmodial activity and cytotoxicity assays of amino acids functionalized magnetite nanoparticles: Hyperthermia and flow cytometry applications, Materials Science and Engineering: C. 125 (2021) 112097. https://doi.org/10.1016/j.msec.2021.112097.
- [38] A.C. Vale, P.R. Pereira, A.M. Barbosa, E. Torrado, N.M. Alves, Optimization of silver-containing bioglass nanoparticles envisaging biomedical applications, Materials Science and Engineering: C. 94 (2019) 161. https://doi.org/10.1016/j.msec.2018.09.027.
- [39] A. Senthamizhan, K. Sambathkumar, S. Nithiyanantham, Physico-chemical, structural, optical and NLO studies on pure and La3+ doped l-arginine acetate crystals, Materials Science for Energy Technologies. 3 (2020) 282. https://doi.org/10.1016/j.mset.2019.11.005.
- [40] S. Mashjoor, M. Yousefzadi, H. Zolgharnein, E. Kamrani, M. Alishahi, Phyco-linked vs chemogenic magnetite nanoparticles: Route selectivity in nano-synthesis, antibacterial and acute zooplanktonic responses, Materials Science and Engineering: C. 102 (2019) 324. https://doi.org/10.1016/j.msec.2019.01.049.
- [41] R. Ghosh Chaudhuri, S. Paria, Core/Shell Nanoparticles: Classes, Properties, Synthesis Mechanisms, Characterization, and Applications, Chem. Rev. 112 (2012) 2373. https://doi.org/10.1021/cr100449n.
- [42] Z.A. ALOthman, A Review: Fundamental Aspects of Silicate Mesoporous Materials, Materials (Basel). 5 (2012) 2874. https://doi.org/10.3390/ma5122874.
- [43] C.G. Malar, M. Seenuvasan, K.S. Kumar, Improvisation of diffusion coefficient in surface modified magnetite nanoparticles: A novel perspective, Materials Science and Engineering: C. 103 (2019) 109832. https://doi.org/10.1016/j.msec.2019.109832.
- [44] M. Suto, Y. Hirota, H. Mamiya, A. Fujita, R. Kasuya, K. Tohji, B. Jeyadevan, J. Magn. Magn. Mater. 321 (2009) 1493.
- [45] A.E. Deatsch, B.A. Evans, Heating efficiency in magnetic nanoparticle hyperthermia, Journal of Magnetism and Magnetic Materials. 354 (2014) 163. https://doi.org/10.1016/j.jmmm.2013.11.006.
- [46] W. Ji, P. Hu, X. Wang, B. Chen, T. Chang, F.F. Yang, Q. Cao, W. Zhang, R. Dang, K. Wang, High heating ability of one-step carbothermal reduction method of Fe3O4 nanoparticles upon magnetic field, Journal of Alloys and Compounds. 866 (2021) 158952. https://doi.org/10.1016/j.jallcom.2021.158952.
- [47] S. A. Shah, M. U. Hashmi, S. Alam, A. Shamim, J. Magn. Magn. Mater. 322 (2010) 273.

- [48] T. W. Wang, H. C. Wu, W. R. Wang, F. H. Lin, P. J. Lou, M. J. Shieh, T. H. Young, J. Biomed. Mater. Res. A 83 (2007) 828.
- [49] X. Wang, H. Gu, Z. Yang, The heating effect of magnetic fluids in an alternating magnetic field, Journal of Magnetism and Magnetic Materials. 293 (2005) 334. https://doi.org/10.1016/j.jmmm.2005.02.028.
- [50] X. Kesse, A. Adam, S. B. Colin, D. Mertz, E. Larquet, T. Gacoin, I. Maurin, C. Vichery, J. M. Nedelec, ACS Appl. Mater. Interfaces. 12 (2020) 47820.
- [51] T. Houlding, E. Rebrov, Application of alternative energy forms in catalytic reactor engineering, Green Processing and Synthesis. 1 (2012). https://doi.org/10.1515/greenps-2011-0502.
- [52] M. Suto, Y. Hirota, H. Mamiya, A. Fujita, R. Kasuya, K. Tohji, B. Jeyadevan, Heat dissipation mechanism of magnetite nanoparticles in magnetic fluid hyperthermia, Journal of Magnetism and Magnetic Materials. 321 (2009) 1493. https://doi.org/10.1016/j.jmmm.2009.02.070.
- [53] null Suriyanto, E.Y.K. Ng, S.D. Kumar, Physical mechanism and modeling of heat generation and transfer in magnetic fluid hyperthermia through Néelian and Brownian relaxation: a review, Biomed Eng Online. 16 (2017) 36. https://doi.org/10.1186/s12938-017-0327-x.
- [54] S.A. Shah, M.U. Hashmi, S. Alam, Effect of aligning magnetic field on the magnetic and calorimetric properties of ferrimagnetic bioactive glass ceramics for the hyperthermia treatment of cancer, Materials Science and Engineering: C. 31 (2011) 1010. https://doi.org/10.1016/j.msec.2011.02.024.
- [55] S.A. Shah, M.U. Hashmi, S. Alam, A. Shamim, Magnetic and bioactivity evaluation of ferrimagnetic ZnFe2O4 containing glass ceramics for the hyperthermia treatment of cancer, Journal of Magnetism and Magnetic Materials. 322 (2010) 375.
- [56] T.-W. Wang, H.-C. Wu, W.-R. Wang, F.-H. Lin, P.-J. Lou, M.-J. Shieh, T.-H. Young, The development of magnetic degradable DP-Bioglass for hyperthermia cancer therapy, J Biomed Mater Res A. 83 (2007) 828. https://doi.org/10.1002/jbm.a.31411.
- [57] G. Li, K. Zhang, Z. Pei, N. Zhang, Y. Yu, S. Zhao, G. Liang, J. Zhou, Y. Xing, A novel method to enhance magnetic property of bioactive glass-ceramics for hyperthermia, Ceramics International. 45 (2019) 4945. https://doi.org/10.1016/j.ceramint.2018.11.194.
- [58] X. Kesse, A. Adam, S. Begin-Colin, D. Mertz, E. Larquet, T. Gacoin, I. Maurin, C. Vichery, J.-M. Nedelec, Elaboration of Superparamagnetic and Bioactive Multicore–Shell Nanoparticles (γ-Fe 2 O 3 @SiO 2 -CaO): A Promising Material for Bone Cancer Treatment, ACS Appl. Mater. Interfaces 12 (2020) 47820. https://doi.org/10.1021/acsami.0c12769.
- [59] F. Kurtuldu, N. Mutlu, M. Michálek, K. Zheng, M. Masar, L. Liverani, S. Chen, D. Galusek, A.R. Boccaccini, Cerium and gallium containing mesoporous bioactive glass nanoparticles for bone regeneration: Bioactivity, biocompatibility and antibacterial activity, Materials Science and Engineering: C. 124 (2021) 112050. https://doi.org/10.1016/j.msec.2021.112050.
- [60] A. Farzin, S. Hassan, R. Emadi, S.A. Etesami, J. Ai, Comparative evaluation of magnetic hyperthermia performance and biocompatibility of magnetite and novel Fe-doped hardystonite nanoparticles for potential bone cancer therapy, Materials Science and Engineering: C. 98 (2019) 930. https://doi.org/10.1016/j.msec.2019.01.038.
- [61] B.C. Evans, C.E. Nelson, S.S. Yu, K.R. Beavers, A.J. Kim, H. Li, H.M. Nelson, T.D. Giorgio, C.L. Duvall, Ex vivo red blood cell hemolysis assay for the evaluation of pH-responsive endosomolytic agents for cytosolic delivery of biomacromolecular drugs, J Vis Exp. (2013) e50166. https://doi.org/10.3791/50166.
- [62] D. Uhlirova, M. Stankova, M. Docekalova, B. Hosnedlova, M. Kepinska, B. Ruttkay-Nedecky, J. Ruzicka, C. Fernandez, H. Milnerowicz, R. Kizek, A Rapid Method for the

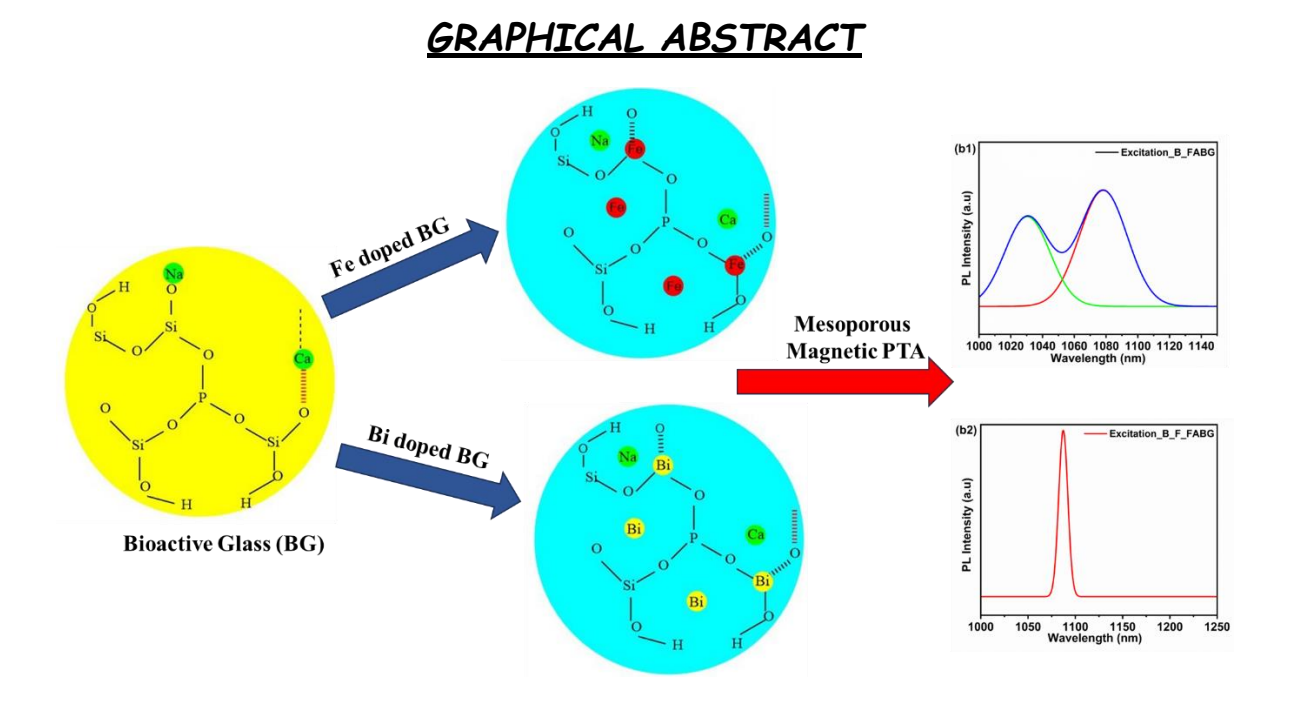
- Detection of Sarcosine Using SPIONs/Au/CS/SOX/NPs for Prostate Cancer Sensing, Int J Mol Sci. 19 (2018) 3722. https://doi.org/10.3390/ijms19123722.
- [63] V. Vinotha, A. Iswarya, R. Thaya, M. Govindarajan, N.S. Alharbi, S. Kadaikunnan, J.M. Khaled, M.N. Al-Anbr, B. Vaseeharan, Synthesis of ZnO nanoparticles using insulin-rich leaf extract: Anti-diabetic, antibiofilm and anti-oxidant properties, Journal of Photochemistry and Photobiology B: Biology. 197 (2019). https://doi.org/10.1016/j.jphotobiol.2019.111541.
- [64] In vivo biodistribution, antioxidant and hemolysis tendency of superparamagnetic iron oxide nanoparticles Potential anticancer agents, Arabian Journal of Chemistry. 16 (2023) 104602. https://doi.org/10.1016/j.arabjc.2023.104602.

# CHAPTER 3

Mesoporous bioactive glass nanoparticles with dopants bismuth and iron as magnetic photothermal agents for biomedical applications

### **CHAPTER 3**

# Mesoporous bioactive glass nanoparticles with dopants bismuth and iron as magnetic photothermal agents for biomedical applications



#### 3.1 Introduction

Bioactive glasses (BG) have been developed into a diverse class of biomaterials with potential applications in the management of numerous illnesses [1]. BG have long been linked to their ability to connect bone [2]. Currently, these materials are considered for soft and bone tissue regeneration, implant coatings, additive manufacturing for 3D printing, drug carriers etc [3]. Interestingly, role of BG in biomedical applications can be widened through the incorporation of unique metallic ions/organic molecules into silicate (or phosphate) network [4]. As a result, these functionalised BG can be employed as various therapeutic agents such as to produce heat for phototherapy or magnetic-induced hyperthermia, supply radiation for brachytherapy, and help deliver drugs to fight against cancer and infections [5].

High incidence and mortality rates led researchers to investigate on effective cancer treatment

methods as well as faster and more precise diagnostic techniques. The most frequently used traditional clinical treatments include surgery, radiation, and chemotherapy [6,7]. These treatments withheld a significant chance of failure or side effects. Currently, photothermal therapy (PTT) is drawing attention in cancer therapy. In PTT, use of photothermal agents (PTAs) convert absorbed light energy into heat to inflict thermal burns on malignant cells [8,9]. PTAs can display modest photothermal conversion in healthy tissues but robust photothermal conversion at the location of malignant cells [10,11]. As a result, it causes the targeted heating of the malignant location while posing little or no threat to healthy cells.

The present research work aims to synthesize BG based PTAs. Dual functions such as network formation and modification of dibismuth trioxide (Bi<sub>2</sub>O<sub>3</sub>) in oxide glasses are well known [12]. In addition to their outstanding properties, including great mechanical strength, thermal stability, and chemical endurance, glasses containing Bi<sub>2</sub>O<sub>3</sub> are attractive candidates for practical applications [13,14]. Bismuth (Bi) is regarded as less toxic than other heavy metals and is currently used in the production of pharmaceutical products [15]. Bi doped materials can be visualized by using X-ray imaging techniques like computed tomography and radiography. These doped materials are particularly useful for bone and dental implants. As a result, it is possible to track implant adhesion and long-term morphological changes at the implant site [16,17]. Doping iron (Fe) successfully into BG is demonstrated by the creation of osteostimulatory materials that have a variety of advantages. By increasing osteoblast proliferation, boosting calcification, and having the ability to create apatite, these materials have shown to improve bone metabolism [18–20]. Importantly, Fe compounds especially in its oxide state (Fe<sub>2</sub>O<sub>3</sub>) have demonstrated notable anticancer action. These substances are also known to start chemical processes, such as the Fenton's reaction, which eventually cause tumour cells to die. All the materials are mostly synthesized by sol-gel method using organic solvents [21].

The bio-inspired method at ambient conditions was developed by taking inspiration from naturally occurring nanostructured materials like silica found in diatoms [22–24]. The selected bio-inspired approach utilizes an aqueous-based methodology. Importantly, the methodology follows simple, cost-effective, and environmentally friendly steps, while also ensuring oversight for calcination [22,23]. Presently, hybrid materials are also produced using this technique [24]. 45S5 BG based PTAs have never been developed earlier. In this study, we attempted first time to synthesize a novel Bi and Fe co-doped mesoporous 45S5 BG as PTA using folic acid (FA) as a template through bio-inspired approach. The use of therapeutic FA template in BG synthesis can help in the targeted delivery of anti-cancer drugs to the cancer site, as cancer cells are rich in folate receptors [25]. Bi and Fe are co-doped in 45S5 BG composition (B\_F\_FABG) for a combination of photothermal effect due to Bi and magnetic effect due to Fe. Such a combinational effect of both the doped metals can be used in various biomedical applications.

The novelty of our study on sample B\_F\_FABG is to display an intriguing combination of capabilities. The multifunction of the material includes mesoporosity, bioactivity for apatite mineralization in addition to photothermal activity and magnetic property. The elemental analysis of folic acid templated bioactive glass (FABG), Fe doped folic acid templated bioactive glass (F\_FABG), Bi doped folic acid templated bioactive glass (B\_FABG) and Bi as well as Fe co-doped folic acid templated bioactive glass (B\_F\_FABG) BG nanoparticles (NPs) was performed using X-ray photoelectron spectroscopy (XPS) followed by other characterizations like XRD, FTIR, TGA, FE-SEM, TEM, NMR, BET. In addition, magnetic property and photothermal property of BG are tested using Vibrating Sample Magnetometer (VSM) and photoluminescence (PL) respectively. *Invitro* bone binding ability (bioactivity), and *in-vitro* hemolysis assay to test biocompatability of the materials were also carried out. A thorough comparative analysis of the characteristic properties of B\_F\_FABG was carried out with FABG, F\_FABG and B\_FABG to draw the importance of B F FABG.

#### 3.2 Experimental Section

#### *3.2.1* Materials:

All the precursors used for synthesis of BG, such as tetraethyl orthosilicate (TEOS) (CAS No. 78-10-4), triethyl phosphate (TEP) (CAS No. 78-40-0), sodium acetate (NaAc) (CAS No. 127-09-3), and calcium acetate (CaAc) (CAS No. 114460-21-8), were purchased from Sigma-Aldrich. Additionally, Folic Acid (FA) (CAS No. 59-30-3), Ferric Chloride Hexahydrate (FeCl<sub>3</sub>.6H<sub>2</sub>O) (CAS No. 10025-77-1), Bismuth Nitrate Pentahydrate (Bi(NO<sub>3</sub>)<sub>3</sub>.5H<sub>2</sub>O) (CAS No. 10035-06-0), Hank's Balanced Salt solution (HBSS), which is also known as simulated bodily fluid (SBF) is supplied by Sigma Aldrich. The highest purity analytical reagent (AR) grade was used for all other chemicals used. All experiments were conducted with Milli-Q water. Unless otherwise specified, all experiments were carried out at room temperature.

# 3.2.2 Bio-inspired Synthesis of FABG NPs doped with metals:

The BG NPs synthesis protocol was followed exactly, with very few modifications [26]. The template FA (1 mg/ml) was first dissolved in 100 ml of trizma buffer with a pH of 8 (10 mM). On the digital magnetic stirrer, the solution was continuously stirred at 500 rpm for 20 min at room temperature. After an interval of 30 min, the BG precursors were then introduced in order, starting with TEOS (9.29 g). TEP (1 g), NaAc (6.36 g), and CaAc (4.21 g) were then added sequentially each at a gap of 30 min as per the mentioned procedure. For synthesis of F\_FABG, B\_FABG and B\_F\_FABG, Ferric Chloride Hexahydrate (FeCl<sub>3</sub>.6H<sub>2</sub>O), Bismuth Nitrate Pentahydrate (Bi(NO<sub>3</sub>)<sub>3</sub>.5H<sub>2</sub>O) and both FeCl<sub>3</sub>.6H<sub>2</sub>O, Bi(NO<sub>3</sub>)<sub>3</sub>.5H<sub>2</sub>O respectively were added after 30 min of adding last precursor CaAc. The solution was continually agitated for 30 min, and then it was left to incubate for 24 h in a silicone

oil bath. The obtained solution was centrifuged at room temperature at 13000 rpm to obtain the precipitate, which was then cleaned, dried in an air oven at 40 °C for 48 h, and stored in a desiccator.

# 3.3 Characterization of FABG, F\_FABG, B\_FABG and B F FABG NPs:

#### 3.3.1 X-ray photoelectron spectroscopy (XPS):

XPS measurements were performed in an Ultra-high Vacuum (UHV) chamber using a non-monochromatized Al K X-ray source and a home-made hemispherical electron energy analyser (ESA-31). The angle between the direction of the photon beam and the axis of the analyser was  $70^{\circ}$ . Photoelectrons were gathered in a plane parallel to the surface. The survey spectra were acquired using the fixed retarding ratio (FRR) mode, with a retarding ratio of k = 4 for the survey spectra and k = 8 for the energy zones of interest. The measurement control and data collection programme was created using C++. Conductive double-sided adhesive tape (3M-9713-Cu) was used to mount the samples on the sample holder.

# 3.3.2 X-ray diffraction (XRD) analysis:

Using a Panalytical X'Pert Pro Diffractometer that ran at 45 kV and 40 mA current with Cu-K $\alpha$  radiations as the source of X-rays, the prepared NPs were subjected to XRD analysis. With an extremely slow scan rate of 0.2  $^{o}$ /min and a slow scan speed of 5 $^{o}$  to 90 $^{o}$ , it captured the spectrum in the 2 $\theta$  range.

#### 3.3.3 Fourier transform infrared spectroscopy (FTIR):

All samples, including FABG, F\_FABG, B\_FABG and B\_F\_FABG NPs, were captured using the spectrophotometer's ATR-FTIR mode. The FTIR spectra of the synthesized material were assessed using the Perkin Elmer (Model Spectrum 2) spectrometer, which has a resolution of 1 cm<sup>-1</sup> and operates in the 400 cm<sup>-1</sup> to 4000 cm<sup>-1</sup> range.

#### 3.3.4 Thermogravimetric (TGA) analysis:

The Perkin Elmer thermogravimetric analyzer (Model TGA 4000) was used to perform the TGA analysis on the samples. The thermal stability of the sample was tested by heating the magnetic samples to temperatures ranging from 0 °C to 800 °C in a nitrogen environment at a heating rate of 10 °C/min and nitrogen gas flow of 50 ml/min.

# 3.3.5 <sup>29</sup>Si solid state nuclear magnetic resonance (NMR):

Using <sup>29</sup>Si solid state NMR, the atomic level silicate structure has been elucidated on doping with various transition metal ions and insight into the Q<sup>n</sup> species distribution of BG was gained. A 9.4 T ECX-II Jeol 400 MHz FT-NMR spectrometer was used in an experiment using magic-angle spinning (MAS) NMR, which operates at a frequency of 79.5 MHz.

# 3.3.6 Morphological studies

#### 3.3.6.1. Field emission scanning electron microscopy (FE-SEM):

The morphology of the NPs was investigated using a scanning electron microscope (ZESIS EVO MA15). Gold-coated FABG, F\_FABG, B\_FABG, and B\_F\_FABG NPs were seen under SEM at 10,000 times the normal magnification and an accelerating voltage of 5.0 kV.

#### 3.3.6.2. High resolution transmission electron microscopy (HR-TEM):

A high-resolution Transmission Electron Microscope (HR-TEM) model (TALOS S) from Thermo Scientific in the United States, which runs at an accelerating voltage of 200 kV, was used to measure the sizes of FABG, F\_FABG and B\_F\_FABG NPs. The 64-bit Java 1.8.0 172 ImageJ program was used for the TEM analysis.

#### 3.3.7 Nitrogen sorption analysis:

Before analysis, the material was degassed for 2 h at 200 °C in a vacuum. Nitrogen was utilised as the adsorptive gas (N<sub>2</sub>, cross-sectional area 0.162 nm<sup>2</sup>) in the nitrogen adsorption-desorption analysis, which was performed using a Microtrac BEL (Model BELSORP-max), Japan, at -196 °C. In this investigation, the porosity of FABG, F\_FABG, B\_FABG and B\_F\_FABG NPs was determined. The Brunauer-Emmett-Teller (BET) equation was used to determine the surface area of the nitrogen adsorption data. The Barret-Joyner-Halenda (BJH) method was applied to examine the distribution of pore sizes in the desorption part of the isotherm.

#### 3.3.8 Magnetic measurement:

The vibrating sample magnetometer (VSM) instrument (Microsense, Model ADE - EV9) was used to plot the magnetic hysteresis or M-H magnetization curve for FABG, F\_FABG, B\_FABG and B\_F\_FABG NPs at ambient temperature. Up to 2.2 Tesla of magnetic field was observed. Magneto resistance was kept between 1  $\Omega$  and 10,000  $\Omega$  according to the Field resolution of 0.001 Oe and sensitivity of 0.00005 emu.

#### 3.3.9 Bioactivity test:

The procedure described by [20] depicted the development of a hydroxylapatite (HAp) layer on the surface of BG. The technique entailed assessing the *in-vitro* bioactivity of FABG, F\_FABG, B\_FABG and B\_F\_FABG NPs. The samples were immersed in SBF at a concentration of 1 mg/ml and incubated at 37 °C under sterile conditions for 4 d, 7 d, 15 d, and 30 d. In order to maintain the concentration of ions in the solution and to facilitate the formation of the HAp layer, the SBF solution was changed every 4 d. The sample was then centrifuged, dried at 48 °C in air oven, and maintained in desiccator for further characterizations, such as XRD, FTIR, SEM and magnetic measurements, once the necessary time period passed.

#### 3.3.10 Photoluminescence study (PL):

A Xenon lamp was used as the source of excitation for the Time Resolved PL (TR-PL) spectral recordings, which were conducted using an Edinburgh FLSP 900 Spectro fluorophotometer with a spectral resolution of 0.1 nm. The characterization was done at room temperature.

#### 3.3.11 In-vitro hemolysis assay:

When using human blood, a few minor adjustments were performed to the experimental procedure for the *in-vitro* hemolysis assay [27]. PBS buffer was made in distilled water that was initially autoclaved. Human blood was extracted (0.5 ml), centrifuged for 5 min at 4 °C with an RCF of 500\*g, and the plasma as supernatant was discharged in surfactant. During that time, 1 mg of FABG, F FABG, B FABG and B F FABG NPs were sonicated in 1 ml of autoclaved distilled water to get the necessary stock solution of 1 mg/ml. The different concentrations (from 1 mg/ml stock solution): 1 μg/ml, 5 μg/ml, 10 μg/ml, 25 μg/ml, 50 μg/ml were prepared. After removing the plasma, the blood was correctly mixed in micro-centrifuge tubes and washed twice with 500 µl and 1000 µl of PBS, respectively. The mixture was adequately centrifuged, and the supernatant was removed with caution so as not to disturb the red blood cells. Up till a clear supernatant was obtained, washing was performed. Once clear supernatant had been collected, it was discarded. Red human blood was then added to five micro-centrifuge tubes at concentrations of 1 µg/ml, 5 µg/ml, 10 µg/ml, 25 µg/ml, 50 μg/ml. One microcentrifuge tube containing 1 ml of PBS in red human blood was termed as a negative control, and a seventh microcentrifuge tube containing blood was assigned as a positive control on adding 950 ml of PBS and 50 ml of Triton X-100 (until a transparent solution was noticed). For various incubation times of 0 h, 1 h, 2 h, and 24 h, absorbance at 570 nm and the absorption spectrum from 300 nm to 800 nm were determined. Additionally, 2 h of fluorescent microscope imaging were also recorded. The following equation was used to calculate the percentage hemolysis rate:

% Hemolysis = 
$$\left[\frac{A_t - A_c}{A_{100\%} - A_c}\right] \times 100$$

Where, A<sub>c</sub> is the absorbance of the supernatant from the negative control (PBS), and A<sub>100%</sub> is the absorbance of the supernatant from the positive control (Triton X 100), A<sub>t</sub> is the absorbance of the supernatant of samples incubated with the particles. Experiments were run in triplicate, and an error analysis was conducted. In our research, hemolysis of less than 5% was regarded as nontoxic. This value is consistent with ASTM 75633 [28] and has been reported in several sources [27].

#### 3.4 Results and Discussions

#### 3.4.1 X-ray photoelectron spectroscopy (XPS):

The XPS survey spectra of BG depicted the presence of Si 2p (~103 eV), Ca 2p (~347 eV), C 1s (~284 eV), P 2p (~133 eV), Na 1s (~1071 eV) and O 1s (~531 eV) as shown in Fig. 1(a-d). Doped samples showed peaks corresponding to Fe 2p (~709 eV) in F\_FABG, Bi 4f (~156 eV) in B\_FABG and Fe 2p (~712 eV) as well as Bi 4f (~160 eV) in B\_F\_FABG respectively (Fig. 1(a-d)). As illustrated in Fig. S1(a-d), high resolution XPS spectra of Si 2p, Ca 2p, C 1s, P 2p, Na 1s, O 1s, Fe 2p and Bi 4f were gathered to determine the chemical status of the corresponding elements as depicted in Table I. The experiments were performed with the VGESCALAB II system using AlKα radiation. The Si 2p peak around ~103 eV and Ca 2p showed Ca 2p<sub>1/2</sub> and Ca 2p<sub>3/2</sub> peaks around ~347.0 eV and ~350 eV respectively in all the samples. The observations confirmed the existence of Si and Ca species in all BG and are in good agreement with Barrioni *et al.* [29].

Fe peaks were reported in both F\_FABG (Fig. S1b) and B\_F\_FABG samples (Fig. S1d). Noticeably, two peaks can be seen at 727.8 eV and 711.8 eV, that were associated with characteristic signal of Fe 2p<sub>1/2</sub> and 2p<sub>3/2</sub> in B\_F\_FABG (Fig. S1d) respectively. While a single peak located at 723.1 eV can be associated with Fe 2p<sub>1/2</sub> in F\_FABG (Fig. S1b) [30]. The broad peak at 737.4 eV in F\_FABG is attributed to satellite peak of Fe. The observed Fe 2p signals in F\_FABG and B\_F\_FABG indicated the existence of dopant Fe. The peaks of Bi 4f around ~158.5 eV and ~164 eV XPS exclusively

depicted the presence of Bi in B\_FABG and B\_F\_FABG [31]. In general, a shift in the XPS peaks to higher or lower binding energies compared to the control (Fig. S1a) confirmed the presence of dopant moieties and their participation in the BG network. O 1s signals were reported at 532.1 eV in FABG, 531.3 eV in F\_FABG, 532.3 eV in B\_FABG and 531.5 eV in B\_F\_FABG and are assigned to oxygen atoms in phosphates, hydroxyl and adsorbed water. The peak at 530.0 eV in B\_FABG is attributed to metal oxides present in the compound. The peak around ~1071 eV is associated with Na 1s in FABG, F\_FABG, B\_FABG and B\_F\_FABG. The P 2p peak was at 134.9 eV, 133.9 eV, 133.2 eV and 132.0 eV for FABG, F\_FABG, B\_FABG and B\_F\_FABG respectively. The observation corresponded to characteristic of phosphate moieties in BG network [32]. For all BG peaks appeared around ~284.4 eV and around ~288 eV are attributed to the C – C bond in C 1s that might have derived from FA template. Hence, XPS studies confirmed the presence of dopants Fe in F\_FABG and B\_F\_FABG while Bi in B\_FABG and B\_F\_FABG in comparison to control FABG.

**Table 3.1:** Binding energy (eV) of FABG, F\_FABG, B\_FABG and B\_F\_FABG by XPS analysis.

	XPS				
Various	Binding energy (eV)				
Elements	FABG	F_FABG	B_FABG	B_F_FABG	
Na (1s)	1071.1	1071.3	1071.4	-	
O (1s)	532.1	531.3	530.0, 532.3	531.5	
Ca (2p)	346.8, 350.4	347.0, 350.6	346.7, 350.6	347.2, 351.1	
C (1s)	284.4, 287.2	284.4, 288.0	284.4, 287.3	284.3	
P (2p)	134.9	133.9	133.2	132.0	
Si (2p)	103.0	102.2	103.0	102.3	
Fe (2p)	-	723.1, 737.4	-	711.7, 728.0	
Bi (4f)	-	-	158.5, 163.9	158.7, 164.0	

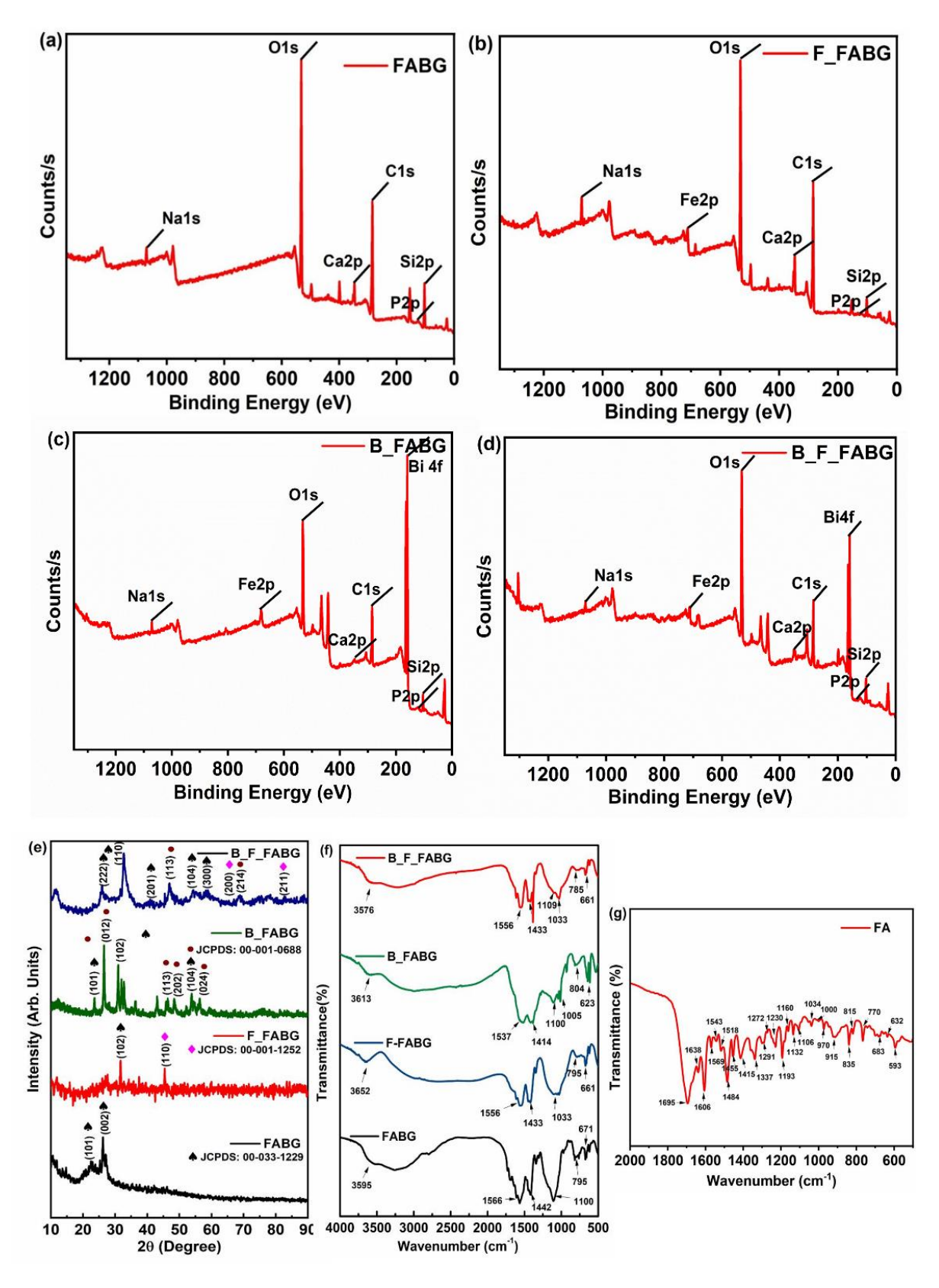


**Fig. 3.1:** (a-d) XPS survey spectra of FABG, F\_FABG, B\_FABG and B\_F\_FABG, (e) XRD patterns of FABG, F\_FABG, B\_FABG and B\_F\_FABG, (f) FTIR spectrum of FABG, F\_FABG, B\_FABG and B F FABG and (g) FTIR spectrum of FA.

#### 3.4.2 X-ray diffraction (XRD) analysis:

The XRD patterns of FABG, F\_FABG, B\_FABG, B\_FABG are depicted in Fig. 1e. Comparing the doped BG samples to the FABG, it is interesting to note that phase change was seen after the incorporation of Bi and Fe metal ions (Fig. 1e). When sodium calcium phosphate silicate (Ca0.89Na0.11O3P0.11Si0.89) was present in FABG, typical reflections (JCPDS 00-033-1229 at 2θ values of 22.2° (101), 26.1° (002) were seen. These reflections of BG are common in all the prepared samples, F\_FABG (at 2θ values of 31.7° (102)), B\_FABG (at 2θ values of 23.3° (101), 30.8° (102), 53.9° (104)) and B\_F\_FABG (at 2θ values of 25.9° (222), 40.9° (201), 54.1° (104), 58.7° (300)). The XRD pattern for F\_FABG (Fig. 1e) revealed that the material was in an amorphous form and presence of Fe species was seen corresponding to JCPDS 00-001-1252 at 2θ value of 45.6° (110). Similarly, for B\_F\_FABG, Fe species is reported according to JCPDS 00-001-1252 at 2θ values of 65.0° (200), 83.5° (211) [18].

The increase in the characteristic diffraction peak intensities in B\_FABG (JCPDS 00-001-0688 at 2θ values of 26.60 (012), 46.20 (113), 48.30 (202), and 56.20 (024)) indicated the inclusion of Bi species with increased crystallinity [33,34]. Similarly, XRD pattern of B\_F\_FABG with 2θ values of 47.20 (113) and 68.70 (214) confirmed the incorporation of Bi species in B\_F\_FABG sample [30, 31]. The observation of XRD analysis is in good agreement with XPS data (Fig. 1)

The Debye-Scherrer formula, which is  $(D = k\lambda / \beta cos\theta)$  where K is the constant,  $\lambda$  is the X-ray wavelength,  $\beta$  is the peak width of the half-maximum of the diffraction peak, and  $\theta$  is the X-ray diffraction angle, can be used to quantitatively determine the mean crystallite size which was found to be  $0.1 \pm 0.04$  nm for FABG,  $0.2 \pm 0.03$  nm for F\_FABG,  $0.3 \pm 0.01$  nm for B\_FABG and  $0.2 \pm 0.04$  nm for B\_F\_FABG by the XRD patterns. The results shown here are the average of triplicates performed.

Hence, XPS and XRD results depicted the presence of trace amount of Fe in F\_FABG, B\_F\_FABG and Bi in B FABG, B F FABG.

#### 3.4.3 Fourier transform infrared spectroscopy (FTIR):

An FTIR spectrum of FA is depicted in Fig. 1g from 2000 cm<sup>-1</sup> to 400 cm<sup>-1</sup> wavelength region. The characteristic IR absorption peaks of native FA were seen at 1606 cm<sup>-1</sup> because of the amide I (N-H bending), 1697 cm<sup>-1</sup> due to amide II (C=O stretching), and 1484 cm<sup>-1</sup> due to the absorption band of phenyl ring, respectively [35].

Fig. 1f depicted FTIR spectra of FABG, B\_FABG, F\_FABG and B\_F\_FABG. The existence of characteristic FA peaks (amide I and amide II) in FABG and doped BG informed the presence of template FA in BG. A huge shift in amide II peak towards lower wavenumber that is 1566 cm<sup>-1</sup> in FABG, 1556 cm<sup>-1</sup> in F\_FABG, 1537 cm<sup>-1</sup> in B\_FABG and 1556 cm<sup>-1</sup> in B\_F\_FABG are reported compared to native FA molecule (1697 cm<sup>-1</sup>). It might be due to -C=O group interactions with dopants/BG network (Fig. 1f) as reported earlier [22,36]. Apart from this, —COO symmetrical stretching vibration of native FA at 1415 cm<sup>-1</sup> is also reported in FABG at 1442 cm<sup>-1</sup> and doped BG around 1433 cm<sup>-1</sup> with significant shift towards higher wavenumbers. The observation confirmed the chemical interaction of —COO group of FA with dopants/BG network [37]. All the other peaks of FA at about 3500 cm<sup>-1</sup>, which is caused by O-H/N-H stretching vibrations was also reported in BG. These observations confirmed the existence of FA molecules in BG. Importantly, peaks corresponds to the silicate network at 1100 cm<sup>-1</sup> (Si-O-, Si-O-C. Si-O-Si\_bonds) and 795 cm<sup>-1</sup> (typical silicate network ring structures) were observed for all BG, confirming successful formation of the BG network [22].

Interestingly, in addition to silicate network peak at 1100 cm<sup>-1</sup>, an additional peak around 1061 cm<sup>-1</sup> and 1033 cm<sup>-1</sup> were found for F\_FABG and B\_F\_FABG respectively compared to FABG. The finding confirmed the rearrangement of silicate network due to doped metal ions (M), which might lead to

form Si–O–M bond [32, 33]. In the case of B\_FABG the additional peak was at 1006 cm<sup>-1</sup>, which appeared at much lower wave number compared to other doped BG indicating existence of the highly polarizable the largest Bi ions in the silicate network.

FTIR results were in good agreement with XPS and XRD data that proved silicate network formation along with FA molecules in FABG. In doped BG, metal ions are evidenced into the BG network. along with the existence of FA template.

### 3.4.4 Thermogravimetric (TGA) analysis:

Fig. 2(a-b) depicted TGA thermograms of FA, FABG and doped FABG. Initial weight loss of FABG was 10.5 w/w% in the temperature range from 50.3 °C to 276.4 °C due to evaporation of sorbed water molecules. Thereafter, from 276.4 °C to 677 °C, 45.6 w/w% weigh loss of FABG was reported. The observed weight loss pattern is in good agreement with FA thermogram. In temperature range of 213.7 °C to 600 °C a steep increase in weight loss was observed for native FA, whereas weight loss of FA content of FABG was reported at slightly higher temperature range from 276.4 °C to 600 °C. The observation can be corroborated to the interaction between FA molecules and the BG network and is in good agreement with XRD and FTIR results (Fig. 1e and Fig. 1 (f-g)). Thermograms of F FABG and B F FABG were also showed majorly two steps of degradation but elevated stability of the material from the temperature range 430 °C to 850 °C. The observation indicated existence of FA content in lesser amount in F\_FABG and B\_F\_FABG compared to FABG. Interestingly, thermogram of B FABG was reported with single step degradation with the highest stability in the temperature range 430 °C to 850 °C. The residual weight of various BG was reported in the order FABG (56.5 w/w%) < F FABG (32.2 w/w%)  $\approx$  B F FABG (28.8 w/w%) < B FABG (19.8 w/w%). The observation evidenced existence of FA content in BG network depending on the dopants. The heaviest and highly polarizable Bi ions showed greater affinity towards BG network compared to Fe ions and FA molecules and in corroboration with FTIR and XRD findings (Fig. 1(e-g)).

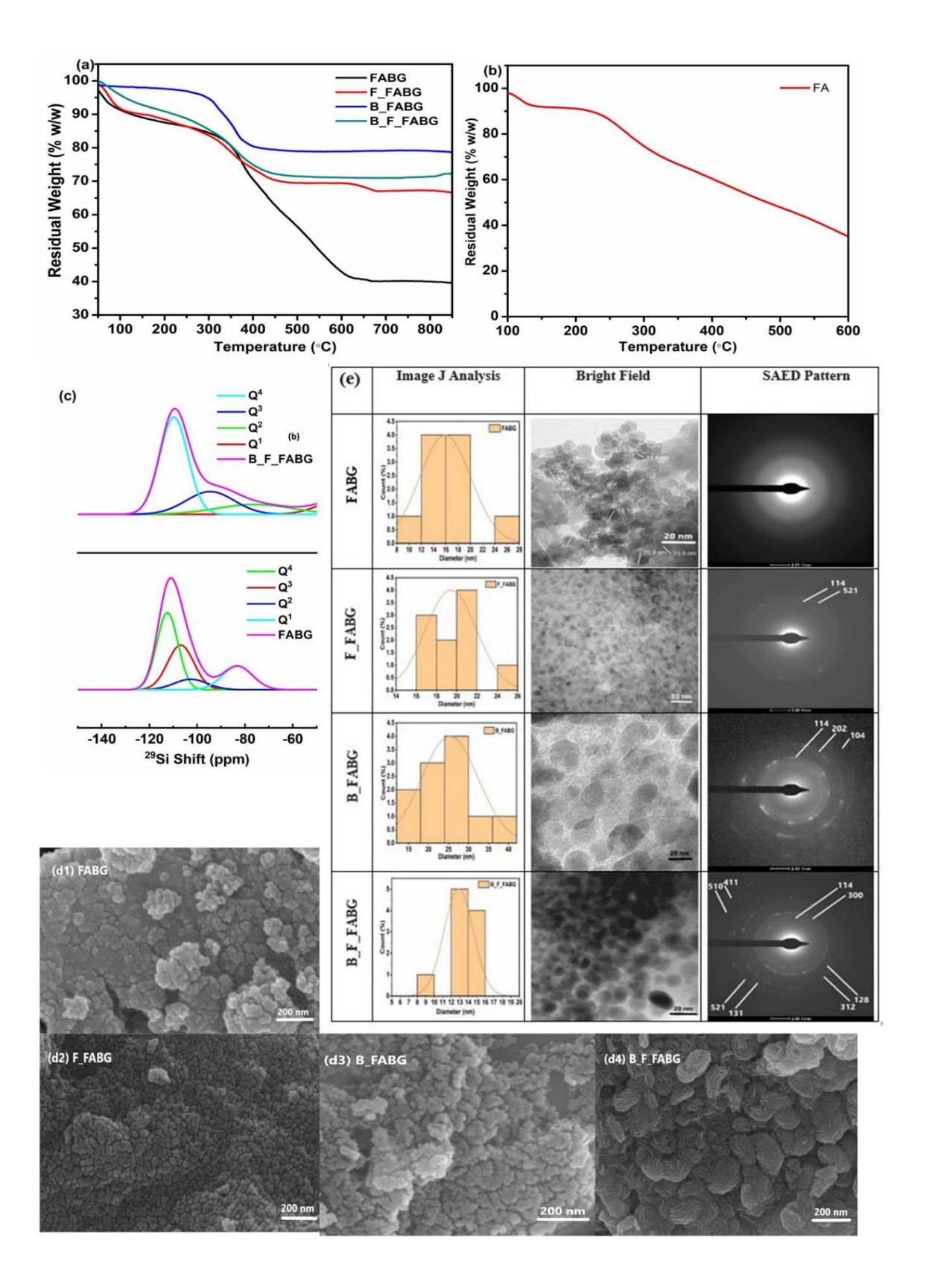


**Fig. 3.2:** (a) Thermogravimetric analysis of FABG, F\_FABG, B\_FABG and B\_F\_FABG, (b) Thermogravimetric analysis of FA, (c) NMR spectrum of FABG, F\_FABG, B\_FABG and B\_F\_FABG, (d) FE-SEM micrographs of FABG, F\_FABG, B\_FABG and B\_F\_FABG, (e) Image J Analysis for particle size, HR-TEM micrographs in bright field and SAED pattern of FABG, F FABG, B FABG and B F FABG.

# 3.4.5 <sup>29</sup>Si solid state nuclear magnetic resonance (NMR):

The structure of silicate glasses can be determined using <sup>29</sup>Si-NMR, which provides in-depth knowledge of the connectivity and distribution of Q<sup>n</sup> species. As seen in Fig. 2c, Q denotes tetrahedral structural unit and bridging oxygen atoms are referred by n. By analysing the chemical shift produced by a magic angle spinning (MAS) NMR, the presence of different chemical species can be detected in BG. Using <sup>29</sup>Si MAS solid state NMR, it has been possible to understand the doped metal ions Fe and Bi in these glasses with the network modifiers sodium and calcium [39]. As shown in Fig. 2c, Q<sup>4</sup> dominates the glass structure for individual BG samples (FABG and B\_F\_FABG), with Q3, Q2 and Q<sup>1</sup> species following in decreasing order. It is significant to note that each glass sample that underwent gaussian fitting deconvolution displayed an uneven peak. A small shift to a negative value of 2.4 ppm is visible in glasses co-doped with Fe and Bi as compared to the total peak position of the signal associated with Si [40]. The observed shift in the <sup>29</sup>Si signal is most likely the result of a modification to the parent glass structure's network modifier cation. The increase in Q<sup>4</sup> in the glass network, which is neutralised by Bi and Fe<sup>2+</sup>/Fe<sup>3+</sup> ions, together with an increase in Q<sup>3</sup> and Q<sup>2</sup> species for B\_F\_FABG, resulted in the observed alteration [41]. The rise in Q<sup>4</sup> percentage may also be supported by the FTIR spectra (Fig. 3a), in which results demonstrated a broadening of peak at 1033 cm<sup>-1</sup> of the Si-O-Si linkage in the doped sample in comparison to pure BG. When compared to FABG, B F FABG's <sup>29</sup>Si signal's FWHM (full width at half maximum) decreased from 14.87 ppm (-1.03 ppm) to 13.84 ppm. Table 2 lists the Q<sup>n</sup> distribution percentages and resulting network connection (NC). Using equation II,  $NC = \frac{4Q^4 + 3Q^3 + 2Q^2 + 1Q^1}{100}$  was calculated. A repolymerization impact produced by the introduction of dopant metal ions Bi and Fe into the BG network is suggested by the increased network connectivity for the doped glass samples (B F FABG) compared to the pure BG control (FABG), which agrees with the published literature [40].

**Table 3.2:**  $Q^n$  content and chemical shift data ( $\delta$ ) of FABG and B F FABG

Sample	Q <sup>4</sup>	$Q^3$	$Q^2$	Q <sup>1</sup>	NC
	δ(ppm)	δ(ppm)	δ(ppm)	δ(ppm)	
FABG	-112.4	-107.1	-102.6	-83	10.59
B_F_FABG	-110	-94.6	-73.6	-50.2	9.21

**Note:** NC stands for the network connectivity defined as  $NC = \frac{4Q^4 + 3Q^3 + 2Q^2 + 1Q^1}{100}$ . Errors:  $\delta \pm 0.5$  ppm and NC  $\pm 0.05$ .

# 3.4.6 Morphological Studies

#### 3.4.6.1. Field emission scanning electron microscopy (FE-SEM):

SEM analysis to test morphology of the prepared BG has been done. Highly aggregated BG particles with irregular shape of FABG, F\_FABG, B\_FABG, and B\_F\_FABG were visible in corresponding FE-SEM images (Fig. 2d).

#### 3.4.6.2. High resolution transmission electron microscopy (HR-TEM):

The BG were also visualized using HR-TEM (Fig. 2e) and observed to be nanosized as well as aggregated. Additionally, using image J analysis, particle sizes for FABG, F\_FABG, B\_FABG, and B\_F\_FABG were found to be in the range of  $15.9 \pm 0.3$  nm,  $19.4 \pm 0.7$  nm,  $25.3 \pm 0.9$  nm, and  $12.8 \pm 0.3$  nm respectively. It is evident that in comparison to bare BG, BG doped with both Fe and Bi were reduced in the particle size. This may be explained by a greater silica matrix deformation brought on by the inclusion of metal ions [42]. This observation is in good accord with FE-SEM (Fig.

2d). SAED pattern of FABG depicted amorphous nature of the material. For F\_FABG, d- spacing 0.425 Å and 0.380 Å corresponded to (114) and (521) hkl values respectively. Similarly for B\_FABG, d- spacing 2.644 Å, 1.814 Å and 1.322 Å corresponded to (104), (202) and (114) hkl values respectively. B\_F\_FABG has d- spacing 0.68 Å, 0.54 Å, 0.44 Å, 0.38 Å, 0.33 Å, 0.31 Å, 0.27 Å and 0.24 Å corresponded to (411), (510), (521), (131), (312), (128), (300) and (114) hkl values respectively. Some of the hkl values from SAED pattern are in combination with XRD values like (104), (202) in B\_FABG and (300), (114) in B\_F\_FABG. It depicted that F\_FABG, B\_FABG and B\_FABG are nano-crystalline and in good agreement with XRD analysis (Fig. 1e).

# 3.4.7 Nitrogen sorption analysis:

The pore diameter, pore volume, and surface area for all BG are shown in Table III. All doped and undoped BG are determined to be mesoporous as pore diameters lie between 2 nm to 50 nm range. According to the IUPAC classification of adsorption isotherms, the adsorption-desorption isotherm for FABG, F\_FABG, and B\_F\_FABG exhibit a conventional type IV isotherm with an hysteresis loop of H3 type (Fig. 3 (a-d)) [43].

This phenomenon shows that the pore size distribution of all BG NPs, is generally narrow and has slit-like pores [42]. In Fig. 3(a-d), Barrett-Joyner-Halenda (BJH) model displays pore diameter and the pore size of all BG NPs that lies in range of 10 nm to 27 nm. The B\_FABG showed the largest mean pore size and B\_F\_FABG showed largest pore volume compared with the FABG and F\_FABG. The total surface area recorded for F\_FABG is highest which is 86.680 m²/g and slightly less that is 80.621 m²/g for B\_F\_FABG. This is important data about the material's physical composition since the size of a solid's surface influences how that solid will respond to its environment. Numerous characteristics, such as dissolution rates, enzyme activity, retention of humidity, and shelf life, are typically correlated with a substance's surface area. Pore diameter of FABG is 1.699 nm which

increased to 3.412 nm in F\_FABG and 9.680 nm in B\_FABG, indicating participation of dopants in BG network. Interestingly, pore diameter increases with increase in the size of the dopant. On the other hand, in co-doping, we could get the more or less same pore diameter and surface area compared to F\_FABG depicting that Fe ions functions mostly as network former while Bi as both former and modifier [44]. So, above data is in good accord with NMR findings where values of Q<sup>4</sup>, Q<sup>3</sup>, Q<sup>2</sup>, Q<sup>1</sup> for FABG is more than the respective values of B\_F\_FABG.

**Table 3.3:** Surface area, pore volume and pore size data of FABG, F\_FABG and B\_F\_FABG.

	FABG	F_FABG	B_FABG	B_F_FABG
Total Surface Area (a <sub>s,BET</sub> [m <sup>2</sup> g <sup>-1</sup> ])	1.439	86.680	15.218	80.621
Total pore volume( $p/p_0$ =0.944) [cm <sup>3</sup> g <sup>-1</sup> ]	0.003	0.076	0.056	0.065
Mean pore diameter [nm]	1.699	3.412	9.680	3.435

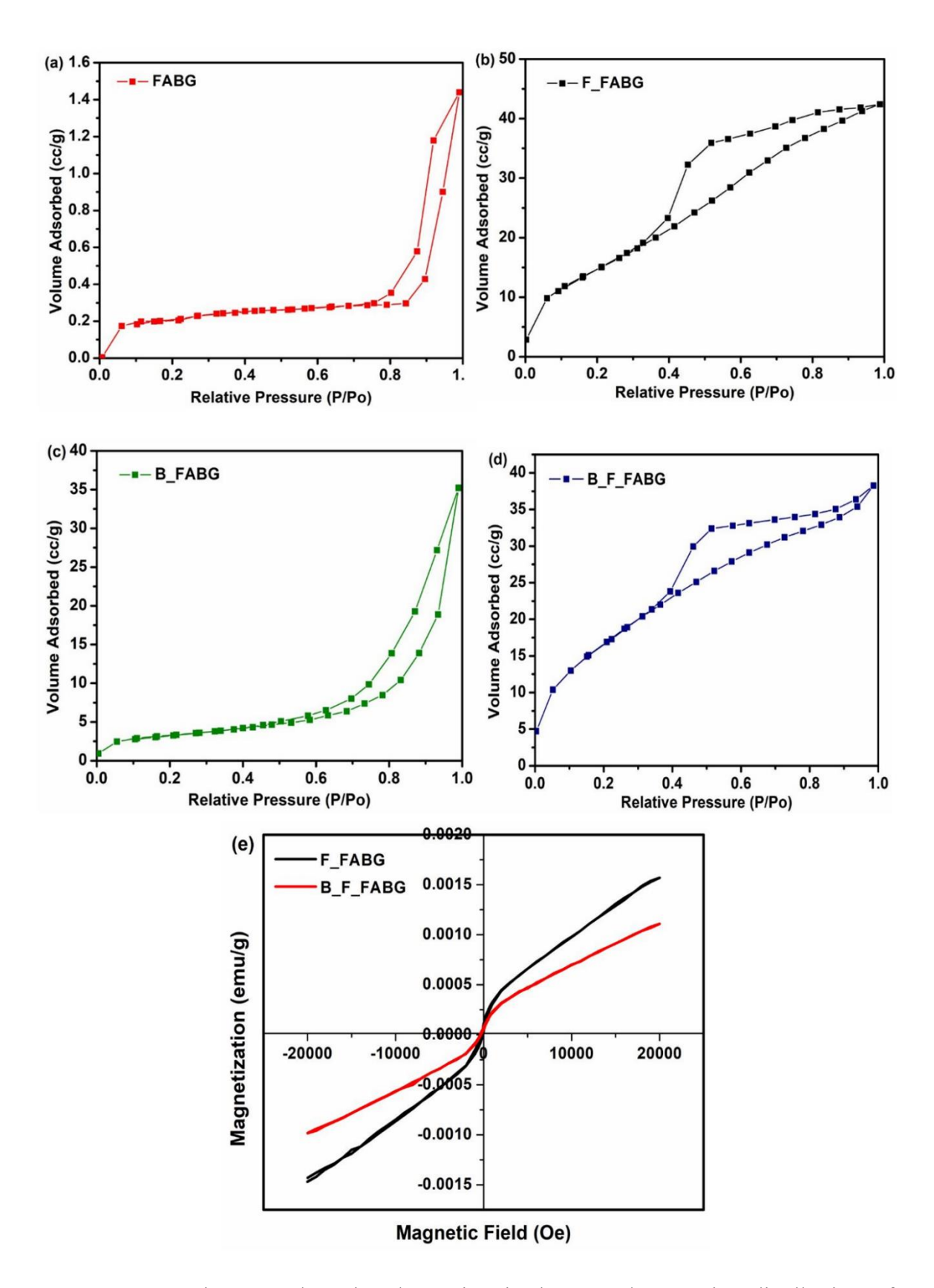


**Fig. 3.3:** (a–d) Nitrogen adsorption-desorption isotherm and pore size distribution of FABG, F\_FABG, B\_FABG and B\_F\_FABG, (e): Magnetization curve of F\_FABG and B\_F\_FABG NPs.

#### 3.4.8 Magnetic measurement:

An essential physical characteristic of materials is magnetism. The saturation magnetization (Ms) of B F FABG (20001.1 Oe) and F FABG (20001 Oe) is achieved significantly at same magnetic field. The hysteresis curve calculated the remanent magnetization (M<sub>r</sub>) values for F FABG and B F FABG, which are found to be 0.0002 emu/g and 0.0001 emu/g, respectively. After doping BG with Fe in F FABG and Bi, Fe in B F FABG, the saturation magnetization of both materials was found to have increased to 0.001 emu/g (Fig. 3e). Due to its deformed silica network, the obtained pure FABG sample demonstrated diamagnetic nature. Due to the inherent ferromagnetism of Fe, it is doped with 2% (wt.) Fe in FABG and 2% (wt.) each with Bi, Fe in B F FABG, which reduced the diamagnetism of both samples. When placed in an external magnetic field, F FABG and B F FABG exhibited some magnetic effects compared to FABG due to the decrease in diamagnetism. The F FABG and B FABG samples' crystallinity, as opposed to FABG, which is wholly amorphous in nature, justifies the high magnetizations [45]. It is important to note that XRD and TEM data have already confirmed the crystalline nature of both the samples. The results mentioned above support the inclusion of magnetic characteristics in BG NPs. In contrast to F FABG, B F FABG is a soft magnetic material with a low remanence; as a result, it has a reduced coercivity, the potential to shift polarity frequently, and relatively low electrical losses. Due to its magnetic effect, the material created with Fe and Bi doping is thus also suitable for biomedical applications [46].

**Table 3.4:** Saturation and Remanent Magnetization of F FABG and B F FABG NPs

	Saturation Magnetization (M <sub>s</sub> )	Remanent Magnetization (M <sub>r</sub> )	
	(emu/g)	(emu/g)	
F_FABG	0.0015	0.0002	
B_F_FABG	0.0011	0.0001	

#### 3.4.9 Bioactivity test:

The inclusion of network formers and modifiers like Fe and Bi metal ions disturbs the BG network consistency [47]. Unbridged oxygen groups are connected to Si–O bonds because of breaking of some of the silicate bonds. To stimulate the synthesis at the glass surface of silanol groups, the quantity of silicon oxygen bonds bounded to unbridged oxygen groups regulates the pace of silica dissolution. When exposed to bodily fluids, the biological reaction is directed towards the interface of the BG material.

The structure, material composition, and ions contained in the BG have a significant impact on its chemical susceptibility (i.e., physiological fluid dissolution) [48]. Protein-protein interactions and bioactivity are subsequently impacted by this. Additionally assessed was the material's bioactivity, or its capacity to produce HAp when in contact with biological fluid. According to Kokubo et al. [49], bioactivity was assessed in the current study using simulated bodily fluid (SBF). The doped bioactive glass samples were submerged in SBF from 4 d to 30 d before being examined for the development of a HAp layer using XRD, FTIR, SEM, and VSM.

According to the JCPDS file number 00-024-0033, the observed reflections in the matching XRD pattern pertained to (Ca<sub>5</sub>(PO<sub>4</sub>)<sub>3</sub>(OH). Interesting reflections at 2θ values between 20° and 60° corresponding to the production of HAp was found in the XRD data of the SBF treated doped and undoped samples (Fig. 4(a-d)). After contact with SBF, a small number of new diffraction maxima with modestly increasing intensities from 4 d to 30 d developed for all of the samples. Furthermore, FTIR spectra depicted the existence of distinctive phosphate and carbonate vibration modes (Fig. 4(e-h)) of doped samples when undergone bioactivity from 4 d to 30 d that supported the production of HAp. For the deposited samples, a peak about 1633 cm<sup>-1</sup> that is attributed to the hydroxyl group was seen. Additionally, from 4 d to 30 d, the peaks ranging from 1300 cm<sup>-1</sup> to 1720 cm<sup>-1</sup> signifies carbonate peaks and peaks at 900 cm<sup>-1</sup> signifies phosphate peaks, were noticed to have gradually

emerged. Additionally, it is interesting to note how the intensity of the identifiable silicate network peak at 795 cm<sup>-1</sup> fell to a hardly noticeable level from FABG to other doped samples. It demonstrated that, in line with Hench's proposed bioactivity process, ions dissolve on the doped BG surface, enhancing the conversion of silicate to silanol groups. The production of HAp is interestingly indicated by the presence of phosphate, hydroxyl, and carbonate groups simultaneously.

FE-SEM micrographs showed the contact with SBF, bone-like HAp microcrystals formed on the surface of the BG NPs. The micrographs of BG NPs (Fig. 5(a-d)) revealed a significantly bare surface morphology after 15 d of interaction with SBF and because of the HAp deposition. It is intriguing that in comparison to control, other doped samples showed thick layer of HAp deposition from 4 d to 30 d. The key factor contributing to the quick HAp deposition in the doped BG samples, was mesoporosity in general.

The VSM measurement for bioactivity of F\_FABG and B\_F\_FABG NPs from 4 d to 30 d indicated a hysteresis curve of magnetization with the magnetic field, as depicted in Fig. 5(e-f). It clearly showed that saturation magnetization (M<sub>s</sub>) is increasing from 4 d to 30 d while remanent magnetization shows slight change with increasing days of bioactivity. This showed that ability of magnetization is maximum when deposition of HAp is maximum.

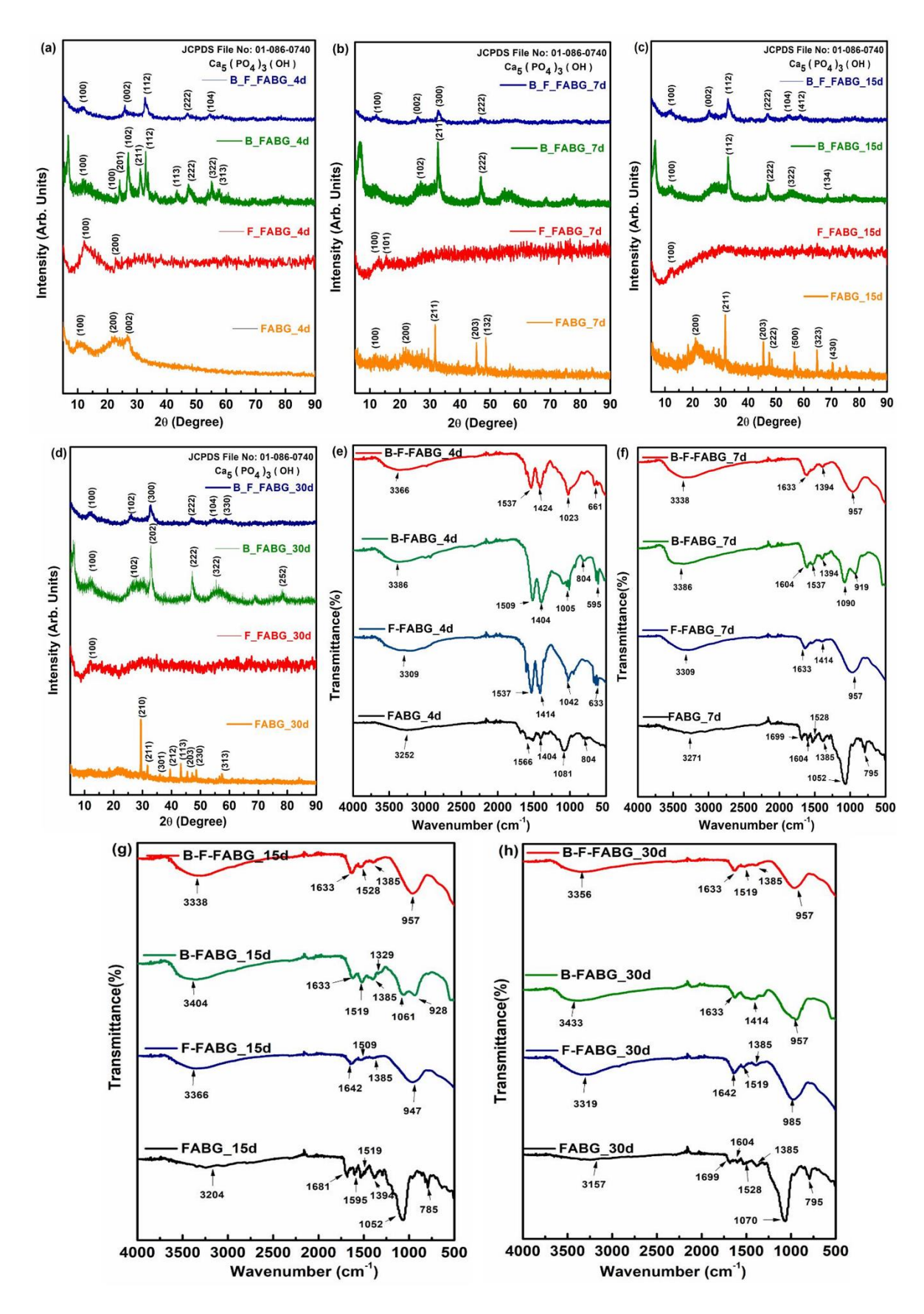


**Fig. 3.4: (a-d)** XRD patterns and **(e-h)** FTIR spectra of FABG, F\_FABG and B\_F\_FABG after 4 d, 7 d, 15 d and 30 d of bioactivity in SBF solution.

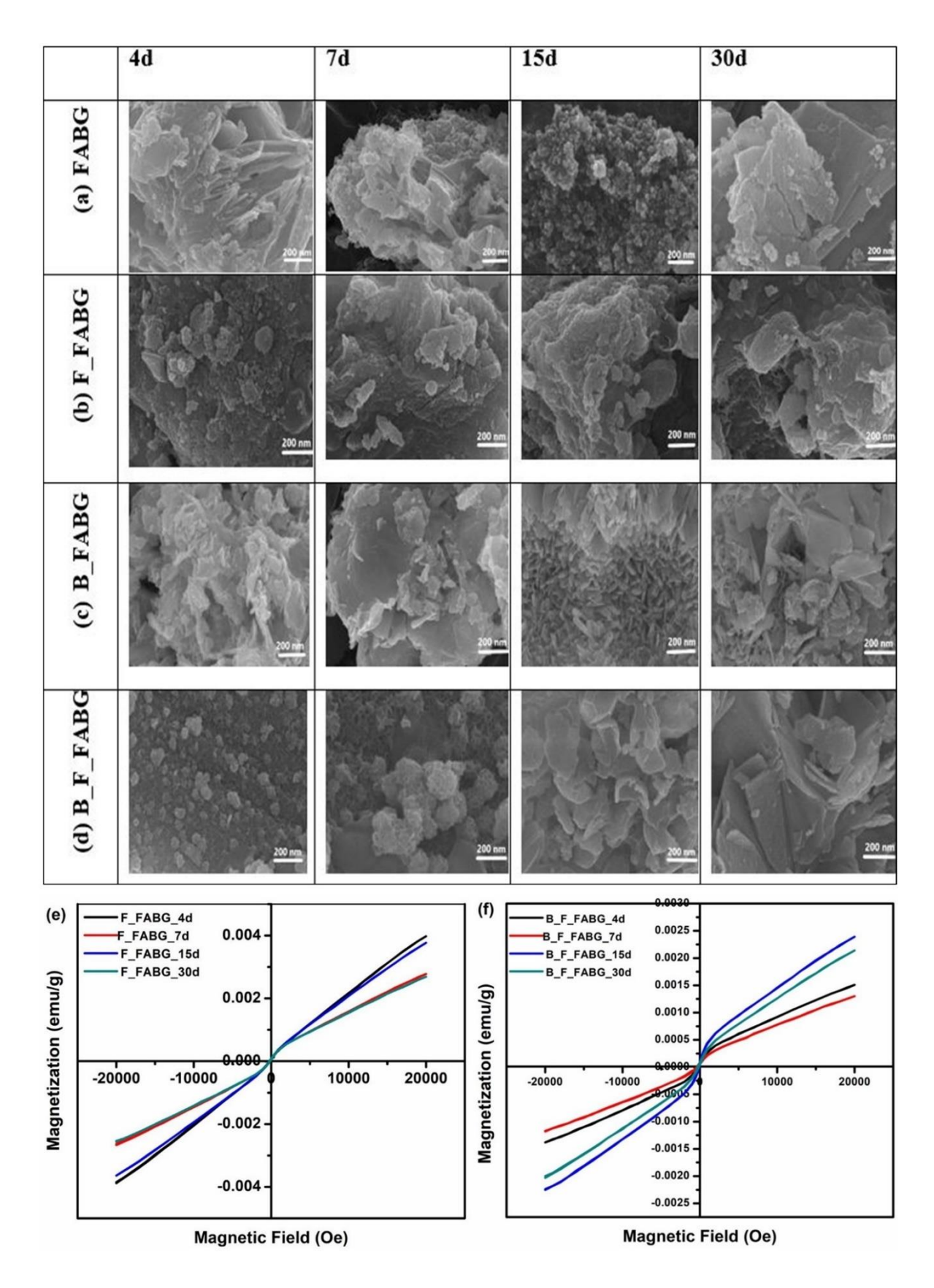


**Fig. 3.5:** (a-d) FE-SEM micrographs of FABG, F\_FABG and B\_F\_FABG and Ge-f) Magnetization Curve of F\_FABG and B\_F\_FABG after 4 d, 7 d, 15 d and 30 d of bioactivity in SBF solution.

#### 3.4.10 Photoluminescence study (PL):

The phenomenon known as PL occurs when a substance emits light after absorbing photons. The host glass matrix of BG NPs often contains an array of ions. During the synthesis process, the glass structure is doped with  $Bi^{3+}$  and  $Fe^{+2}/Fe^{+3}$  ions. The exact glass composition and doping concentration are key factors in influencing the PL properties [50].

The NIR absorption peak absorbed around 600 nm is seen in the usual materials for PT therapy applications in order to achieve optimum luminescence of the converter species and perfect radiation transmission into the tissue [50].

Bi-doped 45S5 BG NPs require an excitation wavelength in the ultraviolet (UV) or visible light range to cause photoluminescence. Typically, the emission peak occurs between the wavelengths of 250 nm and 550 nm (Fig. 6a) [51]. Numerous variables, including the glass composition, the doping level, and the experimental apparatus, might affect the precise excitation wavelength. In contrast to the undoped sample FABG, the doped BG showed emission peaks at ~480 nm for B\_FABG, and B\_F\_FABG (Fig. 6a). Depending on the particular glass composition and Bi concentration, the exact excitation peaks can change. For B\_FABG, the excitation peaks are located about ~1100 nm and ~1208 nm and for B\_F\_FABG at ~1017 nm and ~1092 nm respectively (Fig. 6b). Previous studies have suggested that these peaks correspond to the transitions of Bi<sup>+</sup> from 3P<sub>0</sub> to 3P<sub>2</sub> and Bi<sub>0</sub> from 4S<sub>3/2</sub> to 2D<sub>3/2</sub>(2) and 2D<sub>3/2</sub>(1), respectively [52]. When exposed to radiation, the samples' active species of Bi absorbed this photon energy, allowing transitions to higher excited states. Radiative and non-radiative contributions can both lead to a subsequent relaxation. The latter causes the transfer of heat as a result of multiphoton relaxation, energy transfer between different states of Bi. Therefore, once PL is suppressed, the thermal effect tends to be enhanced.

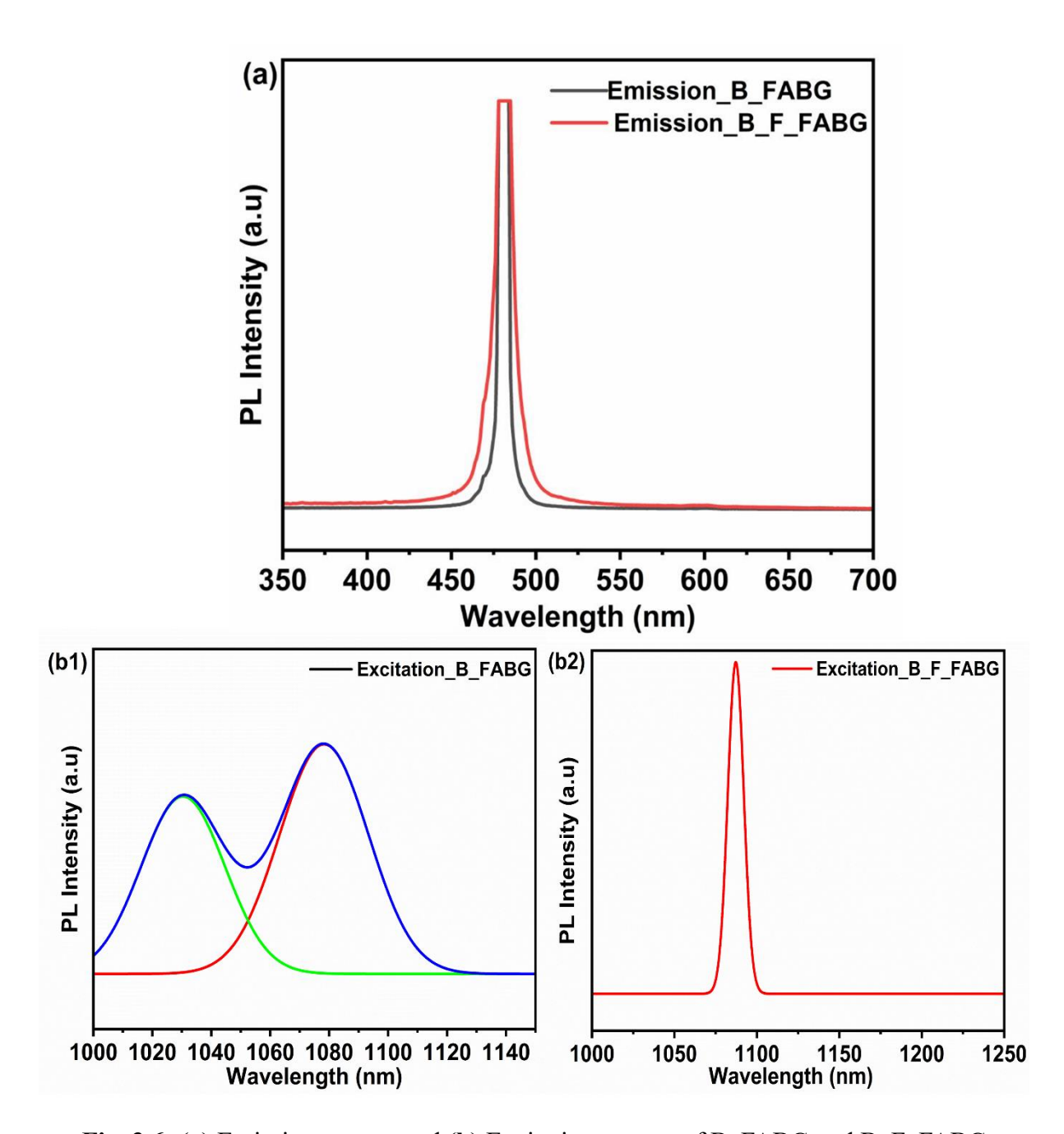
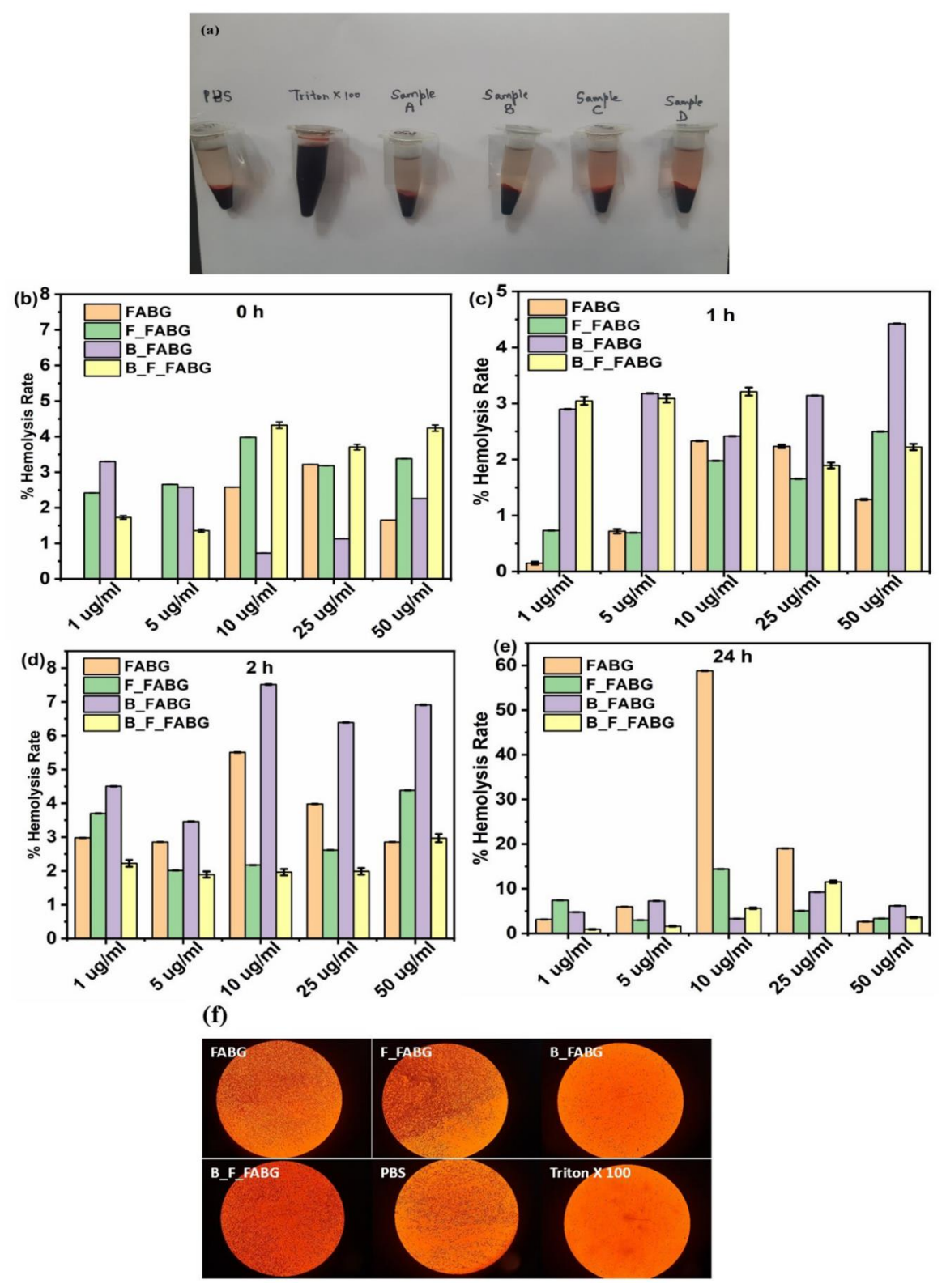


Fig. 3.6: (a) Emission spectra and (b) Excitation spectra of B FABG and B F FABG

### 3.4.11 *In-vitro* hemolysis assay:

The hemolytic effects on RBCs are closely related to elements such as the porosity, shape, and surface functioning of NPs [53]. External surface area is known to have an impact on hemolysis via altering the quantity of RBCs that bind to NPs or the ability of cell membranes to encircle NPs [54]. To evaluate the overall cytotoxicity of the synthesized NPs, the hemolysis assay was performed. We

generated NPs with low or insignificant hemolysis rates, in contrast to recent studies on comparable materials with various dopants [55,56]. Images of various samples, such as positive and negative control attributed to Triton X 100 and PBS respectively. FABG, F FABG, B FABG, and B F FABG NPs (1, 5, 10, 25, 50 g/mL), were centrifuged at 500× g for 5-6 min so as to obtain a fully transparent solution as shown in Fig. 7a. To find out how NPs affected the lysis of human red blood cells, spectrophotometric measurement of haemoglobin absorbance at 570 nm was performed. Each of the synthesized NPs displayed a very low hemolytic activity, as shown in (Fig. 7 (b-e)). According to this picture, all of the prepared NPs are hemocompatible and might not be dangerous at these concentrations. Increasing levels of hemolysis often occur at increasing test material concentrations, and hemolysis typically follows a dose-dependent pattern. With FABG, F FABG, B FABG, and B F FABG NPs, this is not the case, so it may be concluded that it might take place at the lower pH ranges under consideration. Therefore, it can be inferred that at physiological pH of 7.4, FABG, F FABG, B FABG, and B F FABG NPs display negligible hemolysis as seen in Fig. 7(b-e). We further attempted to explain the compatibility of the material with red blood cells (RBCs) using optical microscopy, as seen from UV-based data and optical micrographs (Fig. 7f). In both the control and sample cases, we were able to see intact RBCs on the slides in a variety of locations. However, with Triton X 100, no intact RBCs could be seen; instead, an extensive spread of debris was seen, which may have been caused by the breakdown or lysis of RBCs.



**Fig. 3.7:** Determination of hemolytic activity. **(a)** Images of each variant (centrifugation 500× g, 5 min to a completely clear solution). **(b-e)** Relative comparison of hemolytic activity after 0 h, 1 h, 2 h and 24 h of FABG, F\_FABG, B\_FABG and B\_F\_FABG (1, 5, 10, 25, 50 μg/mL) with 100% of Triton X 100 as a positive control and PBS as the negative control. **(f)** Microscope images of FABG, F\_FABG, B\_FABG and B\_F\_FABG, Negative Control (PBS) and Positive Control (Triton X 100) after 2 h interaction. All experiments were carried out in three replications.

### 3.5 B F FABG as an efficient magnetic PTA:

In this study, BG precursors were interacted with FA and metal ion dopants (Fe and Bi) to synthesize mesoporous B F FABG under ambient conditions. It is aqueous based sustainable synthesis. XPS confirmed the metal ions doping and the composition of BG network (Fig. 1(a-d)). The doping of Fe and Bi increased the crystallinity in the BG network. The average crystallite size of doped samples have been identified with the Scherrer formula which is found to be  $0.2 \pm 0.04$  nm for B F FABG confirmed by XRD (Fig. 1e). FA is retained in BG network as per the FTIR and TGA analysis by physical interactions (Fig. 1(f-g) 2(a-b)). NMR evidenced the decrease in Q<sup>4</sup>, Q<sup>3</sup>, Q<sup>2</sup>, and Q<sup>1</sup> structures of B F FABG compared to FABG confirming the doping of metal ions compared to BG (Fig. 2c). BET confirmed that pore diameter of Bi in B FABG is highest compared to other samples and pore volume is highest for F FABG compared to other samples which depicted that Fe and Bi ions are network former as well as network modifier (Fig. 3(a-d)) [57]. Hence, the presence of Bi and Fe in BG network is also confirmed by XPS studies (Fig. 1(a-d)). As a result, it was possible to synthesize nanosized, mesoporous B F FABG with an average pore diameter of 3.435 nm and a very high surface area of 80.621 m<sup>2</sup>/g. FE-SEM (Fig. 2d) and HR-TEM (Fig. 2e) depicted that the samples are nanosized (FABG, F FABG, B FABG, and B F FABG were found to be in the range of  $15.9 \pm 0.3$ nm,  $19.4 \pm 0.7$  nm,  $25.3 \pm 0.9$  nm, and  $12.8 \pm 0.3$  nm respectively) and are in good agreement with NMR findings. Pl luminescence and VSM (Fig. 6(a-b) and Fig. 3e) depicted B F FABG work as an efficient nanosized PTAs with magnetic property (Fig. 3e). By deposition of HAp on its surface, mesoporous B F FABG interacted with SBF and demonstrated good *in-vitro* bioactivity (Fig. 4(a-h) 5(a-f)). The observation promised for bone bonding nature of B\_F\_FABG. The in-vitro hemolysis assay's cytotoxicity test results showed that BG are biocompatible and perhaps safe at tested concentrations (Fig. 7(a-f)). The effective qualities for biomedical applications are thus confirmed by a detailed comparison of B F FABG with other BGNPs (FABG, F FABG, and B FABG). According to researches we found that only the sol-gel process, which combines artificial polymer templates, strong organic solvents, and calcination at high temperatures with organometallic precursors, can produce such mesoporous BG materials. Truth to be told, organometallic precursors along with synthetic or biological molecules are demanding in bio-inspired synthesis of BG where they act as a structure directing template [26,58]. Significantly, it becomes difficult with the aforementioned methods for synthesizing such BG samples which are property dependent. Therefore, we can say that nanosized mesoporous B\_F\_FABG is an environmental friendly biocompatible and bioactive magnetic PTA for biomedical applications.

### 3.6 Conclusion

A straightforward and carefully monitored process for the bio-inspired synthesis of BGNPs has been developed, using FA as a template and metal ions (Fe and Bi) as dopants. The material developed (B\_F\_FABG) is a bioactive mesoporous magnetic PTA having optical, magnetic and regenerative properties for wide biomedical applications. It is significant to remember that FA behaves as a templating agent for the synthesis of BG NPs such that metal dopants Fe and Bi ions function as network former as well as modifier. The presence of metal dopants in the BG network was confirmed by thorough elemental, FTIR, and TGA analysis while maintaining the BG composition necessary for demonstrating the bioactive property. The mesoporous nature of the BG NPs with large surface area and pore volume was revealed by nitrogen sorption studies, and its nanosize was validated by HR-TEM. In a comparison of the four BG NPs, mesoporous B\_F\_FABG performed as a better multifunctional material in terms of both magnetic and optical properties with excellent bioactivity as well as biocompatibility.

### Reference

- [1] A. Shearer, M. Montazerian, J.C. Mauro, Modern definition of bioactive glasses and glass-ceramics, J. Non-Cryst. Solids. 608 (2023) 122228. https://doi.org/10.1016/j.jnoncrysol.2023.122228.
- [2] J.R. Jones, Reprint of: Review of bioactive glass: From Hench to hybrids, Acta Biomater. 23 Suppl (2015) S53. https://doi.org/10.1016/j.actbio.2015.07.019.
- [3] N. Li, J. Cui, M. Chi, F. Thieringer, N. Sharma, Building a Better Bone: The Synergy of 2D Nanomaterials and 3D Printing for Bone Tissue Engineering. Mater. Des. 234 (2023) 112362. https://doi.org/10.1016/j.matdes.2023.112362.
- [4] H. Qu, H. Fu, Z. Han, Y. Sun, Biomaterials for bone tissue engineering scaffolds: a review, RSC Adv. 9 (2019) 26252. https://doi.org/10.1039/C9RA05214C.
- [5] J. Hum, A.R. Boccaccini, Bioactive glasses as carriers for bioactive molecules and therapeutic drugs: a review, J Mater Sci: Mater Med. 23 (2012) 2317. https://doi.org/10.1007/s10856-012-4580-z.
- [6] K.S. Mallikarjun, R.W. Eldaya, M.M. Miller-Thomas, H.L. Orlowski, M.S. Parsons, Good Gone Bad: Complications of Chemotherapy, Immunotherapy, and Radiotherapy on the CNS, Current Problems in Diagnostic Radiology. 53 (2024) 133. https://doi.org/10.1067/j.cpradiol.2023.06.016.
- [7] S. Khizar, N.M. Ahmad, N. Zine, N. Jaffrezic-Renault, A. Errachid-el-salhi, A. Elaissari, Magnetic Nanoparticles: From Synthesis to Theranostic Applications, ACS Appl. Nano Mater. 4 (2021) 4284. https://doi.org/10.1021/acsanm.1c00852.
- [8] W. Bian, Y. Wang, Z. Pan, N. Chen, X. Li, W.-L. Wong, X. Liu, Y. He, K. Zhang, Y.-J. Lu, Review of Functionalized Nanomaterials for Photothermal Therapy of Cancers, ACS Appl. Nano Mater. 4 (2021) 11353. https://doi.org/10.1021/acsanm.1c01903.
- [9] Z. Bao, X. Liu, Y. Liu, H. Liu, K. Zhao, Near-infrared light-responsive inorganic nanomaterials for photothermal therapy, Asian Journal of Pharmaceutical Sciences. 11 (2016) 349. https://doi.org/10.1016/j.ajps.2015.11.123.
- [10] P. Tang, Y. Liu, Y. Liu, H. Meng, Z. Liu, K. Li, D. Wu, Thermochromism-induced temperature self-regulation and alternating photothermal nanohelix clusters for synergistic tumor chemo/photothermal therapy, Biomaterials. 188 (2019) 12. https://doi.org/10.1016/j.biomaterials.2018.10.008.
- [11] Q. Tian, F. Jiang, R. Zou, Q. Liu, Z. Chen, M. Zhu, S. Yang, J. Wang, J. Wang, J. Hu, Hydrophilic Cu<sub>9</sub>S<sub>5</sub> Nanocrystals: A Photothermal Agent with a 25.7% Heat Conversion Efficiency for Photothermal Ablation of Cancer Cells in Vivo, ACS Nano. 5 (2011) 9761. https://doi.org/10.1021/nn203293t.
- [12] A.N. D'Souza, N.S. Prabhu, K. Sharmila, M.I. Sayyed, H.M. Somshekarappa, G. Lakshminarayana, S. Mandal, S.D. Kamath, Role of Bi<sub>2</sub>O<sub>3</sub> in altering the structural, optical, mechanical, radiation shielding and thermoluminescence properties of heavy metal oxide borosilicate glasses, Journal of Non-Crystalline Solids. 542 (2020) 120136. https://doi.org/10.1016/j.jnoncrysol.2020.120136.
- [13] H. Yang, F. Yan, Y. Lin, T. Wang, Enhanced energy storage properties of Ba0.4Sr0.6TiO3 lead-free ceramics with Bi2O3-B2O3-SiO2 glass addition, Journal of the European Ceramic Society. 38 (2018) 1367. https://doi.org/10.1016/j.jeurceramsoc.2017.11.058.
- [14] T. Zhang, X. Zeng, Y. Xia, H. Zhang, B. Sun, H. Wang, Y. Zhao, Morphology evolution and photocatalytic applications of W-doped Bi2O3 films prepared using unique oblique angle cosputtering technology, Ceramics International. 45 (2019) 21968. https://doi.org/10.1016/j.ceramint.2019.07.211.

- [15] P. Babula, V. Adam, R. Opatrilova, J. Zehnalek, L. Havel, R. Kizek, Uncommon Heavy Metals, Metalloids and Their Plant Toxicity: A Review, in: E. Lichtfouse (Ed.), Organic Farming, Pest Control and Remediation of Soil Pollutants: Organic Farming, Pest Control and Remediation of Soil Pollutants, Springer Netherlands, Dordrecht, 2010: pp. 275–317. https://doi.org/10.1007/978-1-4020-9654-9 14.
- [16] A.A. El-Rashidy, J.A. Roether, L. Harhaus, U. Kneser, A.R. Boccaccini, Regenerating bone with bioactive glass scaffolds: A review of in vivo studies in bone defect models, Acta Biomaterialia. 62 (2017) 1. https://doi.org/10.1016/j.actbio.2017.08.030.
- [17] S. Sadeghzade, J. Liu, H. Wang, X. Li, J. Cao, H. Cao, B. Tang, H. Yuan, Recent advances on bioactive baghdadite ceramic for bone tissue engineering applications: 20 years of research and innovation (a review), Materials Today Bio. 17 (2022) 100473. https://doi.org/10.1016/j.mtbio.2022.100473.
- [18] F. Kermani, A. Vojdani-Saghir, S. Mollazadeh Beidokhti, S. Nazarnezhad, Z. Mollaei, S. Hamzehlou, A. El-Fiqi, F. Baino, S. Kargozar, Iron (Fe)-doped mesoporous 45S5 bioactive glasses: Implications for cancer therapy, Translational Oncology. 20 (2022) 101397. https://doi.org/10.1016/j.tranon.2022.101397.
- [19] M. Cannas, E. Indemini, A. Krajewski, A. Ravaglioli, S. Contoli, In vitro observations of iron-doped bioactive glasses, Biomaterials. 11 (1990) 281. https://doi.org/10.1016/0142-9612(90)90011-E.
- [20] S. Grasso, R. Chinnam, H. Porwal, A. Boccaccini, M. Reece, Low temperature spark plasma sintering of 45S5 Bioglass (R), Journal of Non-Crystalline Solids. 362 (2012) 25. https://doi.org/10.1016/j.jnoncrysol.2012.11.009.
- [21] H. Ranji-Burachaloo, P.A. Gurr, D.E. Dunstan, G.G. Qiao, Cancer Treatment through Nanoparticle-Facilitated Fenton Reaction, ACS Nano. 12 (2018) 11819. https://doi.org/10.1021/acsnano.8b07635.
- [22] H. Goel, D. Santhiya, Effect of pH on bio-inspired synthesis of L-Lysine templated bioactive glass hybrid xerogels for tailored textural and rheological properties, Materials Chemistry and Physics. 281 (2022) 125828. https://doi.org/10.1016/j.matchemphys.2022.125828.
- [23] N. Gupta, D. Santhiya, S. Murugavel, A. Kumar, A. Aditya, M. Ganguli, S. Gupta, Effects of transition metal ion dopants (Ag, Cu and Fe) on the structural, mechanical and antibacterial properties of bioactive glass, Colloids and Surfaces A: Physicochemical and Engineering Aspects. 538 (2018) 393. https://doi.org/10.1016/j.colsurfa.2017.11.023.
- [24] N. Dey, D. Santhiya, A. Das, Bio-Inspired Synthesis of Hollow Mesoporous Bioactive Glass Nanoparticles Using Calcium Carbonate as Solid Template, ChemistrySelect. 7 (2022). https://doi.org/10.1002/slct.202200392.
- [25] K. Vinothini, N.K. Rajendran, A. Ramu, N. Elumalai, M. Rajan, Folate receptor targeted delivery of paclitaxel to breast cancer cells via folic acid conjugated graphene oxide grafted methyl acrylate nanocarrier, Biomedicine & Pharmacotherapy. 110 (2019) 906. https://doi.org/10.1016/j.biopha.2018.12.008.
- [26] D. Santhiya, H. kumari Alajangi, F. Anjum, S. Murugavel, M. Ganguli, Bio-inspired synthesis of microporous bioactive glass-ceramic using CT-DNA as a template, J. Mater. Chem. B. 1 (2013) 6329. https://doi.org/10.1039/C3TB21212B.
- [27] M.A. Dobrovolskaia, J.D. Clogston, B.W. Neun, J.B. Hall, A.K. Patri, S.E. McNeil, Method for Analysis of Nanoparticle Hemolytic Properties in Vitro, Nano Lett. 8 (2008) 2180. https://doi.org/10.1021/nl0805615.
- [28] F. Molly, W. Sean, S. Mark, M. Colleen, A. Scott, R. Don, Standard practice for assessment of hemolytic properties of materials, American Society for Testing of Materials. ASTM F756-00. (2000).

- [29] B. Barrioni, E. Norris, J. Jones, M. Pereira, The influence of cobalt incorporation and cobalt precursor selection on the structure and bioactivity of sol–gel-derived bioactive glass, Journal of Sol-Gel Science and Technology. 88 (2018). https://doi.org/10.1007/s10971-018-4823-7.
- [30] L. Li, P. Ma, S. Hussain, L. Jia, D. Lin, X. Yin, Y. Lin, Z. Cheng, L. Wang, FeS<sub>2</sub>/carbon hybrids on carbon cloth: a highly efficient and stable counter electrode for dye-sensitized solar cells Sustainable Energy & Fuels, 3 (2019) 1749. https://doi.org/10.1039/C9SE00240E.
- [31] A.K. Potbhare, P.B. Chauke, S. Zahra, V. Sonkusare, R. Bagade, M. Ummekar, R. Gomaji Chaudhary, Microwave-mediated Fabrication of Mesoporous Bi-doped CuAl2O4 Nanocomposites for Antioxidant and Antibacterial Performances, Materials Today: Proceedings. 15 (2019) 454. https://doi.org/10.1016/j.matpr.2019.04.107.
- [32] F. Unal, C. Tasar, B. Ercan, Fabrication and in vitro characterization of antibacterial magneto-luminescent core-shell bioactive glass nanoparticles, Ceramics International. 49 (2023) 20118. https://doi.org/10.1016/j.ceramint.2023.03.135.
- [33] A.E. Pazarçeviren, A. Tahmasebifar, A. Tezcaner, D. Keskin, Z. Evis, Investigation of bismuth doped bioglass/graphene oxide nanocomposites for bone tissue engineering, Ceramics International. 44 (2017). https://doi.org/10.1016/j.ceramint.2017.11.164.
- [34] S.K. Mandal, P. Kiran, P.S. Rao, A. Chandra, Green synthesis of Sr2+ doped multiferroic BiFeO3 nanoceramics using Aloe vera biotemplates and their characterizations, Journal of Alloys and Compounds. 922 (2022) 166107. https://doi.org/10.1016/j.jallcom.2022.166107.
- [35] <u>J. Varshosaz</u>, <u>F. Hassanzadeh</u>, <u>H.S. Aliabadi</u>, <u>M. Nayebsadrian</u>, <u>M. Banitalebi</u>, <u>M. Rostami</u>, Synthesis and Characterization of Folate-Targeted Dextran/Retinoic Acid Micelles for Doxorubicin Delivery in Acute Leukemia, BioMed research international, 2014 (2014) 525684. https://doi.org/10.1155/2014/525684.
- [36] H. Goel, D. Santhiya, Role of Trigonella foenum-graecum leaf extract in tailoring the synthesis and properties of bioactive glass nanoparticles, 33 (2022) e00485. https://doi.org/10.1016/j.susmat.2022.e00485.
- [37] H.-M. Lin, H.-Y. Lin, M.-H. Chan, Preparation, characterization, and in vitro evaluation of folate-modified mesoporous bioactive glass for targeted anticancer drug carriers, J. Mater. Chem. B. 1 (2013) 6147. https://doi.org/10.1039/C3TB20867B.
- [38] M.A. Karakassides, D. Gournis, D. Petridis, An infrared reflectance study of Si–O vibrations in thermally treated alkali-saturated montmorillonites, Clay Minerals. 34 (1999) 429. https://doi.org/10.1180/000985599546334.
- [39] V. Rajendran, A. Nishara Begum, M.A. Azooz, F.H. El Batal, Microstructural dependence on relevant physical–mechanical properties on SiO2–Na2O–CaO–P2O5 biological glasses, Biomaterials. 23 (2002) 4263. https://doi.org/10.1016/S0142-9612(02)00189-8.
- [40] H. Eckert, Structural characterization of bioactive glasses by solid state NMR, Journal of Sol-Gel Science and Technology, 88 (2018) 263. https://doi.org/10.1007/s10971-018-4795-7.
- [41] J. Šesták, M. Liška, P. Hubík, Oxide Glass Structure, Non-bridging Oxygen and Feasible Magnetic Properties due to the Addition of Fe/Mn Oxides, in: J. Šesták, J.J. Mareš, P. Hubík (Eds.), Glassy, Amorphous and Nano-Crystalline Materials: Thermal Physics, Analysis, Structure and Properties, Springer Netherlands, Dordrecht, 2011: pp. 199–216. https://doi.org/10.1007/978-90-481-2882-2 12.
- [42] Y. Zhang, J. Liu, Z. Wu, X. Mei, W. Zhu, A. Wang, Rapid promoting thrombus formation and fibrin cross-linked Bi-doped mesoporous bioglass for hemostatic agent, Materials Today Chemistry. 25 (2022) 100980. https://doi.org/10.1016/j.mtchem.2022.100980.
- [43] M.D. Donohue, G.L. Aranovich, Classification of Gibbs adsorption isotherms, Advances in Colloid and Interface Science. 76–77 (1998) 137. https://doi.org/10.1016/S0001-8686(98)00044-X.

- [44] E.A. Mahdy, S. Ibrahim, H.A. Abo-Mosallam, The influence of Bi2O3 on structural and enhancing physical properties of Li<sub>2</sub>O–Fe<sub>2</sub>O<sub>3</sub>–In<sub>2</sub>O<sub>3</sub>–P<sub>2</sub>O<sub>5</sub> glasses, Materials Chemistry and Physics. 309 (2023) 128406. https://doi.org/10.1016/j.matchemphys.2023.128406.
- [45] D. Makovec, A. Kosak, A. Žnidaršič, M. Drofenik, The synthesis of spinel–ferrite nanoparticles using precipitation in microemulsions for ferrofluid applications, Journal of Magnetism and Magnetic Materials. 289 (2005) 32. https://doi.org/10.1016/j.jmmm.2004.11.010.
- [46] L. Mohammed, H.G. Gomaa, D. Ragab, J. Zhu, Magnetic nanoparticles for environmental and biomedical applications: A review, Particuology. 30 (2017) 1. https://doi.org/10.1016/j.partic.2016.06.001.
- [47] S. Targonska, M. Sikora, K. Marycz, A. Smieszek, R.J. Wiglusz, Theranostic Applications of Nanostructured Silicate-Substituted Hydroxyapatite Codoped with Eu<sup>3+</sup> and Bi<sup>3+</sup> Ions—A Novel Strategy for Bone Regeneration, ACS Biomater. Sci. Eng. 6 (2020) 6148. https://doi.org/10.1021/acsbiomaterials.0c00824.
- [48] R.A. Martin, H.L. Twyman, G.J. Rees, J.M. Smith, E.R. Barney, M.E. Smith, J.V. Hanna, R.J. Newport, A structural investigation of the alkali metal site distribution within bioactive glass using neutron diffraction and multinuclear solid state NMR, Phys. Chem. Chem. Phys. 14 (2012) 12105. https://doi.org/10.1039/C2CP41725A.
- [49] T. Kokubo, H. Takadama, How useful is SBF in predicting in vivo bone bioactivity?, Biomaterials. 27 (2006) 2907. https://doi.org/10.1016/j.biomaterials.2006.01.017.
- [50] L. Wang, N.J. Long, L. Li, Y. Lu, M. Li, J. Cao, Y. Zhang, Q. Zhang, S. Xu, Z. Yang, C. Mao, M. Peng, Multi-functional bismuth-doped bioglasses: combining bioactivity and photothermal response for bone tumor treatment and tissue repair, Light Sci Appl. 7 (2018) 1. https://doi.org/10.1038/s41377-018-0007-z.
- [51] L. Yuan, S. Gu, X. Zhang, Y. Zhao, W. Luo, L. Wang, W. Jiang, Low-temperature sintering of bismuth-doped glass with high fluorescence properties from mesoporous silica SBA-15, Ceramics International. 46 (2020) 1164. https://doi.org/10.1016/j.ceramint.2019.09.085.
- [52] H.C. Swart, R.E. Kroon, (INVITED) Ultraviolet and visible luminescence from bismuth doped materials, Optical Materials: X. 2 (2019) 100025. https://doi.org/10.1016/j.omx.2019.100025.
- [53] T. Yu, A. Malugin, H. Ghandehari, Impact of silica nanoparticle design on cellular toxicity and hemolytic activity, ACS Nano. 5 (2011) 5717. https://doi.org/10.1021/nn2013904.
- [54] Y. Zhao, X. Sun, G. Zhang, B.G. Trewyn, I.I. Slowing, V.S.-Y. Lin, Interaction of mesoporous silica nanoparticles with human red blood cell membranes: size and surface effects, ACS Nano. 5 (2011) 1366. https://doi.org/10.1021/nn103077k.
- [55] I.I. Slowing, B.G. Trewyn, V.S.-Y. Lin, Mesoporous Silica Nanoparticles for Intracellular Delivery of Membrane-Impermeable Proteins, J. Am. Chem. Soc. 129 (2007) 8845. https://doi.org/10.1021/ja0719780.
- [56] G. Pouroutzidou, G. Theodorou, E. Kontonasaki, I. Tsamesidis, A. Pantaleo, D. Patsiaoura, L. Papadopoulou, J. Rhoades, E. Likotrafiti, C. Lioutas, K. Chrissafis, K. Paraskevopoulos, Effect of ethanol/TEOS ratios and amount of ammonia on the properties of copper-doped calcium silicate nanoceramics, Journal of Materials Science: Materials in Medicine. 30 (2019). https://doi.org/10.1007/s10856-019-6297-8.
- [57] R. Parmar, R.S. Kundu, R. Punia, P. Aghamkar, N. Kishore, Iron modified structural and optical spectral properties of bismuth silicate glasses, Physica B: Condensed Matter. 450 (2014) 39. https://doi.org/10.1016/j.physb.2014.05.056.
- [58] M. Todea, R.V.F. Turcu, M. Vasilescu, D.L. Trandafir, S. Simon, Structural characterization of heavy metal SiO<sub>2</sub>–Bi<sub>2</sub>O<sub>3</sub> glasses and glass–ceramics, Journal of Non-Crystalline Solids. 432 (2016) 271. https://doi.org/10.1016/j.jnoncrysol.2015.10.021.

# **CHAPTER 4**

Effect of Magnesium and Bismuth Codoping on Structural Optical and Bioactive properties of Bioactive Glass Nanoparticles for Biomedical Applications

### **CHAPTER 4**

# Effect of Magnesium and Bismuth co-doping on Structural Optical and Bioactive properties of Bioactive Glass Nanoparticles for Biomedical Applications

# Mg-O-Bi bond Mg/Bi-O-Si bond Mg and Bi doped BG Mesoporous Multifunctional PTA Enhanced photoluminescence and hemocompatibility

### 4.1 Introduction

Ceramics and bioactive glasses (BG) stand out among all biomaterials as interesting options for biomedical applications involving hard and soft tissue regeneration [1–3]. BG form a hydroxyl apatite-like layer (HA) on the surface upon implantation at defective wound site, which resembles the mineral phase of bone. The recently formed HA layer not only bind with bone and also promote binding of soft tissue by neovascularization [4]. There exists a numerous reports on the effect of therapeutic ion dopants to BG on bioactivity and clinical applicability [5]. Aluminum (Al), zirconium (Zr), magnesium (Mg), strontium (Sr), zinc (Zn), copper (Cu), cobalt (Co) [6] and silver (Ag) are few metal ions, which were incorporated individually/co-dopants in BG. These metal ions in critical concentrations are known to substitute for Ca in BG network to improve osteogenesis, angiogenesis, and biocide activity of BG [7–9]. Mg is an important content of human body especially in hard tissues and plays essential role in energy metabolism, macromolecule synthesis, bone

development as well as maintenance and expression of genetic information [5]. Doped Mg ions in BG functions as a network modifier and offers an excellent mechanical strength to the material. In addition, presence of Mg<sup>2+</sup> in BG also promotes human osteoblast cell adhesion, proliferation, and calcification [10]. Mg doped mesoporous BG were shown to promote bone regeneration with excellent biocompatibility and also providing sustained drug release [11]. As a result, Mg shows widespread use in a variety of implants such as porous bone scaffolds, cardiovascular stents, and internal fixing components for bone fractures [12].

Biomaterials with bismuth (Bi) or its compounds can release Bi ions in physiological conditions, which can potentially have detrimental biological effects [3]. Bi is less toxic than other heavy metals and is also widely used in pharmaceutical products [13] and bio markers [14]. Various Bi containing materials are reported to show antibacterial [15,16], anticancer properties [17] and are used in treating gastrointestinal infections, syphilis, hypertension [18] and tumors [5]. Bismuth ferrite reinforced BG composites were demonstrated as scaffold for cellular support with enhanced bone tissue formation and accelerated osseointegration under magnetic field exposure. Bismuth oxide-doped BG synthesized by flame spray was shown as a radiopacifier to improve the functionality of dental implants [19]. However, human osteoporosis and soft tissue damages can result from an overly high concentration of Bi [20,21]. Addition of Bi<sub>2</sub>O<sub>3</sub> to 45S5 nano-bioactive glass powders by flame spray technology displayed radiopaque to X-rays with enhanced bioactivity.

Bi based nanoparticles (NPs) have been the recent subject for investigation, as they have proven to be very effective agents for photothermal therapy (PTT) [22]. The use of PTT for numerous biomedical applications has become popular due to its non-invasive, controllable and weak side effects [23,24]. PTT essentially needs photothermal agents (PTA) for enhanced targeted treatments that include various inorganic, organic and inorganic-organic composite materials. Under visible and near infrared light radiation (NIR), PTA molecules absorb light energy, which cause electronic transition from the ground singlet state to an excited singlet state [25]. Consequently, electronic

excitation energy undergoes non-radiative vibrational relaxations and return to the ground state by collisions with the surrounding molecules. Resulted increased kinetic energy generates heat, which is subjected to various biomedical applications namely to target tumors, wound healing, and infection control measures. NIR light assisted PTT with polymer scaffolds can promote bone cell proliferation and bone regeneration by delivering PTA [26]. A mild heat-induced high efficacy osteogenesis was demonstrated by a biodegradable osteo-implant, composed of black phosphorus nanosheets and poly(lactic-co-glycolic acid) [27]. A novel magnetic nanoparticles modified-mesoporous Bioglass/Chitosin scaffold (MBCS) was fabricated for enhancing bone regeneration capacity and PTT against bone tumors [28]. However, most PTA developed till today are non-degradable and are not known for long term toxicity as well as target specificity. Multifunctional PTA including tissue regeneration, drug delivery, real time imaging are still in need [29].

Dual ion-doped bioactive glass has drawn high attention because of well-improved tailored therapeutic characteristics and mechanical properties [5]. Doping of Mg and La elements in BG resulted as potential regenerative bone substitutes [30]. Interestingly, Zn and Ag co-doping on BG nanoparticles were shown to promote bone regrowth, eradicates bone cancer, and guards against bone infection [31]. The effects of Sr<sup>2+</sup> and Li<sup>+</sup> single and binary doped bioactive glass offered a way to supply bioactive substances that will hasten bone mending and improve bone implant anchoring in orthopaedic surgery [32]. Mg and Cu co-doped MBG were demonstrated as promising candidates for bone regeneration owing to bioactivity, cell proliferation and antibacterial properties [5].

In this study, Mg and Bi were co-doped first time in 45S5 BG composition to tailor therapeutic and photothermal properties in BG. Co-doped BG are synthesized by bio-inspired approach using curcumin (CC) as template that utilizes an aqueous-based methodology. Most importantly, the bio-inspired method uses simple, economical, and eco-friendly processes, considering calcination oversight with great care [15,31]. CC is an widely known therapeutic agents for numerous biological potentialities and pharmacological activity [33,34]. A series of BG nanoparticles (NPs) were

synthesized by varying the concentration of Bi from 0.5 mol% to 1.5 mol% by maintaining Mg concentration constant (M\_B1\_CCBG, M\_B2\_CCBG and M\_B3\_CCBG). Throughout the study CC templated 45S5 composition of BG (CCBG) was used as a control material. The structure, morphology, pore size distribution of BGNPs were tested using XRD, XPS, FTIR, FE-SEM, HR-TEM, BET, NMR and TGA. We also demonstrated *in-vitro* bioactivity as well as cytotoxicity trials and photoluminescence tests to examine the effects of Mg and Bi doping in 45S5 BG for biomedical applications.

### **4.2 Experimental Section**

### 4.2.1 Materials:

The precursors such as tetraethyl orthosilicate (TEOS) (CAS No. 78-10-4), triethyl phosphate (TEP) (CAS No. 78-40-0), sodium acetate (NaAc) (CAS No. 127-09-3), and calcium acetate (CaAc) (CAS No. 114460-21-8) were used in the synthesis of BG NPs. All these precursors were obtained from Sigma-Aldrich. Furthermore, Hank's Balanced Salt solution (HBSS), also referred to as simulated bodily fluid (SBF), Bismuth Nitrate Pentahydrate (Bi (NO<sub>3</sub>)<sub>3</sub>.5H<sub>2</sub>O) (CAS No. 10035-06-0), Magnesium Chloride (MgCl<sub>2</sub>.6H<sub>2</sub>O) (CAS No. 7791-18-6), and Curcumin (CC) (CAS No. 458-37-7) were also purchased from Sigma-Aldrich. For all other compounds, the highest purity analytical reagent (AR) grade was used. All the experiments used Milli-Q water, and were carried out at room temperature.

# 4.2.2 Bio-inspired Synthesis of co-doped (Bi<sup>3+</sup> and Mg<sup>2+</sup>) CCBG NPs:

The synthetic procedure for BG NPs was meticulously adhered with minimal modifications to our previous findings [31,35]. First, 100 mL of pH 8 (10 mM) trizma buffer was used to dissolve the

template solution (CC (1 mg/mL) in 2 mL of ethanol). The solution was constantly stirred at 500 rpm using a digital magnetic stirrer for 20 min at room temperature. The BG precursors were added sequentially at an interval of 30 min. According to the specified protocol, TEOS (9.29 g) was added first, followed by TEP (1 g), NaAc (6.36 g), and CaAc (4.21 g) for 45S5 composition. The solution was incubated in a silicone oil bath for 24 h after being continuously stirred for 30 min. The resultant mixture was then centrifuged at room temperature and 13000 rpm to separate the precipitate. After a thorough cleaning with MilliQ water, the precipitate (CCBG) was dried for 48 h at 40 °C in an air oven, and it was then kept in a desiccator. A series of doped CCBG (M CCBG, M B1 CCBG, M B2 CCBG and M B3 CCBG) were synthesized with fixed quantity of (1 mol%) MgO and varying (0.5 mol%, 1 mol% and 1.5 mol %) quantities of Bi<sub>2</sub>O<sub>3</sub> respectively. The BG NPs composition was maintained as 45SiO<sub>2</sub>-6P<sub>2</sub>O<sub>5</sub>-(24.5-x-y) CaO-24.5Na<sub>2</sub>O-xMgO (x= 0, 0.5)yBi<sub>2</sub>O<sub>3</sub>(y= 0, 0.5, 1.5). Mg<sup>2+</sup> doped CCBG (M CCBG (1 mol% MgO)) was synthesized by adding required amount of Magnesium Chloride (MgCl<sub>2</sub>.6H<sub>2</sub>O) after the addition of all BG precursors as mentioned previously. Similarly, CCBG was also co-doped with Mg<sup>2+</sup> and Bi<sup>3+</sup> by using Magnesium Chloride (MgCl<sub>2</sub>.6H<sub>2</sub>O) and Bismuth Nitrate Pentahydrate (Bi (NO<sub>3</sub>)<sub>3</sub>.5H<sub>2</sub>O) respectively. The resulted BGNPs were washed, dried and preserved as described for CCBG.

### 4.3 Characterization of CCBG, M CCBG and co-doped CCBG:

### 4.3.1 X-ray photoelectron spectroscopy (XPS):

XPS measurements were carried out using a non-monochromatized Al K X-ray source and a specially designed hemispherical electron energy analyser (ESA-31) in an Ultra-high Vacuum (UHV) chamber. Photoelectrons were gathered on a plane parallel to the surface, with the photon beam direction forming a  $70^{\circ}$  angle with the analyser's axis. Retarding ratios (k) of 4 for survey spectra and k = 8 for the energy zones of interest were used to obtain survey spectra in the fixed retarding ratio (FRR)

mode. C++ was used in the development of the measurement control and data collection programme. The samples were attached to the sample holder with 3M-9713-Cu conductive double-sided adhesive tape.

### 4.3.2 X-ray diffraction (XRD) analysis:

XRD analysis of BG NPs was performed using a Panalytical X'Pert Pro Diffractometer, operating at 45 kV and 40 mA current. The X-ray source was Cu-K $\alpha$  radiation. A very slow scan rate of 0.2 °/min and a slow scan speed ranging from 5° to 90° were used to record the 20 spectrum.

### 4.3.3 Fourier transform infrared spectroscopy (FTIR):

CCBG, M\_CCBG, M\_B1\_CCBG, M\_B2\_CCBG and M\_B3\_CCBG were recorded by using ATR-FTIR mode of the spectrophotometer. The Perkin Elmer (Model Spectrum 2) spectrometer operating in the range of 400 cm<sup>-1</sup> to 4000 cm<sup>-1</sup> with a resolution of 1 cm<sup>-1</sup> was used to record FTIR spectra for various BG NPs.

### 4.3.4 Thermogravimetric (TGA) analysis:

BG NPs were subjected to a TGA analysis using a Perkin Elmer thermogravimetric analyzer (Model TGA 4000). The samples were heated from 0 °C to 800 °C in a nitrogen environment at a heating rate of 10 °C/min with a nitrogen gas flow of 50 mL/min to examine the thermal stability.

### 4.3.5 Morphological studies

### 4.3.5.1. Field emission scanning electron microscopy (FE-SEM):

Using a Zeiss EVO MA15 scanning electron microscope, the morphology of BG NPs was examined. Gold-coated CCBG, M\_CCBG, M\_B1\_CCBG, M\_B2\_CCBG and M\_B3\_CCBG were observed under a 5.0 kV accelerating voltage and 10,000 times the normal magnification.

### 4.3.5.2. High resolution transmission electron microscopy (HR-TEM):

CCBG, M\_CCBG, M\_B1\_CCBG, M\_B2\_CCBG and M\_B3\_CCBG NPs were visualized under a high-resolution Transmission Electron Microscope (HR-TEM) model (TALOS S) from Thermo Scientific in the United States. This model operates at an accelerating voltage of 200 kV. For the particle size analysis, the 64-bit Java 1.8.0 172 ImageJ software was used. SAED pattern analysis was done by a 4k × 4k Ceta camera using Velox software (Thermo Fisher).

## 4.3.6 Nitrogen sorption analysis (BET):

The substance was degassed in a vacuum for 2 h at 200 °C prior to analysis. Using a Microtrac BEL (Model BELSORP-max), Japan, at -196 °C, nitrogen was used as the adsorptive gas (N<sub>2</sub>, cross-sectional area 0.162 nm<sup>2</sup>) in the nitrogen adsorption-desorption analysis. The porosity of the CCBG, M\_CCBG, M\_B1\_CCBG, M\_B2\_CCBG and M\_B3\_CCBG NPs was ascertained in this study. Based on nitrogen adsorption data surface area of each NP was calculated using the Brunauer-Emmett-Teller (BET) equation. The distribution of pore diameters in the desorption portion of the isotherm was also examined for all samples using the Barret-Joyner-Halenda (BJH) method.

# 4.3.7 <sup>29</sup>Si solid state nuclear magnetic resonance (NMR):

The atomic level silicate structure was rationalized on doping with different metal ions using <sup>29</sup>Si solid state NMR, providing insight into the Q<sup>n</sup> species distribution of various BG NPs. For the magicangle spinning (MAS) NMR experiment, a 9.4 T ECX-II Jeol 400 MHz FT-NMR spectrometer operating at a frequency of 79.5 MHz was used.

# 4.3.8 Photoluminescence study (PL):

The Time Resolved PL (TR-PL) spectrum records were made for M\_B1\_CCBG, M\_B2\_CCBG and M\_B3\_CCBG NPs at room temperature with an Edinburgh FLSP 900 Spectro fluorophotometer. The instrument has a 0.1 nm spectral resolution, excited by a Xenon lamp.

### 4.3.9 Bioactivity test:

The *in-vitro* bioactivity of CCBG, M\_CCBG, M\_B1\_CCBG, M\_B2\_CCBG and M\_B3\_CCBG NPs were evaluated as per the procedure described earlier [36]. The samples were immersed in SBF at a concentration of 1 mg/mL and sterilely incubated for 4 d, 7 d, 15 d, and 30 d at 37 °C. The SBF solution was replaced for every 4 d to maintain the ion concentration in the solution and promote the development of the HAP layer. After the required time had elapsed, each sample was centrifuged, dried at 48 °C in an air oven, and kept in a desiccator. Further, the samples were characterized using XRD, FTIR as well as FE-SEM.

### 4.3.10 In-vitro hemolysis assay:

Small modifications were made to the experimental protocol of the *in-vitro* hemolysis assay while using human blood [37].1 mg/mL stock solution was prepared for all the BG NPs such that five stock suspensions can be prepared from original stock solution (1  $\mu$ g/mL, 5  $\mu$ g/mL, 10  $\mu$ g/mL, 25  $\mu$ g/mL, and 50  $\mu$ g/mL). A volume of 0.5 mL of human blood was collected, centrifuged at 4 °C for 5 min with a 500×g RCF, and the plasma-containing supernatant was released into surfactant. The blood sample was properly mixed in micro-centrifuge tubes after the plasma was removed, and it was then twice cleaned with 500  $\mu$ L and 1000  $\mu$ L PBS autoclaved PBS buffer. Washing was done up until a clear supernatant was seen. The clear supernatant obtained was discarded. Subsequently, micro-centrifuge tubes containing each BGNPs at various concentrations (1  $\mu$ g/mL, 5  $\mu$ g/mL, 10  $\mu$ g/mL, 25  $\mu$ g/mL, and 50  $\mu$ g/mL) were interacted with the human red blood cells. A negative control was designated as one microcentrifuge tube containing 1 mL of PBS in red human blood, whereas a positive control was designated as a seventh microcentrifuge tube containing blood after adding 50  $\mu$ L of Triton X 100 and 950  $\mu$ L of PBS. The absorbance at 570 [38] nm was measured for different incubation durations of 0 h, 1 h, 2 h, and 24 h. The hemolysis rate as a percentage was determined using the following equation:

% Hemolysis = 
$$\left[\frac{A_t - A_c}{A_{100\%} - A_c}\right] \times 100$$

Where, A<sub>c</sub> is the absorbance of the supernatant from the negative control (PBS), and A<sub>100%</sub> is the absorbance of the supernatant from the positive control (Triton X 100), A<sub>t</sub> is the absorbance of the supernatant of samples incubated with the particles. The experiments were conducted in triplicate, and error analysis was carried out. In our study, hemolysis levels below 5% were considered non-toxic. This criterion aligns with ASTM 75633 [39] and has been corroborated by various sources [37].

### 4.3.11 MTT Assay:

In MTT assay, the cytotoxicity and biocompatibility of the BG samples was evaluated. The colorimetric MTT method was used to assess the vitality of U2OS cells (osteoblasts in osteosarcoma), in the presence of BG NPs. By evaluating the conversion of MTT into formazan crystals, which represents cellular metabolic activity, the MTT assay assesses the viability of cells. To conduct the experiment, distinct BG specimens with varying concentrations (1  $\mu$ g/mL, 5  $\mu$ g/mL, 10  $\mu$ g/mL, 25  $\mu$ g/mL, and 50  $\mu$ g/mL) were UV-sterilized for half an hour and thereafter cultured with cells (10,000 cells per well) on a 96-well plate at 37 °C for a full day. The MTT assay was then carried out by filling each well with 100  $\mu$ L of 1 mg/mL of MTT reagent. After covering the plate with foil and leaving some space for air, it was incubated under cell culture conditions for 2 h at 37 °C. Following the incubation period, the medium and MTT were aspirated, and the plate was removed. After dissolving the formazan crystals with 100  $\mu$ L of dimethyl sulfoxide, the plate was incubated for an additional 20 min under cell culture conditions. A TECAN multimode plate reader was used to read the plate at 570 nm and 630 nm wavelengths after it had been incubated. The positive control was made up of cells grown in DMEM media. Every experiment was carried out three times, and the results were reported as means  $\pm$  standard deviation.

### 4.4 Results and Discussions

### 4.4.1 X-ray photoelectron spectroscopy (XPS):

The XPS survey spectrum of CCBG, M CCBG, M B1 CCBG, M B2 CCBG and M B3 CCBG NPs confirmed respectively the existence of Ca 2p (346.6 eV, 347 eV, 346.7 eV, 346.7 eV and 348 eV), O 1s (532 eV, 532.3 eV, 532.1 eV, 532.6 eV and 533.4 eV), P 2p (127.2 eV), Na 1s (1071 eV), Si 2p (102.8 eV, 102.8 eV, 102.7 eV, 10.3.3 eV and 104.4 eV) as well as the spurious C 1s peak (284.1 eV, 284.1 eV, 284.1 eV, 284.4 eV and 285.3 eV) (Fig. 1(a-e)). The C 1s peak (284.1 eV) might have arrived from template molecule [40]. Doping of Mg<sup>2+</sup> in M CCBG was represented by Mg 1s (1303.6 eV). Co-doping of Mg<sup>2+</sup> and Bi<sup>3+</sup> in M B1 CCBG, M B2 CCBG and M B3 CCBG were indicated by peaks corresponding to Mg 1s (1303.3 eV, 1302.6 eV, 1305.4 eV) and Bi 4f (158.7 eV, 158.7 eV, 159.1 eV) respectively [30,41]. In case of Bi<sup>3+</sup> doping, intensities of Bi 4f peak increased with increase in doping concentration (0.5 mol% to 1.5 mol%). As illustrated in Fig. S1(a-e), high resolution XPS spectra of Si 2p, Ca 2p, C 1s, P 2p, Na 1s, O 1s, Mg 1s and Bi 4f were also recorded to determine the chemical status of the corresponding elements as depicted in Table I. The experiments were performed with the VGESCALAB II system using AlKα radiation. A single peak at 1071 eV and 127.2 eV reported for Na 1s and P 2p as phosphate moieties [42] respectively for BG NPs. The observation is in good agreement with similar characteristic of phosphate moieties as reported elsewhere in other reported BG network [43]. Ca 2p signals showed two peaks correspond to Ca 2p<sub>1/2</sub> and Ca 2p<sub>3/2</sub>, which are separated by approximately ~3.5 eV. The broad XPS peaks of O 1s was divided into two peaks located at 532.6 eV and 529.7 eV, revealing two different kinds of chemical status of oxygen in BG NPs. The peak at 529.7 eV is ascribed to the lattice oxygen. O 1s signals show major contribution of a band at 532.6 eV assigned to oxygen atoms in phosphates, hydroxyl, and adsorbed water [44]. C 1s signal at 284.1 eV in BG samples confirm the contribution of C atoms appeared from a carbonate environment, probably from the template CC. M CCBG showed signal due to Mg 1s while M B1 CCBG, M B2 CCBG and M B3 CCBG indicated both

the signals due to Mg 1s and Bi 4f respectively. Binding energy (BE) value of Mg 1s at 1303.6 eV indicated the existence of MgO [45] in M\_CCBG, M\_B1\_CCBG and M\_B2\_CCBG. The O 1s peak showed a shoulder around 529.7 eV, which is due to existence further confirm the existence of MgO in M\_B2\_CCBG [45]. The XPS spectra of Bi 4f depicted the two peaks at 164 eV and 158.7 eV can be assigned to Bi 4f5/2 and Bi 4f7/2, respectively [30]. The reported two shoulders revealed the existence of Bi species as Bi<sup>3+</sup> in the form of Bi<sub>2</sub>O<sub>3</sub> [46]. Also, slight change in binding energies of Bi 4f from M\_B1\_CCBG (158.7 eV, 164 eV), M\_B2\_CCBG (158.9 eV, 164.1 eV) to M\_B3\_CCBG (159.1 eV, 164.4 eV) confirmed changes in the environment of Bi<sup>3+</sup> in BG network due to its increasing concentrations as 0.5 mol%, 1 mol% and 1.5 mol% respectively. Hence, XPS studies confirmed the presence of dopant Mg<sup>2+</sup> as MgO in M\_CCBG and co-doped BG. Importantly, co-doped BG contain Bi species in the form of Bi<sub>2</sub>O<sub>3</sub>.

**Table 4.1:** Binding energy (eV) of CCBG, M\_CCBG, M\_B1\_CCBG, M\_B2\_CCBG and M\_B3\_CCBG by XPS analysis.

XPS									
Various	Binding energy (eV)								
Elements	CCBG	M_CCBG	M_B1_CCBG	M_B2_CCBG	M_B3_CCBG				
C (1s)	284.1	284.1	284.1	284.4	285.3				
Ca (2p)	346.6,	347, 350.6	346.7, 350.5	346.7, 350.1	348, 351.6				
	350								
Na (1s)	1071	-	-	-	-				
O (1s)	532	532.3	532.1	529.7, 532.6	533.4				
P (2p)	127.2	127.2	-	-	-				
Si (2p)	102.8	102.8	102.7	103.3	104.4				
Mg (1s)	-	1303.6	1303.3	1302.6	1305.4				
Bi (4f)	-	-	158.7, 164	158.7, 164	159.1, 164.4				

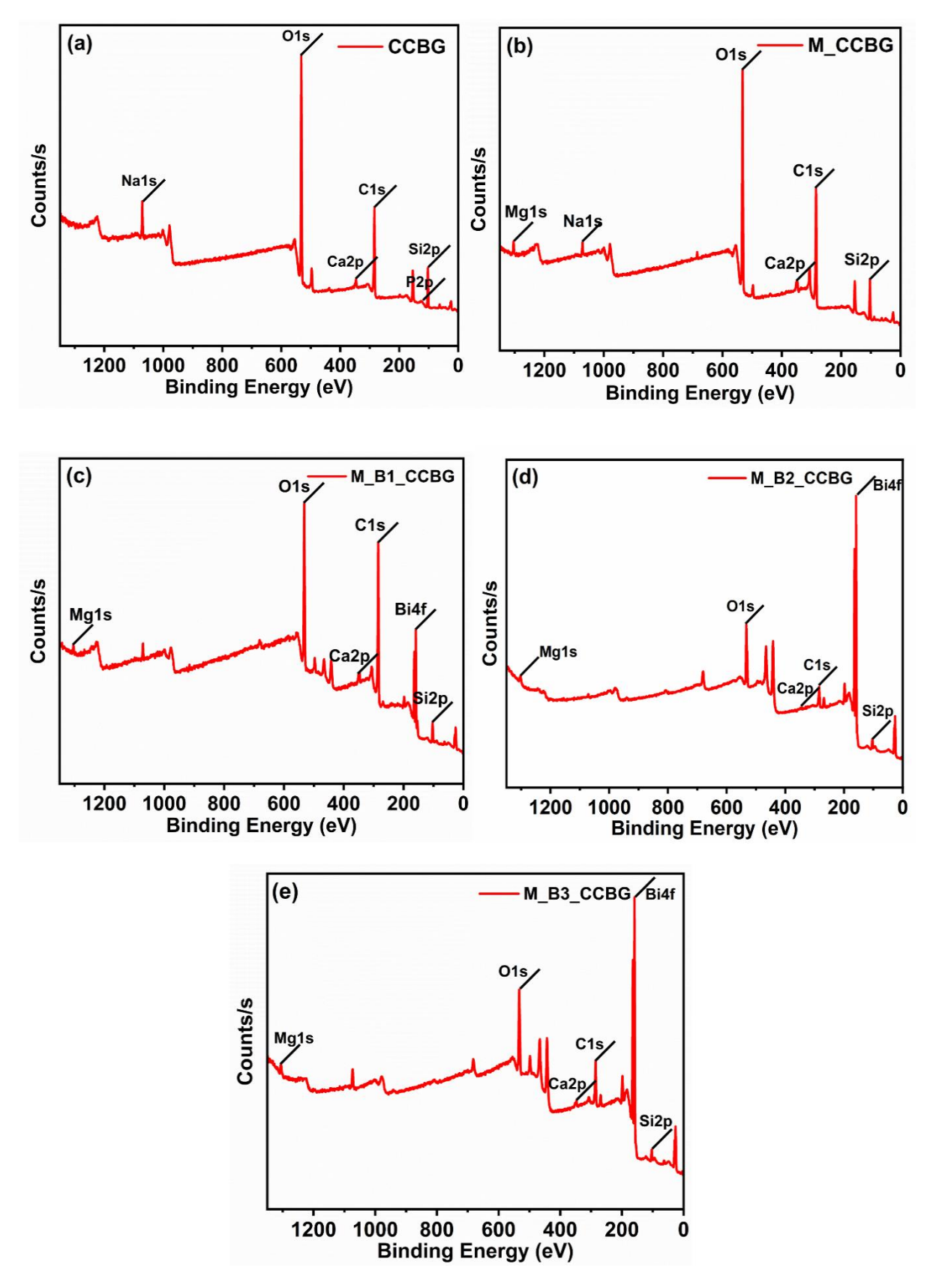


**Fig. 4.1(a-e):** XPS survey spectra of CCBG, M\_CCBG, M\_B1\_CCBG, M\_B2\_CCBG and M\_B3\_CCBG

### 4.4.2 X-ray diffraction (XRD) analysis:

The XRD patterns of various BG NPs are shown in Fig. 2 (a-b). A broad diffracting domain in  $2\theta$ range of 15° and 30° with few less intense reflections observed for CCBG and M CCBG indicated semi-crystalline nature. In CCBG, typical diffraction patterns correspond to Ca<sub>0.89</sub>Na<sub>0.11</sub>O<sub>3</sub>P<sub>0.11</sub>Si<sub>0.89</sub> (JCPDS 00-033-1229) at 2θ values of 24.5° (002), 29.7° (102), 37.6° (200), 40.8° (201), and 44.4° (202) were seen [31], which confirm the formation of BG network. The XRD pattern of M CCBG (Fig. 2a) showed only a few diffracting domains correspond to Ca<sub>0.89</sub>Na<sub>0.11</sub>O<sub>3</sub>P<sub>0.11</sub>Si<sub>0.89</sub> (JCPDS 00-033-1229) at  $2\theta$  values at  $224.5^{\circ}$  (002),  $29.7^{\circ}$  (102). Other reflections reported at  $2\theta$  values of  $31.6^{\circ}$ (100) and 45.4° (102) confirmed existence of Mg species and in good agreement with JCPDS 00-001-1148. This indicates that even after Mg<sup>2+</sup> doping, there was not much crystalline phase present in M CCBG [32]. The reported minimal diffraction domains in CCBG and M CCBG suggested a disorganised structure. Co-doped M B1 CCBG, M B2 CCBG, and M B3 CCBG samples exhibited distinctive reflections of BG Ca<sub>0.89</sub>Na<sub>0.11</sub>O<sub>3</sub>P<sub>0.11</sub>Si<sub>0.89</sub> (JCPDS 00-033-1229) with 20 values of 25.9° (002) and 54.3° (104) along with diffracting domains due to both Mg as well as Bi species. For all co-doped samples, presence of Mg species was confirmed by appearance of similar diffracting domains as seen in the case of M CCBG. The existence of Bi species in M B1 CCBG, M B2 CCBG, and M B3 CCBG was confirmed from 2θ values of 40.5° (110) and 58.5° (024) (JCPDS 00-001-0688). As the concentration of Bi doping rises (from 0.5 mol% to 1.5 mol%), the corresponding diffraction patterns move towards low angles and narrow with a full width half maximum (FWHM). The observation indicated good crystalline nature of co-doped samples compared to CCBG and M CCBG. Fig. 2b also depicts an increase in the intensity of XRD patterns corresponds to Bi<sup>3+</sup> dopant concentration (2θ values of 40.5° (110) and 58.5° (024) (JCPDS 00-001-0688)). The incorporation of large sized metallic dopant (Bi<sup>3+</sup> ions) into the amorphous BG network enhances the crystallinity and increases the intensity of corresponding diffraction pattern with increase in Bi<sup>3+</sup> concentration. The Debye-Scherrer formula, which is  $(D = k\lambda / \beta \cos\theta)$  where K is the

constant,  $\lambda$  is the X-ray wavelength,  $\beta$  is the peak width of the half-maximum of the diffraction peak, and  $\theta$  is the X-ray diffraction angle, can be used to quantitatively determine the mean crystallite size. The mean crystallite size of M\_B1\_CCBG, M\_B2\_CCBG and M\_B3\_CCBG was calculated as 0.1  $\pm$  0.01 nm for, 0.2  $\pm$  0.01 nm, and 0.25  $\pm$  0.04 nm respectively. Herein, each size value represented is an average of triple tests. At the lowest concentration of Bi<sup>3+</sup> (0.5 mol%) the average crystallite size is comparatively smaller than that of M\_B2\_CCBG and M\_B3\_CCBG. The observation confirms a reduction of amorphous phase in co-doped BG with increase in Bi<sup>3+</sup> concentration, which is metallic in nature. The above results are in good accord with XPS and evidence the incorporation of MgO and Bi<sub>2</sub>O<sub>3</sub> species in BG network.

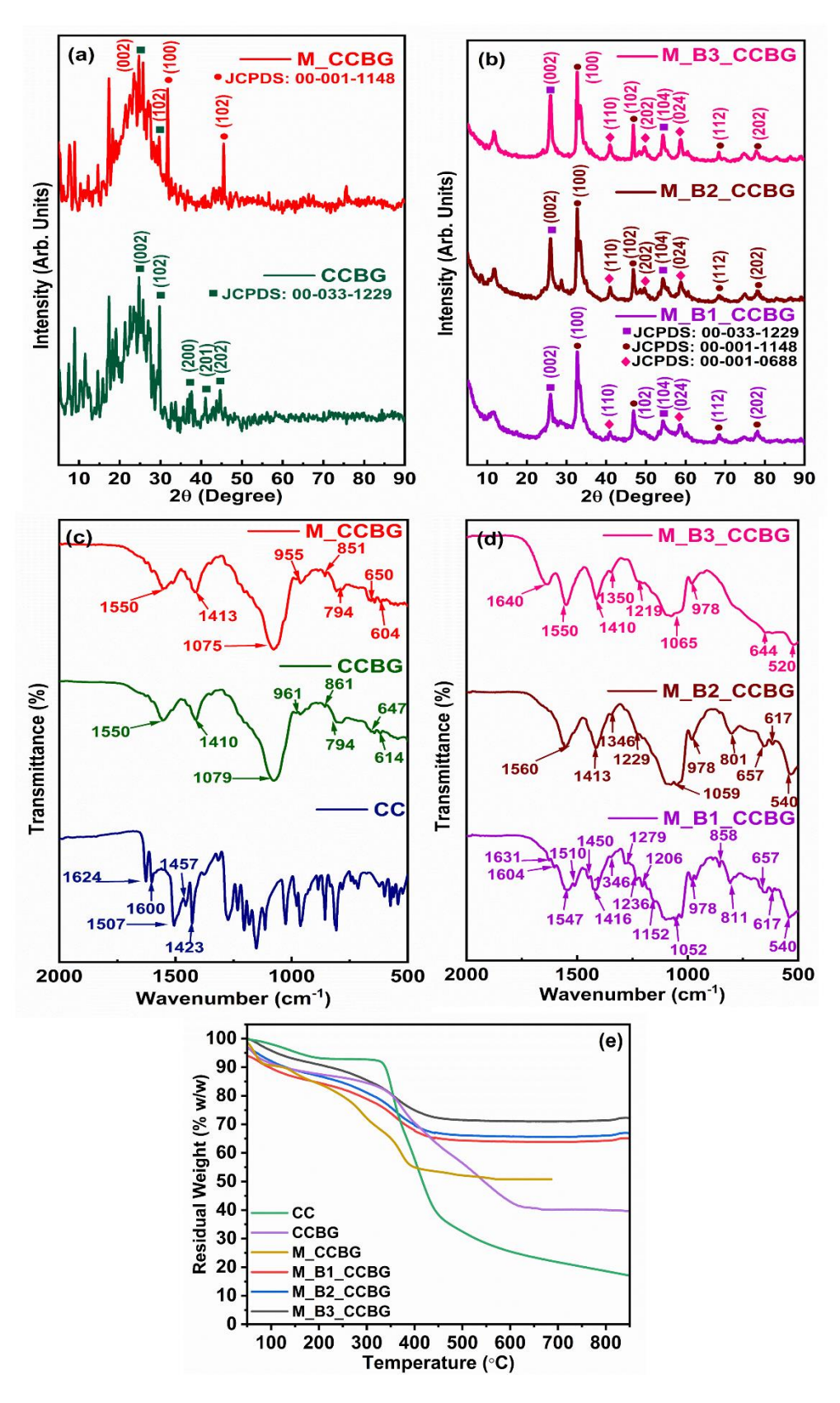


**Fig. 4.2(a-b):** XRD patterns of CCBG, M\_CCBG, M\_B1\_CCBG, M\_B2\_CCBG and M\_B3\_CCBG, **(c-d)** FTIR spectra of CCBG, M\_CCBG, M\_B1\_CCBG, M\_B2\_CCBG and M\_B3\_CCBG and **(e)** Thermogravimetric analysis of CC, CCBG, M\_CCBG, M\_B1\_CCBG, M\_B2\_CCBG and M\_B3\_CCBG.

### 4.4.3 Fourier transform infrared spectroscopy (FTIR):

In CCBG, two broad peaks at 1550 cm<sup>-1</sup> due to overlapping vibrations of carbonyl C=O stretching as well as skeletal vibrations of keto-enol configuration and at 1410 cm<sup>-1</sup> due to aromatic C=C stretching vibrations were reported. These characteristic vibrations must be emerged from remnant CC (template) molecules of CCBG (Fig. 2c) [47]. The reported carbonyl peak in CCBG (1550 cm<sup>-1</sup>) was at higher wavenumber compared to native CC molecule (1507 cm<sup>-1</sup>). It might be indicating interactions of -C=O group with BG network and in good agreement with our earlier reports [48]. Stretching vibrations due to Si—O—Si, Si—O—C and Si–O– of CCBG were reported at 1079 cm<sup>-1</sup>. A shoulder at 961 cm<sup>-1</sup> is due to P—O—C, P—O—Si vibrations. Symmetric stretching vibration of Si-O appeared at 861 cm<sup>-1</sup>. The characteristic ring vibration of the silicate network was appeared at 794 cm<sup>-1</sup>. The P-O stretching and Si-O-Si vibrations were shown at 647 cm<sup>-1</sup> and 614 cm<sup>-1</sup> respectively. All these FTIR peaks were also seen more or less at the same positions for Mg<sup>2+</sup> doped and co-doped BG. Interestingly, sharper silicate network peak found around 1075 cm<sup>-1</sup> for CCBG and M CCBG was broadened and centred at lower wavenumber 1050 cm<sup>-1</sup> for co-doped samples (Fig. (c-d)). The finding confirmed the rearrangement of silicate network due to largest dopant Bi<sup>3+</sup>, which might lead to form Si-O-Bi bond [49,50]. In addition, M-O bending vibration was reported at 540 cm<sup>-1</sup> for all co-doped BG. The above FTIR peaks of BG NPs confirm the entrapped CC molecule in BG network. In addition, the existence of dopants in the glass structure of doped BG were also evidenced [51] by supporting finds of XPS and XRD analysis (Fig. 1(a-e) and Fig. 2(a-b))

### 4.4.4 Thermogravimetric (TGA) analysis:

Thermograms of BG NPs were portrayed in (Fig. 2e). CCBG showed 9.8 w/w% weight loss in the temperature range from 50 °C to 215 °C due to evaporation of sorbed water molecules. The weight loss of 46.8 w/w% was seen for CCBG in the temperature range 215 °C -699 °C. The reported weight

loss pattern is more or less in good agreement with CC thermogram, evidencing existence of CC content in BG network [52]. The observation also corroborates with XPS, XRD and FTIR results (Fig. 1(a-e) and Fig. 2(a-d)). Similarly, M\_CCBG and co-doped BG NPs displayed majorly two steps of degradation with elevated material stability in the temperature range of 456 °C to 850 °C in comparison with CCBG (215 °C to 841 °C). The thermal stability of various BG NPs was reported in the order CCBG < M\_CCBG < M\_B1\_CCBG ≈ M\_B2\_CCBG < M\_B3\_CCBG. The observation evidenced existence of CC content in BG network is depending on the dopants (Mg²+ and Bi³+). The heaviest and highly polarizable Bi³+ showed greater affinity towards BG network compared to Mg²+ and CC molecules and in good agreement with FTIR findings (Fig. 2(c-d)).

### 4.4.5 Morphological studies

### 4.4.5.1. Field emission scanning electron microscopy (FE-SEM):

FE-SEM micrographs (Fig. 3(a-e)) of CCBG and doped BG portrayed highly aggregated particles with regular morphology. HR-TEM micrographs of BG were observed to be nanosized as well as aggregated (Fig. 3(a-e)).

### 4.4.5.2. High resolution transmission electron microscopy (HR-TEM):

Particle sizes of CCBG, M\_CCBG, M\_B1\_CCBG, M\_B2\_CCBG and M\_B3\_CCBG were analyzed using Image J analysis and reported as  $10.1 \pm 0.3$  nm,  $16.7 \pm 0.7$  nm,  $50 \pm 0.9$  nm,  $47 \pm 0.9$  nm and  $46.7 \pm 0.3$  nm respectively. The doping of Mg<sup>2+</sup> has significant effect on particle size of M\_CCBG ( $16.7 \pm 0.7$  nm) compared to CCBG ( $10.1 \pm 0.3$  nm), which showed increase in particle size due to the phase change. Similarly, co-doped sample M\_B1\_CCBG ( $50 \pm 0.9$ ) also showed increase in particle size. Further increase in the concentration of Bi<sub>2</sub>O<sub>3</sub> from 0.5 mol% to 1.5 mol % did not show much effect on the particles size. Furthermore, SAED patterns of CCBG and M\_CCBG depicted

amorphous nature. Doping of Bi<sup>3+</sup> makes M\_B1\_CCBG, M\_B2\_CCBG and M\_B3\_CCBG crystalline in nature due to its metallic behavior. In SAED pattern, M\_B1\_CCBG exhibit the diffraction rings (JCPDS: 00-033-1229 for BG, JCPDS: 00-001-1148 for Mg, JCPDS: 00-001-0688 for Bi) (002 (BG)), (100 (Mg)), (110 (Bi)), (102 (Mg)), (104 (BG)) and (112 (Mg)) corresponding to d-spacing 3.3 Å, 2.7 Å, 2.2 Å, 1.9 Å, 1.5 Å and 1.3 Å respectively (Fig. 3(c)). Similarly, SAED pattern of M\_B2\_CCBG (Fig. 3(d)) was reported with d-spacing 3.2 Å, 2.6 Å, 2.1 Å, 1.8 Å, 1.6 Å and 1.5 Å corresponds to (002 (BG)), (100 (Mg)), (110 (Bi)), (102 (Mg)), (104 (BG)) and (024 (Bi)) respectively. M\_B3\_CCBG (Fig. 3(e)) also exhibited diffraction rings (002 (BG)), (100 (Mg)), (202 (Bi)), (104 (BG)), (024 (Bi)), (112 (Mg)) and (208 (Bi)) with d-spacing at 3.2 Å, 2.6 Å, 1.8 Å, 1.6 Å, 1.5 Å, 1.3 Å and 1.1 Å respectively. Few of these hkl values of BG NPs are in good accord with XRD analysis (Fig. 2(a-b)).

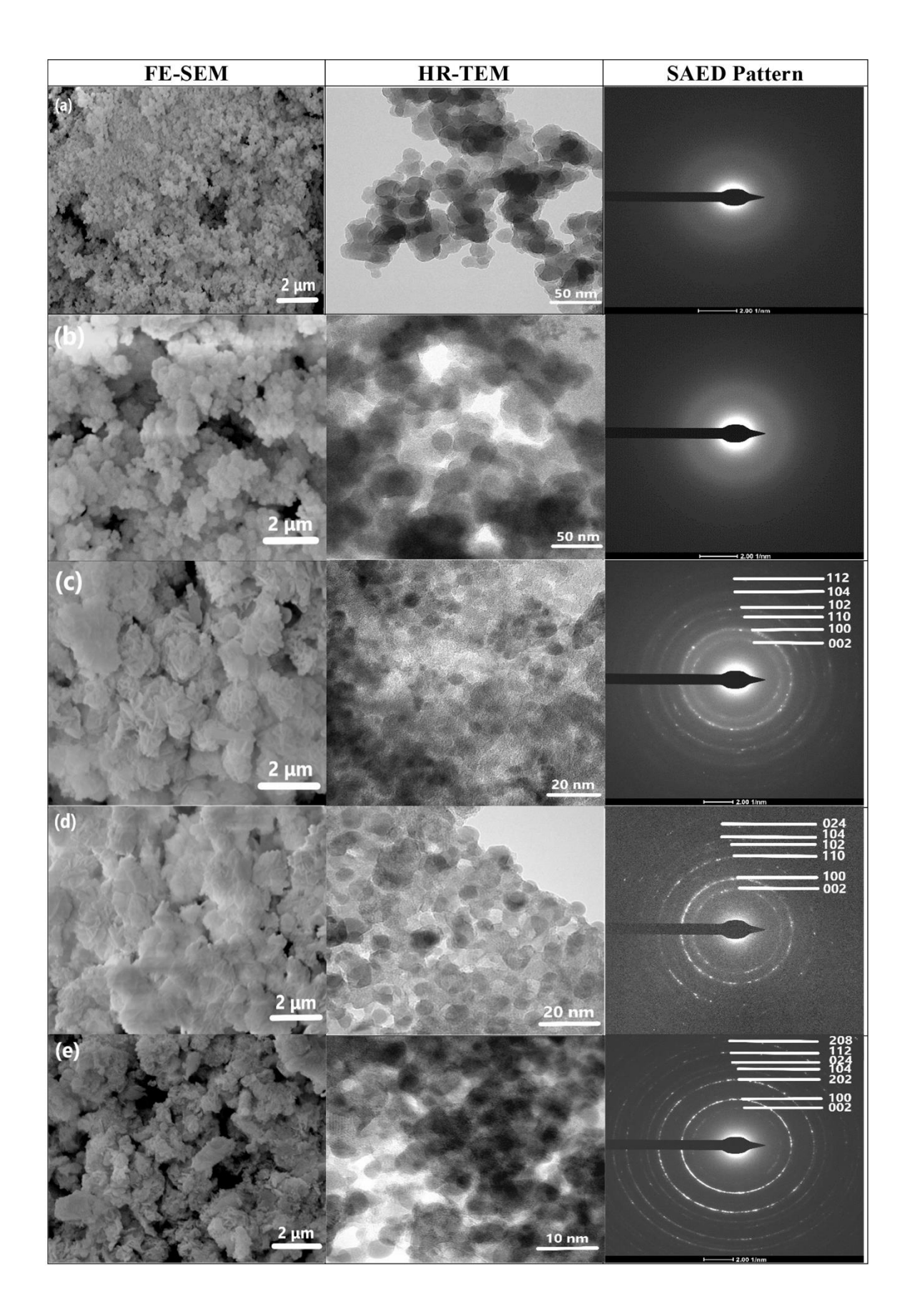


**Fig. 4.3(a-e):** FE-SEM, HR-TEM micrographs in bright field and SAED pattern of CCBG, M\_CCBG, M\_B1\_CCBG, M\_B2\_CCBG and M\_B3\_CCBG.

### 4.4.6 Nitrogen sorption analysis (BET):

The porosity and surface area of BG NPs were evaluated using nitrogen sorption analysis (Fig.4 (ae)) and the pore width, pore volume, and surface area are shown in Table II. Based on nitrogen adsorption-desorption isotherms and the BET analysis, surface area of each BG NPs was determined. The adsorption isotherm of all BG were classified as Type IV by the IUPAC standard nomenclature, with an H1 hysteresis loop that is typical of mesoporous materials with uniform pore diameters [50]. M B2 CCBG was reported with the highest specific surface area (52.863 m<sup>2</sup>/g) among the other samples. The pore sizes of all BG NPs were reported in the lower mesoporous range (2 nm-50 nm) by Barrett-Joyner-Halenda (BJH) method. The highest pore diameter 25.7 nm was reported for CCBG. However, pore diameter for M CCBG and M B1 CCBG drastically decreased to 2.499 nm and 2.482 nm, respectively, suggesting reorganization BG network in the presence of dopants. In contrast, an increase in pore diameter was reported for co-doped BG with increase in Bi3+ concentration (M B1 CCBG (2.482 nm) < M B2 CCBG (7.143 nm) < M B3 CCBG (8.672 nm)). The observation suggested the discontinuity of BG network due to the largest size and increase in concentration of Bi<sup>3+</sup>. The pore diameters of doped and co-doped BG are in good agreement with the corresponding pore volume data. Surface area of each doped and co-doped BG was found more or less same compared to CCBG (control). All these findings indicate that the dopants Bi<sup>3+</sup> as well as Mg<sup>2+</sup> primarily function as network modifiers and Bi<sup>3+</sup> as network former [53,54] and in consistent with NMR (Fig. 5(a-b)) and XPS (Fig. 1(a-e)) findings.

**Table 4.2:** Surface area, pore volume and pore size data of CCBG, M\_CCBG, M\_B1\_CCBG, M\_B2\_CCBG and M\_B3\_CCBG.

	CCBG	M_CCBG	M_B1_CCBG	M_B2_CCBG	M_B3_CCBG
Total Surface Area (a <sub>s,BET</sub> [m <sup>2</sup> g <sup>-1</sup> ])	29.506	45.696	50.826	52.863	47.187
Total pore volume( $p/p_0$ =0.944) [cm <sup>3</sup> g <sup>-1</sup> ]	0.247	0.083	0.115	0.168	0.175
Mean pore diameter [nm]	25.682	2.499	2.482	7.143	8.672

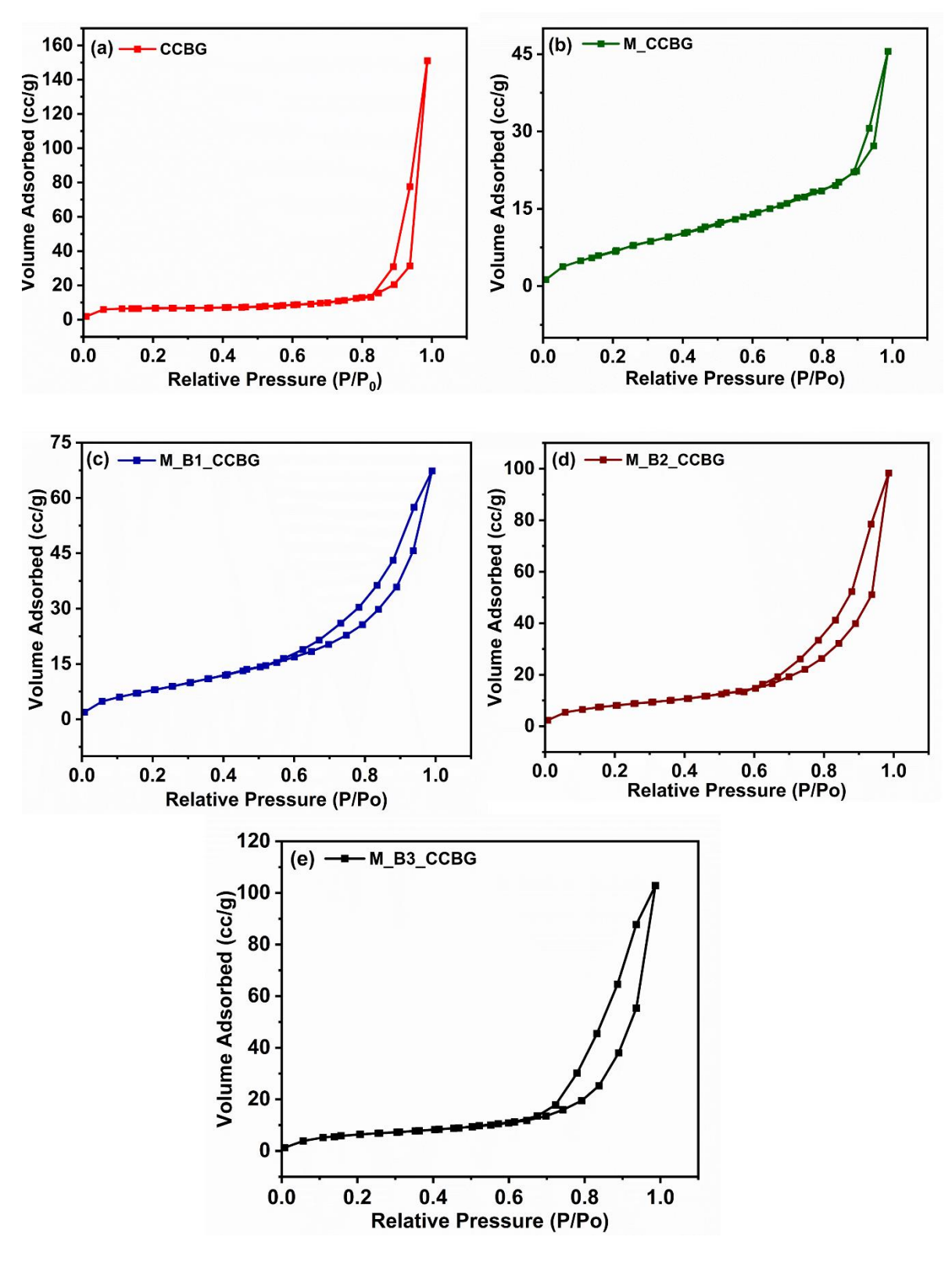


**Fig. 4.4(a–e):** Nitrogen Sorption Analysis of CCBG, M\_CCBG, M\_B1\_CCBG, M\_B2\_CCBG and M\_B3\_CCBG.

# 4.4.7 <sup>29</sup>Si solid state nuclear magnetic resonance (NMR):

The structure of silicate glasses can be well described by <sup>29</sup>Si NMR technique by connectivity and distribution of Q<sup>n</sup> species. Q stands for tetrahedral structural unit and n for number of bridging oxygen atoms [31]. The chemical shift from magic angle spinning (MAS) nuclear magnetic resonator (NMR) is an indicative of the type of chemical species present in the glass sample. The effect of dopants (Mg<sup>2+</sup> and Bi<sup>3+</sup>) on substituting network modifiers namely, Na<sup>+</sup> and Ca<sup>2+</sup> within 45S5 BG composition are elucidated via <sup>29</sup>Si MAS solid state NMR (Fig. 5(a-b)). For each undoped and doped BG NPs an asymmetrical peak was reported and was deconvolved by Gaussian fitting. A negative shift was observed in peak position of the Si-related signal by 0.18, 5.93, 1.02, and 6.82 ppm values for M\_CCBG, M\_B1\_CCBG, M\_B2\_CCBG respectively compared to CCBG. The reported <sup>29</sup>Si signal shift indicates a change in the network modifier cation of the control sample. In detail, an increase of the Q<sup>3</sup> species were seen for M CCBG; with the simultaneous increase in Q<sup>4</sup> in the glass network neutralized with Mg<sup>2+</sup>. For co-doped BG, upto 1.5 mol% increase in Bi<sup>2+</sup>, Q<sup>4</sup> and Q<sup>2</sup> species increase with a decrease in Q3 and Q1 species. Further, increasing the concentration of Bi2+ to 1.5 mol% a drastic change in network structure was reported by elevating the existence of O<sup>3</sup> species compared to other species. In general, increase in Q<sup>4</sup> fraction for doped BG could also supported by the FTIR spectra (Fig. 2(c-d)) with a broadening in the peak centered at 1079 cm<sup>-1</sup> attributed to Si-O-Si vibrations compared to the control. In comparison with CCBG, a broader <sup>29</sup>Si peak is seen for M\_CCBG, M\_B1\_CCBG, M\_B2\_CCBG (10.33) and M\_B3\_CCBG (10.33) with FWHM of the <sup>29</sup>Si signal 10.48 ppm (-0.15 ppm), 27.38 ppm (-17.05 ppm), 29.05 ppm (-18.72 ppm) and 19.09 ppm (-8.76 ppm) respectively. The fractions of Q<sup>n</sup> distribution and resulting network connectivity (NC) were calculated as per the equation (Eq1) (Table 2).

Eq1 
$$NC = \frac{4Q^4 + 3Q^3 + 2Q^2 + 1Q^1}{100}$$

The higher network connectivity was reported for only Mg <sup>2+</sup> doped M\_CCBG in comparison to CCBG, which suggests a repolymerization effect caused by introducing dopant in the form of MgO

value decreased with 0.5 mol% Bi<sup>3+</sup> doping for M\_B1\_CCBG (9.62) and more or less remained at the same for M\_B2\_CCBG (1 mol% Bi<sup>3+</sup>, 10.75) and M\_B3\_CCBG (1.5 mol% Bi<sup>3+</sup> 10.66) compared to M\_CCBG. The observation indicates, incorporation of Bi<sup>3+</sup> as Bi<sub>2</sub>O<sub>3</sub> depolymerizes at low concentration due to its larger size. In contrast, repolymerises with increasing concentration of Bi<sup>3+</sup> indicating the domination of dopant charge affinity towards the negatively charged silica network.

**Table 4.3:** Q<sup>n</sup> content, chemical shift (δ) and relative intensity (I) data of CCBG, M\_CCBG, M\_B1 CCBG, M\_B2 CCBG and M\_B3 CCBG

Samples	Q <sup>4</sup>		$Q^3$		$Q^2$		Q <sup>1</sup>		NC
Samples	δ(ppm)	I(%)	δ(ppm)	I(%)	δ(ppm)	I(%)	δ(ppm)	I(%)	
CCBG	-127.2	5.88	-111.4	64.7	-99.8	29.42	-	-	10.42
M_CCB G	-124.2	9.09	-111.4	68.18	-100.5	18.18	-89.8	4.55	11.21
M_B1_ CCBG	-110.6	15.78	-107	63.15	-99.4	21.05	-	-	9.62
M_B2_ CCBG	-111.9	25.65	-105.7	21.73	-104.4	52.17	-101.7	0.45	10.75
M_B3_ CCBG	-111	15.78	-110.2	21.05	-100.8	10.52	-90.1	52.63	10.66

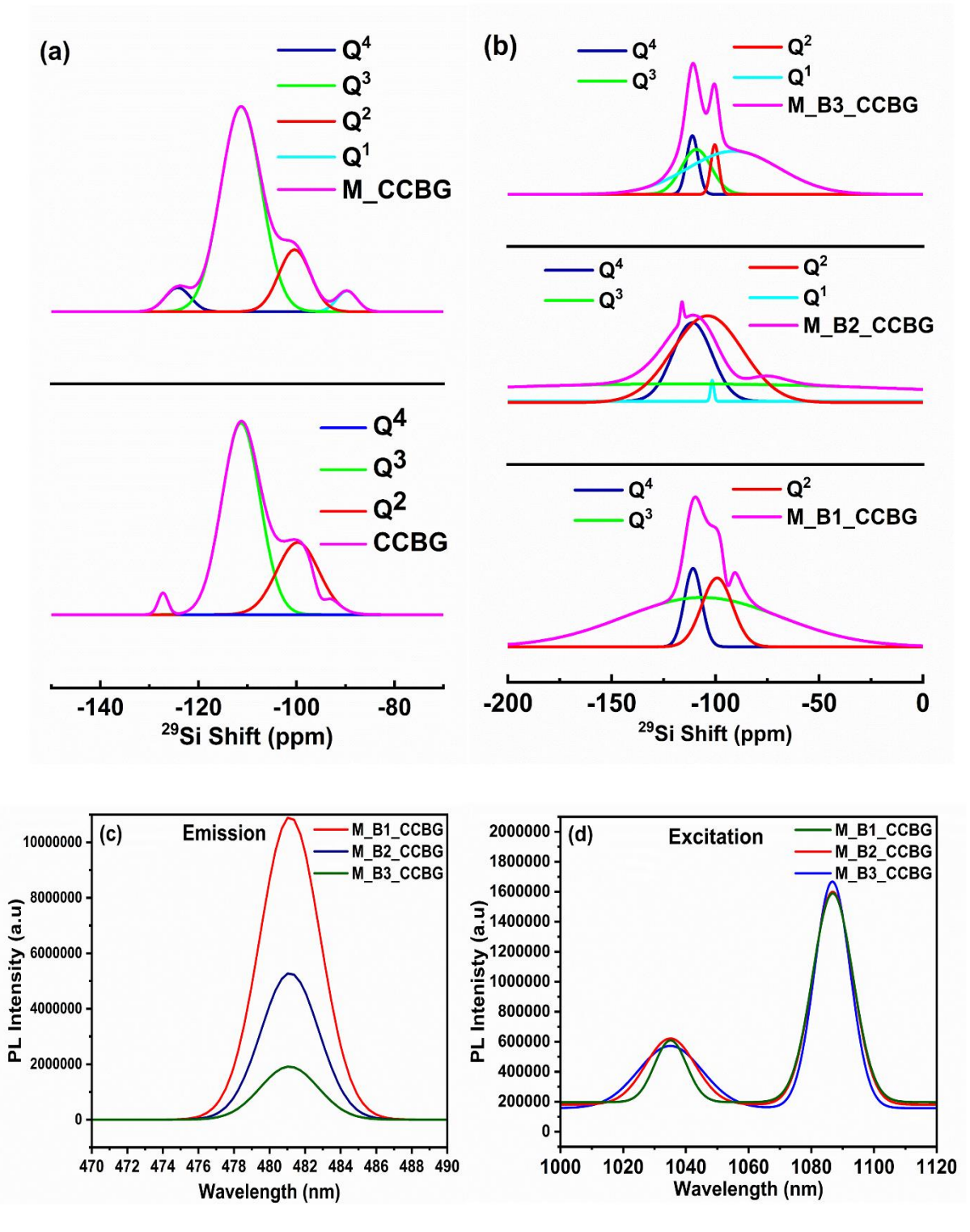


**Fig. 4.5(a–b):** NMR spectra of CCBG, M\_CCBG, M\_B1\_CCBG, M\_B2\_CCBG and M\_B3\_CCBG, **(c-d)** Photoluminescence spectra of M\_B1\_CCBG, M\_B2\_CCBG and M\_B3\_CCBG.

### 4.4.8 Photoluminescence study (PL):

PL spectra of M\_B1\_CCBG, M\_B2\_CCBG, and M\_B3\_CCBG with varying concentrations of Bi3+ (0.5 mol%, 1 mol%, and 1.5 mol%) respectively recorded at room temperature are shown in Fig. 5(cd). At 1086 nm excitation wave length in NIR region co-doped BG NPs showed a strong emission peak at blue region centered around 480 nm. Bi<sup>3+</sup> doped BG samples exhibit two broad excitation bands with marginally same intensities at around ~1035 nm and ~1086 nm. Since, the peak positions of PL signals in excitation spectrum do not change a little, indicates that there are several relatively stable energy levels of excitons and surface states [56]. The single broad band seen at 480 nm for all three co-doped BG samples in the blue region were originating from Bi<sup>3+</sup> ions due to  ${}^{3}P_{1} \rightarrow {}^{1}S_{0}$ transition [57]. For Bi<sup>3+</sup> ions allowed transitions are from  ${}^{1}S_{0} \rightarrow {}^{1}P_{1}$  and  ${}^{1}S_{0} \rightarrow {}^{3}P_{1}$ , and the other transitions to the upper states are spin forbidden. Thus Bi<sup>3+</sup> ions show transitions from the ground level to either the <sup>1</sup>P<sub>1</sub> or <sup>3</sup>P<sub>1</sub> states. Subsequently Bi<sup>3+</sup> ions emit luminescence in the blue area due to non-radiative relaxation to the <sup>3</sup>P<sub>1</sub>/ <sup>1</sup>S<sub>0</sub> states. The PL signal intensity decreases with increasing Bi<sup>3+</sup> doping concentration, suggesting effective suppression of photo-generated electron-hole pair recombination in bulk crystal defects [56]. This observed PL emission of co-doped BG NPs promises for great potential to function as PTA in wide variety of biomedical applications. For example, psoriatic and skin illnesses were shown to be effectively treated with PL due to its strong emission peak at about 480 nm [58].

### 4.4.9 Bioactivity test:

Dissolution of BG in physiological fluids is highly depending on structure as well as composition [59], which further tunes bioactivity and promotes osteoblastic activity followed by cell differentiation [11]. As a result, bone-like apatite forms on the surface of BG. In the present study, bioactivity of BG NPs was evaluated after immersing in simulated body fluid (SBF) using FTIR,

XRD and FE-SEM analysis for the duration of 1 d to 15 d as per the procedure described by Kokubo *et al* [36]. The XRD analysis (Fig. 6 (a-e)) after interaction with SBF for 4 d indicated new diffraction maxima at 2 $\theta$  values of 12.2° (100), 14.5° (101), 17.2° (110), 21.4° (200), 23.4° (111), 25.5° (002), 27.3° (102) (JCPDS file no. 01-024-0033) having chemical formula Ca<sub>5</sub>(PO<sub>4</sub>)<sub>3</sub>(OH) for CCBG in comparison with the corresponding virgin sample (Fig. 6a). The intensity of these new diffraction maxima was observed to slightly increase along with few more new reflections from 4 d to 15 d on interaction with SBF. Similar to the control (0 d) the broad diffracting domain in 2 $\theta$  range of 15° and 30° was retained indicating semi crystalline nature. The observations are almost similar in the case of M\_CCBG. After immersion in SBF, co-doped BG NPs resulted with almost similar diffraction pattern as corresponding virgin BG but with increase in intensity except very few new reflection (2 $\theta$  value of 74.8° (215)). The reported diffraction pattern of co-doped BG NPs mostly in overlap with Ca<sub>5</sub>(PO<sub>4</sub>)<sub>3</sub>(OH) (JCPDS file no. 01-024-0033).

These observations are also in good agreement with FTIR analysis after immersion in SBF (Fig. S3(a-e)). For all BG NPs after immersing in SBF, small shoulder reported at 1634 cm<sup>-1</sup> due to O-H deformation and phosphate peaks at 800 cm<sup>-1</sup>, 600 cm<sup>-1</sup> and 560 cm<sup>-1</sup> were reported from 0 d to 15 d with increase in intensity by supporting the deposition of Ca<sub>5</sub>(PO<sub>4</sub>)<sub>3</sub>(OH) on BG NPs. FE-SEM micrographs of various BG NPs after 1 d, 7 d and 15 d of interaction with SBF are shown in Fig. 7(a-e). These micrographs display markedly distinct rough surface morphology compared to the bare surface morphology of untreated BG NPs possibly due to the deposition of Ca<sub>5</sub>(PO<sub>4</sub>)<sub>3</sub>(OH). The rapid apatite deposition on BG samples can be due to their mesoporous nature of the sample (Fig. 7(a-e)). In general, micrographs display dense apatite deposition from 4 d to 15 d of SBF incubation for codoped BG NPs. After interaction with SBF, smaller particle size, high surface area, larger pore volume and pore diameter (Fig. 4(a-e) and Table II) help in faster dissolution of ions from the co-doped BG NPs into the surrounding SBF solution. Further, introduction of larger network modifier Bi<sup>3+</sup> provoked and broke some of the Si–O–Si bonds leading to the formation of non-bridging oxygen

groups (Si–O–NBO) (Fig. 5(a-b)) and increase the silica dissolution rate through the formation of silanol groups at the glass surface. As a result, faster deposition of apatite onto the surface of BGNPs can be seen within few days of incubation in SBF [60].

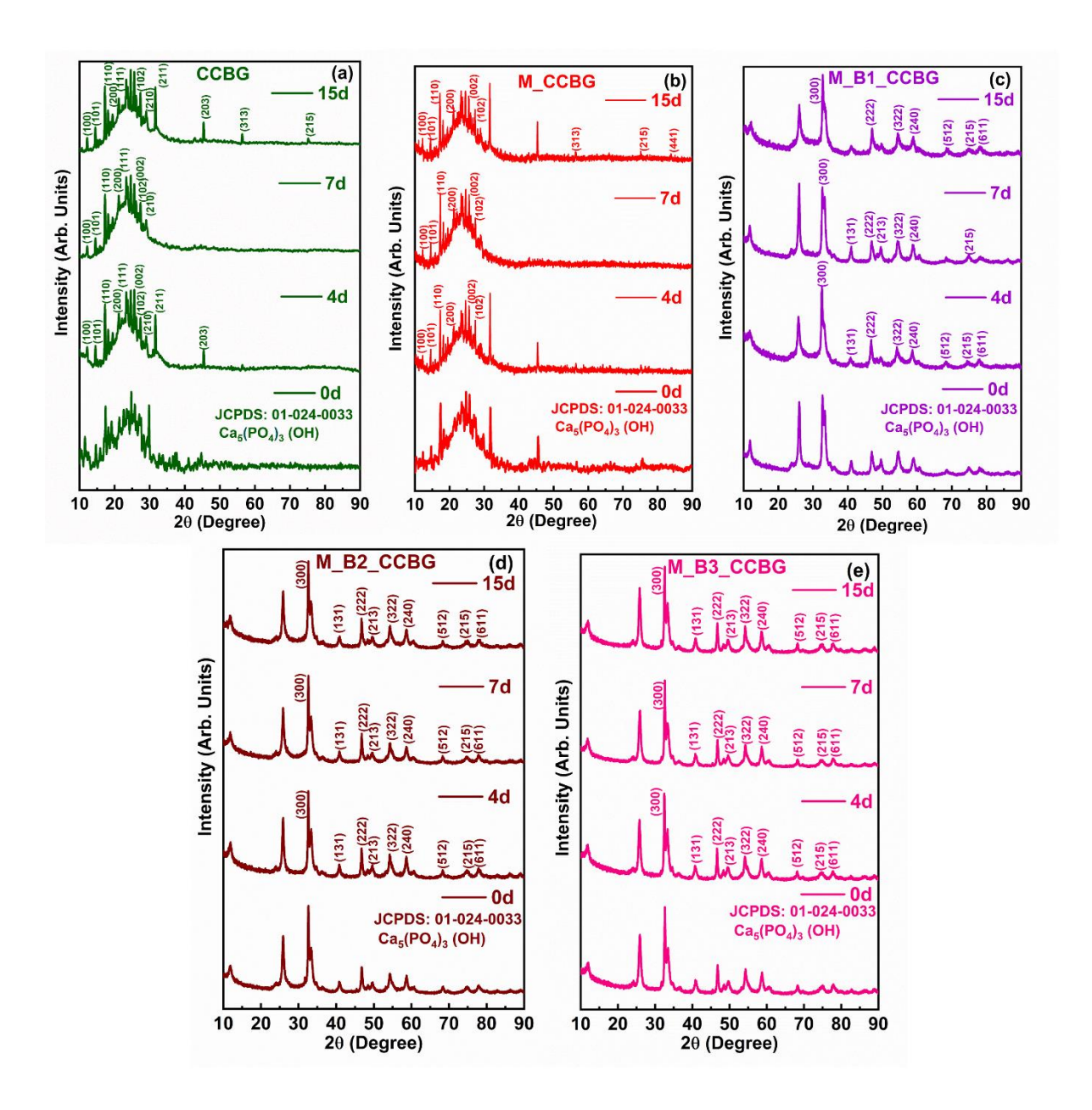


**Fig. 4.6(a-e):** XRD patterns of CCBG, M\_CCBG, M\_B1\_CCBG, M\_B2\_CCBG and M\_B3\_CCBG after 1 d, 4 d, 7 d, and 15 d of bioactivity in SBF solution.

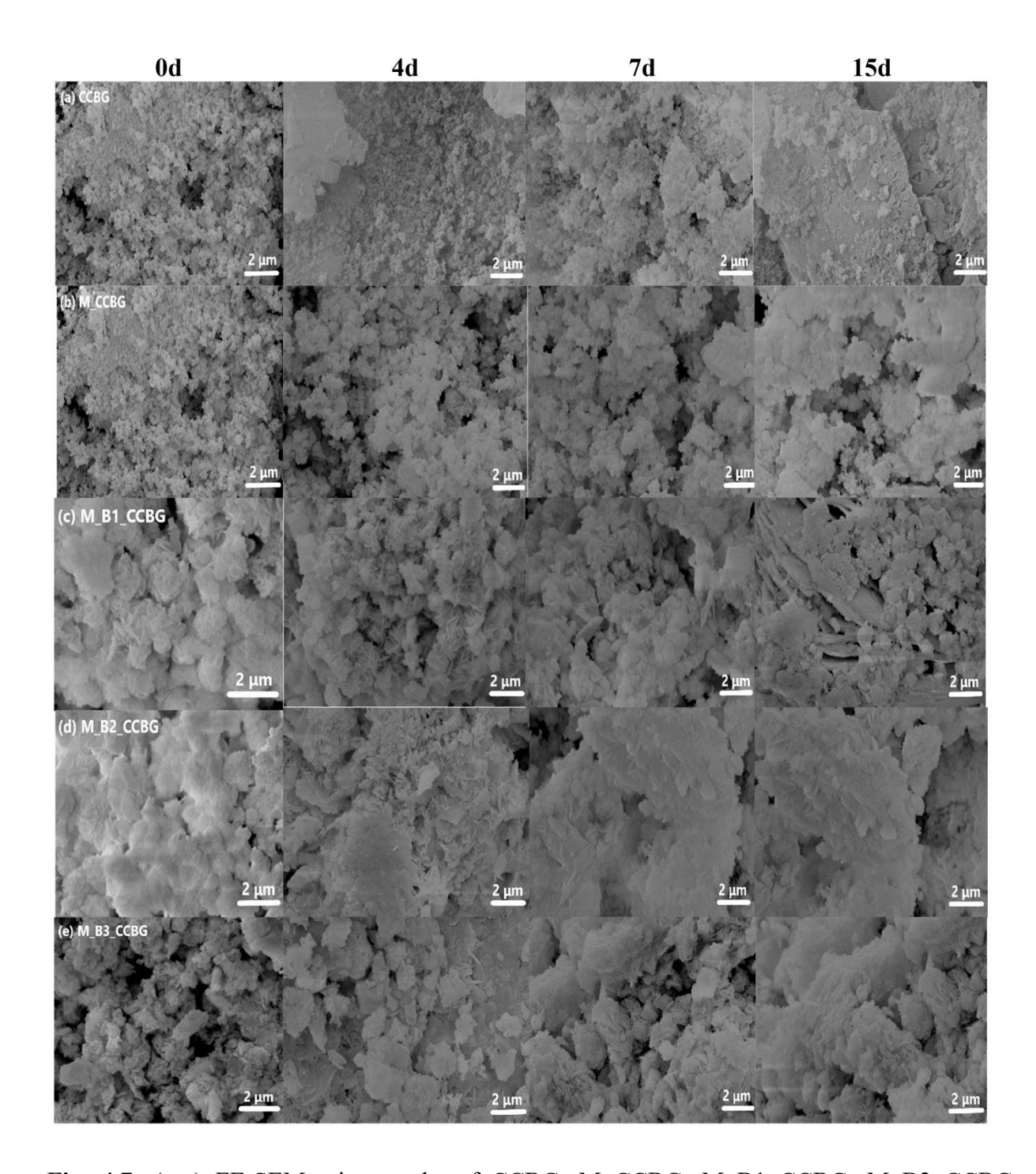


**Fig. 4.7: (a-e)** FE-SEM micrographs of CCBG, M\_CCBG, M\_B1\_CCBG, M\_B2\_CCBG and M\_B3\_CCBG after 1 d, 4 d, 7 d, and 15 d of bioactivity in SBF solution.

## 4.4.10 *In-vitro* hemolysis assay:

The cytotoxicity and hemocompatibility of BG NPs were evaluated through *in-vitro* hemolysis assay. Each BG NPs at various concentrations (1  $\mu$ g/mL, 5  $\mu$ g/mL, 10  $\mu$ g/mL, 25  $\mu$ g/mL and 50  $\mu$ g/mL)

were prepared such that hemoglobin absorbance at 570 nm was measured spectrophotometrically to determine the corresponding lysis of human red blood cells. The quantitative hemolysis evaluation of BG NPs was done with reference to the positive control (Triton X 100, 100 % hemolysis) and the negative control (PBS, 0% hemolysis). As shown in Fig. 8(a-e), the maximal hemolysis (~20 %) was noted at the highest concentration of 50 μg/mL at 24 h. On the other hand, less than 5% hemolytic activity was observed for all lower concentrations upto 24 h, which is consistent with the safety limits set in earlier research. So, we can say that hemolysis follows dose-dependent pattern such that percentage of hemolysis increases at higher concentrations. Hence, all the BG NPs showed a very modest hemolytic activity and have excellent hemo-biocompatibility as well as low cytotoxicity. Therefore, *in-vitro* hemolysis test decreases the possible dangers of using the synthesized NPs in external biological environments.

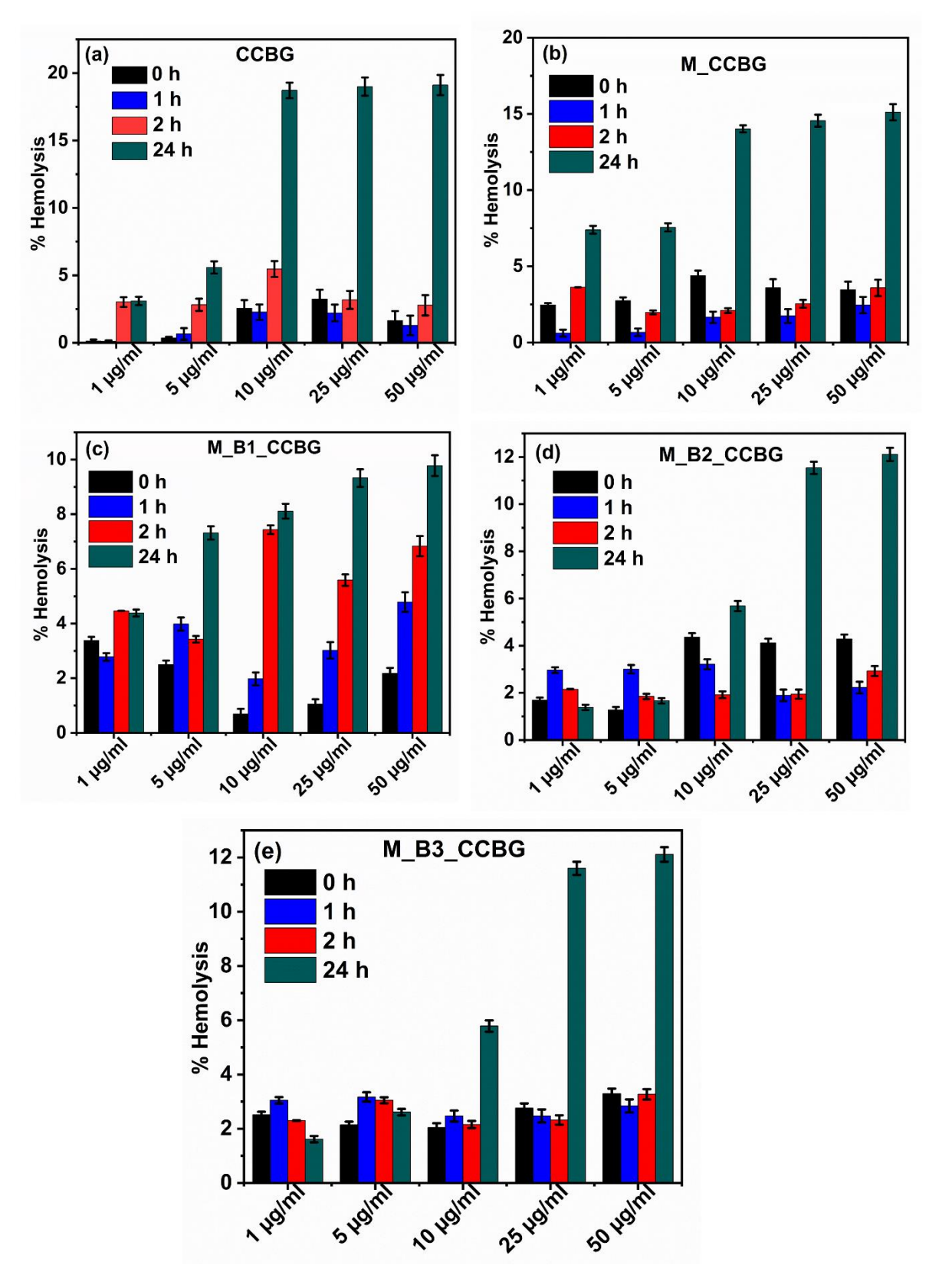


**Fig. 4.8(a–e):** *In-vitro* hemolysis assay of CCBG, M\_CCBG, M\_B1\_CCBG, M\_B2\_CCBG and M\_B3\_CCBG.

### **4.4.11 MTT Assay:**

The biocompatibility of all the doped BG NPs was evaluated with CCBG as the control via *in-vitro* MTT assay for biomedical applications in the U2OS osteosarcoma cell line (Fig. 9(a-e)). The cytotoxicity of the synthesized BG NPs at different concentrations (1  $\mu$ g/mL, 5  $\mu$ g/mL, 10  $\mu$ g/mL, 25  $\mu$ g/mL, and 50  $\mu$ g/mL) was observed using untreated human osteoblast-like osteosarcoma cells (U2OS) grown in DMEM medium as positive control. All the BG NPs depicted 80% cell viability at dosages varying from 1  $\mu$ g/mL to 10  $\mu$ g/mL. At 25  $\mu$ g/mL doses of BG NPs, there was a slight decrease in cellular viability below 80%. At the highest concentration of BG (50  $\mu$ g/mL) cell viability was reduced around 70%. Over all, BG NPs were demonstrated for excellent biocompatibility up to 25  $\mu$ g/mL concentrations even after co-doped with Mg<sup>2+</sup> and Bi<sup>3+</sup>.

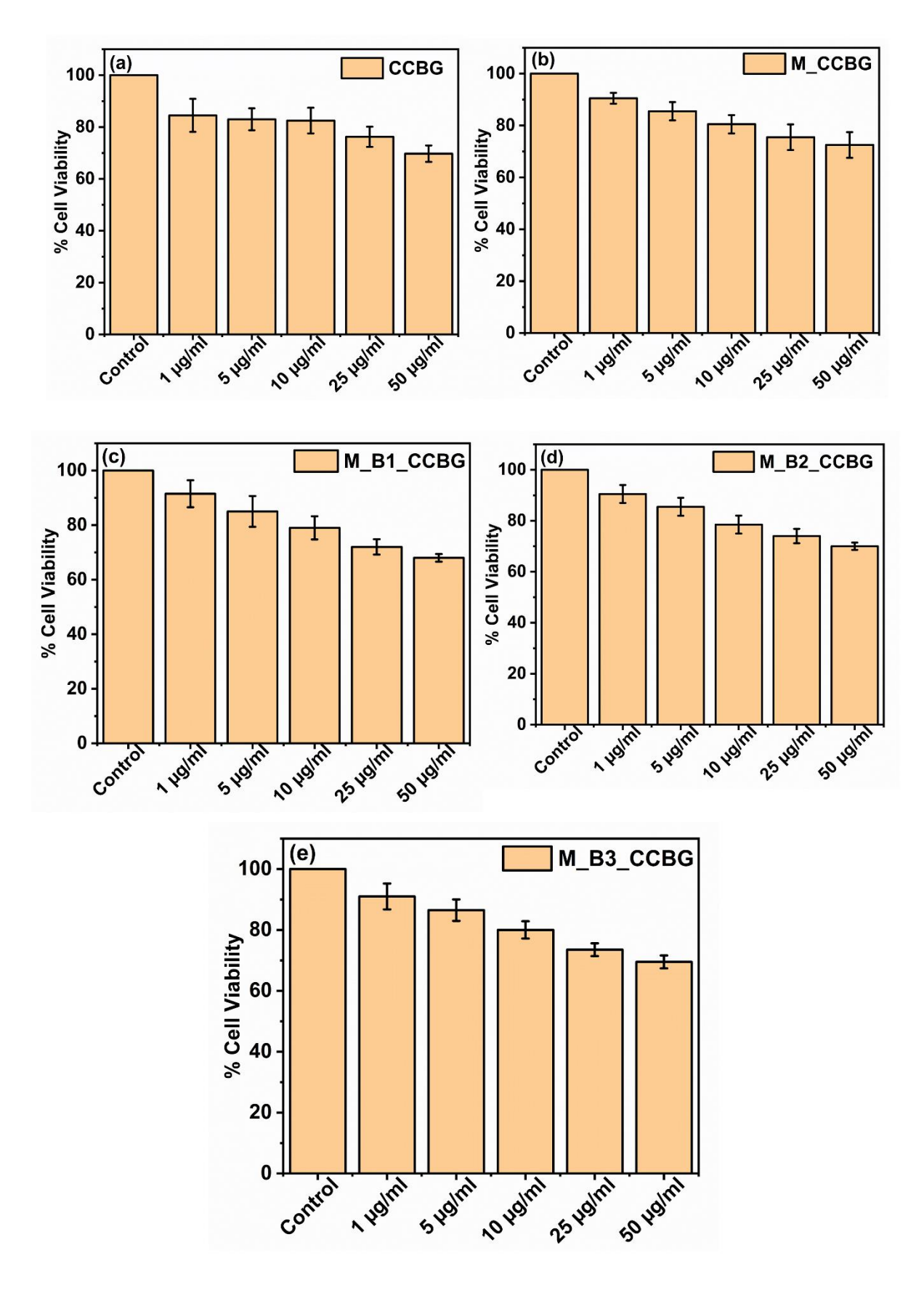


**Fig. 4.9(a–e):** MTT assay of CCBG, M\_CCBG, M\_B1\_CCBG, M\_B2\_CCBG and M\_B3\_CCBG at 24 h interaction

### 4.5 Discussion

In present research, BG precursors were interacted with CC a therapeutic molecule and metal ion dopants (Mg<sup>2+</sup> and Bi<sup>3+</sup>) to synthesize mesoporous co-doped NPs under ambient conditions. High resolution XPS spectra validated existence of doped metal ions as MgO and Bi<sub>2</sub>O<sub>3</sub> in the BG network Fig. S1(a-e). The incorporation of Mg<sup>2+</sup> and Bi<sup>3+</sup> dopants led to an increase in crystallinity within the BG network (Fig. 2(a-b)) due to the metallic nature of Bi<sup>3+</sup>. The average crystallite size of the doped samples was determined using the Debye-Scherrer formula, which increased from 0.1 to 0.25 nm with increase in the concentration of Bi<sup>3+</sup> in co-doped BG (Fig. 2(a-b)). The presence of CC within the BG network was proven by two distinct broad FTIR peaks at 1550 cm<sup>-1</sup> and 1410 cm<sup>-1</sup>due to carbonyl C=O and aromatic C=C stretching vibrations (Fig. 2(c-d). TGA analysis indicated the highest thermal stability of co-doped BG (Fig. 2e). NMR findings depicted the domination of Bi<sup>3+</sup> charge affinity towards the negatively charged silica network with increasing concentration (Fig. 5(ab)). FE-SEM (Fig. 3(a-e)) and HR-TEM (Fig. 3(a-e)) illustrated that CCBG, M CCBG, M B1 CCBG, M B2 CCBG, and M B3 CCBG exhibited nanosized characteristics. The sizes were determined to be  $10.1 \pm 0.3$  nm,  $16.7 \pm 0.7$  nm,  $50 \pm 0.9$  nm,  $47 \pm 0.9$  nm, and  $46.7 \pm 0.3$  nm, respectively. BET analysis further validated mesoporous nature of co-doped BG with an increase in the pore diameter and pore volume with increase in Bi<sup>3+</sup> concentration (Table II). This observation suggests that Mg<sup>2+</sup> functions as a network modifier, while Bi ions work as both network former and modifier which is well corroborated with NMR (Fig. 5(a-b)) [57]. PL analysis (Fig. 5(c-d)) indicated that co-doped BG NPs function as efficient PTA by emitting blue light at 480 nm. Upon the deposition of HAP on its surface in SBF, BG NPs depicted in-vitro bioactivity (Fig. 6(a-e), Fig. S3(a-e), 7(a-e)). These observations suggest the bone bonding ability of the co-doped BG samples. *In-vitro* hemolysis and MTT assays revealed biocompatibility of BG NPs and were proven to be safe at the tested concentrations (Fig. 8(a-e) and Fig. 9(a-e)). The comprehensive assessment of co-doped BG NPs in comparison to CCBG confirms their efficacy as soft and hard tissue regenerating therapeutic loaded PTAs for biomedical applications.

### 4.6 Conclusion

The current study focusses on the synthesis of BG NPs, using CC as a template and co-doping metal ions (Mg<sup>2+</sup> and Bi<sup>3+</sup>). Bio-inspired strategy, the synthetic method adopted was made use of minimal precursors and solvents as well as omits calcination step. The co-doped BG NPs synthesized with 1 mol% MgO and increasing amount of Bi<sub>2</sub>O<sub>3</sub> (From 0.5 mol% to 1.5 mol%). The template CC a therapeutic agent was incorporated in BG network during BG synthesis, while metal ions Mg<sup>2+</sup> and Bi<sup>3+</sup> function as network modifier and both former and modifier respectively. The existence of metal ion dopants within the BG network was confirmed through comprehensive elemental XPS, XRD, FTIR and TGA analysis. The structural determination of BG NPs was done by NMR. Nitrogen sorption studies revealed the mesoporous nature of the BG NPs, characterized by a large surface area and pore volume. The surface morphology and nanosize of BG NPs was confirmed by FE-SEM and HR-TEM. The *in-vitro* bioactivity, hemolysis and MTT assay confirmed the bioactive nature, minimum cytotoxicity, and good biocompatibility of BG NPs. The co-doped NPs resulted as bioactive mesoporous PTAs with versatile optical and regenerative properties for a broad spectrum of biomedical applications.

### References

- [1] Y. Gao, M.A. Seles, and M. Rajan, Role of bioglass derivatives in tissue regeneration and repair: A review, *Rev. Adv. Mater.* 62 (2023) 20220318.
- [2] G. Kaur, V. Kumar, F. Baino, J.C. Mauro, G. Pickrell, I. Evans, O. Bretcanu, Mechanical properties of bioactive glasses, ceramics, glass-ceramics, and composites: State-of-the-art review and future challenges, Mater. Sci. Eng. C. 104 (2019) 109895. https://doi.org/10.1016/j.msec.2019.109895.
- [3] B. Ben-Nissan, A.H. Choi, I. Macha, Advances in Bioglass and Glass Ceramics for Biomedical Applications, in: Q. Li, Y.-W. Mai (Eds.), Biomaterials for Implants and Scaffolds, Springer, Berlin, Heidelberg, 2017: pp. 133–161. https://doi.org/10.1007/978-3-662-53574-5 5.
- [4] S.M. Rabiee, N. Nazparvar, M. Azizian, D. Vashaee, L. Tayebi, Effect of ion substitution on properties of bioactive glasses: A review, Ceram. Int. 41 (2015) 7241. https://doi.org/10.1016/j.ceramint.2015.02.140.
- [5] A. Anand, H. Kaňková, Z. Hájovská, D. Galusek, A. R. Boccaccini, D. Galusková, Bioresponse of copper–magnesium co-substituted mesoporous bioactive glass for bone tissue regeneration, J. Mater. Chem. B. 12 (2024) 1875. https://doi.org/10.1039/D3TB01568H.
- [6] I.E. Pinto e Souza, B.R. Barrioni, N.M.L. Miriceia, D. Sachs, G.C. Ribeiro, D.C.F. Soares, M.M. Pereira, E.H.M. Nunes, Synergistic effect of cobalt and cerium on the structural properties and biological behavior of sol-gel-derived mesoporous bioactive glass nanoparticles, J. Non-Cryst. 613 (2023) 122391. https://doi.org/10.1016/j.jnoncrysol.2023.122391.
- [7] M. Zhu, Y. Zhu, (2022). Bioactive Glasses as Carriers for the Controlled Release of Therapeutic Species, in: F. Baino and S. Kargozar) (Eds.) Bioactive Glasses and Glass-Ceramics, John Wiley & Sons, Inc., 2022: pp. 227-261. https://doi.org/10.1002/9781119724193
- [8] V. Stanić, Variation in Properties of Bioactive Glasses After Surface Modification, in: G. Kaur (Ed.), Clinical Applications of Biomaterials: State-of-the-Art Progress, Trends, and Novel Approaches, Springer International Publishing, Cham, 2017: pp. 35–63. https://doi.org/10.1007/978-3-319-56059-5\_2.
- [9] S. Kargozar, M. Montazerian, S. Hamzehlou, H.-W. Kim, F. Baino, Mesoporous bioactive glasses: Promising platforms for antibacterial strategies, Acta Biomater. 81 (2018) 1. https://doi.org/10.1016/j.actbio.2018.09.052.
- [10] G. Sa, T. Das, Anti cancer effects of curcumin: cycle of life and death, Cell Div. 3 (2008) 1. https://doi.org/10.1186/1747-1028-3-14.
- [11] M. Shoaib, A. Bahadur, S. Iqbal, M.M. AL-Anazy, A. Laref, M.A. Tahir, P.A. Channar, S. Noreen, M. Yasir, A. Iqbal, K.W. Ali, Magnesium doped mesoporous bioactive glass nanoparticles: A promising material for apatite formation and mitomycin c delivery to the MG-63 cancer cells, J. Alloys Compd. 866 (2021) 159013. https://doi.org/10.1016/j.jallcom.2021.159013.
- [12] H. Zhou, B. Liang, H. Jiang, Z. Deng, K. Yu, Magnesium-based biomaterials as emerging agents for bone repair and regeneration: from mechanism to application, J. Magnes. Alloy. 9 (2021) 779. https://doi.org/10.1016/j.jma.2021.03.004.
- [13] C.F. Carolin, P.S. Kumar, A. Saravanan, G.J. Joshiba, Mu. Naushad, Efficient techniques for the removal of toxic heavy metals from aquatic environment: A review, J. Environ. Chem. Eng. 5 (2017) 2782. https://doi.org/10.1016/j.jece.2017.05.029.
- [14] J. Yin, A.P. Wang, W.F. Li, R. Shi, H.T. Jin, J.F. Wei, Time-response characteristic and potential biomarker identification of heavy metal induced toxicity in zebrafish, Fish Shellfish Immunol. 72 (2018) 309. https://doi.org/10.1016/j.fsi.2017.10.047.

- [15] H. Goel, D. Santhiya, Role of *Trigonella foenum-graecum* leaf extract in tailoring the synthesis and properties of bioactive glass nanoparticles, Sustain. Mater. Technol. 33 (2022) e00485. https://doi.org/10.1016/j.susmat.2022.e00485.
- [16] N. Yang, C. Cao, H. Li, Y. Hong, Y. Cai, X. Song, W. Wang, X. Mou, X. Dong, Polymer-Based Therapeutic Nanoagents for Photothermal-Enhanced Combination Cancer Therapy, Small Structures. 2 (2021) 2100110. https://doi.org/10.1002/sstr.202100110.
- [17] I.M. Marzano, D. Tomco, R.J. Staples, E.H. Lizarazo-Jaimes, D.A. Gomes, M. Bucciarelli-Rodriguez, W. Guerra, Í.P. de Souza, C.N. Verani, E.C. Pereira Maia, Dual anticancer and antibacterial activities of bismuth compounds based on asymmetric [NN'O] ligands, J. Inorg. Biochem. 222 (2021) 111522. https://doi.org/10.1016/j.jinorgbio.2021.111522.
- [18] W. Wei, X. Zhang, S. Zhang, G. Wei, Z. Su, Biomedical and bioactive engineered nanomaterials for targeted tumor photothermal therapy: A review, Mater. Sci. Eng. C. 104 (2019) 109891. https://doi.org/10.1016/j.msec.2019.109891.
- [19] Y. Hsu, Y. Lu, S. Wang, Y. Zheng, D. Xia, Y. Liu, Magnesium alloys in tumor treatment: Current research status, challenges and future prospects, J. Magnes. Alloy. 11 (2023) 3399. https://doi.org/10.1016/j.jma.2023.08.008.
- [20] D. Zhi, T. Yang, J. O'Hagan, S. Zhang, R.F. Donnelly, Photothermal therapy, *J. Control. Release*. 325 (2020) 52. https://doi.org/10.1016/j.jconrel.2020.06.032.
- [21] X. Li, J.F. Lovell, J. Yoon, X. Chen, Clinical development and potential of photothermal and photodynamic therapies for cancer, Nat. Rev. Clin. Oncol. 17 (2020) 657. https://doi.org/10.1038/s41571-020-0410-2
- [22] L. Cheng, C. Wang, L. Feng, K. Yang, Z. Liu, Functional Nanomaterials for Phototherapies of Cancer, Chem Rev, 114 (2014) 10869. https://doi.org/10.1021/cr400532z
- [23] C. Zhang, D. Ni, Y. Liu, H. Yao, W. Bu, J. Shi, Magnesium silicide nanoparticles as a deoxygenation agent for cancer starvation therapy, Nat. Nanotechnol. 12 (2017) 378. https://doi.org/10.1038/nnano.2016.280.
- [24] B. Guo, N.-W. Cao, H.-Y. Zhou, X.-J. Chu, B.-Z. Li, Efficacy and safety of bismuth-containing quadruple treatment and concomitant treatment for first-line Helicobacter pylori eradication: A systematic review and meta-analysis, Microb. Pathog. 152 (2021) 104661. https://doi.org/10.1016/j.micpath.2020.104661.
- [25] F. An, Y. Zhao, H. Li, J. Meng, L. Jiao, Z. Zhang, X. Li, X. Sun, Intramolecular charge transfer versus intersystem crossing: The way toward super-high photothermal efficiency by thionation, *Dyes Pigm.* 217 (2023) 111411. https://doi.org/10.1016/j.dyepig.2023.111411.
- [26] N. Sezer, Z. Evis, S.M. Kayhan, A. Tahmasebifar, M. Koç, Review of magnesium-based biomaterials and their applications, J. Magnes. Alloy. 6 (2018) 23. https://doi.org/10.1016/j.jma.2018.02.003.
- [27] L. Tong, Q. Liao, Y. Zhao, H. Huang, A. Gao, W. Zhang, X. Gao, W. Wei, M. Guan, P.K. Chu, H. Wang, Near-infrared light control of bone regeneration with biodegradable photothermal osteoimplant, Biomater. 193 (2019) 1. https://doi.org/10.1016/j.biomaterials.2018.12.008.
- [28] J.-W. Lu, F. Yang, Q.-F. Ke, X.-T. Xie, Y.-P. Guo, Magnetic nanoparticles modified-porous scaffolds for bone regeneration and photothermal therapy against tumors, Nanomed.: Nanotechnol. *Biol. Med.* 14 (2018) 811. https://doi.org/10.1016/j.nano.2017.12.025.
- [29] L. Zhang, Y. Liu, H. Huang, H. Xie, B. Zhang, W. Xia, B. Guo, Multifunctional nanotheranostics for near infrared optical imaging-guided treatment of brain tumors, Adv. Drug Deliv. Rev. 190 (2022) 114536. https://doi.org/10.1016/j.addr.2022.114536.
- [30] Y. Cui, X. Zhang, R. Guo, H. Zhang, B. Li, M. Xie, Q. Cheng, X. Cheng, Construction of Bi<sub>2</sub>O<sub>3</sub>/g-C<sub>3</sub>N<sub>4</sub> composite photocatalyst and its enhanced visible light photocatalytic performance and mechanism, Sep. Purif. Technol. 203 (2018) 301. https://doi.org/10.1016/j.seppur.2018.04.061.

- [31] N. Gupta, D. Santhiya, S. Murugavel, A. Kumar, A. Aditya, M. Ganguli, S. Gupta, Effects of transition metal ion dopants (Ag, Cu and Fe) on the structural, mechanical and antibacterial properties of bioactive glass, Colloids Surf. A: Physicochem. Eng. Asp. 538 (2018) 393. https://doi.org/10.1016/j.colsurfa.2017.11.023.
- [32] M.H. Misbah, M. El-Kemary, R. Ramadan, Effect of Mg<sup>2+</sup> coordination on the structural and optical properties of iron magnesium phosphate glasses, J. Non-Cryst. 569 (2021) 120987. https://doi.org/10.1016/j.jnoncrysol.2021.120987.
- [33] S.I. Sohn, A. Priya, B. Balasubramaniam, P. Muthuramalingam, C. Sivasankar, A. Selvaraj, A. Valliammai, R. Jothi, S. Pandian, Biomedical Applications and Bioavailability of Curcumin—An Updated Overview, Pharm. 13 (2021) 2102. https://doi.org/10.3390/pharmaceutics13122102.
- [34] B. Salehi, Z.S. Radić, J. Matejić, M.S. Rad, N.V.A. Kumar, N. Martins, J.S. Rad, The therapeutic potential of curcumin: A review of clinical trials, *Eur. J. Med. Chem.* 163 (2019) 527. https://doi.org/10.1016/j.ejmech.2018.12.016.
- [35] D. Santhiya, H. kumari Alajangi, F. Anjum, S. Murugavel, M. Ganguli, Bio-inspired synthesis of microporous bioactive glass-ceramic using CT-DNA as a template, J. Mater. Chem. B. 1 (2013) 6329. https://doi.org/10.1039/C3TB21212B.
- [36] T. Kokubo, H. Takadama, How useful is SBF in predicting in vivo bone bioactivity?, Biomater. 27 (2006) 2907. https://doi.org/10.1016/j.biomaterials.2006.01.017.
- [37] M.A. Dobrovolskaia, J.D. Clogston, B.W. Neun, J.B. Hall, A.K. Patri, S.E. McNeil, Method for Analysis of Nanoparticle Hemolytic Properties in Vitro, Nano Lett. 8 (2008) 2180. https://doi.org/10.1021/nl0805615.
- [38] Z. Zhen, X. Tingfei, Z. Yufeng, L. Li, L. Lugee, In Vitro Study on Mg–Sn–Mn Alloy as Biodegradable Metals, J. Mater. Sci. Technol. 30 (2014) 675. https://doi.org/10.1016/j.jmst.2014.04.005.
- [39] F. Molly, W. Sean, S. Mark, M. Colleen, A. Scott, R. Don, Standard practice for assessment of hemolytic properties of materials, American Society for Testing of Materials. ASTM F756-00. (2000).
- [40] J. Serra, P. González, S. Liste, C. Serra, S. Chiussi, B. León, M. Pérez-Amor, H.O. Ylänen, M. Hupa, FTIR and XPS studies of bioactive silica-based glasses, J. Non-Cryst. 332 (2003) 20. https://doi.org/10.1016/j.jnoncrysol.2003.09.013.
- [41] F. Uhl, V. Staemmler, An ab initio study of the O1s and Mg1s, Mg2s, Mg2p core electron binding energies in bulk MgO, J. Electron Spectros. Relat. Phenomena. 233 (2019) 90. https://doi.org/10.1016/j.elspec.2019.03.009.
- [42] C. S., B. S., Insight into the impingement of different sodium precursors on structural, biocompatible, and hemostatic properties of bioactive materials, Mater. Sci. Eng. C. 123 (2021) 111959. https://doi.org/10.1016/j.msec.2021.111959.
- [43] V. Sugumaran, E. Krishnamoorthy, A. Kamalakkannan, R.C. Ramachandran, B. Subramanian, Unscrambling the Influence of Sodium Cation on the Structure, Bioactivity, and Erythrocyte Compatibility of 45S5 Bioactive Glass, ACS Appl Bio Mater, 18 (2022) 1576. https://doi.org/10.1021/acsabm.1c01322
- [44] A.M. Deliormanlı, B. Rahman, S. Oguzlar, M.Z. Ongun, Investigation of the structural, photoluminescence properties, bioactivity and 5-fluorouracil delivery behavior of Dy<sup>3+</sup> and Dy: Eu<sup>3+</sup>-doped bioactive glasses, J. Alloys Compd. 944 (2023) 169153. https://doi.org/10.1016/j.jallcom.2023.169153.
- [45] Y. Song, E.-H. Han, K. Dong, D. Shan, C.D. Yim, B.S. You, Microstructure and protection characteristics of the naturally formed oxide films on Mg–xZn alloys, Corros. Sci. 72 (2013) 133. https://doi.org/10.1016/j.corsci.2013.03.021.

- [46] R. Zhang, J. Ren, X. Yuan, Y. Cui, L. Zhang, L. Zhang, Structural Studies of Bi<sub>2</sub>O<sub>3</sub>–NaPO<sub>3</sub> Glasses by Solid State Nuclear Magnetic Resonance and X-ray Photoelectron Spectroscopy, J. Phys. Chem. C. 121 (2017) 10087. https://doi.org/10.1021/acs.jpcc.7b01871.
- [47] S.S. Hettiarachchi, S.P. Dunuweera, A.N. Dunuweera, R.M.G. Rajapakse, Synthesis of Curcumin Nanoparticles from Raw Turmeric Rhizome, ACS Omega. 6 (2021) 8246. https://doi.org/10.1021/acsomega.0c06314.
- [48] Z. Neščáková, K. Zheng, L. Liverani, Q. Nawaz, D. Galusková, H. Kaňková, M. Michálek, D. Galusek, A.R. Boccaccini, Multifunctional zinc ion doped sol gel derived mesoporous bioactive glass nanoparticles for biomedical applications, Bioact. Mater. 4 (2019) 312. https://doi.org/10.1016/j.bioactmat.2019.10.002.
- [49] M. Erol Taygun, A.R. Boccaccini, 10 Nanoscaled bioactive glass particles and nanofibers, in: H. Ylänen (Ed.), Bioactive Glasses (Second Edition), Woodhead Publishing, 2018: pp. 235–283. https://doi.org/10.1016/B978-0-08-100936-9.00012-5.
- [50] M.A. Al-Ghouti, D.A. Da'ana, Guidelines for the use and interpretation of adsorption isotherm models: A review, J. Hazard. Mater. 393 (2020) 122383. https://doi.org/10.1016/j.jhazmat.2020.122383.
- [51] Z. Azari, F. Kermani, S. Mollazadeh, F. Alipour, A.S. Avalshahr, M.R. Mohammadi, B.J. Kondori, Z. Mollaei, S.A. Hosseini, S. Nazarnezhad, K. Zheng, F. Baino, S. Kargozar, Fabrication and characterization of cobalt- and copper-doped mesoporous borate bioactive glasses for potential applications in tissue engineering, Ceram. Int. 49 (2023) 38773. https://doi.org/10.1016/j.ceramint.2023.09.214.
- [52] S.S. Salcedo, C. Heras, D. Lozano, M.V. Regí, A.J. Salinas, Nanodevices based on mesoporous glass nanoparticles enhanced with zinc and curcumin to fight infection and regenerate bone, Acta Biomater. 166 (2023) 655. https://doi.org/10.1016/j.actbio.2023.04.046.
- [53] F.A. Adam, M.G. Ghoniem, M. Diawara, S. Rahali, B.Y. Abdulkhair, M.R. Elamin, M.A.B. Aissa, M. Seydou, Enhanced adsorptive removal of indigo carmine dye by bismuth oxide doped MgO based adsorbents from aqueous solution: equilibrium, kinetic and computational studies, RSC Adv. 12 (2022) 24786. https://doi.org/10.1039/D2RA02636H.
- [54] L. Wang, M. Peng, X. Li, Y. Wang, H. Luo, J. Cao, X. Li, Suppressing the thermal degradation of bismuth near-infrared luminescence in optical amorphous materials via topologically polymerized network structures, J. Mater. Chem. C. 7 (2019) 5074. https://doi.org/10.1039/C9TC00718K.
- [55] P. Dang, D. Liu, G. Li, A.A. Al Kheraif, J. Lin, Recent Advances in Bismuth Ion-Doped Phosphor Materials: Structure Design, Tunable Photoluminescence Properties, and Application in White LEDs, Adv. Opt. Mater. 8 (2020) 1901993. https://doi.org/10.1002/adom.201901993.
- [56] J. Liqiang, Q. Yichun, W. Baiqi, L. Shudan, J. Baojiang, Y. Libin, F. Wei, F. Honggang, S. Jiazhong, Review of photoluminescence performance of nano-sized semiconductor materials and its relationships with photocatalytic activity, Sol. Energy Mater. Sol. Cells. 90 (2006) 1773. https://doi.org/10.1016/j.solmat.2005.11.007.
- [57] P. Rohilla, A. Prasad, A. Srinivasa Rao, Structural and luminescence studies on thermally stable Bi<sup>3+</sup>-activated Ba<sub>3</sub>MoTiO<sub>8</sub> phosphors for near UV-pumped w-LED applications, Int. J. Appl. Ceram. 21 (2024) 1208. https://doi.org/10.1111/ijac.14580.
- [58] D.R. Taikar, S. Tamboli, S.J. Dhoble, Synthesis and photoluminescence properties of Li<sub>2</sub>SO<sub>4</sub>: RE (RE = Eu<sup>3+</sup>, Tb<sup>3+</sup>, Gd<sup>3+</sup> and Ce<sup>3+</sup>) phosphors, Optik. 139 (2017) 111. https://doi.org/10.1016/j.ijleo.2017.03.115.
- [59] A. Hoppe, N.S. Güldal, A.R. Boccaccini, A review of the biological response to ionic dissolution products from bioactive glasses and glass-ceramics, Biomater. 32 (2011) 2757. https://doi.org/10.1016/j.biomaterials.2011.01.004.

[60] M.L. Dittler, I. Unalan, A. Grünewald, A.M. Beltrán, C.A. Grillo, R. Destch, M.C. Gonzalez, A.R. Boccaccini, Bioactive glass (45S5)-based 3D scaffolds coated with magnesium and zinc-loaded hydroxyapatite nanoparticles for tissue engineering applications, *Colloids Surf.* B. 182 (2019) 110346. https://doi.org/10.1016/j.colsurfb.2019.110346.

# **FUTURE PROSPECTS**

Research on bone tissue engineering over the past few decades has paved the way for the creative design of novel materials with improved performance, broader applications, and new synthesizing methods. Since the discovery of bioactive glass, there has been a great deal of advancement in this subject, but there is still chance for improvement in terms of processing, functioning, and targeted delivery. The need for new research horizons is important because of the viability of bioactive glass in the administration of hormones, steroids, vaccines, and therapeutic proteins, as well as the validation of growth factors and gene delivery. It would be dynamic approach in the future if bioactive glass materials could be orally or through the skin in a non-invasive manner. The delivery route is important in this situation.

The approach to mould the bioactive glass into the appropriate defect shape during operation periods is still a practical big challenge facing the medical community. Moreover, bioactive glass needs to be investigated for its limited application in the field of connective tissue engineering. In addition, with the introduction of magnetic bioactive glass-ceramics, research activity is rapidly expanding for potential substantial advancements in the field of cancer. Most crucially, a bioinspired bioactive glass in-vivo clinical test has not yet been conducted, much like any other biomaterial that must undergo clinical tests before being introduced to the market.

# LIST OF PUBLICATIONS

1. Divya Goel, Deenan Santhiya, Subodh Kumar, Ajit Kumar Mahapatro. "Synthesis of Mesoporous Core Shell Magnetite Bioactive Glass Nanoparticles for Magnetic Hyperthermia Treatment of Cancer." ChemistrySelect" 9 (2024): e202302119. (SCIE indexed) (Impact

**Factor: 2.307)** 

ChemistrySelect

Research Article doi.org/10.1002/slct.202302119



Please check the marked ( ) text passages carefully, if any are present.

www.chemistryselect.org

# Synthesis of Mesoporous Core Shell Magnetite Bioactive Glass Nanoparticles for Magnetic Hyperthermia Treatment

Divya Goel, [a] Deenan Santhiya, \*[a] Subodh Kumar, [b] and Ajit Kumar Mahapatro\*[b]

Multiple biological advances have made use of bioactive glass (BG) nanoparticles (NPs) in regenerative medicine, bone and tooth repair, drug and gene transfer, cancer treatment, and cosmetics. Normal biocompatible coatings alongside hydrocarbons, polymers, and silica significantly affect fundamental attributes of NPs. In this study, we synthesized a novel mesoporous BG NPs with magnetite core shell (AMAG\_BG) using L-arginine as a template processing magnetic hyperthermia (MH). BG network coverage on magnetite (AMAG) NPs were orchestrated first time by bio-inspired synthesis in watery dissolvable. AMAG and AMAG\_BG NPs were characterized by utilizing FE-SEM, HR-TEM, and BET analysis. The elemental composition of L-arginine templated magnetite (AMAG) and

AMAG\_BG NPs was also determined by XPS and EDX analysis. Characteristics of AMAG\_BG were contrasted with bare AMAG NPs in morphology, particle size, porosity, and composition. The fabricated BG NPs' in-vitro bioactivity and heat studies were successfully monitored after interaction with simulated bodily fluid (SBF). Magnetic studies and in-vitro heat studies together demonstrated the behavior of BG NPs towards MH treatment of cancerous cells. Cytotoxicity tests on AMAG BG NPs using U2OS and human blood cells with appropriate control experiments revealed biocompatibility. The study represents magnetic and thermal property-dependent sustainable synthetic process of AMAG BG NPs for cancer treatment.

#### Introduction

Cancer is a comprehensive term which is used to address an enormous gathering of illnesses influencing human frame. Cancer is one of the destructive and deadly disorder causing an enormous killing of people around the globe, independent of developed nations.[1,2] There is no single treatment to fix this disorder. Rather, a blend of different methods is to be included for improved results. The most accomplished strategies for cancer treatment incorporate radiotherapy (to operate disease cells with light), chemotherapy (to operate disease cells with synthetic substances/drugs), medical procedure (by slicing), immunotherapy (by supporting resistant framework to battle against malignant growth), gene therapy (by utilizing genes), hormonotherapy (by dialing back or halting development of disease) and magnetic hyperthermia (MH) (to expose malignant growth of cells with temperature).[3,4]

MH is the encouraging method that has exhibited incredible ability to destroy malignant growth of cells through heat treatment. MH is typically utilized in mix with other therapeutic treatments like radiation therapy and anti-angiogenic therapy

of malignant growth cells.[5] It can be explained as the heat increase is due to the raise in hyperthermia cycle. This will further amplify the responsiveness of cells towards radiation therapy as well as anti-angiogenic therapy.<sup>[6]</sup> Generally, the word hyperthermia implies increasing the temperature of a particµµµar body part more than the typical internal heat level and maintaining it for a particular time span. It includes exposing of cancerous cells to excess heat (temperature close to 43 °C) without damaging the healthy cells present in that part of the human body.  $^{\prime\prime}$ 1 The cell apoptosis process occurs when the temperature ranges between 42 °C to 46 °C and when the temperature rises to 48°C, cell putrefaction begins. Both these systems lead to the killing of cells.16

The hyperthermic potential of multiple magnetic nanoparticles (NPs) has been studied, including nanomaterials with SPIONs, NPs containing metals such as Mn, Zn, Co, Fe, Ni, Gd and related oxides.[9] Some of the best-known hyperthermic substances containing iron-oxide include magnetite (Fe<sub>3</sub>O<sub>4</sub>) NPs and maghemite (Fe<sub>2</sub>O<sub>3</sub>) NPs. Fe<sub>3</sub>O<sub>4</sub> NPs are stabilized by ligands like hydrogel, cationic liposomes, dextran and polyvinyl alcohol while Fe<sub>2</sub>O<sub>3</sub> NPs are stabilized by dextran. Another classification is of ferrites. It includes mixed ferrites of zinc, nickel, and copper (NinesZnassCuarFersO4), cobalt-nickel ferrites (Co., Nines FerO4), nickel ferrites (NiFe2O4), lithium ferrites (Liq3Fe23O4), and manganese-nickel ferrites (MnFe<sub>2</sub>O<sub>4</sub>). Additional ferromagnetic NPs include Mn-Gd-Zn doped iron oxide composites (Mn, Zn, Gd, Fe<sub>12-x|</sub> O<sub>4</sub>), Fe-doped Au and Zn-Mn-doped iron oxides (Zn<sub>x</sub> Mn<sub>(1-4)</sub> Fe<sub>3</sub>O<sub>4</sub>).<sup>[10]</sup> Out of all these materials, bioglass materials have been the most efficient in hard tissue regeneration. They are used as drug carriers in the treatment of cancer.[11] They are known for their bioactive reaction with physiological liquids

ChemistrySelect 2024, 9, e202302119 (1 of 13)

© 2024 Wiley-VCH GmbH

<sup>[</sup>a] D. Goel, Dr. D. Santhiyo

Department of Applied Chemistry, Delhi Technological University, Delhi, India-110042 E-mail: deenan.santhiya@dce.ac.in

<sup>[</sup>b] S. Kumar, Prof. A. Kumar Mahapatro

Department of Physics and Astrophysics, University of Delhi, Delhi, India-E-mail: amahapatro@physics.du.ac.in

https://doi.org/10.1002/slct.202302119

Divya Goel, Deenan Santhiya. "Mesoporous bioactive glass nanoparticles with dopants bismuth and iron as magnetic photothermal agents for biomedical applications." "Bio Nano Science" (2024). (ESCI indexed) (ImpactFactor: 3.0)

BioNanoScience https://doi.org/10.1007/s12668-024-01396-y

RESEARCH



# Mesoporous Bioactive Glass Nanoparticles with Dopants Bismuth and Iron as Magnetic Photothermal Agents for Biomedical Applications

Divya Goel1 · Deenan Santhiya1

Accepted: 4 April 2024

© The Author(s), under exclusive licence to Springer Science+Business Media, LLC, part of Springer Nature 2024

#### Abstrac

The nanosized 45S5 bioactive glass (BG) containing iron (Fe) and bismuth (Bi) as magnetic photothermal agent (PTA) (B\_F\_FABG) was first time synthesized by bio-inspired route using folic acid (FA) template. Similarly, for comparative analysis, BGs doped with Fe<sup>2+</sup>/Fe<sup>3+</sup> or Bi<sup>3+</sup> separately (F\_FABG and B\_FABG) were also synthesized. XPS and FTIR analysis of B\_F\_FABG revealed the presence of FA and dopants Fe<sup>2+</sup>/Fe<sup>3+</sup> and Bi<sup>3+</sup> in the BG network. Based on the XRD pattern, B\_F\_FABG was semi-crystalline in nature, with an average crystallite size of 0.2 ± 0.04 nm. Fe<sup>2+</sup>/Fe<sup>3+</sup> ions and FA molecules have a lower affinity for the BG network than the heaviest and most polarizable Bi<sup>3+</sup> ions, according to TGA analysis. An increase of Q<sup>4</sup> species in the B\_F\_FABG network was revealed by <sup>29</sup>Si NMR investigation due to the presence of Fe<sup>2+</sup>/Fe<sup>3+</sup> and Bi<sup>3+</sup> ions. For B\_F\_FABG, there was also a rise in Q<sup>3</sup> and Q<sup>2</sup> species due to the dual dopants. B\_F\_FABG is nano-crystalline, with an average diameter of 12.8 ± 0.3 nm, according to HR-TEM and SAED pattern. The BG samples, both doped and undoped, were found to be mesoporous, with pore diameters ranging from 2 to 50 nm. Due to the presence of Bi<sup>3+</sup> ions, B\_F\_FABG showed remarkable photoluminescence along with bone-bonding ability during excitation in the range of ~1092 nm. The magnetic characteristics were also induced in B\_F\_FABG due to Fe<sup>2+</sup>/Fe<sup>3+</sup> doping. The novel B\_F\_FABG NPs reported the least toxicity through *in-vitro* hemolysis assay and is an ultimate multifunctional material to treat bone abnormalities.

Keywords Bioactive · Mesoporous · Magnetic · Photothermal effect · Cytotoxicity

### 1 Introduction

Bioactive glasses (BGs) have been developed into a diverse class of biomaterials with potential applications in the management of numerous illnesses [1]. BGs have long been linked to their ability to connect bone [2]. Currently, these materials are considered for soft and bone tissue regeneration, implant coatings, additive manufacturing for 3D printing, drug carriers, etc. [3]. Interestingly, the role of BG in biomedical applications can be widened through the incorporation of unique metallic ions/organic molecules into a silicate (or phosphate) network [4]. As a result, these functionalized BG can be employed as various therapeutic agents such as to produce heat for phototherapy or magneticinduced hyperthermia, supply radiation for brachytherapy, and help deliver drugs to fight against cancer and infections [5]

High incidence and mortality rates led researchers to investigate effective cancer treatment methods as well as faster and more precise diagnostic techniques. The most frequently used traditional clinical treatments include surgery, radiation, and chemotherapy [6, 7]. These treatments withheld a significant chance of failure or side effects. Currently, photothermal therapy (PTT) is drawing attention in cancer therapy. In PTT, the use of photothermal agents (PTAs) converts absorbed light energy into heat to inflict thermal burns on malignant cells [8, 9]. PTAs can display modest photothermal conversion in healthy tissues but robust photothermal conversion at the location of malignant cells [10, 11]. As a result, it causes the targeted heating of the malignant location while posing little or no threat to healthy cells.

Published online: 15 April 2024

Springer

 <sup>□</sup> Deenan Santhiya deenan.santhiya@dce.ac.in

Department of Applied Chemistry, Delhi Technological University, Delhi 110042, India

3. Divya Goel, and Deenan Santhiya. "Effect of Magnesium and Bismuth Co-doping on Structural Optical and Bioactive properties of Bioactive Glass Nanoparticles for Biomedical Applications." (SCIE indexed) (ImpactFactor: 2.7)



Article DOI:10.1557/s43578-024-01433-2



# Tunable structural, optical and bioactive properties of magnesium and bismuth co-doping on bioactive glass nanoparticles for biomedical applications

Divya Goel1, Deenan Santhiya1,a)

Received: 3 May 2024; accepted: 27 August 2024; published online: 9 September 2024

The current study focused to synthesize magnesium  $(Mg^{2^{\circ}})$  and bismuth  $(Bi^{3^{\circ}})$  co-doped bioactive glass (BG) nanoparticles (NPs) at ambient conditions. XPS studies confirmed the existence of  $Mg^{2^{\circ}}$  as MgO and  $Bi^{3^{\circ}}$  as  $Bi_2O_3$  in co-doped BG NPs. XRD reported an increase in mean crystallite size from  $0.1\pm0.01$  nm to  $0.25\pm0.04$  nm with 0.5 to 1.5 mol% increase in  $Bi_2O_3$  content. TGA revealed co-doping of  $Mg^{2^{\circ}}$  and  $Bi^{3^{\circ}}$  to BG NPs increased their thermal stability by 20 to 30 w/w% in comparison to the control. FTIR and NMR studies depicted open  $SiO_2$  network in co-doped BG NPs. HR-TEM evidenced co-doped BG NPs were of  $\sim 50$  nm. The optical transmittance showed strong emission peak at 480 nm for co-doped BG NPs with decreased intensity with increasing  $Bi^{3^{\circ}}$  ion concentration. In-vitro bioactivity, hemolysis and MTT assay revealed excellent bone binding ability, least toxicity and excellent biocompatibility.

#### Introduction

Ceramics and bioactive glasses (BG) stand out among all biomaterials as interesting options for biomedical applications involving hard and soft tissue regeneration [1-3]. BG form a hydroxyl apatite-like layer (HA) on the surface upon implantation at defective wound site, which resembles the mineral phase of bone. The recently formed HA layer not only bind with bone and also promote binding of soft tissue by neovascularization [4]. There exists a numerous reports on the effect of therapeutic ion dopants to BG on bioactivity and clinical applicability [5]. Aluminum (Al), zirconium (Zr), magnesium (Mg), strontium (Sr), zinc (Zn), copper (Cu), cobalt (Co) [6] and silver (Ag) are few metal ions, which were incorporated individually/ co-dopants in BG. These metal ions in critical concentrations are known to substitute for Ca in BG network to improve osteogenesis, angiogenesis, and biocide activity of BG [7-9]. Mg is an important content of human body especially in hard tissues and plays essential role in energy metabolism, macromolecule synthesis, bone development as well as maintenance and expression of genetic information [5]. Doped Mg ions in BG functions as a network modifier and offers an excellent mechanical strength to the material. In addition, presence of Mg2+ in BG also promotes human osteoblast cell adhesion, proliferation, and calcification [10]. Mg doped mesoporous BG were shown to promote bone regeneration with excellent biocompatibility and also providing sustained drug release [11]. As a result, Mg shows widespread use in a variety of implants such as porous bone scaffolds, cardiovascular stents, and internal fixing components for bone fractures [12].

Biomaterials with bismuth (Bi) or its compounds can release Bi ions in physiological conditions, which can potentially have detrimental biological effects [3]. Bi is less toxic than other heavy metals and is also widely used in pharmaceutical products [13] and bio markers [14]. Bismuth, in lower concentrations, is generally considered non-toxic and is even used in biomedical applications such as cancer treatment and for treating gastrointestinal disorders etc. [15]. However, at higher concentrations, bismuth can become toxic [16]. The specific toxic concentration of bismuth varies depending on the form of bismuth, the duration of exposure, and the route of administration [16-18]. For blood levels, bismuth concentrations of less than 50 µg/L are generally considered safe and can provide beneficial properties, such as photothermal effects, without causing harm to surrounding tissues [19, 20]. Blood levels above 50-100 μg/L can start to indicate potential toxicity. Severe toxicity is often associated with blood levels exceeding 150-200 µg/L potentially

2889

<sup>&</sup>lt;sup>1</sup>Department of Applied Chemistry, Delhi Technological University, Delhi 110042, India

<sup>\*</sup> Address all correspondence to this author. e-mail: deenan.santhiya@dce.ac.in

# **PLAGIARISM REPORT**

### **Similarity Report**

PAPER NAME

### Thesis\_12\_11\_24.docx

WORD COUNT CHARACTER COUNT

45794 Words 261639 Characters

PAGE COUNT FILE SIZE 177 Pages 33.1MB

SUBMISSION DATE REPORT DATE

Nov 11, 2024 1:30 PM GMT+5:30 Nov 11, 2024 1:33 PM GMT+5:30

# 7% Overall Similarity

The combined total of all matches, including overlapping sources, for each database.

- 4% Internet database
- 5% Submitted Works database
- 3% Publications database
- Excluded from Similarity Report
- · Crossref database
- · Bibliographic material
- · Cited material

- · Crossref Posted Content database
- Quoted material
- Small Matches (Less then 8 words)

# **CURRICULUM VITAE**

DIVYA GOEL goel.divya17@gmail.com +91-9811538400



### **OBJECTIVE**

To take my career to greater heights through innovation, research, excellence, ethics and to work in teaching intensive environment to explore my potentials, to enrich my knowledge and value addition for professional growth in the fast-growing area of Chemistry.

### **EDUCATIONAL QUALIFICATION**

Degree	Year of Completion	University/Board	Institution	%/CGPA
PhD	Ph.D. Submitted	Delhi Technological University	Applied Chemistry, Delhi Technological University	8.46/10
M.Sc.	2018-2020	Thapar University, Patiala	Thapar University, Patiala	8.63/10
B.Ed.	2016-2018	GGSIP University, Delhi	Gitarattan Institute of Advanced Studies and Training	9.09/10
B.Sc.	2013-2016	University of Delhi	Daulat Ram College, University of Delhi	66.1%
Class XII	2012-2013	CBSE	Sachdeva Public School, Pitampura	92.8%
Class X	2010-2011	CBSE	Sachdeva Public School, Pitampura	9.4/10

### **PUBLICATIONS**

### **Research Publications**

- Divya Goel, Deenan Santhiya, Subodh Kumar, Ajit Kumar Mahapatro. "Synthesis of Mesoporous Core Shell Magnetite Bioactive Glass Nanoparticles for Magnetic Hyperthermia Treatment of Cancer." "ChemistrySelect" 9 (2024): e202302119. (SCIE indexed) (Impact Factor: 2.307)
- **Divya Goel,** Deenan Santhiya. "Mesoporous bioactive glass nanoparticles with dopants bismuth and iron as magnetic photothermal agents for biomedical applications."" BioNanoScience" (2024). **(ESCI indexed) (Impact Factor:3.0)**

• **Divya Goel,** and Deenan Santhiya. "Effect of Magnesium and Bismuth Co-doping on Structural Optical and Bioactive properties of Bioactive Glass Nanoparticles for Biomedical Applications." Journal of Materials Research" (2024). (SCIE indexed) (Impact Factor: 3.0)

### **Book Chapters**

- Divya Goel, Deenan Santhiya, *Biosafety aspects of nanobiotechnology for use in livestock industries*, in Nanobiotechnology for the livestock industry, Elsevier (2023) pp.395-423. (Invited Book Chapter)
- Divya Goel, Deenan Santhiya, Controlling the Size, Shape, and Composition of Nanogel, in Nanogels: Fundamentals to Pharmaceutical and Biomedical Applications, Elsevier (2025) pp.395-420. (Invited Book Chapter)

### **Conference Proceedings/ Abstracts/ Articles**

- **Divya Goel**, Deenan Santhiya, "Synthesis and characterization of Bioactive glass Particles for Bone Cancer Treatment," Recent Developments on Materials, Reliability, Safety and Environmental issues, IMRSE 2021 organized by "Dr B R Ambedkar National Institute of Technology Jalandhar", India during 25-27 June, 2021 (oral presentation)
- **Divya Goel**, Deenan Santhiya, "Studies on bioactivity of Folic acid templated bioglass nanoparticles for bone regeneration," International online conference on Advanced Nanomaterials, ICAN 2021 organized by Gdansk University of Technology", India during 14 16 December, 2021. (oral presentation)
- **Divya Goel**, Deenan Santhiya, "In-situ mineralization of Bioactive glass Nanoparticles for Bone Cancer Treatment," Recent Advancements in Chemical Sciences: Health, Environment and Society, ICRACS 2022 organized by Deshbandhu College, University of Delhi, India during 8-9 April, 2022. (oral presentation)
- **Divya Goel**, Deenan Santhiya, "Bio-Inspired Route for Synthesis of Bioactive Glass Nanoparticles for treating Bone Ailments," International Analytical Conference and Exhibition, IAC 2022 organized by Graphic Era University and CSIR- Indian Institute of Petroleum, India during 26-28 May, 2022. (Poster Presentation)
- **Divya Goel**, Deenan Santhiya, "Synthesis of Bioactive glass nanoparticles by bio-inspired route for Bone regeneration," Platinum Jubilee Conference entitled 'Perspectives in Materials Research,' PMR 2022 organized by the Department of Materials Engineering, IISc, Bengaluru during 21-23, Dec 2022. (Poster Presentation)
- **Divya Goel**, Deenan Santhiya, "Bio-inspired Synthesis of Bioactive Glass Nanoparticles for Biomedical Applications," 1<sup>st</sup> International Conference on "Recent Trends in Chemical Sciences & Sustainable Energy", RTCSSE 2023 organized by National Institute of Technology Delhi and University of Delhi during 24-25 Mar, 2023. (Poster Presentation)
- **Divya Goel**, Deenan Santhiya, "Synthesis of Modified Bioactive Glass Nanoparticles for Biomedical Applications", Materials Today Conference, MATA 2023 organized by Elsevier in Singapore Expo, Singapore during 2-5 Aug 2023. (**Best Poster Award**)

### **RESEARCH EXPERIENCE**

### Indian Institute of Technology, Delhi

Summer Research Project in Organic Chemistry under supervision of Prof. V. Haridas, Indian Institute of Technology, Delhi on topic "Synthesis and UV-Visible Studies of BOC Tryptophan and Tryptophan Ester" for a period of 2 months. (1 June 2019- 29 July 2019)

#### **TEACHING EXPERIENCE DURING INTERNSHIP**

• Sovereign Public School, Rohini, Delhi

Taught Science and Chemistry from classes 6-12 for a period of 6 months. (2017)

• Mata Shiv Devi Sr. Sec. School, Keshav Puram, Delhi

Teaching of Science and Mathematics for a period of 1 month. (2016)

- M.Sc. Chemistry Practical at Department of Applied Chemistry, DTU, Delhi (2021-2024)
- B.Tech Chemistry Practical at Department of Applied Chemistry, DTU, Delhi (2021-2024)

#### **AREAS OF INTERESTS**

Material Science, Nanobiotechnology, Biochemistry, Bio-Physical studies, Nanotherapeutics

### SCIENTIFIC AND TECHNICAL SKILLS

- Analytical Techniques: Dynamic Light Scattering (DLS), TGA, XPS, Fourier transform infrared spectroscopy (FTIR), UV-Vis and Fluorescence Spectroscopy, X-ray Diffractometer (XRD), Scanning Electron Microscopy (SEM), Transmission Electron Microscopy (TEM), Dynamic Mechanical analyzer, Brunauer–Emmett–Teller (BET) machine, Magnetic measurements, Photoluminescence, In vitro hemolysis, MTT Assay, Bioactivity
- Software: ChemDraw, Origin, Image J, Xpert Hyscore
- Languages: English and Hindi (Native).
- Operating Systems: Linux, Windows, MACOS.
- Word Processors: Microsoft Word, Excel, and PowerPoint.
- Basic Knowledge of computational chemistry.
- Good Interpersonal and communication skills.
- Analytic and technical Problem-solving skills.
- Well versed with Internet Applications.

### **VOLUNTEER WORK**

- Teach underprivileged students under "MANTHAN" project.
- Valuable contribution in NAAC visits on 20-21 March 2017.
- Participated in "Faculty Development Programme" on 22 December 2017.
- Participated in National Seminar on "School teachers should be subjected to Psychometric Tests" as presenter on 2 February 2018.
- Awarded several certificates in Sanskrit and English Debate Competitions at school and state levels.
- Volunteer with NGO- Divya Jyoti Jagrati Sansthan.

### **PERSONAL DETAILS**

Date of Birth June 19, 1995

Gender Female Nationality Indian

Marital Status Single

Languages Known English, Hindi, Sanskrit

### **REFERENCE**

## • Dr. Deenan Santhiya (PhD Supervisor)

Assistant Professor, Department of Applied Chemistry, Delhi Technological University (Formerly Delhi College of Engineering (DCE)), Delhi 110042, India

Contact No. +91-9958580295 E - mail: deenan.santhiya@dce.ac.in